Impurity immersed in a two-component Fermi gas

Matthieu Pierce

PSL
UNIVERSITÉ PARIS

THÈSE DE DOCTORAT
DE L'UNIVERSITÉ PSL
Préparée à l'Ecole Normale Supérieure

Impurity immersed in a two-component Fermi gas

Impureté dans un gaz de Fermi à deux composantes

Soutenue par
Matthieu PIERCE
Le 20 septembre 2019

Ecole doctorale n°564
Ecole Doctorale Physique en Ile-de-France

Spécialité
Physique

Composition du jury :

Anna, MINGUZZI DR, CNRS	*Présidente du jury*
Selim, JOCHIM Professeur, Physikalisches Institut	*Rapporteur*
Thierry, LAHAYE CR, Institut d'optique	*Rapporteur*
Pietro, MASSIGNAN Chercheur, UPC	*Examinateur*
Frédéric, CHEVY Professeur, ENS	*Directeur de thèse*
Christophe, SALOMON DR, CNRS	*Membre invité*

ENS | PSL

Contents

Introduction

The macroscopic properties of a system are connected to the statistical distributions of its particles at the microscopic scale. In quantum physics, the form of the statistical distribution depends on the nature of the particles, with strong differences between fermions and bosons. Furthermore, particles are described by quantum mechanical wavefunctions. At low temperatures, when the extent of the particles wavefunctions becomes comparable to the inter-particle distance, the system is in the quantum degenerate regime: the particles manifest collective behaviors that differ strongly between bosons and fermions. In this thesis, we will study systems with many particles in the degenerate regime, or in other terms quantum many-body systems. At zero-temperature, the statistical distributions determine the characteristics of the ground state of non-interacting particles. The ground state of an ensemble of indistinguishable bosons is called a Bose-Einstein Condensate (BEC), for which all bosons are in the state of lowest energy, whereas identical fermions cannot be in the same quantum state, a principle known as Pauli exclusion principle [1], and the ground state of an ensemble of identical fermions is characterized by the occupation of the lowest energy states with one fermion each from bottom-up. On top of quantum statistical effects, interactions between individual particles can affect the ground state, modifying the microscopic properties as well as the macroscopic properties of the system. For instance, depending on the interactions, a fermionic or a bosonic ensemble can manifest superfluid properties, meaning they can flow without any viscosity.

Experimental evidence of the remarkable properties of a quantum many-body system was first obtained with the discovery of the superconductivity (absence of resistivity) of mercury, under a critical temperature of approximately 4.2 K, in 1911 by Kamerlingh Onnes [2], pioneering the study of the properties of such systems. In the following decades, several very unusual phenomena in many-body systems caused by the strong quantum correlations were unearthed. Such examples of unexpected properties are the superfluidity of bosonic liquid ^{4}He under a critical temperature of 2.17 mK, highlighted in the experiments of Kapitza [3] and Allen and Misener [4] in 1938, the superfluidity of fermionic liquid ^{3}He by Osheroff in 1970 [5], or, to give a different example, the fractional quantum Hall effect, first observed in 1982 [6, 7]. The deep understanding of such many-body systems is very challenging. Even if the Hamiltonian of the system is known, the dimension of the Hilbert space grows exponentially with the number of particles and the strong correlations add another layer of complexity to the system. The theoretical or numerical study of such systems is generally hindered by the absence of general methods so experimental works are strongly needed to help overcome these difficulties. For instance, although London understood that the superfluidity of liquid ^{4}He is connected to the Bose-Einstein condensation [8] only months after the discovery, the precise determination of the critical temperature requires the knowledge of the correlations in the system which is very challenging. Another example is the problem of superconductivity of certain metals at low temperature, that was only solved in the 1950's, more than forty years after the

experimental discovery: Bardeen, Schrieff and Cooper established the so-called BCS theory [9], explaining the superconductivity of the system by valence electrons pairing up thanks to an attractive interaction to form Cooper pairs. However, the discovery of a new type of superconductors in quasi-2D cuprates in 1986, with high critical temperature [10], was failed by BCS theory and has yet to be completely understood.

Ultracold quantum gases and quantum simulation

Quantum many-body systems are not restricted to condensed matter systems. Thanks to the development of laser technology following the seminal work of Kastler and Brossel on optical pumping in the 1950's [11], the cooling and trapping of cold atom gases was made possible in the 1980's using the radiation pressure of laser beams and magnetic fields [12]. The achievement of Bose-Einstein condensation in 1995 with alkali atoms [13, 14], and later in 1999 the obtention of a degenerate Fermi gas [15] marked the advent of the field of quantum gases. Following these discoveries, ultracold gases have proven to be an excellent system to study quantum properties observed in condensed matter [16], due to their high versatility. First, the trapping potential of the gas can be tailored to one's need: the trapping can be harmonic, box-like, periodic or even disordered [17] and it even enables to select the dimensionality of the system. Furthermore, the access to single atom resolution in recent experiments for atoms trapped in lattices or even propagating freely [18–24] gives access to multi-particle correlations (full counting statistics). Second, the interactions between the atoms are short-ranged and can be tuned experimentally with high precision using an external magnetic field through a Feshbach resonance [25]. This enables to explore all interaction regimes, from the ideal gas to a strongly interacting many-body system. Long-range interactions can also be obtained with the use of highly magnetic atoms [26–28], polar molecules [29] or Rydberg atoms [30]. Another possibility includes the coupling to artificial gauge fields to mimic the effect of a magnetic field or charged particles [31].

This high versatility has enabled to use ultracold quantum gases to perform quantum simulation. This notion, first introduced by R. Feynman in 1982 [32], consists in emulating the behavior of a strongly correlated quantum system, either theoretical or hard to investigate in condensed matter physics. Ultracold quantum systems can then be used to investigate the properties of strongly correlated condensed matter systems or even to verify the predictions made for more exotic systems such as neutron stars [33] or quark-gluon plasmas [34].

Many-body physics in ultracold quantum gases

Ultracold atoms have been used to investigate several types of many-body systems. The most emblematic one is the implementing of the Bose-Hubbard model [35], which describes the physics of interacting particles in a lattice, with the observation of a transition between a Mott insulating phase for strong on-site repulsive interactions and a superfluid state for lower interactions [36]. Mott insulators were observed for fermionic and bosonic species [37–39], and the quantum phase transition to a superfluid state was reported for bosons in [37]. Another important example is the study of strongly correlated quantum gases.

Bose gas

Since the obtention of a BEC in 1995, the weakly interacting Bose gas has been studied thoroughly experimentally. As it is condensed, we expect a superfluid behavior which was demonstrated experimentally through the observation of quantized vortices in a rotating cloud [40–42].

The strongly interacting Bose gas, accessible thanks to Feshbach resonances, is of great value since it bridges the gap between the ideal Bose gas and superfluid liquid Helium. Unfortunately, the lifetime of the gas is strongly reduced due to the enhancement of the losses near the resonance [43–45]. This phenomenon can be explained using three-body physics, in particular the Efimov effect, which predicts the existence of an infinite set of three-body bound states near the resonance.

Fermi gas

An ultracold two-component Fermi gas realizes the BCS-BEC crossover: depending on the interactions, the Fermi gas can go from a BCS-like behavior for weak attractive interactions to a BEC-like behavior for strong attractive interactions, as predicted by Leggett [46] as well as Nozières and Schmitt-Rink [47]. On the BEC side of the crossover, a bound-state between fermions of opposite spin exist and they can form dimers, bosonic in nature, that forms a BEC at low temperatures. On the BCS side of the crossover, fermions of opposite spins can form Cooper pairs that are stabilized by the Fermi sea, even though no bound-state exist. Superfluidity in a two-component Fermi gas is realized in the whole BEC-BCS crossover for low enough temperatures: on the BEC side the superfluidity is similar to that of a condensed Bose gas, whereas on the BCS side, the superfluidity is analogous to the superconductivity in metals explained by BCS theory. In-between those two regimes lies the unitary regime where fermions are interacting resonantly and exhibit remarkable properties such as a scale invariance and a high critical temperature for superfluidity.

This crossover can be explored experimentally by changing the interactions from weakly attractive to strongly attractive through the means of a Feshbach resonance [48]. Contrary to Bose gases, Fermi gases are stable, even in the strongly interacting regime: strongly interacting degenerate Fermi gases were obtained in many laboratories [49–54]. Superfluidity of the two-component Fermi gas was observed experimentally unambiguously through the gas reponse to a rotating confining potential, with a resistance to rotation in the low rotation speed regime [55] and the formation of quantized vortices in the large rotation speed regime [56]. Another experimental demonstration of superfluidity was obtained through the observation of the second sound in the unitary Fermi gas [57]: an entropy wave in which the superfluid phase and the normal phase of the gas oscillate with opposite phases.

The realization of Bose [58] and Fermi [59] gases in box-like potential, enabling to have homogeneous systems, opens new possibilities to study their properties and for instance look for new exotic phases such as the FFLO (Fulde, Ferrell, Larkin, Ovchinnikov) phase [60,61] characterized by Cooper pairs with non-zero momentum and spatial modulation of the order parameter. This phase can be observed in a two-component Fermi gas with imbalanced spin populations (partially polarized Fermi gas). The limiting case of a partially polarized Fermi gas is a Fermi sea with exactly one impurity, that presents very rich physics. The generalization of this system is the case of a single impurity immersed

in a many-body ensemble, that we present in the following paragraph.

Impurity in a many-body ensemble

While being one of the simplest problem in many-body physics, the physics of an impurity immersed in a many-body ensemble remains non-trivial and very rich.

One of the most fundamental examples is the polaron problem introduced by Landau in 1933 in a one-page long article [62]. In 1948, Landau and Pekar further described the properties of this system [63]. The term was introduced to describe the quasiparticle arising from the interactions between the conduction electron and its induced polarization in a polar semiconductor or an ionic crystal. The polaron problem then consisted in the study of the interactions between a charge carrier (electron, hole) and the phonons of an ionic crystal, described by a field-theoretical Hamiltonian derived by Frölich in 1954 [64]. This quasiparticle has different properties compared to the original impurity: in particular, it is characterized by an effective mass, a binding energy and a renormalized response to an external electric or magnetic field. The notion of polaron has then been generalized to describe various physical systems across all fields of physics that shares its general properties such as the polaronic exciton (exciton in a plar crystal), the spin polaron (phonons interacting with a magnon field), or the piezopolaron (quasiparticle arising from the piezoelectric interaction between an electron and acoustic phonons) [65].

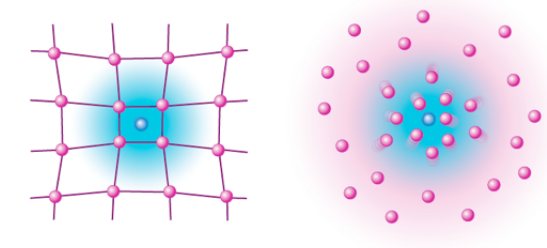

Figure 0.1: Sketch of a polaron in two different systems, where the interaction between the impurity and the background is attractive. On the left-hand side, the impurity is interacting with a crystal lattice, on the right-hand side the impurity is interacting with a background quantum gas.

The presence of impurities in a many-body system can affect its macroscopic properties in a spectacular way, with for instance the Kondo effect. In the 1930's, puzzling properties of gold were revealed: at low temperature, the resistivity of the material decreases with tempearture until it reaches a minimum at a non-zero temperature and then rise as the temperature is lowered even further [66]. This property was observed in other metals in the following years and was linked to the presence of impurities in the material [67] (iron impurities in this work). It is only in the early 1960's that Kondo suggested that this behavior was due to the presence of magnetic impurities in the metallic sample, and the possibility of a scattering process in which the internal spin state of the impurity and a scattered electron are exchanged [68]. The third order perturbative calculations he performed explained well the presence of a minimum but lead to a divergence of the resisitivity of the material as $T \to 0$. This problem, known as the Kondo problem, was

revisited in 1975 by Wilson [69], using a non-perturbative renormalization group method based upon the seminal work of Anderson on localized magnetic impurities immersed in a Fermi sea [70].

Even the presence of one impurity can drastically modify the properties of the many-body background as introduced in the historical problem of Anderson's orthogonality catastrophe (AOC) in 1967 [71]. Anderson showed that when a motionless impurity is introduced in a Fermi sea, the ground state of this now perturbed system becomes orthogonal to the ground state without the impurity, with an overlap between the two states that decreases with the size of the system with a power law. In cold atoms, an impurity immersed in a Fermi sea can be dressed by the background and forms a polaronic quasiparticle, but due to AOC, a motionless impurity or a heavy impurity will not form a quasiparticle. The decoherence of "massive" ^{41}K impurities immersed in a Fermi sea of ^{6}Li was measured in Innsbruck [72, 73], and direct observation of AOC may be realized in this group by pinning the potassium atoms using a deep species-selective optical lattice [74] to render them effectively motionless.

Other impurity problems can be found also in high energy physics, for instance in neutron stars where protonic impurities can interact with the background neutronic superfluid [75, 76], or in quantum chromodynamics where the Polyakov loop describes the properties of a test color charge in a hot gluonic medium [77].

Furthermore, the impurity problems can be used as toy-models for more complex many-body problems [78] for instance in the case of dynamical mean-field approaches [79]: the idea is to replace a lattice model by a single-site quantum impurity problem, with a self-consistency condition that encompasses the translation invariance and coherence effects of the lattice, an approach also known as LISA (local impurity self-consistent approximation). This mapping provides a simpler description of highly-correlated systems, and may be used for instance to solve the Kondo problem in a lattice system, or to study Heavy fermions systems [80, 81] (Ce or U based metallic compounds with a strongly enhanced effective mass for the conduction electrons, up to 1000 times the mass of an electron).

An impurity in a system can also be used to probe experimentally the properties of the background system itself, acting as a test particle. For instance, the observation of the crossover from few-body physics to many-body physics of a fermionic ensemble was studied via the measurement of the interaction energy between an impurity and a few indistinguishable fermions [82] in a quasi one-dimensional trap. This study revealed a rapid convergence to the many-body limit of a single impurity in a Fermi sea, showing that the many-body description is already valid for a very low number of fermions in the background (in [82] for $N \geq 5$).

In this thesis, we focus on the problem of an impurity immersed in a two-component Fermi gas, which is analogous to the original polaron problem. An impurity immersed in a Fermi sea is called a Fermi polaron and an impurity immersed in a BEC is called a Bose polaron, with both systems described in details in Chapter 2. In the last chapter of this thesis, we will see how our specific impurity problem bridges between the Fermi polaron and the Bose polaron thanks to the crossover between the BCS and the BEC limits.

Outline of this thesis

This thesis is divided in six chapters.

- In the first chapter, we focus on the characterization of interactions in cold atoms systems. Starting with two-body interactions, we introduce the scattering length, a single parameter that encompasses all the details of the interaction potential for low-energy scattering physics. We will see how the interactions can be tuned with high precision by changing the magnetic field thanks to Feshbach resonances. Lastly, we will briefly describe three-body physics and the Efimov effect.

- In the second chapter, we will present the physics of ultracold quantum gases. Starting with the ideal Bose and Fermi gas, we will then study the effect of interactions on these many-body systems. In the case of a two-component Fermi gas, we will investigate the BCS-BEC crossover, and introduce the two-body fermionic contact C_2 to encapsulate the short-range correlations of this many-body system. Finally, the problem of an impurity in a quantum gas will be explored with the study of the Fermi and the Bose polaron.

- In the third chapter, we present an overview of the experimental set-up used to obtain a degenerate Bose-Fermi mixture. We also present the physics of ultracold gases trapped harmonically and our techniques to obtain the physical characteristics of the Bose-Fermi mixture using absorption imaging.

- In the fourth chapter, we present experimental results obtained in [83], on the lifetime of an impurity in a two-component Fermi gas and show how this measurement yields a measurement of the fermionic two-body contact C_2. We measure the contact on the BEC side and at unitarity, and we present some preliminary results on the measurement of the contact at finite temperature at unitarity.

- In the fifth chapter, we present experimental results obtained in [84] on the counterflow of an impurity and a superfluid Fermi gas. We observe long-lived oscillations and the study of their frequency informs us on the interactions between the impurity and the Fermi superfluid. We then investigate the damping of these oscillations that arise at high amplitude that we interpret as the presence of a critical velocity, characteristic of superfluids, or at high temperature due to the loss of superfluidity.

- Finally, in the last chapter, we investigate theoretically the properties of an impurity immersed in a superfluid. After giving a brief overview of the phase diagram of the system, we focus on the calculation of the energy of the polaron beyond the mean-field approximation. We highlight a logarithmic divergence of the second order perturbative calculation that we regularize thanks to an insight from the three-body problem. Lastly, we analyze the consequences of this energy calculation on the experimental results presented in the fifth chapter.

Chapter 1

Interactions in cold atoms

The study of interactions in ultracold gases is essential to explain fully their properties. We will present in this chapter the main concepts underlying the interactions between the atoms that constitute such systems. We will start by describing the interactions between two particles and build the simplest potential that can describe them without omitting important details, by studying the low-energy scattering of two particles. We will then see how we can tune experimentally these interactions through the use of Feshbach resonances. Finally, we will review some aspects of three-body physics that can affect strongly interacting quantum gases.

1.1 Interactions between two particles

To describe the interactions that take place in a quantum many-body system, we have to start with the interactions between two particles.

1.1.1 Interaction potential

The typical shape of the interaction potential is given in Fig. 1.1. The generic interaction potential between two atoms is the sum of a repulsive interaction at short distance with a strong electron exchange repulsive barrier [85] and an attractive interaction at long distance, corresponding to a Van der Waals interaction arising from their induced dipoles. The attractive interaction between two lithium atoms is behaving as $-C_6/r^6$. From this potential, we can build dimensionally the Van der Waals length $l_{VdW} = \frac{1}{2}\left(\frac{mC_6}{\hbar^2}\right)^{1/4}$, typically a few nanometers for alkali atoms, which corresponds to the range of this potential.

The interaction potential can present several bound states, with the deepest bound states having binding energies of the order of several hundred Kelvins.

Experiments with ultracold atoms operate in a regime where the typical size of the wavepackets, given by the De Broglie wavelength λ_{dB}, is much bigger than l_{VdW}. Consequently, in a first approximation, the atoms do not feel the details of the interaction potential. This limit constitutes the universal limit: physical systems that are completely different at short distances exhibit similar behaviors at long distances. Hence we want to find a simplified expression of this potential that can still describe accurately the behavior of cold atom gases. In order to do so, we will first study the collisions between two particles interacting with a potential V and characterize their scattering properties.

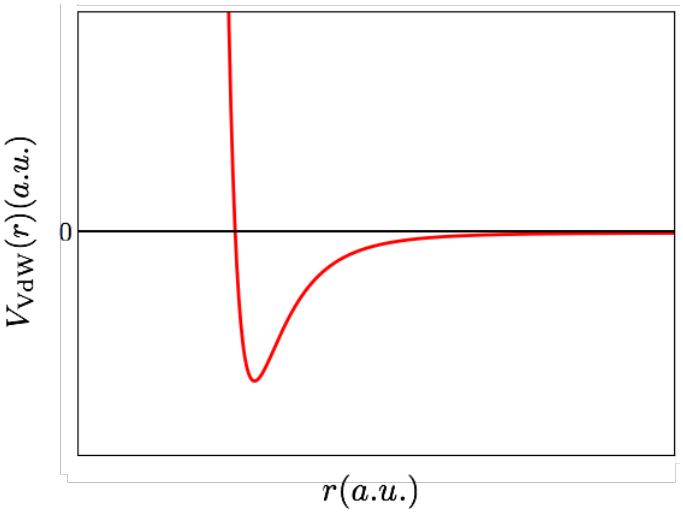

Figure 1.1: Shape of the interaction potential V_{VdW}. The sum of an attractive attraction at long distances and a repulsive barrier at small distances induces a minimum of the potential and several possible bound states for negative energies.

1.1.2 Low-energy scattering theory

Scattering amplitude and differential cross-section

We will work from now on in the center-of-mass frame of the two interacting particles. The problem for two particles of mass m_1 and m_2, with positions $\boldsymbol{r}_1$ and $\boldsymbol{r}_2$, is reduced to a one-body problem for a particle of reduced mass $m_r = \frac{m_1 m_2}{m_1+m_2}$ and position $\boldsymbol{r} = \boldsymbol{r}_2 - \boldsymbol{r}_1$. In that case, stationary states must obey the Schrödinger equation

$$\widehat{H}\psi(\boldsymbol{r}) = \left[-\frac{\hbar^2}{2m_r}\nabla^2 + V(\boldsymbol{r})\right]\psi(\boldsymbol{r}) = E\psi(\boldsymbol{r}), \tag{1.1}$$

where V is the interacting potential of range b[1] and E the energy of the stationary state.

For negative energies E, we obtain the bound states mentioned in the previous section. For positive energies E, the two particles will scatter. In the center-of-mass frame, this problem amounts to the scattering of an incident planewave of momentum $\boldsymbol{k}$ on a potential V. We represent schematically this situation in Fig. 1.2, and we define two unitary vectors $\boldsymbol{n} = \boldsymbol{k}/k$, which corresponds to the direction of propagation of the incoming wavepacket, and $\boldsymbol{n}' = \boldsymbol{r}/r$, the direction in which it is scattered.

At long distance, the stationnary scattering state ψ obeys the following asymptotic form

$$\psi(\boldsymbol{r}) \underset{r\gg b}{\simeq} e^{i\boldsymbol{k}.\boldsymbol{r}} + f(k,\boldsymbol{n},\boldsymbol{n}')\frac{e^{ikr}}{r} = \psi_0(\boldsymbol{r}) + \psi_{\mathrm{sc}}(\boldsymbol{r}). \tag{1.2}$$

This solution corresponds to the sum of the incident plane wave $|\psi_0\rangle$ and of a spherical wave $|\psi_{\mathrm{sc}}\rangle$ centered on the center of the potential, with an amplitude determined by the function f called the scattering amplitude and which has the dimension of a length.

This scattering amplitude is linked to another important physical quantity, the differential scattering cross-section $\frac{\mathrm{d}\sigma}{\mathrm{d}\Omega}$, which corresponds to the number of particles scattered in the solid angle $\mathrm{d}\Omega$ per unit time over the number of incident particles per unit of area

[1] For a Van der Waals interaction, $b = l_{\mathrm{VdW}}$.

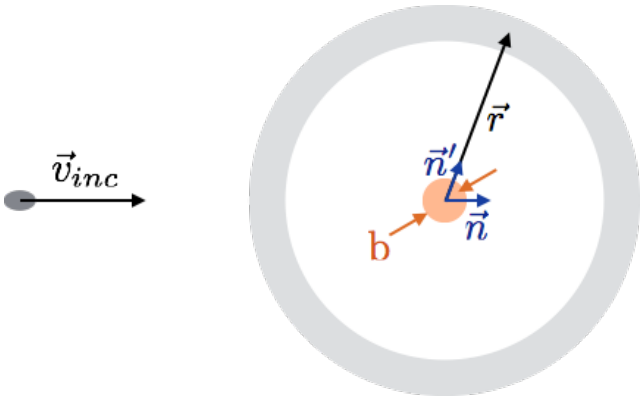

Figure 1.2: Schematics of the scattering problem. An incoming wave plane of wavevector $\boldsymbol{k} = m\boldsymbol{v}_{\text{inc}}/\hbar$ is scattered by a potential V which range b is represented in orange. The unitary vectors $\boldsymbol{n}$ and $\boldsymbol{n}'$ defined in the text are represented in blue.

and time, thus describing how efficient the scattering is in a given direction. They are related through the simple equation

$$\frac{\mathrm{d}\sigma}{\mathrm{d}\Omega} = |f(k, \boldsymbol{n}, \boldsymbol{n}')|^2 . \tag{1.3}$$

Low energy limit

The scattering states can be expanded onto a basis of partial spherical waves indexed by the associated angular momentum quantum number ℓ. A centrifugal barrier term of order $\ell(\ell+1)\hbar^2/m_r b^2 \gtrsim$ mK strongly suppress partial waves with $\ell > 0$ at low temperatures, so the scattering in ultracold systems is purely s-wave. In this low-energy limit, f is isotropic and does not depend on the directions $\boldsymbol{n}$ and $\boldsymbol{n}'$ anymore: it can be written simply as $f(k)$.

For indistinguishable particles, the symmetrization (or anti-symmetrization) of the wave function leads to $\mathrm{d}\sigma = |f(k, \boldsymbol{n}, \boldsymbol{n}') + \epsilon f(k, \boldsymbol{n}, -\boldsymbol{n}')|^2 \mathrm{d}\Omega$ with $\epsilon = 1$ for identical bosons and $\epsilon = -1$ for identical fermions. In the low-energy limit, since f does not depend on $\boldsymbol{n}$ and $\boldsymbol{n}'$, we obtain the well-known result that two identical fermions do not interact via s-wave channel ($\mathrm{d}\sigma = 0$).

Furthermore, when $k \to 0$, f has a limit that we will express as

$$\lim_{k\to 0} f(k) = -a \tag{1.4}$$

where a is called the scattering length, with values which can vary from $-\infty$ to $+\infty$. The regime in which a goes to infinity is called the unitary regime.

It is also possible to go beyond this simple limit, in which case the s-wave scattering amplitude can also be expanded in powers of k and reads [86]

$$\frac{1}{f(k)} \underset{k\to 0}{=} -\left(1/a + ik - \frac{1}{2} r_e k^2\right), \tag{1.5}$$

with r_e the effective range of the interaction. Systems that can be appropriately described in the limit $a \gg r_e$ are universal, with the behavior at long distances well described by a scattering amplitude that only depends on the scattering length a. As soon as r_e is needed, the system can no longer be considered universal.

In the low-energy limit, we have simply $\mathrm{d}\sigma/\mathrm{d}\Omega = |f(k)|^2$, and a total cross-section $\sigma_{\mathrm{tot}} = 4\pi|f(k)|^2$. For $k \to 0$, we obtain $\sigma_{\mathrm{tot}} = 4\pi a^2$ for distinguishable particles ($\sigma_{\mathrm{tot}} = 8\pi a^2$ for identical bosons) so we can interpret the scattering length a as the effective size of the atoms for the collision problem.

In the unitary regime, the cross-section does not diverge but rather "saturates". Using eq. (1.5), we find that the cross-section has the universal behavior $\sigma \sim 4\pi/k^2$ for two distinguishable particles and $\sigma \sim 8\pi/k^2$ for two identical bosons.

In short, the scattering length a encapsulates the details of the potential into a single parameter describing the low-energy scattering properties.

1.1.3 Born's approximation

We want to explicit the relation between the interaction potential V and the scattering properties. The goal of this paragraph is to do it at the lowest order in V that gives a finite result. This approximation is known as the Born approximation.

Scattering amplitude in Born's approximation

To introduce Born's approximation, we will focus on the expression of the scattered state $|\psi\rangle$ as a function of the incoming planewave $|\psi_0\rangle = |k_0\boldsymbol{n}\rangle$.

We can show readily using the Schrödinger equation that the stationary scattering states $|\psi\rangle$ are also solutions of the Lippman-Schwinger equation

$$|\psi\rangle = |\psi_0\rangle + \widehat{G}_0(E_0)\widehat{V}|\psi\rangle \tag{1.6}$$

where $|\psi_0\rangle$ is the incident plane wave, G_0 is the retarded Green function with $G_0(E) = (E + i\epsilon - \widehat{H}_0)^{-1}$ with $\widehat{H}_0$ the hamiltonian of the free particles without interactions, and E_0 is the energy of the incident plane wave $|\psi_0\rangle$.

We see that this equation is an implicit equation on $|\psi\rangle$ and may be written as an expansion

$$|\psi\rangle = |\psi_0\rangle + \widehat{G}_0(E_0)\widehat{V}|\psi_0\rangle + \widehat{G}_0(E_0)\widehat{V}\widehat{G}_0(E_0)\widehat{V}|\psi_0\rangle + ... \tag{1.7}$$

The Born approximation consists here in keeping the first order term in $\widehat{V}$, yielding the expression

$$|\psi^{Born}\rangle = |\psi_0\rangle + \widehat{G}_0(E_0)\widehat{V}|\psi_0\rangle \tag{1.8}$$

In the position space, it reads

$$\psi^{Born}(\boldsymbol{r}) = \psi_0(\boldsymbol{r}) + \int \mathrm{d}^3\boldsymbol{r}' G_0(E_0, \boldsymbol{r} - \boldsymbol{r}')V(\boldsymbol{r}')\psi_0(\boldsymbol{r}') \tag{1.9}$$

where $\boldsymbol{r} = r\boldsymbol{n}'$, with $\boldsymbol{n}'$ the direction in which the particle is scattered.

The expression of $G_0(E_0, \boldsymbol{r} - \boldsymbol{r}')$ can be calculated readily from its definition, and we obtain

$$\psi^{Born}(\boldsymbol{r}) = e^{i\boldsymbol{k}_0.\boldsymbol{r}} - \frac{m_r}{2\pi\hbar^2}\int \mathrm{d}^3\boldsymbol{r}' \frac{e^{ik_0|\boldsymbol{r}-\boldsymbol{r}'|}}{r - r'}V(\boldsymbol{r}')\psi_0(\boldsymbol{r}) \tag{1.10}$$

The potential $V(\boldsymbol{r}')$ is negligible for $r' > b$ with b the range of the potential. At long distances $r \gg b$, we can simplify this expression as

$$\psi^{Born}(\boldsymbol{r}) = e^{ik_0\boldsymbol{n}.\boldsymbol{r}} - \frac{m_r}{2\pi\hbar^2}\frac{e^{ik_0 r}}{r}\int \mathrm{d}^3\boldsymbol{r}' e^{ik_0\boldsymbol{n}'.\boldsymbol{r}'}V(\boldsymbol{r}')\psi_0(\boldsymbol{r}') \tag{1.11}$$

Identifying this expression with eq. (1.2), we deduce

$$f^{\mathrm{Born}}(k_0, \boldsymbol{n}, \boldsymbol{n}') = -\frac{m_r}{2\pi\hbar^2}\int \mathrm{d}^3\boldsymbol{r}' e^{ik_0\boldsymbol{n}'.\boldsymbol{r}'}V(\boldsymbol{r}')\psi_0(\boldsymbol{r}') = -\frac{m_r\Omega}{2\pi\hbar^2}\langle k_0\boldsymbol{n}'|\widehat{V}|k_0\boldsymbol{n}\rangle \quad (1.12)$$

with Ω the quantization volume.

Zero-range limit

Since we saw that in cold atoms experiment the atoms do not see the details of the potential, the simplest model that we can consider is actually a contact interaction. In this case, the simplest contact interaction we can write is a delta function:

$$V(\boldsymbol{r}) = g^{\mathrm{Born}}\delta(\boldsymbol{r}) \quad (1.13)$$

where g^{Born} is the coupling constant with the dimension of an energy times a volume. This is what we will call the pseudopotential.

In this limit, we have $\langle k_0\boldsymbol{n}'|\widehat{V}|k_0\boldsymbol{n}\rangle = g^{\mathrm{Born}}/\Omega$, and using eq. (1.12) we deduce a relation between the coupling constant g^{Born} and the scattering length in the Born approximation. We obtain:

$$g^{\mathrm{Born}} = \frac{2\pi\hbar^2 a}{m_r} \quad (1.14)$$

Therefore, we find that as long as we take the value from eq. (1.14) for the coupling constant in the expression of the pseudopotential, the physics of the atomic gas will be the same when considered in the Born approximation.

Beyond Born approximation...

We can wonder now what happens if we want to use this expression of the pseudopotential to describe physics beyond the Born approximation. For instance, we can focus on the second order expansion of the scattered state. The perturbative expansion of the scattered state reads up to second order, for an interaction described by the zero-range pseudopotential, in the direction $\boldsymbol{n}'$

$$\langle \boldsymbol{k}'|\psi\rangle = \langle \boldsymbol{k}'|\psi^{Born}\rangle + \langle \boldsymbol{k}'|\widehat{G}_0(E_0)\widehat{V}\widehat{G}_0(E_0)\widehat{V}|\psi_0\rangle \quad (1.15)$$

To evaluate the second-order term, we introduce completeness relations and use the fact that

$$\langle \boldsymbol{k}_1|\widehat{G}_0(E_0)|\boldsymbol{k}_2\rangle = \frac{\delta_{k_1,k_2}}{E_0 + i\epsilon - E_{\boldsymbol{k}_1}} \quad (1.16)$$

to obtain

$$\langle \boldsymbol{k}'|\psi\rangle = \langle \boldsymbol{k}'|\psi^{Born}\rangle + \langle \boldsymbol{k}'|\widehat{G}_0(E_0)|\boldsymbol{k}'\rangle\frac{(g^{\mathrm{Born}})^2}{\Omega^2}\sum_{\boldsymbol{k}''}\frac{1}{E_0 + i\epsilon - \varepsilon^{(r)}_{k''}} \quad (1.17)$$

with $\varepsilon^{(r)}_{k''} = \hbar^2 k''^2/2m_r$.

We can see that the sum that appears in the second-order term behaves as $\sum_{\boldsymbol{k}} 1/k^2$, which is highly divergent (the sum is over the three dimensions) when $k \to \infty$. In conclusion, we saw with this example that as soon as we want to study the scattering problem beyond Born's approximation, the pseudopotential from eq. (1.13) with $g = g^{\mathrm{Born}}$ fails miserably. To overcome this issue, we introduce in the next paragraph the T-matrix formalism.

1.1.4 Transition matrix

Definition

In order to solve the scattering problem out of Born's approximation, we go back to the Lippman-Schwinger equation defined in eq. (1.6). We then define the transition matrix or more simply the T-matrix as an operator satisfying the relation

$$\widehat{T}(E_0)|\psi_0\rangle = \widehat{V}|\psi\rangle \tag{1.18}$$

where the transition operator depends on the energy E_0 of the initial state $|\psi_0\rangle$ (conserved during the collision).

We can then inject eq. (1.18) into eq. (1.6) and we get

$$|\psi\rangle = \left(1 + \widehat{G}_0(E_0)\widehat{T}(E_0)\right)|\psi_0\rangle \tag{1.19}$$

The equation is now explicit in $|\psi\rangle$ and we see how we can calculate the *transition* between the incident state $|\psi_0\rangle$ and the scattered state $|\psi\rangle$. Following the same reasoning as in section 1.1.3, without using an expansion of the scattered state $|\psi\rangle$, we can show that

$$f(k, \boldsymbol{n}, \boldsymbol{n}') = -\frac{m_r\Omega}{2\pi\hbar^2}\langle k_0\boldsymbol{n}'|\widehat{T}|k_0\boldsymbol{n}\rangle \tag{1.20}$$

We have then obtained an exact expression of the scattering amplitude, which involves the matrix elements of the transition operator.

Dyson equation

We want to obtain an expression for $\widehat{T}$ that can be used more easily than eq. (1.18). For this purpose, we combine eq. (1.18) and (1.19) to finally deduce that the operator T satisfies an implicit equation:

$$\widehat{T}(E_0)|\psi_0\rangle = \widehat{V}|\psi\rangle = \left(\widehat{V} + \widehat{V}\widehat{G}_0(E_0)\widehat{T}(E_0)\right)|\psi_0\rangle \tag{1.21}$$

yielding the Dyson equation

$$\widehat{T}(E_0) = \widehat{V} + \widehat{V}\widehat{G}_0(E_0)\widehat{T}(E_0). \tag{1.22}$$

From this last equation, we can get another insight on the Born approximation. Indeed, the implicit Dyson equation defining the transition operator seems like a perfect basis for a perturbative expansion. Indeed, eq. (1.22) can be expanded as

$$\widehat{T}(E_0) = \widehat{V} + \widehat{V}\widehat{G}_0(E_0)\widehat{V} + \widehat{V}\widehat{G}_0(E_0)\widehat{V}\widehat{G}_0(E_0)\widehat{V} + ... \tag{1.23}$$

The Born approximation consists in simply stopping this expansion at the leading order $\widehat{T}_{\text{Born}} = \widehat{V}$. The issue we get when we want to go beyond Born's approximation is that the expansion we wrote for the T-matrix is not always convergent, at least not for the pseudopotential we obtained in the previous paragraph. This pseudopotential thus needs to be regularized, as we will see in the next paragraph.

1.1.5 Regularization of the pseudopotential

We start again with a simple contact interaction, written as a delta function:

$$V(\boldsymbol{r}) = g_0 \delta(\boldsymbol{r}) \tag{1.24}$$

where the coupling constant g_0 is not assumed to be equal to g^{Born}.

The coupling constant g_0

To go beyond the approximation, we have to calculate the matrix element $\langle \boldsymbol{k}'|\widehat{T}|\boldsymbol{k}\rangle$, with $\boldsymbol{k} = k\boldsymbol{n}$ and $\boldsymbol{k}' = k\boldsymbol{n}'$. To do this, we expand the Dyson equation, whose diagrammatic representation is given in Fig. 1.3:

$$\langle \boldsymbol{k}'|\widehat{T}|\boldsymbol{k}\rangle = \langle \boldsymbol{k}'|\widehat{V}|\boldsymbol{k}\rangle + \langle \boldsymbol{k}'|\widehat{V}\widehat{G}_0(\varepsilon_k^{(r)})\widehat{V}|\boldsymbol{k}\rangle + ... \tag{1.25}$$

where $\varepsilon_k^{(r)} = \hbar^2 k^2/2m_r$ the energy of the particle with the reduced mass m_r in the center-of-mass frame.

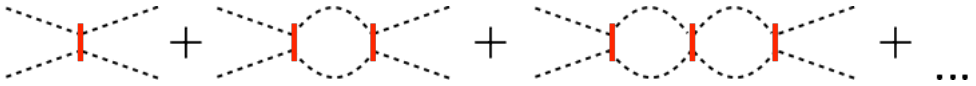

Figure 1.3: Diagrammatic representation of the expansion of the matrix element $\langle \boldsymbol{k}'|\widehat{T}|\boldsymbol{k}\rangle$ using the Dyson equation.The dashed lines correspond to the two particles. Each vertical red line correspond to an interaction term $\widehat{V}$, and in-between two red lines there is a propagation term $\widehat{G}_0$.

This expansion can be written as a geometric sum by introducing the completeness relations between two subsequent operator and yields:

$$\langle \boldsymbol{k}'|\widehat{T}|\boldsymbol{k}\rangle = \frac{g_0/\Omega}{1 - \frac{g_0}{\Omega}\sum_{\boldsymbol{k}''} \frac{1}{\varepsilon_k^{(r)} + i\epsilon - \varepsilon_{k''}^{(r)}}} \tag{1.26}$$

We now take the limit $k \to 0$ to connect this expression to the scattering length and we get

$$a = \frac{m_r \Omega}{2\pi\hbar^2} \frac{g_0/\Omega}{1 - \frac{g_0}{\Omega}\sum_{\boldsymbol{k}''} \frac{-1}{\varepsilon_{k''}^{(r)}}}. \tag{1.27}$$

By using the inverse of this expression, we finally write

$$\frac{1}{g_0} = \frac{1}{g} - \frac{1}{\Omega}\sum_{\boldsymbol{k}''} \frac{1}{\varepsilon_{k''}^{(r)}} \tag{1.28}$$

In this last expression, the sum is highly divergent. We need to introduce a UV-cutoff Λ in momentum space, so now g_0 becomes a running coupling constant $g_0(\Lambda)$, and the sum is performed over $\boldsymbol{k}''$, $k'' < \Lambda$. We will thus call it the "bare" coupling constant as opposed to $g = 2\pi\hbar^2 a/m_r$ which is finite and therefore called the"physical" coupling constant (and coincides with what we obtained in Born's approximation). This regularization is inherent of the nature of the pseudopotential itself and the zero-range

limit that was taken, the UV-cutoff Λ is related to the inverse of the effective range of the potential r_e.

We see that when Λ increases, the sum over k starts dominating eq. (1.28) and $g_0(\Lambda)$ is small and negative. This fact that it is negative means that we have an attractive potential, and provides an illustration that a zero-range approximation can only be achieved with attractive potentials; for a purely repulsive potential there is always a finite range $\gtrsim a$. The fact that $g_0(\Lambda)$ becomes vanishingly small when the cutoff increases is also expected, because the divergence that comes from decreasing the effective range of the potential must be compensated by decreasing the coupling constant.

For the two-body problem, we can then apply this regularization of the pseudopotential inspired from renormalization techniques. Other regularization approaches exist, such as the use of Bethe-Peirls boundary conditions [87] or corrected expressions of the pseudopotential [88, 89], but we will stay within this approach for the remaining of this thesis.

Calculation of $f(k)$

Now that we have an expression for the bare coupling constant g_0, we can calculate the full scattering amplitude $f(k)$ in the zero-range limit. We come back to eq. (1.26) and we write

$$\Omega\langle \boldsymbol{k}'|\widehat{T}|\boldsymbol{k}\rangle = \frac{1}{\frac{1}{g_0} - \frac{1}{\Omega}\sum\limits_{\boldsymbol{k}'',\, k''<\Lambda} \frac{1}{\varepsilon_k^{(r)} + i\epsilon - \varepsilon_{k''}^{(r)}}} \tag{1.29}$$

$$\Omega\langle \boldsymbol{k}'|\widehat{T}|\boldsymbol{k}\rangle = \frac{1}{\frac{1}{g} - \frac{1}{\Omega}\sum\limits_{\boldsymbol{k}'',\, k''<\Lambda} \left[\frac{1}{\varepsilon_k^{(r)} + i\epsilon - \varepsilon_{k''}^{(r)}} + \frac{1}{\varepsilon_{k''}^{(r)}}\right]} \tag{1.30}$$

where Λ is the UV-cutoff that can now be set to infinity since the sum in the last expression is convergent after using the regularization of g_0.

The sum at the denominator can be calculated using the residue theorem and performing an integration over the upper part of the complex plane (positive imaginary parts). We get

$$\frac{1}{\Omega}\sum_{\boldsymbol{k}''}\left[\frac{1}{\varepsilon_k^{(r)} + i\epsilon - \varepsilon_{k''}^{(r)}} + \frac{1}{\varepsilon_{k''}^{(r)}}\right] = -\frac{im_r}{2\pi\hbar^2}k \tag{1.31}$$

which gives for the expression of the s-wave scattering amplitude in the zero-range limit

$$f(k) = \frac{-a}{1+ika} \tag{1.32}$$

We see that we recover the expression of the scattering amplitude we gave with eq. (1.5), but with an effective range $r_e = 0$, consistent with the zero-range limit we are in.

1.2 Feshbach resonance

To change the interaction strength between two atoms, we have to modify their associated scattering length. We will see in this section how we can vary widely the scattering length a by taking advantage of Feshbach resonances. Those resonances are described in details in [25, 86] and we will sum up their principal properties in this section.

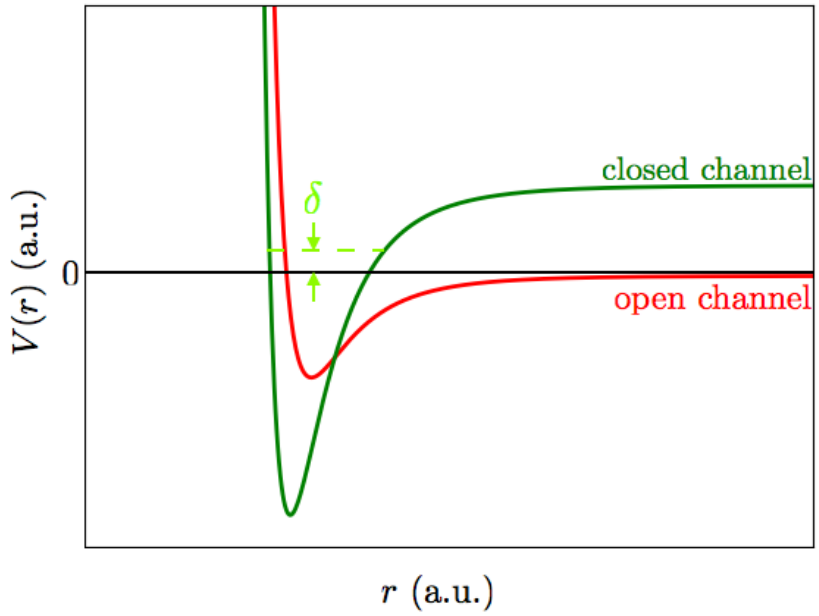

Figure 1.4: Schematics of the potential corresponding to the open (red) and closed (green) channels. The light green dashed line in the closed channel correspond to the energy of the bound state E_{res}. The orange arrow symbolizes the entrance of a pair of atoms of energy E in the open channel.

Feshbach resonances can occur when two atoms in their respective initial spin states can be coupled to different states during their collision. The initial spin state configuration is called the entrance channel or open channel and the other state to which they can be coupled is the closed channel, not accessible energetically at low temperatures. The resonance takes place when the energy of the pair of colliding atoms of mass m initially in the open channel is close to the energy of a bound state in the closed channel. We call δ the difference in energy between the bound state in the closed channel and the continuum threshold of the open channel. This is represented in Fig. 1.4, where we plotted two potentials of the Van der Waals kind for the open and closed channels. The closed channel can actually have several bound states but in general it is sufficient to consider only one to describe the resonance [90].

To take advantage of a Feshbach resonance, the shift δ must be tunable with an external parameter, such as the magnetic field. When $\delta \to 0$, the bound-state becomes resonantly coupled to the diffusive states of the open channel and leads to a divergence of the scattering length.

1.2.1 Two-channel model

To investigate the main characteristics of a Feshbach resonance, we can use a two-channel model [91]. We introduce an effective two-body Hamiltonian, in which we explicitly add a molecular state of energy δ as well as a coupling term between the two channels. The effective coupling $\tilde{g}_k$ between the channels is proportional to the overlap between the diffusion state of momentum $\hbar\boldsymbol{k}$ in the open channel and the molecular state in the closed

channel. In the center-of-mass frame, we only have a one-body problem for which the Hamiltonian reads:

$$\underbrace{\sum_{\boldsymbol{k},\sigma} \varepsilon_k^{(r)} a^\dagger_{\boldsymbol{k},\sigma} a_{\boldsymbol{k},\sigma} + \delta b^\dagger b}_{\widehat{H}_0} + \underbrace{\sum_{\boldsymbol{k}} \frac{\tilde{g}_k}{\sqrt{\Omega}} \left(b^\dagger a_{\boldsymbol{k},\uparrow} a_{-\boldsymbol{k},\downarrow} + a^\dagger_{\boldsymbol{k},\uparrow} a^\dagger_{-\boldsymbol{k},\downarrow} b \right)}_{\widehat{V}} \tag{1.33}$$

where $a^\dagger_{\boldsymbol{k},\sigma}$ is an operator that creates a fermion of spin σ and momentum $\boldsymbol{k}$ in the open channel and $b^\dagger$ is the creation operator of a molecule in the bound state of the closed channel. Since we work in the center-of-mass frame, there is no need to consider the momentum of the molecule.

In order to recover the scattering length in this model, we calculate the matrix elements $\langle \boldsymbol{k}|\widehat{T}|\boldsymbol{k}'\rangle$ of the T-matrix, where the state $|\boldsymbol{k}\rangle$ correspond to a pair of atom of relative momentum $\boldsymbol{k}$ in the open channel in the center-of-mass frame. To calculate this matrix element, we will as usual do an expansion of the transition operator in $\widehat{V}$, and since we want the initial and final states to be both in the open channel, there must be an even number of interactions $\widehat{V}$ in each term of the expansion. A diagrammatic representation of each term is given in Fig. 1.5.

Figure 1.5: Diagrammatic representation of the expansion of the matrix element $\langle \boldsymbol{k}'|\widehat{T}|\boldsymbol{k}\rangle$ in the two-channel model.The dashed lines correspond to free atoms, whereas the solid black lines correspond to the atoms in the molecular state. Each vertical red line correspond to an interaction term $\widehat{V}$, and in-between two red lines there is a propagation term.

The first term of the expansion reads

$$\langle \boldsymbol{k}'|\widehat{V}\widehat{G}_0\widehat{V}|\boldsymbol{k}\rangle = \frac{g^*_{k'}}{\sqrt{\Omega}} \frac{1}{\varepsilon_k^{(r)} - \delta} \frac{g_k}{\sqrt{\Omega}} \tag{1.34}$$

The following terms can be calculated similarly, with the propagation term for the free atoms (dashed vertices in the diagrams) corresponding to a sum of the type $\frac{1}{\Omega}\sum_{\boldsymbol{q}} |g_q|^2/(\varepsilon_k^{(r)} - \varepsilon_q^{(r)})$. The total is again a geometric sum and we get:

$$\langle \boldsymbol{k}'|\widehat{T}|\boldsymbol{k}\rangle = \frac{\tilde{g}_k \tilde{g}^*_{k'}}{\Omega} \frac{1}{\varepsilon_k^{(r)} - \delta - \frac{1}{\Omega}\sum_{\boldsymbol{q}} \frac{|\tilde{g}_q|^2}{\varepsilon_k^{(r)} - \varepsilon_q^{(r)}}} \tag{1.35}$$

At low energy, we can approximate $\tilde{g}_k = \tilde{g}_0$ but we have to be careful because applying this directly would make the sum at the denominator divergent. To avoid this singularity, we mimic the regularization used in the previous section with

$$\langle \boldsymbol{k}'|\widehat{T}|\boldsymbol{k}\rangle = \frac{|\tilde{g}_0|^2}{\Omega} \frac{1}{\varepsilon_k^{(r)} - \delta - \frac{1}{\Omega}\sum_{\boldsymbol{q}} \left[\frac{|\tilde{g}_q|^2}{\varepsilon_k^{(r)} - \varepsilon_q^{(r)}} + \frac{|\tilde{g}_q|^2}{\varepsilon_q^{(r)}} \right] + \underbrace{\frac{1}{\Omega}\sum_{\boldsymbol{q}} \frac{|\tilde{g}_q|^2}{\varepsilon_q^{(r)}}}_{\delta_0}} \tag{1.36}$$

where we introduced δ_0 which can be interpreted as an energy shift of the bound state due to the coupling of the two channels. In the remaining sum, we can now apply the limit $\tilde{g}_q = \tilde{g}_0$ without any divergence. This sum has already been calculated in the previous section so we give directly:

$$f(k) = -\frac{\Omega m_r}{2\pi\hbar^2}\langle \boldsymbol{k}'|\widehat{T}|\boldsymbol{k}\rangle = -\frac{\frac{|\tilde{g}_0|^2 m_r}{2\pi\hbar^2(\delta_0-\delta)}}{1 + i\frac{m_r|\tilde{g}_0|^2}{2\pi\hbar^2(\delta_0-\delta)}k + \frac{1}{(\delta_0-\delta)}\frac{\hbar^2k^2}{2m_r}} \tag{1.37}$$

$$f(k) = \frac{-a}{1 + iak + R_e a k^2} \tag{1.38}$$

where we introduced the scattering length

$$a = \frac{m_r|\tilde{g}_0|^2}{2\pi\hbar^2(\delta_0 - \delta)}, \tag{1.39}$$

and the resonance range

$$R_e = \frac{\pi\hbar^4}{m_r^2|\tilde{g}_0|^2}, \tag{1.40}$$

that characterize the Feshbach resonance.

In the following paragraphs we will discuss those two quantities in details, but right now we can already see that the expression of the scattering amplitude we obtained in eq. (1.38) is very similar to the one obtained in eq. (1.5). By identifying them we get the equality $R_e = -r_e/2$, meaning the resonance range is proportional to the effective range obtained in the truncated expansion of the scattering amplitude at the order two in k.

1.2.2 Magnetic Feshbach resonances

The expression we obtained for the scattering length a diverges when $\delta - \delta_0$ goes to zero. In our experiment, we shift the energy δ using an external magnetic field, realizing a magnetic Feshbach resonance.

For alkali atoms, the two channels correspond to the singlet and triplet potentials, which are coupled by the hyperfine interactions between the nuclei and the valence electron. The relative energy between the triplet and singlet channels can be tuned with the magnetic field B through a spin-Zeeman interaction since the two channel are associated to different magnetic moments. If we write $\Delta\mu$ the difference of magnetic moment between the two channels, we can write close to the resonance $\delta - \delta_0 = \Delta\mu(B - B_0)$. If we also include the background scattering length a_{bg} of the open channel, we can write the scattering length as

$$a(B) = a_{bg}\left(1 - \frac{\Delta B}{B - B_0}\right) \tag{1.41}$$

where a_{bg} is the background scattering length in the open channel without the presence of the closed channel, B_0 gives the position of the resonance and ΔB characterizes the width of the resonance, defined by

$$\Delta B = \frac{m_r}{2\pi\hbar^2}\frac{|\tilde{g}_0|^2}{a_{bg}\Delta\mu} = \frac{1}{\Delta\mu}\frac{\hbar^2}{2m_r R_e a_{bg}}. \tag{1.42}$$

We see that the width of the resonance is more important when the magnetic moments of the two channels are closer or for small resonance ranges R_e.

1.2.3 Bound state near the resonance

To find bound states of the Hamiltonian, one can look for bound states with the general form $|\phi\rangle = \left(\sum_{\boldsymbol{k}}(\psi_{\boldsymbol{k}} a^\dagger_{\boldsymbol{k}}) + \alpha b^\dagger\right)|0\rangle$ and solve the stationary Schrödinger equation $\widehat{H}|\phi\rangle = E|\phi\rangle$ with $E < 0$. We then find that a bound state exists for $\delta < \delta_0$, or equivalently $a > 0$, with an energy

$$E = E_0 - (\delta - \delta_0) - \sqrt{(E_0 - (\delta - \delta_0))^2 + (\delta - \delta_0)^2} \tag{1.43}$$

with

$$E_0 = \frac{\hbar^2}{4m_r R_e^2}. \tag{1.44}$$

We can distinguish two regimes:

- The limit $|\delta - \delta_0| \gg E_0$, or equivalently $R_e \gg a$, the energy becomes

$$E = -\left(\sqrt{\delta_0 - \delta}\right)^2 \simeq -\frac{\hbar^2}{2m_r R_e a}. \tag{1.45}$$

  This corresponds to a bound state nearly entirely in the closed channel.

- The opposite limit, $|\delta - \delta_0| \ll E_0$, or $R_e \ll a$, gives the well-known expression of the energy of a shallow dimer

$$E = -\frac{\hbar^2}{2m_r a^2}. \tag{1.46}$$

  This expression, identical to the prediction of the zero-range model[2], does not depend on R_e but only on the scattering length a, it does not depend on the details of the resonance and thus is considered as universal. This energy is typically much smaller than the energy of the deeply-bound dimers, so we will refer to this state as the shallow dimer. This limit on the other hand, corresponds to a bound state essentially present in the open channel: indeed, the fraction of the wavefunction in the closed channel is given by $(2|E|/E_0)^{1/2} \ll 1$.

This shows that the divergence of the scattering length in a Feshbach resonance is associated with the emergence of a universal shallow bound state.

1.2.4 Narrow and broad Feshbach resonances

The universal expression of the binding energy given by eq. (1.46) is only valid in the region $a \gg R_e$, which we will address as the universal region. The size of this domain varies widely depending on the nature of the resonance, and to give a criterion to characterize them, one can use the resonance strength s_{res}, defined in [25]. In the case where the potentials of the two channels can be described at long range with an attractive Van der Waals potential, this parameter amounts to

$$s_{res} \simeq \frac{l_{VdW}}{R_e} \tag{1.47}$$

with l_{VdW} the range of the Van der Waals potential, which is generally of the same magnitude for the two channels. We can then distinguish two asymptotic limits:

[2]The energy of the bound state can also be found by looking for the poles of $\langle \boldsymbol{k}'|\widehat{T}(z)|\boldsymbol{k}\rangle$, which in the case of zero-range interaction directly yields eq. (1.46).

- When $s_{res} \gg 1$ or $R_e \ll l_{VdW}$, the resonance is known as broad. In this limit, the domain over which $a \gg R_e$ is generally very wide, the bound state is strongly dressed by the open channel and the description of the shallow dimers remains universal in a large portion of the Feshbach resonance. The resonance is dominated by the open channel and the scattering of the atoms can be effectively described by a single channel model.

- On the contrary, when $s_{res} \ll 1$ or $R_e \gg l_{VdW}$, the resonance is known as narrow. The domain over which $a \gg R_e$ is much more restricted and the universal description of the dimer is only valid in a domain very close to the resonance. In this case, the resonance is dominated by the closed channel and a single channel description of the scattering is generally not possible. In addition, the resonantly coupled bound state can easily decay into a deeply bound state of the closed channel, because of the overlap between the closed channel bound state wave-function and that of the deeply bound dimer, leading to strong inelastic collisions.

In conclusion, we described the Feshbach resonance with a two channel model. We understand how we can change the scattering length with the use of an external magnetic field and we introduce the resonance range R_e that helps delimiting the boundaries of the universal region, in which the scattering and the energy of the dressed bound state can be described solely with the scattering length a. We can now wonder if this universality of two-body physics close to a Feshbach resonance still holds for a larger number of particles. In the following section, we give the basic principles of the three-body problem.

1.3 Three-body problem

When considering interactions between three particles, new physics can emerge. In 1970, Efimov discovered the so-called Efimov effect [92], a remarkable phenomenon that occurs when at least two pairs of particles out of the possible three have a large scattering length compared to the range of the potential. An infinite sequence of universal three-body bound states called Efimov trimers appears, even when the two-body potential cannot host a two-body bound state.

Considering the system we will study in this PhD thesis, an impurity made of bosonic atoms immersed in a two-component Fermi gas, and taking into account the Pauli exclusion principle, we can be interested in two different types of trimers: three spinless bosons, interacting with the same scattering length, or two fermions of opposite spin and a boson. The latter will be studied briefly in Chapter 6 with more details in Appendix C, while we present the basics of Efimov physics for the former one, simpler because the three particles are of the same nature. Extensive details of three-body physics can be found in the review [93].

1.3.1 A two-channel model for the three-body problem

We consider three bosons of mass m and scattering length a. To study the three-body problem, it is possible to use a two-channel model, similar to the one we introduced in the previous section, that was used in [94]. This method is quite different from the historic calculations made by Efimov based on the study of the three-body wave-function, but

it enables to retrieve the same results in the vicinity of a narrow Feshbach resonance ($a \gg R_e$). We then start with a two-channel effective Hamiltonian, that reads

$$\widehat{H} = \sum_{\boldsymbol{k}} \varepsilon_k \widehat{a}^\dagger_{\boldsymbol{k}} \widehat{a}_{\boldsymbol{k}} + \sum_{\boldsymbol{K}} (\delta + \varepsilon_K/2) \widehat{b}^\dagger_{\boldsymbol{K}} \widehat{b}_{\boldsymbol{K}} + \frac{\tilde{g}}{\Omega} \sum_{\boldsymbol{k},\,\boldsymbol{K}} \left(\widehat{b}^\dagger_{\boldsymbol{K}} \widehat{a}_{\boldsymbol{k}+\boldsymbol{K}/2} \widehat{a}_{-\boldsymbol{k}+\boldsymbol{K}/2} + \text{H.c.} \right). \quad (1.48)$$

where $\varepsilon_k = \hbar^2 k^2/2m$, $\widehat{a}_{\boldsymbol{k}}$ is the boson operator and $\widehat{b}_{\boldsymbol{K}}$ is a boson operator for the molecular state in the closed channel. A difference we can note with the previous model is that now we work in the center-of-mass frame of the three particles and we have to consider the momentum of the molecule.

In [94], the three body problem was solved exactly using the following ansatz

$$\sum_{\boldsymbol{K}} \left(\beta_{\boldsymbol{K}} \widehat{b}^\dagger_{\boldsymbol{K}} \widehat{a}^\dagger_{-\boldsymbol{K}} + \sum_{\boldsymbol{k}} A_{\boldsymbol{K},\boldsymbol{k}} \widehat{a}^\dagger_{\boldsymbol{k}+\boldsymbol{K}/2} \widehat{a}^\dagger_{-\boldsymbol{k}+\boldsymbol{K}/2} \widehat{a}^\dagger_{-\boldsymbol{K}} \right) |0\rangle \quad (1.49)$$

where the first part (featuring the coefficient $\beta_{\boldsymbol{K}}$ corresponds to the creation of a dimer and a free particle whereas the second part (featuring $A_{\boldsymbol{K},\boldsymbol{k}}$) is the creation of three free particles.

By injecting this ansatz into the Schrödinger equation $\widehat{H}|\psi\rangle = E|\psi\rangle$, with $E < 0$ for we are looking for bound states, we obtain a set of two equations. After combination of the two equations and integration over the angular variables, the solution can be expressed as an equation over a "wave function" $\psi(k)$ for a fictitious 1D problem, that reads

$$\left[\sqrt{\lambda^2 + 3k^2/4} + R_e(\lambda^2 + 3k^2/4) - \frac{1}{a} \right] \psi(k) = \frac{2}{\pi} \int_0^\infty dq \ln \left(\frac{k^2 + q^2 + kq + \lambda^2}{k^2 + q^2 - kq + \lambda^2} \right) \psi(q), \quad (1.50)$$

where λ is defined by $E = -\hbar^2 \lambda^2/m$.

We will not dwelve on the details of the resolution of eq. 1.50, but a resolution technique is suggested in Appendix C and the full calculations are presented in [94]. The result of this resolution is an infinite set of bound Efimov trimers, with on-resonance ($a^{-1} = 0$) energies

$$E_n = -\frac{\hbar^2 \kappa_*^2}{m} e^{-2\pi n/s_0} \quad (1.51)$$

with κ_* the three-body parameter and the universal ratio $1/\alpha^2 = E_{n+1}/E_n = e^{-2\pi/s_0} \simeq 1/515.03$. In this model, the three-body parameter can be expressed simply through a numerical calculation by $\kappa_* R_e \simeq 2.6531$.

1.3.2 Properties of the Efimov trimers

These results are very general and not a mere artifact of this model. We have obtained at unitarity an infinite set of bound states, whose energies E_n obey a remarkable universal geometric scaling as α^{-2n}. However, we saw that a is not the only relevant parameter anymore and we had to introduce the three-body parameter κ_* which depends on the details of the potentials, showing the non-universality of the three-body physics.

In our two-channel model, κ^* is directly related to the resonance range R_e. However, this parameter exists independently of this framework and can actually be introduced in a zero-range model, through a boundary condition used to regularize the otherwise singular three-body problem [95, 96]. In the case of a zero-range interaction, there is also an inifinite set of energies, with the same geometric scaling but without any lower bound for

the energies. This property, discovered much earlier (1935) by L.H. Thomas [97], leads to a collapse of the wavefunction known as "Thomas collapse".

As we saw with our model, this is cured as soon as a range is taken into account, the resonance range R_e for the two channel-model, or l_{VdW} for a broad resonance, because the Efimov scenario breaks down when the size of the Efimov trimers becomes comparable to this range. In the same spirit, in realistic systems there is only a finite number of Efimov trimer states, because an upper bound of the energy is imposed by the fact that at low energies, the size of the trimers becomes larger than the interparticle distance, and will consequently be affected by the surrounding atoms.

At finite scattering length, as long as $a \gg R_e$, the Efimov trimers still exist, but their number is reduced as $|a|$ provides a new upper bound for their size. With a dimensional argument, their energies have the general form:

$$E_n = \frac{-\hbar^2\kappa_*^2}{m} f_n(1/\kappa_* a) \tag{1.52}$$

where the function f_n has to follow the scaling

$$f_n(x) = f_0(x/\alpha^n)/\alpha^{2n} \tag{1.53}$$

for E_n to still have the scaling as α^{-2n}. A general scheme of these energy states is given in Fig. 1.6. More generally, any function g of $x = 1/\kappa_* a$ should follow this type of scaling $g(x) = g(x\alpha)$, which corresponds to a log-periodic behavior, signature of Efimov physics.

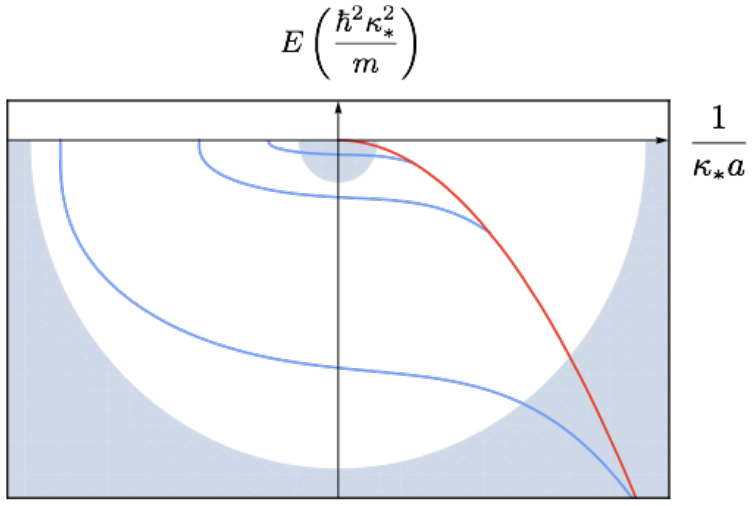

Figure 1.6: Efimov spectrum as a function of the inverse scattering length. The Efimov trimers energy levels (blue) connect to the continuum threshold for negative scattering lengths. For positive a, they branch on the shallow dimer energy level (red curve, $\propto -1/a^2$). The outer shaded area represents the region dominated by short-range physics where the Efimov physics are no longer valid. The inner shaded area is the region where Efimov trimers are larger than the interparticle spacing and interactions with the surrounding atoms have to be considered.

Experimental evidence of the Efimov physics was first obtained with ^{133}Cs atoms [98, 99] by studying the three-body losses in their Bose gas. Indeed, when three particles

get close to each other, as in an Efimov trimer, two of them can form a deeply-bound dimer, with a binding energy of several hundred Kelvins. This energy is converted into kinetic energy and the atoms are lost. The three-body loss rate of bosons is a log-periodic function of $\kappa^* a$ so there are specific values of a for which the losses are enhanced or suppressed. This modulation of the loss rate was observed experimentally, signature of the Efimov physics. This experiment was later extended to other atomic species and the scaling factor α was tested experimentally through the observation of multiple resonances [100–102]. The binding energy was also directly measured via RF spectroscopy, with a three-component Fermi gas of ^{6}Li [103, 104].

1.3.3 The atom-dimer scattering length

To give another striking example of a three-body observable following a log-periodic behavior, we can present the case of the interaction between an atom and a dimer. This interaction is characterized by a scattering length a_{ad}. In the case of three atoms of the same species with scattering length a, close to the resonance a pair of atoms can form a shallow dimer and interact with the third atom.

In the Born approximation, the interaction between an atom and a dimer can be deduced readily from the interaction between two atoms. Indeed, the coupling $g_{ad} = 2\pi\hbar^2 a_{ad}/m_{ad}$between an atom and a dimer, with m_{ad} the atom-dimer reduced mass, is simply the sum of the coupling g between the atom and the first atom of the dimer and again the coupling g between the atom and the second atom of the dimer, leading to $g_{ad} = 2g$. In terms of scattering lengths, taking into account the ratio of m_{ad} and m_r, it becomes

$$a_{ad}^{Born} = \frac{8}{3}a. \tag{1.54}$$

In the limit $a \gg R_e$, Efimov showed that the atom-dimer scattering length also becomes a log-periodic function, with a general expression [105]:

$$a_{ad} = a\left[b_1 - b_0 \tan\left(s_0 \ln(a\kappa_*) + \beta\right)\right] \tag{1.55}$$

where b_0, b_1 and β are universal numbers. This expression is universal in the sense it holds for all identical bosons, independent of short range interactions, provided the shallow-dimer is the only two-body bound state.

In short, three-body physics manifest a plethora of remarkable features. Despite introducing some non-universality through the three-body parameter κ_*, it contains many universal scalings and behaviors, such as the log-periodicity of many three-body observables, signature of the Efimov effect.

Conclusion

In conclusion, we described the two-body interactions in a quantum system using the low-energy scattering theory. We showed that in a certain limit, these interactions were universal and could be described using a single parameter, the scattering length a. We then detailed how it was possible experimentally to vary this parameter, for instance through the use of magnetic field as we do in our experiment. Details on the Feshbach resonances for the Lithium atoms we use will be presented in Chapter 3. Finally, we presented the three-body physics, and showed that the Efimov trimers that arise when the interactions

become resonant also displayed a universal behavior but required the introduction of a three-body parameter.

Hence, in the vicinity of a Feshbach resonance, at ultracold temperatures, we expect many-body systems to exhibit universal properties. In the next chapter, we will describe a few of these properties for ultracold bosons and fermions, highlighting the rich physics that surround the systems that we study with our experiment.

Chapter 2

Ultracold quantum gases: fermionic superfluidity and impurity problems

In this chapter, we outline the physics of ultracold Bose and Fermi gases, the systems we obtain and study with our experimental set-up. We will present the thermodynamics of such systems depending on the interactions between their components. Starting with the ideal quantum gases, we will turn on the interactions and study the weakly interacting Bose gas, followed by the Fermi gas from the weakly interacting regime towards unitarity, where interactions reach their maximum effective value and the scattering length diverges. In this limit, the Fermi gas, as well as various quantum many-body systems from cold atom gases to neutron stars, share the same universal thermodynamic properties [106, 107].

Though, in-between the unitary limit and the weakly interacting regime, no simple description exists. The study of the strongly correlated regime is not just a theoretical issue, and can be observed in various physical systems such as high-T_c superconductors [108], graphene [109] or cold atom gases near a Feshbach resonance. In our set-up, we have a broad Feshbach resonance between the fermions, so most of the domain we explore is in the regime $1/k_F|a_{ff}| < 1$, therefore the study of the strongly interacting regime is of utmost importance. For this purpose, the experimental measurement of the Equation of State (EoS) for any interaction will be presented and we will introduce for the Fermi gas the two-body contact C_2, a thermodynamic quantity that encompasses the short-range correlations of a many-body system, related to many properties of the fermionic ensemble.

Finally, in the last two sections, we will give an overview of the problem of an impurity immersed in either a Fermi sea or a Bose-Einstein condensate, showing how this apparently simple system is actually non trivial and possesses remarkable properties.

2.1 Ideal quantum gases

Before studying the Fermi gas with interactions, let us start by giving the basic concepts concerning ideal quantum gases (Bose and Fermi gases), for which dramatic features already arise. Thus, we consider a gas of non-interacting identical particles of mass m at a temperature T.

For the classical gas, in the grand canonical ensemble at the temperature T and chem-

ical potential μ, the occupation number[1] of a state $|\lambda\rangle$ of energy ϵ_λ is given by

$$\overline{N}_\lambda(\epsilon_\lambda) = e^{-\beta(\epsilon_\lambda - \mu)} \tag{2.1}$$

with $\beta = 1/k_B T$. In classical systems, this occupation number is generally very small compared to one, which means that there are much more available excited states than particles. The equation of state (EoS) associated to the 3D Hamiltonian for the free particles is given by:

$$n\lambda_{th}^3 = e^{\beta\mu} \tag{2.2}$$

where n is the density and $\lambda_{th} = \sqrt{2\pi\hbar^2/mk_BT}$ is the thermal De Broglie wavelength.

In this equation of state appear two length scales: the mean distance between particles $n^{-1/3}$, and the thermal De Broglie wavelength λ_{th}, which can be interpreted as the average size of the wavepacket associated to the particles. When $\lambda_{th} \gtrsim n^{-1/3}$, the wavepackets start interfering and quantum effects arise, the gas can no longer be considered as classical. From equations (2.1) and (2.2), we see that in this same limit, the occupation number also becomes of the order of 1 for the states with low energies ($\epsilon \ll k_B T$): the particles occupy preferentially the lowest energy states and may behave collectively. To enter the quantum regime, either the density has to be increased or the temperature decreased, or a combination of both.

Quantum distributions

In the quantum regime, for identical fermions, the occupation number in a state $|\lambda\rangle$ is given by the Fermi-Dirac distribution

$$\overline{N}_\lambda^{\mathrm{FD}}(\epsilon_\lambda) = \frac{1}{e^{\beta(\epsilon_\lambda - \mu)} + 1} \tag{2.3}$$

and for identical bosonic particles by the Bose-Einstein distribution

$$\overline{N}_\lambda^{\mathrm{BE}}(\epsilon_\lambda) = \frac{1}{e^{\beta(\epsilon_\lambda - \mu)} - 1} \tag{2.4}$$

This occupation number is always smaller than one as the Pauli exclusion principle forbids to have two fermions in the same state, whereas for bosons it can take a priori any positive value. At low fugacity or high temperature, both the Fermi-Dirac and the Bose-Einstein distributions yield the occupation number for a classical gas as expected. For 3D-uniform systems, assuming all states are weakly populated, the equation of states are given by the functions [110]:

$$n_b\lambda_{th}^3 = \mathrm{Li}_{3/2}(e^{\beta\mu}) \tag{2.5}$$

for bosons of density n_b and

$$n_f\lambda_{th}^3 = -\mathrm{Li}_{3/2}(-e^{\beta\mu}) \tag{2.6}$$

for fermions of density n_f and where Li is a polylogarithm function[2].

[1] mean number of particles in a given state

[2] Those functions are defined by:

$$\mathrm{Li}_s(z) = \sum_{k=1}^{\infty} \frac{z^k}{k^s}. \tag{2.7}$$

Low temperature behavior

When the temperature goes to zero, the Fermi-Dirac distribution takes the asymptotic form $\overline{N}_\lambda^{\mathrm{FD}}(\epsilon_\lambda) = \Theta(\mu - \epsilon_\lambda)$ with Θ the Heaviside function: all state with an energy smaller than μ are occupied, all the others are not. We can note that the transition from the classical thermal gas to this degenerate Fermi gas is not a phase transition. We define the Fermi energy $E_F = \mu(T = 0, N_f)$ with N_f the total number of fermions[3] and $T_F = E_F/k_B$ the associated Fermi temperature, which sets a scale for the apparition of quantum effects in Fermi gases.

The Fermi energy is solution of the equation giving the total number of fermions in the system:

$$N_f = \sum_{|\lambda\rangle} \overline{N}_\lambda^{\mathrm{FD}}(\epsilon_\lambda, T = 0, \mu = E_F) \tag{2.8}$$

For a homogeneous 3D system in a box potential it yields for identical fermions[4]

$$E_F = \frac{\hbar^2}{2m}(6\pi^2 n_f)^{2/3} \tag{2.10}$$

Concerning the Bose-Einstein distribution, the occupation number must remain positive so the bosonic chemical potential is then constrained $\mu_b \leq \epsilon_0 = \underset{|\lambda\rangle}{\mathrm{Min}}(\epsilon_\lambda)$, where ϵ_0 corresponds to the energy of the ground state. When $\mu \to \epsilon_0$, the occupation number of the ground state diverges while it remains bounded for the excited states with an upper bound that decreases as the temperature decreases: less and less particles can populate the excited states whereas there is no limit for the ground state. Therefore, under a certain critical temperature $T_{c,b}$ for which $\mu = \epsilon_0$, the particles occupy macroscopically the ground state. The gas forms what is called a Bose-Einstein condensate (BEC) since all atoms are "condensed" in the same state. The behavior of the Bose gas is then drastically different from the behavior of the Fermi gas, for which the Pauli principle forbids completely to have all the fermions occupying the same state. Moreover, the transition to a BEC is a phase transition, a peculiar one since it is purely statistical.

This critical temperature is solution of the equation where we place all particles in the excited states with $\mu = \epsilon_0$: when the temperature is decreased, the upper limit of the occupation of excited states decreases whereas they were already saturated leading to the condensation into the ground state. This equation reads as

$$N_b = \sum_{|\lambda\rangle \neq |0\rangle} \overline{N}_\lambda^{\mathrm{BE}}(\epsilon_\lambda, \mu = \epsilon_0, T = T_{c,b}) \tag{2.11}$$

This equation yields in a box potential for a homogeneous system in 3D:

$$T_{c,b} = \frac{1}{(\mathrm{Li}_{3/2}(1))^{2/3}} \frac{2\pi\hbar^2}{m k_B} n_b^{2/3}. \tag{2.12}$$

[3] Although we stated that we were working in the grand canonical ensemble where the concept of a total number makes no sense, these formulas are also valid in the canonical ensemble as long as we work in the thermodynamic limit ($N \gg 1$ with the density remaining finite), thanks to the equivalence of statistical ensembles.

[4] In the case of fermions of spin s, with possibly $2s + 1$ different spin states, the formula becomes:

$$E_F = \frac{\hbar^2}{2m}\left(\frac{6}{2s+1}\pi^2 n_f\right)^{2/3}. \tag{2.9}$$

The ground state occupation number N_c reads

$$N_c = N_b \left(1 - \left(\frac{T}{T_{c,b}}\right)^{3/2}\right) \tag{2.13}$$

and it was verified recently using ^{87}Rb atoms in a quasi uniform 3D box potential [58].

Now that we covered the ideal Bose and Fermi gases, we will study the effect of the interactions on these many-body ensembles.

2.2 Interacting Bose gas

We consider a gas of N_b spinless bosons, with an interaction characterized by the scattering length a_{bb}, that can be changed by taking advantage of a Feshbach resonance.

In order to describe the weakly interacting Bose gas, we make an assumption that we will call the universality hypothesis: we assume that the properties of a many-body system with short-range interactions do not depend on the details of the interaction potential. This hypothesis can be justified saying that the wavelength associated to the particles is much bigger than the range of the potential, but it does not always work: as we saw before in Chapter 1, close to unitarity, non-universal three-body physics emerges for strongly interacting bosons.

Within the universality hypothesis, we can use the model of a contact interaction in the mean-field approximation, and the Hamiltonian of the system without any external potential reads

$$\widehat{H} = \int \mathrm{d}^3\boldsymbol{r} \left[-\frac{\hbar^2}{2m_b}\widehat{\psi}^\dagger \nabla^2 \widehat{\psi} + \frac{g_{bb}}{2}\widehat{\psi}^\dagger\widehat{\psi}^\dagger\widehat{\psi}\widehat{\psi}\right] \tag{2.14}$$

with $g_{bb} = 4\pi\hbar 2a_{bb}/m_b$ the physical coupling constant and m_b the mass of the bosons.

At zero temperature, all bosons are condensed in the ground state of energy taken equal to 0, so only the interaction part of the Hamiltonian contributes to the energy. In the mean-field approximation, the energy can be calculated simply:

$$E_0 = \frac{1}{2} g_{bb} N_b n_b \tag{2.15}$$

with n_b the density of bosons.

For a system at thermodynamic equilibrium, the stability imposes a positive compressibility which boils down to $\frac{\partial n}{\partial P}\big|_S > 0$ imposing $a_{bb} \geq 0$: a uniform Bose-Einstein condensate can only exist for a positive scattering length, corresponding to repulsive interactions. Otherwise, for attractive interactions, the Bose gas collapses.

The inclusion of fluctuations of the BEC field around its MF value gives the Lee-Huang Yang correction for the ground state energy density [111, 112] first calculated for hard-sphere bosons [113]:

$$\epsilon = \frac{1}{2} n_b^2 g_{bb} \left(1 + \frac{128}{15\sqrt{\pi}}\sqrt{n_b a_{bb}^3}\right) \tag{2.16}$$

The small dimensionless parameter that quantifies the corrections is found to be $\sqrt{n_b a_{bb}^3}$, thus the MF approximation in 3D is valid in the weakly-interacting regime. The use of Feshbach resonances has allowed for the measurement of the LHY correction, using the

excitation spectrum of a BEC through Bragg spectroscopy [114] or the direct measurement of the Equation of State (EoS) [115].

Taking into account three-body physics, Wu pushed further this expansion [116]:

$$\epsilon = \frac{1}{2} n_b^2 g_{bb} \left[1 + \frac{128}{15\sqrt{\pi}} \sqrt{n_b a_{bb}^3} + 8 \left(\frac{4}{3}\pi - \sqrt{3} \right) n_b a_{bb}^3 \left(\ln(n_b a_{bb}^3) + D - \frac{1}{3} \right) + ... \right] \tag{2.17}$$

The coefficient D is a non-universal term obtained with three-body calculations. The logarithmic behaviour is a signature of a singularity in the three-body problem for particles with a contact interaction, first discovered by Wu for three bosons, but more recently studied in the context of cold atoms [117–120].

As the scattering length increases, we enter the strongly interacting regime, where perturbative expansion in $\sqrt{n_b a_{bb}^3}$ cannot be used, and Efimov physics start emerging. Moreover, this regime is not accessible experimentally for Bose gases due to the emergence of three-body losses scaling as $L_3 \propto a_{bb}^4$ [121], a dependence that was first measured with ^{133}Cs atoms in [122]. Since this PhD focuses on a bosonic impurity immersed in a two-component Fermi gas, we will not dwell on further on the strongly interacting Bose gas, but rather focus in the following on the study of the Fermi gas.

2.3 Interacting Fermi gas : the BEC-BCS crossover

In this section, we will study the behaviour of the balanced two-component Fermi gas at low temperature. We consider then a Fermi gas constituted of spin 1/2 fermions, each species being referred to either $\uparrow$ or $\downarrow$ fermions, with a balanced distribution $N_\uparrow = N_\downarrow$. We write a_{ff} the scattering length characterizing the interaction between a $\uparrow$ and a $\downarrow$ fermion.

To describe the properties of the system, we again assume we are within the universality hypothesis. Due to Pauli blocking, three-body physics are suppressed and this hypothesis is valid even for strong interactions. At $T = 0$, only two length scales are available: the scattering length a_{ff} which encompasses the two-body interactions and $1/k_F$, the inverse of the Fermi wavevector, defined with the Fermi energy $E_F = \hbar^2 k_F^2/2m$, and related to the Fermi density in a homogeneous system through $k_F = (3\pi^2 n_f)^{1/3}$ (for a two-component Fermi gas). We see with this equation that $1/k_F$ is directly proportional to the interparticle distance $n_f^{-1/3}$. Consequently, all measurable observables are functions of the universal dimensionless quantity[5] $1/k_F a_{ff}$.

At $T = 0$, the properties of the two-component Fermi gas depend on the interactions. From the BCS limit $1/k_F a_{ff} \to -\infty$ to the BEC limit $1/k_F a_{ff} \to +\infty$, while crossing the unitary limit $1/k_F a_{ff} = 0$, the properties of the Fermi gas vary considerably. The transition between the BCS and the BEC regimes for a Fermi gas in the vicinity of a Feshbach resonance is not a phase transition but a smooth crossover, known as the BEC-BCS crossover, represented in Fig. 2.1. The BEC-BCS crossover was first proposed by Leggett [46], Nozières and Schmitt-Rink [47] and confirmed by various theoretical approaches [48] and experiments [123, 124]. In the whole BEC-BCS crossover, the two-component Fermi gas is superfluid and is characterized by the pairing of fermions of opposite spins, but the nature of this pairing changes drastically with the interactions.

In this section, we will detail the universal properties of Fermi gases in the BEC-BCS crossover.

[5] This parameter is analogous to the bosonic parameter $n_b a_{bb}^3$ since $k_F \propto n_f^{1/3}$.

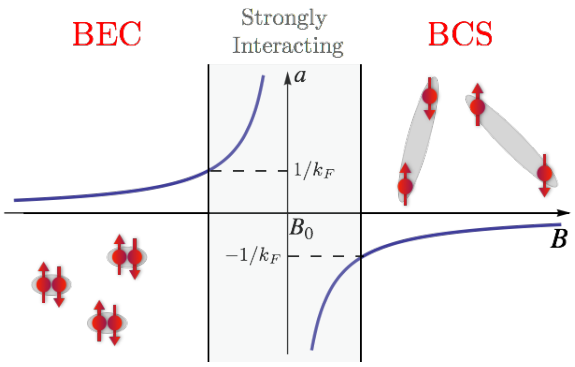

Figure 2.1: Representation of a magnetic Feshbach resonance with a the fermion-fermion scattering length. Three distinct domains are represented: for $0 < k_F a < 1$ the system is in the BEC limit and fermions of opposite spin pair up to form dimers, for $-1 < k_F a < 0$ the system is in the BCS limit and fermions of opposite spin form Cooper pairs, and finally for $k_F|a| > 1$ we are in the strongly interacting regime. Here k_F has been assumed to be constant throughout the BEC-BCS crossover.

2.3.1 The BCS limit

For small negative scattering lengths, the interaction is weakly attractive. Contrary to the Bose gas, there is no collapse of the Fermi gas for $a_{ff} < 0$ because of the Fermi degeneracy pressure, originating from the Pauli exclusion principle, that counters the pressure due to the mean-field term of the energy that increases with density for $a_{ff} < 0$. This phenomenon exists also on a macroscopic level where the Fermi degeneracy pressure prevents the gravitational collapse of white dwarves or neutron stars.

It was shown by Cooper [125] that in this weakly attractive limit, fermions of opposite spins pair together to form Cooper pairs similarly as the electrons in a superconducting metal as described by Bardeen, Cooper and Schrieffer in the so-called BCS theory [126]. This pairing exists despite the absence of a shallow bound state on this side of the Feshbach resonance: the Cooper pair is stabilized by the presence of the background Fermi sea by reducing fluctuations. For $a_{ff} \to 0^-$, the Cooper pairs are very loose and the interactions become negligible: the energy of the Fermi gas is the energy of the ideal gas and we have $E \simeq \frac{3}{5} N E_F$.

In this limit, the energy contribution of the BCS pairing in the superfluid phase is exponentially small (see Appendix B), so the next terms of the energy expansion are simply a perturbative expansion in $k_F a_{ff}$ and does not involve parameters from BCS theory. The energy density is given by the expansion:

$$\epsilon = \frac{3}{5} n E_F \left[1 + \frac{10}{9\pi} k_F a_{ff} + \frac{4(11 - 2\ln 2)}{21\pi^2} (k_F a_{ff})^2 + ... \right] \tag{2.18}$$

where the first order term is the mean-field term and the last term was obtained by Galitskii, Lee and Yang in the context of repulsive hard-sphere fermions [127, 128] before being generalized more recently for attractive interactions [129].

2.3.2 Molecular BEC domain

For small and positive scattering lengths, opposite spin fermions can pair together into the bosonic shallow dimer of binding energy $E_b = -\hbar^2/m a_{ff}^2$, assuming we are still in the

universality domain of the resonance, whereas it was not the case on the BCS side since these dimers do not exist for $a < 0$ in the two-body problem (cf Chapter 1).

The Fermi gas is thus in the strongly attractive limit, though due to the Pauli exclusion principle, the interaction between dimers is repulsive with an associated scattering length of $a_{dd} = 0.6a_{ff}$ [130]. When the temperature goes down to zero, the dimers form a molecular BEC, and behave similarly as a repulsive Bose gas, nearly sharing its equation of state [131]. The Bose-Einstein condensation of the dimers was indeed observed experimentally [50–52, 132, 133].

In this domain the energy density can be written as follows:

$$\epsilon = -\frac{\hbar^2}{ma_{ff}^2}n_d + \frac{1}{2}g_{dd}n_d^2\left(1 + \frac{128}{15\sqrt{\pi}}\sqrt{n_d a_{dd}^3} + ...\right) \tag{2.19}$$

where g_{dd} is the dimer-dimer coupling constant with $g_{dd} = 2\pi\hbar^2 a_{dd}/m_f$ and n_d the density of dimers. In this equation, the first term corresponds to the binding energy of the shallow dimers (this term does not appear in the EoS of the repulsive Bose gas), the second term $g_{dd}n_d^2$ is a mean-field term (obtained in the Born approximation) quantifying the interaction between two dimers, and the last term is the Lee-Huang-Yang correction. We see that it is written as a function of $\sqrt{n_d a_{dd}^3}$ the bosonic equivalent to the fermionic universal dimensionless parameter.

2.3.3 Unitary Fermi gas

The unitary Fermi gas lies in the strongly interacting regime. Contrary to the Bose gas, three-body losses in a two-component Fermi gas are highly suppressed due to the Pauli exclusion principle. The main loss mechanism concerns dimer-dimer collisions on the BEC side, with a loss rate $\gamma \propto a^{-2.55}$ [130], which is vanishing close to unitarity. As a consequence, Fermi gases remain stable over a large region of the BEC-BCS crossover, including the domain of strong interactions. Indeed, the lifetime of Fermi gases on Feshbach resonances was demonstrated to be long compared to equilibration experimentally [134, 135].

At unitarity, the length scale corresponding to the scattering length a_{ff} vanishes and only k_F remains. Consequently, all its properties are proportional to that of a non-interacting Fermi gas and involve a few universal numerical constants. In particular, the chemical potential is simply given by:

$$\mu = \xi E_F \tag{2.20}$$

where ξ is the universal Bertsch parameter. The knowledge of ξ yields directly the EoS at unitarity so it is essential to determine it. The theoretical description of the Unitary Fermi gas remains challenging since perturbative methods cannot be used. A review of the different theoretical and numerical techniques used to determine ξ can be found in [48]. The parameter ξ has been measured experimentally with high precision in [136], leading to the now accepted value of:

$$\xi = 0.376(4). \tag{2.21}$$

In the rest of the strongly interacting regime, no such simple expression of the EoS exists, but it can still be investigated experimentally since the Fermi gas remains stable in a large portion of the crossover. Therefore, we present in the next paragraph an experimental measurement of the EoS in the BEC-BCS crossover

2.3.4 Fermi equation of state at zero-temperature

In this paragraph, we present the experimental measurement of the EoS of the Fermi gas in the crossover at zero-temperature that was obtained in our group [137].

In the grand canonical ensemble, the pressure, obtainable directly with the experiment, can be written as:

$$P(\mu, a) = 2P_0(\tilde{\mu})h_S(\tilde{\delta}) \tag{2.22}$$

$$\tilde{\mu} = \mu + \frac{\hbar^2}{2ma^2}\Theta\left(\frac{1}{a}\right) \tag{2.23}$$

$$\tilde{\delta} = \frac{\hbar}{a\sqrt{2m\tilde{\mu}}} \tag{2.24}$$

$$P_0(\mu) = \frac{1}{15\pi^2}\left(\frac{2m}{\hbar^2}\right)^{3/2}\mu^{5/2} \tag{2.25}$$

where Θ is the Heaviside function, $\tilde{\mu}$ corresponds to the chemical potential shifted by the binding energy of the dimers when they exist and P_0 is the pressure of the non interacting single-component Fermi gas hence the factor 2 in the expression of the pressure. Here δ measures the strength of the interactions and h_S is the dimensionless pressure.

In Fig. 2.2, we represent the equation of state in the crossover measured in our group [137]. The data obtained was fitted with an expansion in terms of Padé approximants, using rational functions containing logarithms to get the best approximation, yielding an analytical expression of the EoS measured experimentally. The Padé approximants were constrained using asymptotic behaviors and known theoretical limits such as the Lee-Huang Yang correction to the energy. The expression of h_S obtained through this method is different on the BEC side and the BCS side but it is continuous, its first order derivative is also continuous but not the higher order ones. It is given by[6]

$$h_S(\delta) = \begin{cases} \frac{\beta_1+\beta_2\delta+\beta_3\delta\log(1+\delta)+\beta_4\delta^2+\beta_5\delta^3}{1+\beta_6\delta^2} & \text{for } \delta < 0 \text{ (BCS} \\ \frac{\delta^2+\alpha_1\delta+\alpha_2}{\delta^2+\alpha_3\delta+\alpha_4} & \text{for } \delta > 0 \text{ (BCS)} \end{cases} \tag{2.26}$$

This result is in good agreement with a Nozières Schmitt-Rink calculation and with a node Monte-Carlo method [138,139]. A full comparison with theories can be seen in [48].

In Fig. 2.2 is also represented the normalized energy $\xi(x = 1/k_F a_{ff})$ defined as

$$\xi = \frac{E/N - E_b/2}{E_{FG}} \tag{2.27}$$

where E/N is the energy per particle, $E_b = \Theta(a_{ff})(-\hbar^2/ma_{ff}^2)$ is the binding energy of the dimers (when they exist hence the Heaviside function Θ) and $E_{FG} = (3/5)E_F$ is the total energy of the ideal Fermi gas. It can be deduced from the grand canonical EoS expressed with the Padé approximants using a Legendre transformation[7].

[6] The coefficient of the Padé approximants determined by the fit are: $\alpha_1 = -1.137$, $\alpha_2 = 0.533$, $\alpha_3 = -0.606$, $\alpha_4 = 0.141$, $\beta_1 = 3.78$, $\beta_2 = 8.22$, $\beta_3 = 8.22$, $\beta_4 = -4.21$, $\beta_5 = 3.65$, $\beta_6 = 0.186$.

[7] The Legendre transformation writes as:

$$x(\delta) = \frac{\delta}{\left(h_S(\delta) - \frac{\delta}{5}h'_S(\delta)\right)^{1/3}}, \qquad \xi(\delta) = \frac{h_S(\delta) - \frac{\delta}{3}h'_S(\delta)}{\left(h_S(\delta) - \frac{\delta}{5}h'_S(\delta)\right)^{5/3}} \tag{2.28}$$

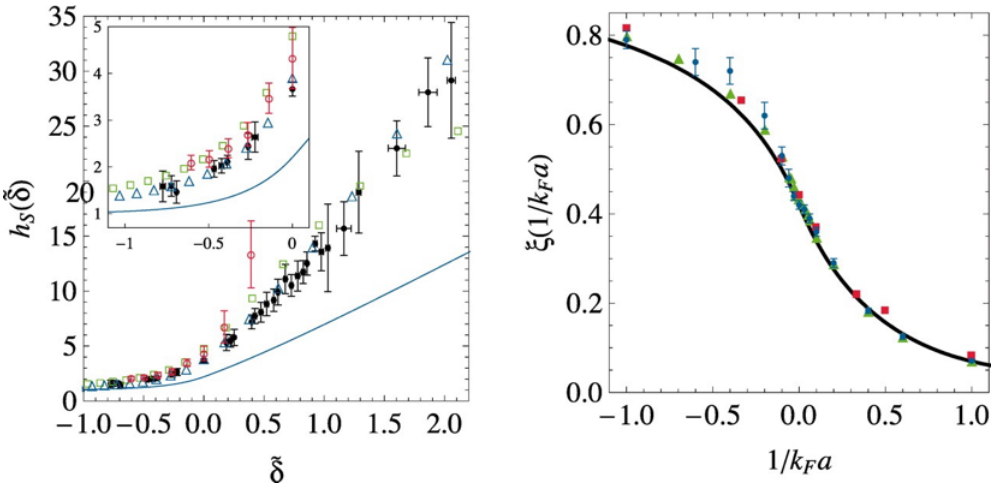

Figure 2.2: Equation of state of the balanced Fermi gas at zero temperature, taken from [137]. Left panel: dimensionless pressure in the BEC-BCS crossover and comparison to many-body theories. Black dots: experimental data. It is compared to a Monte-Carlo calculation (red open circles) [139], a diagrammatic method (green open squares) [140], a Nozières-Schmitt-Rink approximation (blue open triangles) [138], and the BCS mean-field theory (solid blue line). The inset is a zoom on the BCS side. Right panel: dimensionless energy (EoS in the canonical ensemble). The solid black line is deduced from the Padé approximants obtained fitting $h_S(\tilde{\delta})$. It is compared to Fixed-Node Monte-Carlo theories: red squares [141], blue circles [142], and green triangles [143].

2.4 Tan's contact for a two-component Fermi gas

We saw in the last section that in the strongly interacting regime, where many-body effects have to be taken into account, we can measure experimentally the equation of state in the BEC-BCS crossover for a Fermi gas but finding a theory without approximations to describe these systems is very difficult.

In this section, we introduce a new parameter, Tan's contact C_2 first introduced by Shina Tan in 2008 [144, 145], a fundamental thermodynamic quantity that appears in a set of exact universal relations connecting thermodynamic observables to various other microscopic or macroscopic quantities that would seem otherwise unrelated. Those relations actually hold for any temperature, number of atoms, trap geometry or interaction strength, in particular they hold in the strongly interacting regime. Detailed review on the contact can be found in [146, 147], we will present in this section its most relevant properties.

2.4.1 Universality hypothesis

In order to introduce this new parameter, we use for the interaction potential a contact interaction, regularized by using a UV cut-off Λ and the running coupling constant $g_0(\Lambda)$ introduced in Chapter 1, instead of the one valid in the Born approximation as it was done to determine the properties of the weakly interacting Bose and Fermi gases. In this context, the universality hypothesis means that if we use the regularized pseudopotential then all physical quantities will remain finite. As we will see later, this is not completely true. As we will see, in the context of two-body problem, the kinetic energy of the system

T actually diverges but so does its interaction energy I: it is the binding energy $E = T+I$ that remains finite.

2.4.2 Momentum distribution and adiabatic sweep theorem

Let us write then the Hamiltonian of a two-component Fermi gas, an experimentally relevant case, by using the pseudopotential $g_0(\Lambda)\delta(\boldsymbol{r})$ to describe the interactions

$$\widehat{H} = \widehat{T}+\widehat{V} = \int \mathrm{d}^3\boldsymbol{r} \left[-\frac{\hbar^2}{2m}\sum_\sigma \widehat{\psi}^\dagger_\sigma(\boldsymbol{r})\nabla^2\widehat{\psi}_\sigma(\boldsymbol{r})\right] + g_0(\Lambda)\int \mathrm{d}^3\boldsymbol{r}\left[\widehat{\psi}^\dagger_\uparrow(\boldsymbol{r})\widehat{\psi}^\dagger_\downarrow(\boldsymbol{r})\widehat{\psi}_\downarrow(\boldsymbol{r})\widehat{\psi}_\uparrow(\boldsymbol{r})\right] \tag{2.29}$$

where σ corresponds to the two possible spin states noted $\uparrow$ and $\downarrow$.

To know perfectly the thermodynamics of our system, we would need to obtain its free-energy F, or simply its energy at zero-temperature. This is not an easy problem since we cannot calculate analytically the ground state of this Hamiltonian. However, we will see that we can get some information about one of its derivative.

For this purpose, we will apply the Hellman-Feynman's theorem [148] which states that for any parameter λ, we have

$$\frac{\mathrm{d}F}{\mathrm{d}\lambda} = \left\langle \frac{\partial \widehat{H}}{\partial \lambda} \right\rangle \tag{2.30}$$

where $\langle ... \rangle$ correspond to the mean value taken in the canonical ensemble.

Here, we will consider g_0 as the parameter λ and we can write

$$\frac{\mathrm{d}F}{\mathrm{d}g_0} = \left\langle \int \mathrm{d}^3\boldsymbol{r}\left[\widehat{\psi}^\dagger_\uparrow(\boldsymbol{r})\widehat{\psi}^\dagger_\downarrow(\boldsymbol{r})\widehat{\psi}_\downarrow(\boldsymbol{r})\widehat{\psi}_\uparrow(\boldsymbol{r})\right]\right\rangle \tag{2.31}$$

$$\frac{\mathrm{d}F}{\mathrm{d}g_0} = \left\langle \frac{\widehat{H}-\widehat{T}}{g_0}\right\rangle = \frac{1}{g_0}\left(E - \langle\widehat{T}\rangle\right) \tag{2.32}$$

where E is the mean energy of the system related to F by $F = E - TS$.

We can express the mean value of the kinetic energy using as a basis the waveplanes $|\boldsymbol{k}\rangle$ of energy $\varepsilon_k = \hbar^2k^2/2m$ as $\langle\widehat{T}\rangle = \sum_{\boldsymbol{k}} N_k\varepsilon_k$ where N_k represents the mean number of particles of the system with a wavevector of norm k. Not knowing if this sum converges, we also use the UV-cutoff given by Λ for it. The normalization relation we put forth in Chapter 1 concerned not g_0 but $1/g_0$ so we modify the last equation to make $1/g_0$ appear:

$$-\frac{g_0}{g_0^2}\frac{\mathrm{d}F}{\mathrm{d}(1/g_0)} = E - \sum_{\boldsymbol{k},\, k<\Lambda} N_k\varepsilon_k \tag{2.33}$$

$$-\left(\frac{1}{g} - \frac{1}{\Omega}\sum_{\boldsymbol{k},\, k<\Lambda}\frac{1}{E_k}\right)\frac{\mathrm{d}F}{\mathrm{d}(1/g)} = E - \sum_{\boldsymbol{k},\, k<\Lambda} N_k\varepsilon_k \tag{2.34}$$

with $E_k = \hbar^2k^2/m = 2\varepsilon_k$ and where we replaced the derivation of F with respect to $1/g_0$ by one with respect to $1/g$ because F can only depend on the physical coupling g assuming universality. We redistribute the equation by keeping the sums on the same side

$$\sum_{\boldsymbol{k},\, k<\Omega}\left[N_k\varepsilon_k + \frac{1}{\Omega}\frac{\mathrm{d}F}{\mathrm{d}(1/g)}\frac{1}{2\varepsilon_k}\right] = E - \frac{1}{g}\frac{\mathrm{d}F}{\mathrm{d}(1/g)} \tag{2.35}$$

The right-hand of this equation is finite, and according to the universality hypothesis it shall not depend on the UV-cutoff Λ, so the argument of the sum in the left-hand side must converge to 0. This leads to the relation

$$N_k \underset{k\to\infty}{\sim} -\frac{1}{\Omega}\frac{\mathrm{d}F}{\mathrm{d}(1/g)}\frac{1}{2\varepsilon_k^2} \tag{2.36}$$

which gives the behaviour at high k of N_k. From this equation, we see that $N_k \sim 1/k^4$ when $k \to \infty$. Therefore, we can define the contact C_2 as the constant verifying

$$n(k) \underset{k\to\infty}{\sim} \frac{2C_2}{k^4} \tag{2.37}$$

where $n(k)$ is the momentum distribution which verifies $N_f = \int \frac{\mathrm{d}^3\boldsymbol{k}}{(2\pi)^3}\ n(k)$, and the factor 2 accounts for the two spins. This momentum tails also appears in one and two-dimensional systems [146, 149] and is independent of the statistical nature of the particles giving good generality to this definition of the contact. Other definitions, more mathematical, can also be found [146] but the properties remain the same.

From this definition, we get that C_2 is related to the short-range physics ($k \to \infty$) of a many-body system. In addition, using eq. (2.36), we also get a relation between C_2 and the free energy F:

$$C_2 = -\frac{4\pi m}{\hbar^2}\frac{\mathrm{d}F}{\mathrm{d}(1/a)} \tag{2.38}$$

also known as the adiabatic sweep theorem. From this relation we can interpret the two-body contact is coupled to $1/a$ so it corresponds to a generalized displacement associated to the generalized force that constitutes $1/a$. Besides, the adiabatic sweep theorem also opens the way to a measurement of the contact C_2 through the measurement of the EoS of the Fermi gas.

2.4.3 Short-range correlations in a many-body system

We defined the contact using the asymptotic behavior of the momentum distribution at high momenta. This definition establishes a link between C_2 and short-range correlations and we will explicit it even further in this section. The relations we give in this section about correlation functions are demonstrated in [146].

First, the contact is involved in the first order correlations through:

$$G^{(1)}_{\sigma\sigma}(\boldsymbol{r}) = \int \mathrm{d}^3\boldsymbol{R}\left\langle\psi^\dagger_\sigma(\boldsymbol{R}+\boldsymbol{r}/2)\psi_\sigma(\boldsymbol{R}-\boldsymbol{r}/2)\right\rangle \underset{r\to 0}{\simeq} N_\sigma - \frac{C_2}{8\pi}r + O(r^2) \tag{2.39}$$

where N_σ is the total number of fermions in the spin state σ.

In addition, it is also related to the probability of finding two fermions of opposite spins at a short distance. First we define the pair distribution function:

$$g^{(2)}_{\uparrow\downarrow}(\boldsymbol{r}_\uparrow, \boldsymbol{r}_\downarrow) = \left\langle(\psi^\dagger_\uparrow\psi_\uparrow)(\boldsymbol{r}_\uparrow)(\psi^\dagger_\downarrow\psi_\downarrow)(\boldsymbol{r}_\downarrow)\right\rangle. \tag{2.40}$$

The probability of finding two fermions within r is then given by:

$$G^{(2)}_{\uparrow\downarrow}(\boldsymbol{r}) = \int \mathrm{d}^3\boldsymbol{R}\ g^{(2)}_{\uparrow\downarrow}\left(\boldsymbol{R}+\frac{\boldsymbol{r}}{2}, \boldsymbol{R}-\frac{\boldsymbol{r}}{2}\right) \underset{r\to 0}{\sim} \frac{C_2}{(4\pi r)^2} \tag{2.41}$$

We can deduce from this expression the number of pairs of fermions of opposite spins separated by a distance less than s:

$$N_{\uparrow\downarrow}(s) = \int_{r<s} \mathrm{d}^3\boldsymbol{r}\; G^{(2)}_{\uparrow\downarrow}(\boldsymbol{r}) = \frac{C_2}{4\pi} s \tag{2.42}$$

This result is different from the $\sim r^3$ behavior expected for a uniform density, showing that particles cluster at short range.

In short, we see that the contact is intimately related to short-range correlations. We listed relations valid for a two-component Fermi gas in 3D but similar ones can be found for bosons and other dimensions.

2.4.4 Two-body contact in the BEC-BCS crossover

We can use the measure of the EoS and the adiabatic sweep theorem to obtain the two-body contact. First we can list asymptotic behaviors using the expansions of the energies listed in Chapter 1.

BEC side

On the BEC side, the energy is dominated by the binding energy of the molecules so at first order we obtain:

$$C_2 = -\frac{4\pi m}{\hbar^2} \frac{d}{d(1/a_{ff})} \left[\frac{N_f}{2} \left(\frac{-\hbar^2}{m a_{ff}^2} \right) \right] = N_f \frac{4\pi}{a_{ff}} \tag{2.43}$$

where N_f is the total number of fermions.

BCS side

On the BCS side, we have to use the expansion of the energy up to the mean-field term:

$$C_2 = -\frac{4\pi m}{\hbar^2} \frac{d}{d(1/a_{ff})} \left[\frac{3}{5} N E_F \left(1 + \frac{10}{9\pi} k_F a_{ff} \right) \right] = 4\pi^2 N_f n_f a_{ff}^2 \tag{2.44}$$

where n_f is the density of fermions.

Unitarity

An expansion of the energy of the system near unitarity can be found in [145] and writes as

$$E = \frac{3}{5} N E_F \left(\xi - \frac{\zeta}{k_F a_{ff}} \right) \tag{2.45}$$

where ξ is the Bertsch parameter and $\zeta \simeq 0.87(3)$ is another universal constant, whose most precise measurement was done via a local Bragg-spectroscopy experiment in [150]. Theoretical and numerical approaches to determine this parameter are reviewed in [48].

This yields a contact:

$$C_2 = \frac{6\pi\zeta}{5} N_f k_F \tag{2.46}$$

or a volumic contact $\mathcal{C}_2 = C_2/\Omega$, more frequent in literature:

$$\mathcal{C}_2 = \frac{2\zeta}{5\pi} k_F^4 \tag{2.47}$$

In the whole crossover

To obtain the contact in the whole BEC-BCS crossover, we can use the expression of the EoS in terms of the Padé approximants that was obtained in section 2.3.4 and derive it with respect to $1/a$. In Fig. 2.2, we represented the normalized energy ξ. To obtain the contact from it, we use the adiabatic sweep theorem:

$$C_2 = -\frac{4\pi m}{\hbar^2}\frac{\mathrm{d}}{\mathrm{d}(1/a)}\left(\Theta(a)\frac{NE_b}{2} + \frac{3}{5}NE_F\xi\right) \tag{2.48}$$

with Θ the Heaviside function. To compare it with a calculation of the contact in the crossover using a Luttinger-Ward approach [151], we express the dimensionless contact density $s = C_2/k_F^4$. It can be related to ξ through

$$s = \Theta(x)\frac{4}{3\pi}x - \frac{2}{5\pi}\xi'(x) \tag{2.49}$$

with $x = 1/k_F a_{ff}$. We represented the result in Fig. 2.3 along the data from [151]. We see on this graph that they agree well in most of the BEC-BCS crossover, in particular we recover the asymptotic behaviors on the BEC and BCS sides. However, close to unitarity we have a discontinuity of s', yielding some kind of "bump", that is not physical but linked to discontinuity of the second derivative of the Padé approximants.

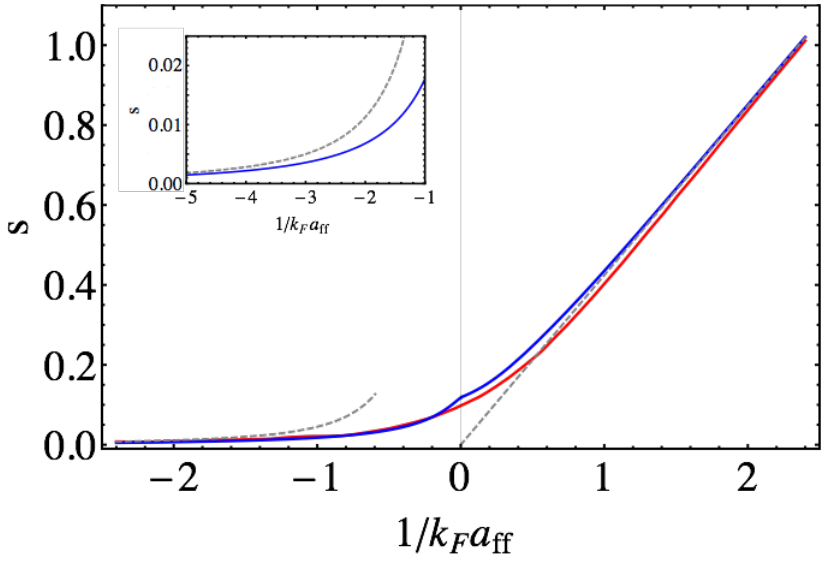

Figure 2.3: Dimensionless contact s in the crossover as a function of $x = 1/k_F a_{ff}$. Blue solid line: contact obtained from the EoS of the Fermi gas. Red solid line: contact obtain with a Luttinger-Ward approach in [151]. Dashed gray line on the $x < 0$ side: BCS asymptotic contact given by $s = (2/3\pi x)^2$. Dashed gray line on the $x > 0$ side: BEC asymptotic contact given by $s = 4x/3\pi$. Inset: zoom on the data in the BCS limit.

2.4.5 Other measurements of the contact

We already presented a first method to measure the contact, with the disadvantage of not being able to recover precisely the contact at unitarity (as we have a "bump" at unitarity). Another method consists in using RF-spectroscopy where interacting atoms are

transferred to a non-interacting state, with a transition rate directly linked to the contact [152, 153]

$$\Gamma(\omega) \propto \frac{C_2}{\omega^{3/2}}. \tag{2.50}$$

This method was used in several experiments [154, 155] and also compared to the results obtained by looking to the tail of the momentum distribution [156].

Other methods include photoassociation of atoms to form deeply-bound molecules [54, 157] or the use of the structure factors measured by Bragg spectroscopy [158, 159].

In Fig. 2.4, we compare several measurements of the contact in the crossover performed using those different techniques. It shows that all measurements are in agreement and validates all the different relations involving the Contact that would seem otherwise disconnected.

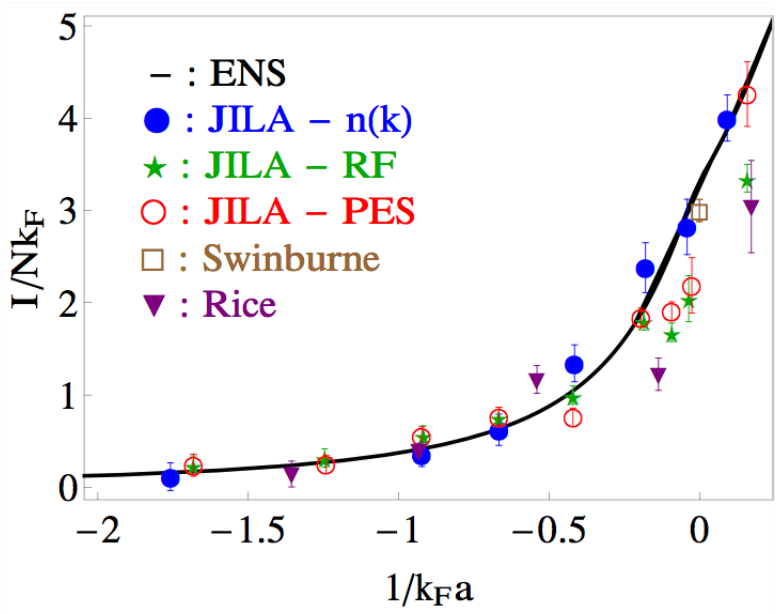

Figure 2.4: Normalized integrated contact ($\mathcal{I} = \int \mathrm{d}^3 r \mathcal{C}_2(\boldsymbol{r})$) over the cloud in the trap in the BEC-BCS crossover (here $k_F = \sqrt{2m_f\overline{\omega}_f(3N)^{1/3}/\hbar}$ is the trap Fermi wavevector with $\overline{\omega}_f$ the geometric average of the trapping frequencies of fermions and N the total number of fermions), taken from [123]. The black plain curve was deduced from measurements of the equation of state performed in [137]. It is compared to three measurements done at JILA: large momentum-tail of the momentum dustribution using a fast magnetic sweep (solid blue circles), photoemission spectroscopy (red circles) and the large frequency tail of the RF lines (green stars) [154, 156]. The brown empty squares correspond to Bragg spectroscopy measurements [159, 160] and the purple down triangle use the number of closed-channel molecules [54].

2.5 The spin-polarized Fermi gas

Up to now, we only presented results on the balanced Fermi gas, for which the number of fermions in each spin state is the same. In this section, we will study the consequence of

an imbalance of the population of the two spin states on the behaviour of the Fermi gas in the BEC-BCS crossover.

We will consider in this section a Fermi gas with two possible spin states $\uparrow$ and $\downarrow$. The polarization of this Fermi gas is defined as

$$P = \frac{N_\uparrow - N_\downarrow}{N_\uparrow + N_\downarrow} \tag{2.51}$$

with N_σ the number of fermions in the spin state $\sigma = \uparrow, \downarrow$. A fully polarized Fermi gas corresponds to $P = \pm 1$ whereas a balanced Fermi gas corresponds to $P = 0$. The species with the greatest number of atoms will be referred to as the majority species, and the other one as the minority species.

As the superfluidity of the Fermi gas relies on the pairing of fermions of opposite spins, the question of the superfluidity of a polarized Fermi gas naturally arises. This problem was first adressed independently by Clogston [161] and Chandrasekar [162], a few years only after the emergence of the BCS theory for superconductivity, who considered the case where the spin polarization comes from the Zeeman coupling of the electrons to an external magnetic field. Their considerations can also be applied to a polarized Fermi gas, for which the effective"magnetic" or spin-polarizing field is given by the chemical potential difference between the two spin states $\overline{\mu} = (\mu_\uparrow - \mu_\downarrow)/2$.

The fate of the superfluidity relies on the competition between the gain in flipping the spin of an atom and the cost of breaking a pair, given in BCS theory by the order parameter Δ which sets the gap for single-particle excitations. A criterion for the maintaining of a superfluid state is obtained by comparing the energy of the unpolarized BCS state $E = E_0 - N_0\Delta_0^2/2$ and the energy of the partially polarized normal state $E = E_0 - N_0\overline{\mu}^2$, where E_0 is the energy of the normal phase, N_0 the density of states at the energy level and Δ_0 is the zero-temperature energy gap for $\overline{\mu} = 0$. Clogston and Chandrasekar evaluated using a mean-field approximation that a superfluid can still exist for $\overline{\mu} < \Delta_0/\sqrt{2}$. Above this value the normal state takes over and superfluidity disappears. This phase transition is of first order because the unpolarized superfluid is still a local minimum in the energy landscape [163]. On the BEC side, the energy cost to flip a spin is the energy of the shallow dimer $\hbar^2/ma_{ff}^2$, which becomes increasingly large in the BEC limit. The system will then be robust in presence of an effective magnetic field and a second order transition to a polarized superfluid occurs [164], corresponding to a molecular Bose gas immersed in a Fermi sea of unpaired excess atoms.

The polarized Fermi gas has been thoroughly discussed in the review [165] and Navon's PhD thesis [123]. We will present in this section its main aspects.

2.5.1 Imbalanced ultracold Fermi gases

The experimental study of a Fermi gas with imbalanced spin populations was rather straightforward once balanced fermionic superfluidity was achieved. The first experimental study of this system was conducted almost simulatenously by groups from Rice University and MIT [166, 167] with unitary Fermi gases. Despite some discrepancies between their results, both experiments are in agreement with Clogston-Chandrasekar's proposal that superfluidity is robust against spin polarization. Both groups were able to observe a phase separation of the cloud in a shell structure, with a fully paired superfluid core with equal density for each spin state surrounded by a"magnetized" rim with imbalanced populations [168, 169]. By rotating the cloud, the MIT group observed the

appearance of vortices in the core, proving unambiguously its superfluidity, but none in the outer rim, proving it is not superfluid.

This structure into two phases is expected for a Fermi gas in a harmonic trap: while the effective spin-polarization field $\overline{\mu}$ is constant in the cloud, the gap Δ decreases with the density that is maximum at the center of the trap and goes to zero at the edge of the cloud. To interpret this shell structure within the Clogston-Chandrasekar scenario, we introduce a critical value of the effective spin-polarizing field $\overline{\mu}_c$ a priori different from the expression obtained with BCS theory ($\Delta_0/\sqrt{2}$) since the Fermi gases are in the unitary regime. A superfluid core will exist if the condition $\overline{\mu} < \overline{\mu}_c$ is verified at the center but, as we move away from the center, the density decreases and eventually the condition is not verified, leading to a normal phase on the outer rim.

Furthermore, for a strong enough polarization, the MIT group observed that no superfluid phase subsisted, corresponding to the case where $\overline{\mu} > \overline{\mu}_c$ is already true at the center of the cloud. They measured a critical polarization $P_c \simeq 0.75$ at unitarity, which was later confirmed by measurements in our group [123].

One particularly interesting featured that was noticed by the MIT group is in the structure of the normal phase at the rim of the trap. Indeed, the normal phase is separated into a fully polarized phase at the edge of the cloud and a mixed phase, in-between the superfluid core and the fully polarized phase, where the two spin components are present[8]. This is also the case in our experiment and a typical analysis of the profile of such a system is detailed in the next chapter.

The EoS of the superfluid phase has been measured in our group and was presented in section 2.3.4 and the EoS of the fully polarized phase corresponds to the EoS of an ideal gas, and the indermediate partially polarized phase can be described as a Fermi liquid of quasiparticles made of minority atoms (here we choose the $\downarrow$ fermions) immersed in an ideal Fermi sea of majority atoms ($\uparrow$ fermions). In order to study this phase, we will focus on the extreme case, on the frontier between the fully polarized and the partially polarized phases, where we have one spin-down fermion and $N_\uparrow \gg 1$ spin-up fermions.

2.5.2 The N+1 body problem: the Fermi polaron

The Fermi polaron is a quasiparticle that arises from the interaction of an impurity with an ensemble of spin-polarized fermions, where the impurity is dressed by the particle-hole excitations of the surrounding Fermi sea. A review on the polaron can be found in [171].

We introduce the Hamiltonian of the system

$$\widehat{H} = \underbrace{\sum_{k,\sigma} \varepsilon_k^{(f)} \widehat{a}_{k,\sigma}^\dagger \widehat{a}_{k,\sigma}}_{\widehat{H}_0} + \underbrace{\frac{g_0(\Lambda)}{V} \sum_{k,k',q} \widehat{a}_{k+q,\uparrow}^\dagger \widehat{a}_{k'-q,\downarrow}^\dagger \widehat{a}_{k'\downarrow} \widehat{a}_{k,\uparrow}}_{\widehat{V}} \tag{2.52}$$

where $a_{k,\sigma}$ is the fermionic operator for a fermion of momentum $\boldsymbol{k}$ and spin σ, $g_0(\Lambda)$ is the bare coupling constant with Λ a UV-cutoff and $\varepsilon_k^{(f)} = \hbar^2 k^2 / 2m_f$.

[8] This feature was not observed by the Rice group, who only observed a fully polarized normal phase. This was explained later in [170] by a metastability of their system, and a dynamical spin-blocking which forbade the formation of the mixed phase.

Energy in the BCS limit

A first insight on the fermi polaron problem can be obtained in the weakly attractive limit, where the interaction between the impurity and the majority fermions remains small. To obtained the shift in energy δE of the system due to the impurity, we perform a perturbative expansion of the energy at the order two in the interaction potential. The bare coupling constant g_0 can be expanded as

$$g_0 = g_{ff} + \frac{g_{ff}^2}{\Omega} \sum_{\boldsymbol{k},\, k<\Lambda} \frac{1}{2\varepsilon_k^{(f)}} \tag{2.53}$$

in the limit $\Lambda a_{ff} \ll 1$, with $g_{ff} = 4\pi\hbar^2 a_{ff}/m_f$.

The perturbative expansion of the energy reads

$$\delta E = \langle 0|\widehat{V}|0\rangle + \sum_{|n\rangle \neq |0\rangle} \frac{|\langle 0|\widehat{V}|n\rangle|^2}{E_0 - E_n} \tag{2.54}$$

with $|0\rangle$ the fundamental state of the Fermi sea, $|n\rangle$ the excited states and $E_0 - E_n$ the difference of energy between those two states. The first excitations consist in extracting a majority fermion from the Fermi sea due to the interaction with the impurity. Its momentum before the interaction must be $k < k_F$ and after the interaction $k' > k_F$. The energy difference $E_0 - E_n$ can be written as $\varepsilon_k^{(f)} - \varepsilon_{k'}^{(f)} - \varepsilon_{|\boldsymbol{k}-\boldsymbol{k}'|}^{(f)}$ where $\boldsymbol{k} - \boldsymbol{k}'$ is the momentum of the impurity after the interaction.

$$\delta E = g_{ff} n_\uparrow \left[1 + \frac{g_{ff}}{\Omega} \sum_{\boldsymbol{k}'} \frac{1}{2\varepsilon_{k'}^{(f)}} + \frac{g_{ff}}{\Omega} \sum_{\substack{\mathbf{k},\mathbf{k}' \\ k<k_F \\ k'>k_F}} \frac{1}{\varepsilon_k^{(f)} - \varepsilon_{k'}^{(f)} - \varepsilon_{|\boldsymbol{k}-\boldsymbol{k}'|}^{(f)}} \right] \tag{2.55}$$

with $n_\uparrow$ the density of the majority species, related to the Fermi wavevector with $k_F = (6\pi^2 n_\uparrow)^{1/3}$. Thanks to the regularization of the coupling constant, this quantity is well-defined at order two. The total sum can be calculated readily and we obtain

$$\delta E = E_F \left[\frac{4}{3\pi}(k_F a_{ff}) + \frac{2}{\pi^2}(k_F a_{ff})^2 + O[(k_F a_{ff})^3] \right] \tag{2.56}$$

Variational method

This method obviously does not hold in the strongly interacting regime where it would lead to a diverging polaron energy. This problem was nevertheless adressed analytically, for instance by F. Chevy who proposed a variational ansatz describing the scattering of the impurity , creating one particle-hole excitation in the Fermi sea [172]:

$$|\psi\rangle = \phi_{\boldsymbol{k}_0} |\boldsymbol{k}_0, 0\rangle + \sum_{\boldsymbol{k},\boldsymbol{q}} \phi_{\boldsymbol{k},\boldsymbol{q}} \widehat{a}_{\boldsymbol{k},\uparrow}^\dagger a_{\boldsymbol{q},\uparrow} |\boldsymbol{k}_0 + \boldsymbol{q} - \boldsymbol{k}, 0\rangle \tag{2.57}$$

where $|\boldsymbol{k}_0, 0\rangle$ is the state where the impurity has a momentum $\boldsymbol{k}_0$ and the Fermi sea of the majority species is in its ground state. The sum describes the particle-hole excitations where a majority atom of the Fermi sea of momentum $\boldsymbol{q}$ ($q < k_F$) is being excited to

a momentum $\boldsymbol{k}$ ($k > k_F$). To determine the properties of the polaron, one finds the parameters $\phi_{\boldsymbol{k}_0}$ and $\phi_{\boldsymbol{k},\boldsymbol{q}}$ that minimize the expectation value of the Hamiltonian presented in eq. (2.52). This ansatz is correct up to second order in a_{ff} and yields eq. (2.56) in the weakly attractive limit.

At low momenta, the dispersion relation of the impurity can be expanded as

$$E(k_0) = AE_F + \frac{\hbar^2 k_0^2}{2m^*} + ... \tag{2.58}$$

From this relation, we see that the dressing of the impurity by the Fermi sea results in a quasiparticle with a dimensionless effective mass m^*/m and binding energy AE_F, the Fermi polaron. These two parameters depend on the interaction strength $1/k_F a_{ff}$. In the BCS limit, the impurity behaves as a free particle so we have $m^* = m_f$ and $A = 0$. At unitarity, the variational approach yields $A \simeq -0.6$ and $m^* = 1.17m$. Even though this result is variational and can only give an upper bound for the value of A, it is remarkably close to the variational Fixed Node Monte-Carlo predictions [173] ($A = -0.59(1)$ and $m^* = 1.09m$) and the diagrammatic Monte-Carlo predictions [174] ($A = -0.61(1)$ and $m^* = 1.20(1)m$). This can be explained by the relatively weak probability of excitation of a particle-hole pair ($\sim 25\%$ in the variational calculation), confirmed by a systematic expansion of the polaron energy as a function of the number of excited particle-hole pairs that converges quite fast [174, 175]. Furthermore, experimental measurements from MIT using a density profile analysis [176] and our group using a collective modes study [177] showed that the effective mass is indeed close to unity, with $m^*/m = 1.06$ and $m^*/m = 1.17(10)$ respectively, thus barely modified by the interactions. We represent in Fig. 2.5 the parameters A and m^* in the crossover obtained using several theories, taken from [123].

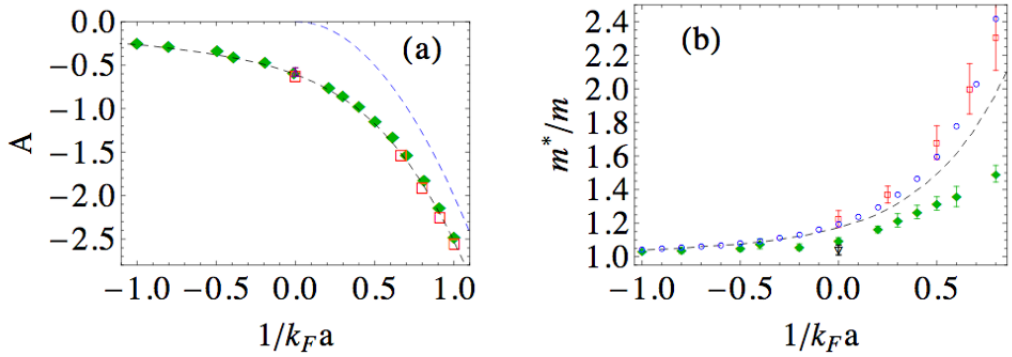

Figure 2.5: (a) Dimensionless binding energy A of the Fermi polaron in the crossover. Dashed black line: single particle-hole ansatz [178]. Red squares: diagrammatic Monte-Carlo calculations [174]. Green diamonds: Fixed-Node Monte Carlo calculations [143]. The purple triangle corresponds to a RF measurement at unitarity in agreement with the theories [179]. The dashed blue curve corresponds to the binding energy of the halo-dimer on the BEC side. (b) Effective mass m^*/m of the Fermi polaron in the crossover. Dashed black line: single particle-hole ansatz [178]. Blue circles: Two-particle-hole analytical calculation [175]. Black triangle: Fixed-node result at unitarity [173]. Green diamonds: Fixed-Node Monte-Carlo calculation [143].

The partially polarized phase that was observed experimentally can then be interpreted as a gas of polarons. It was observed numerically [143, 173] and confirmed analytically

[180] that at finite concentration $x = n_\downarrow/n_\uparrow$, the small amount of Fermi polarons form a degenerate gas with a Landau-Pomeranchuk EoS:

$$E = \frac{3}{5}N_\uparrow E_{F_\uparrow}\left[1 - \frac{5}{3}Ax + \frac{m}{m^*}x^{5/3} + Fx^2 + ...\right] \tag{2.59}$$

where $E_{F_\uparrow}$ is the Fermi energy associated to the majority species (the precision is needed since we no longer have only one impurity) and the term Fx^2 accounting for interactions between quasi-particles when x is not so small. This EoS in the grand canonical ensemble can be written in the crossover as [181]:

$$P(\mu_\uparrow, \mu_\downarrow) = \frac{1}{15\pi^2}\left[\left(\frac{2m}{\hbar^2}\right)^{3/2}\mu_\uparrow^{5/2} + \left(\frac{2m^*}{\hbar^2}\right)^{3/2}(\mu_\downarrow - A\mu_\uparrow)^{5/2}\right] \tag{2.60}$$

where it is separated between an ideal Fermi gas of the majority atoms and an ideal gas of polarons with a renormalized mass m^* and a shifted chemical potential $\mu_\downarrow - A\mu_\uparrow$ due to the binding to the Fermi sea. The interaction term in the canonical EoS can be obtained with the grand canonical one and reads [180]

$$F = \frac{5}{9}\left(\frac{\mathrm{d}A\mu_\uparrow}{\mathrm{d}E_{F_\uparrow}}\right). \tag{2.61}$$

Moreover, the interaction between polarons can also be interpreted as an interaction mediated by the Fermi sea [182].

The grand canonical EoS can also be expressed in the crossover with dimensionless parameters:

$$h_{PP}(\eta, \delta_\uparrow) = 1 + \left(\frac{m^*(\delta_\uparrow)}{m}\right)^{3/2}(\eta - A(\delta_\uparrow))^{5/2} \tag{2.62}$$

where h_{PP} is the dimensionless pressure in the partially polarized phase (with the same definition as in section 2.3.4), $\eta = \mu_\downarrow/\mu_\uparrow$ is the spin imbalance and $\delta_\uparrow$ defined by

$$\delta_\uparrow = \frac{\hbar}{\sqrt{2m(\mu_\uparrow - E_b)a_{ff}}} \tag{2.63}$$

where E_b is the energy of the shallow dimer for $a > 0$ and zero otherwise. We show in Fig. 2.6 the EoS of the partially polarized phase in the grand canonical ensemble measured in our group [137], which were used to measure the effective mass in the crossover by using the theoretical value of A and leaving m^*/m as a free parameter. The extracted effective mass was indeed in good agreement with the theoretical predictions, confirming the validity of this EoS.

2.5.3 Fermi polaron to molecule transition

In the BEC domain, the impurity can form a halo-dimer with an atom from the majority species, giving rise to a bosonic rather than fermionic quasiparticle. Consequently, there is a competition between the Fermi polaron state and the molecular state: the transition between the two states was unveiled by Monte-Carlo simulation of the impurity problem [174]. It shows that the phase transition is of first order and located at $1/k_F a_{ff} = 0.91(2)$, with a sharp crossing between the energy curves of the fermi polaron and the halo-dimer on the BEC side. Above this critical interaction, the impurity can be

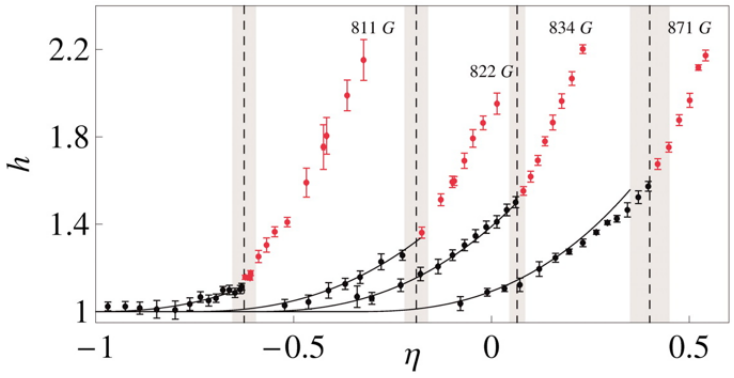

Figure 2.6: Equation of state h of an imbalanced Fermi gas as a function of the spin imbalance η, taken at different magnetic fields: on the BEC side $B = 811$ G ($1/k_F a_{ff} \simeq 0.2$) and $B = 822$ G ($1/k_F a_{ff} \simeq 0.1$), near unitarity $B = 834$ G ($1/k_F|a_{ff}| < 0.01$) and on the BCS side $B = 871$ G ($1/k_F a_{ff} \simeq -0.2$) (from [137]). Points corresponding to the superfluid phase (normal phase) are in red (black). Vertical dashed lines with an uncertainty gray shaded area are located around the normal/superfluid transition for each curve. The black solid lines are fits using eq. (2.62) to determine the effective mass in the crossover.

described as a point-like boson interacting with the Fermi sea with a mean-field energy $g_{ad} n_\uparrow$, with the coupling constant associated to the scattering length $a_{ad} \simeq 1.18 a_{ff}$ [183]. Extensions of the variational description of the polaron in the molecular sector are derived in [164, 184, 185], where the quasiparticle is described as a dimer dressed by single particle-hole excitations, yielding results compatible with the Monte-Carlo calculations and experimental measurements from MIT using RF spectroscopy [179]. From a comparison of both the fermionic and the bosonic ansatz on the BEC side, a $\approx 15\%$ jump in the contact of the system is expected at the transition [164].

In the BEC limit, the system can be described as a mixture of Bose-Einstein condensates of dimers and a Fermi sea of excess fermions using the mean-field EoS [186, 187]:

$$\frac{E}{V} = -\frac{\hbar^2}{m a_{ff}^2} n_b + \frac{3}{5} E_{F,\text{free}} n_{\text{free}} + \frac{1}{2} g_{dd} n_b^2 + g_{ad} n_b n_{\text{free}} + \dots \tag{2.64}$$

where $n_b = n_\downarrow$ is the density of bosonic dimers, $n_{\text{free}} = n_\uparrow - n_\downarrow$ is the density of free excess fermions, g_{dd} is the coupling constant for s-wave dimer-dimer interactions and $E_{F,\text{free}}$ is the Fermi energy calculated considering solely the free fermions.

Contrary to the BCS side of the crossover where the gap maintains a perfect pairing, for $n_{\text{free}} \neq 0$, this equation describes a polarized superfluid. These theoretical predictions on the BEC side still await experimental confirmation whereas the BCS side has been explored thoroughly. The increase in the atomic loss rate on the BEC side (dimer-dimer losses scale as $a^{-2.55}$) makes it very challenging to study this part of the crossover.

2.5.4 Repulsive branch

Another important feature of the Fermi polaron is another polaronic branch on the BEC side of the crossover. Indeed, the variational ansatz obtained by Chevy predicts two solutions for the energy of the polaron for $a > 0$. The lower energy corresponds to the

attractive polaron branch that was discussed before and the higher energy corresponds to another type of polaron: the repulsive polaron. Instead of attracting the majority fermions towards it, the repulsive polaron is dressed by the repulsion of the majority fermions. A detailed theoretical review on the repulsive polaron can be found in [188].

Far on the BEC side, the repulsive polaron is very similar to the attractive polaron far on the BCS side. The expansion of its energy gives exactly what we obtained in eq. (2.56), with a first-order term giving the expected $\delta E = g_{ff} n$. The difference being that since $a > 0$, this energy is also positive, contrary to the energy of the attractive polaron. The effective mass of the repulsive polaron reduces to the impurity mass in the deep BEC domain, and rises rapidly as we go in the strongly interacting regime, where the dressing of the polaron by the particle-hole pairs increases drastically, until it diverges to infinity at unitarity. An expansion of the effective mass in the weakly interacting limit reads [189]

$$\frac{m}{m^*} = 1 - \frac{4}{3\pi^2}(k_F a_{ff})^2 + ... \tag{2.65}$$

The repulsive polaron is not the most stable state since the attractive polaron and the dimer have much lower energies (they both have negative energies), with a discrepancy that increases as we go deeper in the BEC regime. The repulsive polaron is then a metastable state with a finite lifetime. However, it was shown that the decay rate is small compared to E_F for $1/k_F a_{ff} \gg 1$, showing that the repulsive polaron is a well-defined quasiparticle far from resonance [188]. The repulsive polaron was first realized experimentally with a ^{6}Li-^{40}K mixture in [190] but around a narrow Feshbach resonance, for which the universal regime is very restricted, and then realized in [191] with a resonant mixture of ^{6}Li atoms. Using RF spectroscopy, the effective mass, the energy and the decay rate were extracted, in accordance with multiple theoretical predictions [188,192–194]. In Fig. 2.7, we show the measurement of the energy and the effective mass of the repulsive from [191] compared to a few theories.

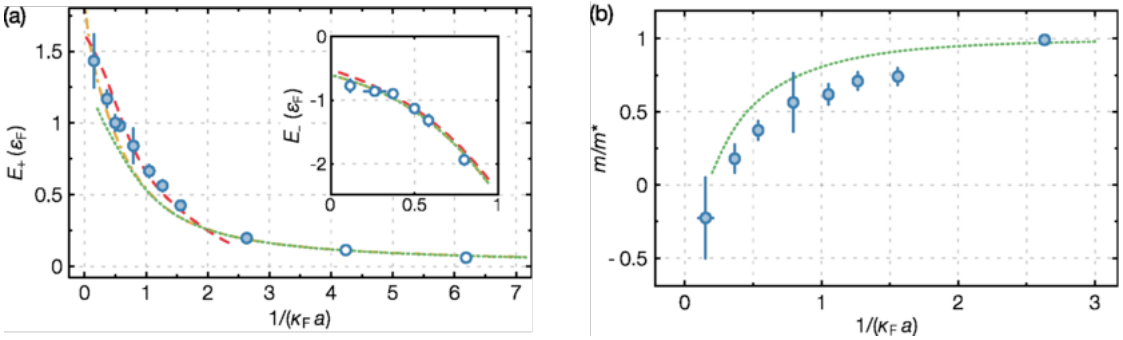

Figure 2.7: Properties of the repulsive branch, taken from [191]. (a) Zero-momentum repulsive polaron energy E_+ as a function of $1/\kappa_F a_{ff}$ (blue circles), with $\kappa_F \simeq 0.86 k_F$ is the averaged Fermi wavevector over the fermion density. Inset: Energy of the attractive polaron E_- (blue circles). They are compared to theoretical predictions from [193] (dot-dashed yellow line), [188] (dotted green line) and [192] (dashed red line) in both panels. (b) Inverse effective mass m/m^* of the repulsive polaron as a function of $1/\kappa_F a_{ff}$ (blue circles), compared to theory predictions from [188]. The point corresponding to a negative effective mass is in the domain where the repulsive polaron is ill-defined.

In short, we have described the main properties of an impurity immersed in a spin-polarized Fermi sea, as well as the structure of the imbalanced Fermi gas at zero-temperature.

A natural extension of this problem is the study of an impurity in a BEC, the Bose polaron, that we will present in the next section.

2.6 The Bose polaron

The Bose polaron problem is connected to the original polaron problem investigated by Landau and Pekar [63], for which a conduction electron is immersed in a phonon bath. In cold atoms, the Bose polaron can be realized by considering an impurity immersed in a Bose-Einstein condensate.

We note a_{ib} the scattering length associated with the interaction between the impurity and a boson of the BEC, m_{ib} the impurity-boson reduced mass and n_b the density of the BEC. Similarly as the case of the Fermi polaron, the interaction strength is often defined as $1/k_n a_{ib}$, with $k_n = (6\pi^2 n_b)^{1/3}$. It is associated to the energy $E_n = \hbar^2 k_n^2 / 2m_b$. Depending on the interaction strength, the Bose polaron exhibits different behaviors.

For weakly attractive interactions, the Bose polaron can be described perturbatively. The mean-field expression of the energy is of the form $\delta E = g_{ib} n_b$ where $g_{ib} = 2\pi\hbar^2 a_{ib}/m_{ib}$, similar to the mean-field term of the Fermi polaron, and the second and third-order terms can be found in [195]. In this limit, the effective mass m^* of the Bose polaron tends towards m_i.

To explore the strongly interacting regime, a variational ansatz adapted from the Fermi polaron ansatz has been used [196], as well as a field-theoretical study [197]. Both studies are in agreement and determined the energy of the polaron for any interaction strength. When $a_{ib} > 0$, an impurity-boson dimer can be formed, but contrary to the Fermi polaron case, there is no sharp transition expected from the Bose polaron to the molecular state. Both studies expect a smooth transition between the two states: the energy of the polaron tends asymptotically towards that of the shallow dimer energy and the effective mass of the Bose polaron tends smoothly towards $m^* = m_i + m_b$, signature of the dimer state.

Similarly to the Fermi polaron, for $a_{ib} > 0$, a repulsive branch of the Bose polaron also exists. While in the weakly interacting regime $a_{ib} \to 0^+$, the Bose polaron is well-defined and can be described with a perturbative expansion, in the strongly interacting regime the Bose polaron is ill-defined for $1/k_n a_{ib} \lesssim 1$, with a strong decay into the lower-lying energy branches.

Despite all these similarities, the Bose and Fermi polarons differ by two important aspects. First, the background BEC can be interacting at low temperatures (which is not the case for a spin-polarized Fermi sea). A comparison of a Bose polaron in an ideal BEC and a weakly interacting BEC can be found in [196]. The boson-boson interactions in the BEC do not seem to change the properties of the Bose polaron in first approximation. Moreover, in the context of the Bose polaron there is the possibility of having three-body Efimov correlations. The three-body effects were not taken into account in [196, 197] but were investigated in [198, 199]. They showed that three-body physics can affect the Bose polaron in the strongly interacting regime with an avoiding crossing between the polaronic energy branch and the trimer energy branch, meaning the impurity becomes smoothly bound into an Efimov trimer in this regime.

The Bose polaron has been investigated experimentally in the strongly interacting regime in JILA with fermionic ^{40}K impurities in a BEC of ^{87}Rb [200] and in Aarhus University with ^{39}K for the impurities and the BEC using two different internal states [201]. In the system used by JILA, the Efimov effects were only expected to take place in a very narrow range around the resonance that they did not resolve, thus their experimental data

matched the theories from [196, 197]. With the system used in Aarhus University, they obtained data compatible with the predictions from [198] including three-body effects, confirmed with a new analysis of their experimental data [202]. We show in Fig. 2.8 the spectral response of the impurity in the BEC obtained in [201] through RF spectroscopy. It proves indeed the presence of an attractive and a repulsive branch for the Bose polaron.

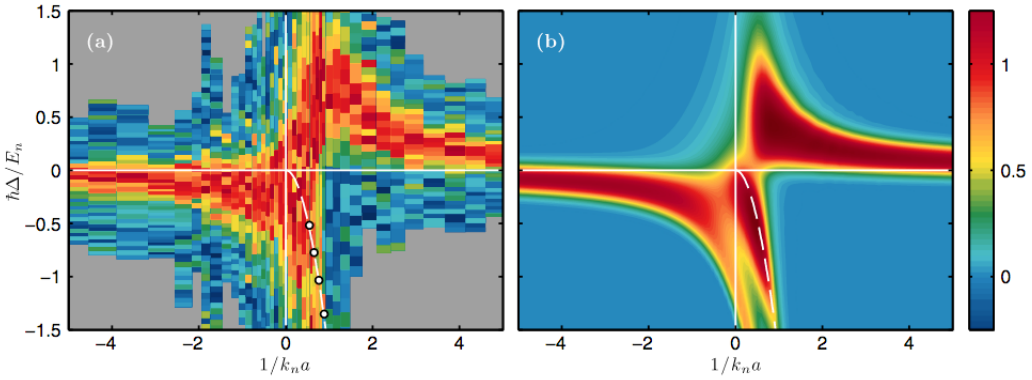

Figure 2.8: Spectral response of the impurity in the BEC obtained with RF spectroscopy, taken from [201]. The false colors represent the spectral weight of the polaron for different values of the detuning Δ between the RF frequency and the frequency of the hyperfine transition used for the RF spectroscopy, and different values of the interaction strength $1/k_n a_{ib}$. The panel (a) corresponds to experimental measurements whereas the panel (b) corresponds to a calculated spectrum. The independently measured molecular energy is represented with white dots and the white dashed line corresponds to a fit to these points.

Conclusion

In this chapter, we have presented the physics of ultracold Bose and Fermi gases, focusing on their most relevant aspects for this PhD thesis. In the next chapter, we will see how superfluidity and the BEC-BCS crossover can be realized experimentally with a sequence of trapping and cooling stages.

In the last two sections, we introduced the Fermi and Bose polarons, quasiparticles arising from the interaction between an impurity and a Fermi or a Bose gas respectively. In our set-up, we use a Fermi superfluid of ^{6}Li interacting weakly with a Bose gas of ^{7}Li with typically much less atoms, thus can be seen as a gas of impurities immersed in the Fermi gas and associated with the problem of an impurity in a two component Fermi gas. On the BCS side of the crossover, the problem is analogous to the Fermi polaron with two Fermi seas instead of one. On the BEC side, the Fermi superfluid becomes a condensate of bosonic dimers, so the problem is analogous to the Bose polaron. Consequently, our system realizes a crossover between the Fermi polaron and the Bose polaron, that we will study thoroughly in the following chapters of this thesis.

Chapter 3

Producing a superfluid Bose-Fermi mixture

In this chapter, we will present the apparatus we used to produce an ultracold Bose-Fermi mixture of Lithium. This experimental apparatus has already been described in great details in the theses of G. Ferrari [203], F. Schreck [204], L. Tarruell [205] or S. Nascimbène [206], so we will simply focus on the main technical aspects of the experimental sequence needed to obtain the degenerate mixture, after having presented the two Lithium species that are used in this set-up.

3.1 Overview of the set-up

The general idea is to cool down our mixture of ^{7}Li and ^{6}Li towards quantum degeneracy using laser cooling and evaporative cooling. Schematics of the set-up are represented in Fig. 3.1. A hot Lithium vapor is produced in the oven and escaping through a collimation tube. The atomic jet is slowed down in the Zeeman slower and then captured in the magnetic optical trap (MOT). Due to the small hyperfine splitting of the excited states, the temperature at the end of our MOT is too high to be directly loaded in an optical dipolar trap, so instead we transfer magnetically the atoms to a strongly confining magnetic trap in an appendage of the glass cell where RF evaporation is used to cool down ^{7}Li atoms whereas ^{6}Li is cooled sympathetically. Atoms are finally transferred in a dipolar trap where a second evaporative cooling is applied at high magnetic field to take advantage of the broad Feshbach resonance for ^{6}Li, and this time ^{7}Li atoms are sympathetically cooled. At the end of this second evaporative cooling, experiments are performed in a hybrid optical-magnetic trap. The different stages of the experimental sequence are further described in the following sections.

3.2 Lithium atoms

Lithium is the third element of the periodic table, the lightest alkali metal, and possesses two stable isotopes: ^{7}Li and ^{6}Li, a boson and a fermion with natural abundances of 92.5% and 7.5% respectively and masses of $m_b = 7.016u$ and $m_f = 6.015u$, with $u = 1.661 \times 10^{-27}$ kg the atomic mass unit.

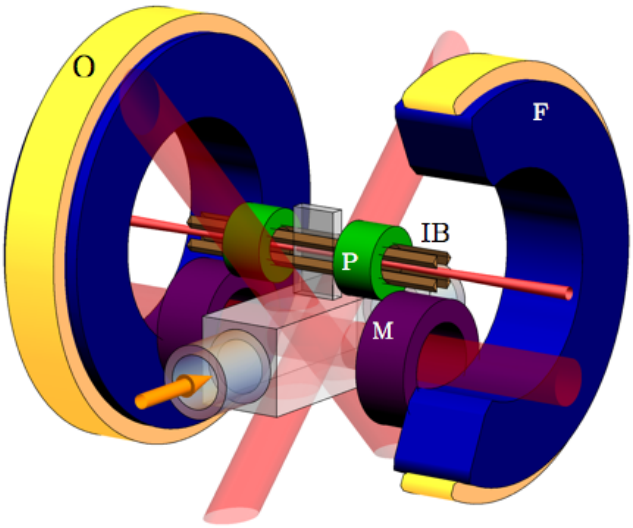

Figure 3.1: Schematics of the set of coils needed for the several trapping and cooling stages. In the middle-bottom part, we have the glass-cell where atoms coming from the Zeeman slower (orange arrow) are loaded in the MOT. The three MOT beams are represented in light red and all cross at the center of the glass cell, the MOT coils are in purple (labeled with a white M). Then, the atoms are loaded in the Ioffe-Pritchard trap in the appendage above the glass cell. The Ioffe bars (in brown, labeled with IB) impose a strong magnetic field gradient and the pinch coils (in green, labeled with a white P) a curvature in the axial direction. The bias field created by the pinch coils can be compensated by the bias field created by the Feshbach coils (in blue with a white F) and finely tuned using the pinch-offset coils (in yellow, with a black O). After an RF evaporative cooling stage, the atoms are loaded in a hybrid dipolar-magnetic trap. The dipolar trap is generated by a red-detuned high-power laser represented by a plain red beam that crosses the appendage. The magnetic trap is realized using the pinch coils to produce an axial curvature and the Feshbach coils to independently tune the bias field, up to $800 - 1000$ G to take advantage of the ^{6}Li Feshbach resonances. After an optical evaporative cooling, the two clouds are quantum degenerate.

3.2.1 Atomic structure

As an alkali, it has a single electron in its outer shell therefore its atomic structure is rather simple and given in Fig. 3.2. The ground state is $2^2S_{1/2}$ and the two lowest excited states are $2^2P_{1/2}$ and $2^2P_{3/2}$. The optical transition from the $2s$ orbital to the $2p$ orbital is around 671 nm, corresponding to red light, available at reasonably high power from commercial sources. The fine splitting between the $2^2P_{1/2}$ and $2^2P_{3/2}$ lines is 10 GHz, which is identical to the isotope shifts between the two species of the $2s \rightarrow 2p$ transition. As a consequence, the $D1$ line ($2^2S_{1/2} \rightarrow 2^2P_{1/2}$) of ^{7}Li is almost in tune with the $D2$ line ($2^2S_{1/2} \rightarrow 2^2P_{3/2}$) of ^{6}Li. The natural linewith of the transition is $\Gamma \simeq 2\pi \times 5.9$ MHz for both isotopes, so the hyperfine splitting of the $2^2P_{3/2}$ state, smaller than Γ, is not resolved.

In Fig. 3.3, we represent the energy levels of the $2^2S_{1/2}$ manifold with respect to the magnetic field. In the following, we will label $|k_{\text{iso}}\rangle$ the associated states, with $k = 1, 2, 3, ..$ the numbering of the states starting from the lowest energy state at high field and

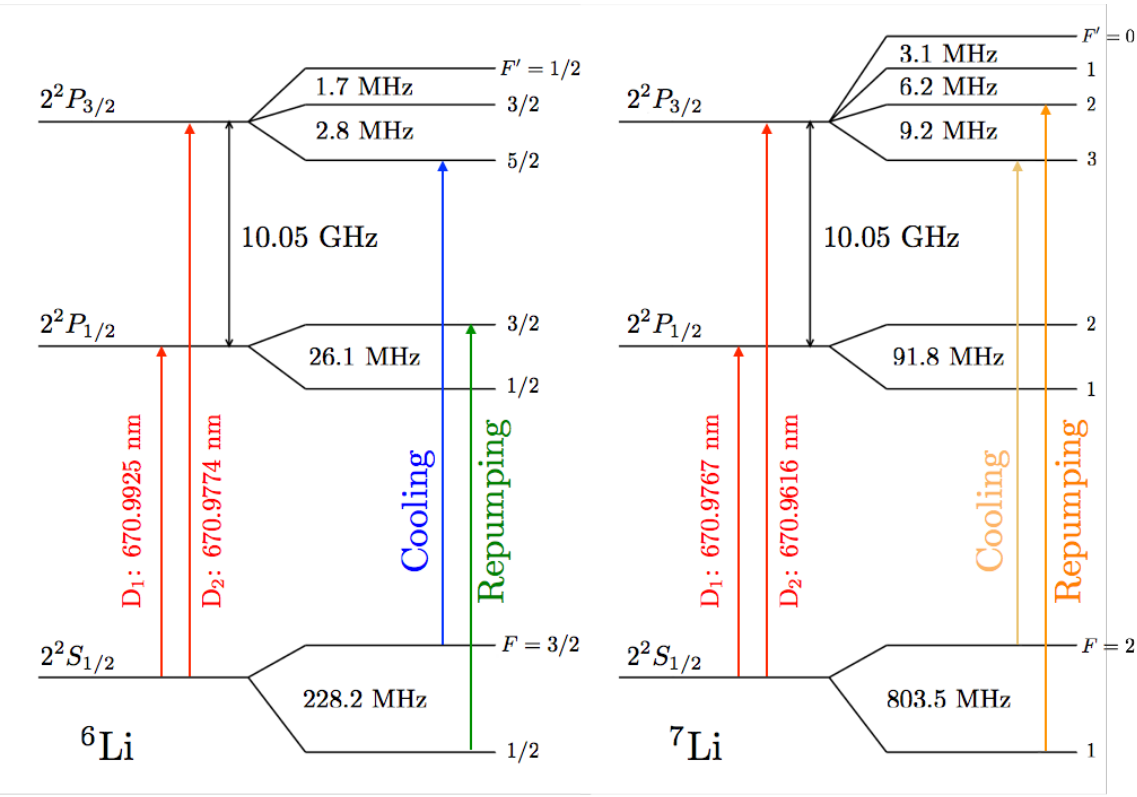

Figure 3.2: Structure of the energy levels of ^{6}Li (left) and ^{7}Li (right). In red are represented the D_1 and D_2 lines for each isotope. The transitions used for cooling and repumping in the MOT and Zeeman slower are represented for ^{6}Li in blue and green respectively and for ^{7}Li in yellow and orange respectively.

iso refers to the isotope (f for ^{6}Li and b for ^{7}Li).

3.2.2 Feshbach resonances

Lithium presents a large number of Feshbach resonances for each of its isotopes that can be exploited for the study of the strongly correlated regime in ultracold gases. In Fig. 3.4, we show the different resonances corresponding to the states used in our experiments. We give in Table 3.1 the parameters corresponding to the position B_0, the magnetic width ΔB and the background scattering a_{bg} of these resonances.

States	s_{res}	B_0(G)	ΔB(G)	$a_{bg}(a_0)$
$\|1_b\rangle - \|1_b\rangle$	0.81	737.8(2)	-171	-21
$\|2_b\rangle - \|2_b\rangle$	~ 1	893.7(4)	-237.8	-18.24
$\|2_b\rangle - \|2_b\rangle$	$\ll 1$	845.5(5)	4.5	-18.24
$\|1_f\rangle - \|2_f\rangle$	59	832.18(8)	$-262.3(3)$	$-1582(1)$

Table 3.1: Parameter values corresponding to the relevant Feshbach resonances in Lithium for our experiment.

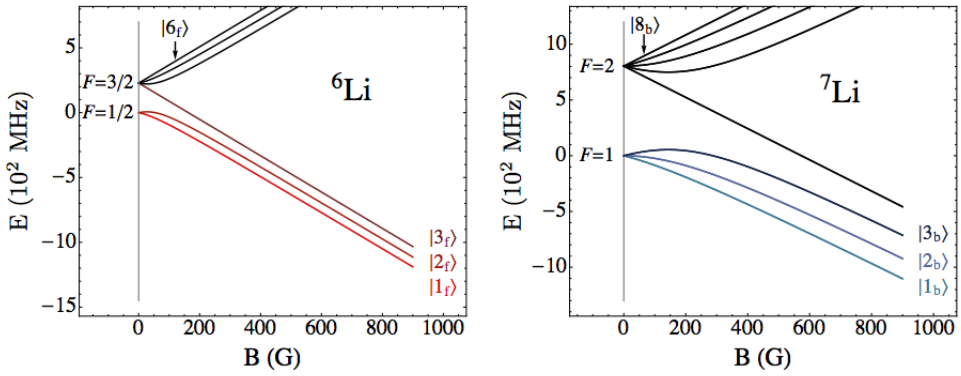

Figure 3.3: Magnetic field dependence of the energy levels of the $2^2S_{1/2}$ manifold of the fermions (left) and the bosons (right). For each panel, we took for the zero of the energy the energy of the lowest hyperfine state at $B = 0$. We see that for strong magnetic fields ($B > 400$ G), we enter in the Paschen-Bach regime where the energy levels have the same magnetic field dependence (modulo the sign).

The resonance we use between our two fermionic states $|1_f\rangle$ and $|2_f\rangle$ is located at $B = 832.18$ G [207] and is very broad $s_{res} = 59$, allowing to explore easily the BEC-BCS crossover. For ^{7}Li, the Feshbach resonances are given for the two lowest energy states. For the $|1_b\rangle$ state, formerly used in the group we see that the corresponding scattering length is negative near the fermionic resonance which forbids to obtain a BEC in this region (see section 2.2). On the contrary, the scattering length associated with the $|2_b\rangle$ state is compatible with having a BEC of bosons in a strongly interacting Fermi gas, which is why we now use this state.

Concerning the boson-fermion interaction, the scattering length remains constant and small in the region of interest, with a value of $a_{bf} = 40.8a_0$, independent of the fermionic spin state. Feshbach resonances between the two isotopes in various internal states exist, some have been calculated or measured [208, 209], but we do not use them in our current set-up.

3.2.3 Stability of the mixture

We have seen in the previous paragraph that we had a broad Feshbach resonance for the fermion-fermion interaction meaning we can explore a wide region of the BEC-BCS crossover. The goal of this section is to determine approximately the limits of the region we can explore while maintaining a stable Bose-Fermi mixture where both species are superfluid.

Obtaining an ultracold Bose-Fermi mixture is not an easy task. Indeed, in the case of liquid Helium mixtures, the strong ^{3}He-^{4}He interaction prevents from having a mixture of the two species at low temperatures with more than 6% of ^{3}He, downshifting the critical temperature for its superfluidity, because of its low density, to $T = 50$ μK, while the coldest temperature reached in such mixtures is so far 100 μK [210, 211]. In our case, the interactions between bosons and fermions are much weaker, relatively to the Fermi energy of the system, but the stability still needs to be investigated.

The stability condition for the Bose-Fermi mixture can be expressed using the com-

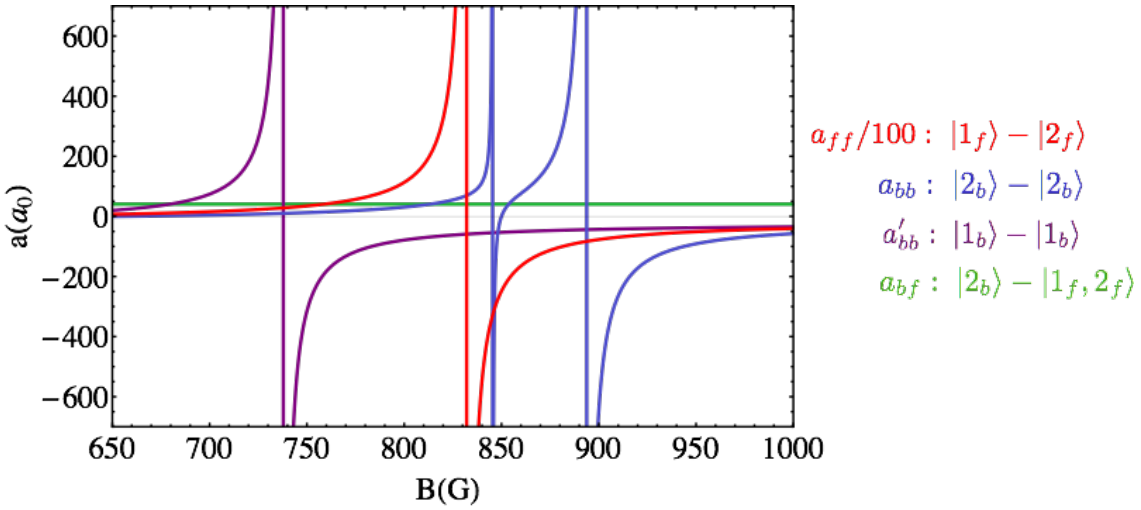

Figure 3.4: Relevant Lithium Feshbach resonances for our set-up. In red we have a very broad Feshbach resonance (the scale has been divided by a factor 100) for the two ^{6}Li spin states. In blue the two Feshbach resonances for the ^{7}Li atoms in the state we use at the end of the experimental sequence. In purple we see the ^{7}Li Feshbach resonance for the $|1_b\rangle$ state: this state cannot be used while exploring the BEC-BCS crossover with the fermions since the scattering length is negative for most of it. Finally, in green is the boson-fermion scattering length, mostly constant in the domain of magnetic field we are interested in.

pressibility matrix $\left(\frac{\partial \mu_i}{\partial n_j}\right)_{i,j}$ with the indexes $i, j = b, f$ corresponding to the two possible isotopes. Indeed, for the mixture to be stable, the matrix must be definite positive [212]. This gives the following stability conditions:

$$\frac{\partial \mu_b}{\partial n_b} > 0, \qquad \frac{\partial \mu_f}{\partial n_f} > 0 \tag{3.1}$$

and

$$\frac{\partial \mu_b}{\partial n_b}\frac{\partial \mu_f}{\partial n_f} - \frac{\partial \mu_f}{\partial n_b}\frac{\partial \mu_b}{\partial n_f} > 0 \tag{3.2}$$

For our system, since the boson-fermion interaction remains very weak for all the magnetic field we can work with, we will describe it with a mean-field approximation (a treatment of this interaction beyond mean-field will be done in Chapter 6). We will also use such an approximation for the weakly-interacting Bose gas. Therefore, we can write the chemical potentials at $T = 0$ as:

$$\mu_b = g_{bb} n_b + g_{bf} n_f \tag{3.3}$$
$$\mu_f = \mu_f(n_f) + g_{bf} n_f \tag{3.4}$$
$$\tag{3.5}$$

with $\mu_f(n_f)$ given by the equation of states of the fermions in the absence of bosons.

The first condition (eq. 3.1), concerning the bosons only, is verified if $g_{bb} > 0$. This is already a condition on the stability of the Bose gas by itself, since for negative values it collapses. For the fermions, eq. (3.1) is actually verified throughout the BEC-BCS crossover. The last condition, corresponding to eq. (3.2) is the one that will be critical to predict whether the mixture will phase separate or remain mixed.

Unitarity

At Unitarity, the EoS yields

$$\mu_f = \xi E_F = \xi \frac{\hbar^2}{2m_f}(3\pi^2 n_f)^{2/3}$$

This expression, injected in the stability condition, determines an upper bound for the fermion density of around $n_{f,\,\max} > 10^{16}$ cm^{-3}, exceeding greatly the typical densities of $n_f \simeq 0.5 \times 10^{13}$ cm^{-3} that we deal with, thus the two clouds will form a mixture.

BCS side

In the BCS regime, when $a_{ff} \to 0^-$, we have $\mu_f = E_F$ so the stability condition will be even less restrictive than at unitarity, except in the domain located around 850 G where we have a zero-crossing of a_{bb}. The range for a_{bb} leading to a phase separation can be evaluated using the typical density of $n_f \simeq 0.5 \times 10^{13}$ cm^{-3} and the former relations: there will be a phase separation for $a_{bb} \lesssim 0.5 a_0$, corresponding to a magnetic field range of less than 50 mG above the true zero-crossing.

BEC side

In the BEC regime, when $a_{ff} \to 0^+$, $\uparrow$ and $\downarrow$ fermions pair together forming dimers and the chemical potentials can be rewritten in the mean-field approximation as:

$$\mu_b = g_{bb} n_b + g_{bd} n_d \tag{3.6}$$
$$\mu_d = g_{dd} n_d + g_{bd} n_b \tag{3.7}$$

with the index $_d$ designating dimers, $g_{dd} = 2\pi\hbar^2 a_{dd}/m_f$ with $a_{dd} = 0.6 a_{ff}$ [130, 213] the dimer-dimer scattering length, the dimer density $n_d = n_f/2$ at $T = 0$ and $g_{bd} n_d = g_{bf} n_f$ in the mean-field approximation.

With these equations, the stability condition becomes:

$$\frac{a_{bf}^2}{a_{bb} a_{ff}} \leq 0.3 \frac{\eta}{(1+\eta)^2} \simeq 0.075 \tag{3.8}$$

with $\eta = m_b/m_f \simeq 7/6$ the ratio of the masses of the two isotopes.

This stability condition at zero temperature will be fulfilled on the BEC side for magnetic fields above $B_{c0} \simeq 730$ G[1] (this theoretical value is only an indication and would need to be measured experimentally since beyond mean-field effects could be involved in this process with $1/k_F a_{ff} \simeq 1.4$).

In conclusion, we have a large domain over which we can have a stable Bose-Fermi mixture: for magnetic fields $B \in$[730 G, 845 G]$\cup$[850 G, 890 G] *ie* for $1/k_F a_{ff} \in [-0.4, -0.14] \cup [-0.1, 1.4]$ calculated with a typical central density of $n_f \simeq 0.5 \times 10^{13}$ cm^{-3}.

[1] This value of the critical magnetic field is valid at zero-temperature. At high temperatures, the mixture is stable even way beyond B_{c0} because the interactions become negligible compared to the thermal part of the energy.

3.3 Laser system

The laser system uses a master-oscillator - power-amplifier scheme where three masters lasers, locked using saturated absorption spectroscopy to act as a frequency reference, inject a few slave lasers and tapered amplifiers to obtain more total optical power.

The master lasers have been changed during the course of my PhD to replace the old homemade mounts which were external cavities in Littrow configuration for new Toptica lasers, of the model DL pro 670 using an "improved", patented, Littrow configuration for a better stability. They also have a better output power after a first fiber coupling thanks to the use of a specialized FiberDock (see Fig. 3.5) and the integration of an optical isolator inside the laser box. For comparison, the output power of the old master laser was around 20 mW compared to the 25 mW of the new lasers which seems similar but after a first fiber coupling, the output for the old masters was typically around 6 mW whereas we can get around 20 mW with the new ones, signature of much better gaussian modes. This enabled us to get rid of one slave laser and to be very confortable with the total power available to inject the slaves. Furthermore, their stability is indeed better since the old masters sometimes had to be re-locked several times a day (sometimes up to ten times a day) whereas the new ones only need to be locked once a day. They are locked on the D_1 and D_2 lines of ^{6}Li and the D_2 line of ^{7}Li, and the different frequencies needed for our set-up are produced using acousto-optic modulators.

Figure 3.5: Photography of the new Master laser box. The box contains a 670 nm diode laser, an anamorphic prism pair for circular beam shaping and an optical isolator. The FiberDock that is directly connected to the laser box includes an adjustable lens and a fiber coupler. Once the FiberDock is optimized, the power after the fiber is very stable, only requires small adjustments every other week.

The optical power is amplified by injecting the light in slave lasers. The slave diodes are high-power laser diodes (Hitachi HL6545MG) with a maximal output power of 620 mW. Their spectrum at room temperature is centered around 660 nm, so we heat them up to around 70°C to reach the Lithium transitions which are around 671 nm. The diodes are mounted inside thermally isolated boxes, which are currently being gradually replaced for Thorlabs mounts (model TCLDM9). The diodes need to be replaced quite regularly (every other month) due to their reduced lifetime at those temperatures. Two tapered

amplifiers are used for the ^{7}Li principal frequencies (corresponding to D_2) to have even more power for the MOT and Zeeman slower since the total number of ^{7}Li atom is critical for the experimental sequence.

Three Fabry-Perot cavities are used to monitor the locking of the different diodes. One is used for the master lasers, another one for the MOT beams and a last one for the Zeeman slower lasers.

3.4 Loading the magnetic-optical trap

3.4.1 The Lithium source

The atomic beam is created by heating Lithium samples (with natural abundances) in the oven. The bottom of the oven is at a temperature around 400°C and the entrance of the collimation tube is around 520°C, ensuring that enough saturated vapor is produced to generate an atomic beam after collimation. To enable the recycling of liquid Lithium that could otherwise form and accumulate in the collimation tube, we make sure there is a negative gradient between the entrance and the end of the tube because the surface tension of liquid Lithium decreases with temperature. Typically, the temperature at the end of the collimation tube is around 190°C. However, this strategy is not 100% reliable and the collimation tube can get clogged from time to time in which case we have to heat it up to 600°C in order to get rid of the accumulated Lithium.

3.4.2 Zeeman slower

At the end of the collimation tube, the atoms have a mean thermal velocity of 1700 m.s^{-1} whereas the capture velocity of the MOT is only about ~ 50 m.s^{-1}. To slow down the atoms we use a Zeeman slower. We send counter propagating beams at resonance on the atoms: they absorb a high number of photons along their trajectory and slow down due to the recoil. Because of the Doppler effect, the Zeeman laser beams cannot be at resonance with the atomic transitions during their whole path. To compensate the Doppler effect, a well designed magnetic field is applied on their way: due to the Zeeman effect, the atomic levels are shifted and the magnetic field profile along the slower is conceived so that the atoms are always at resonance with the laser beam.

Our Zeeman slower is in a spin-flip configuration with currents of opposite signs running through two successive coils so that the magnetic field becomes zero between the two coils and is then reversed. In this configuration, the Zeeman light is made resonant with atoms at the zero of the magnetic field, where their average velocity is around 250 m.s^{-1}, but does not affect the trapped atoms in the MOT. The magnetic field in the Zeeman slower goes from $+800$ G to -200G, and its capture velocity is around 1100 m.s^{-1}.

For each isotope, a principal beam is used to cool down the atoms and a repumping beam is used to recycle atoms falling in the wrong level of the ground state. Moreover, the repumping is needed because there is no adiabatic following near the zero-crossing of the magnetic field and atoms can flip to the wrong m'_F states. The principal beams for ^{6}Li and ^{7}Li are represented in blue and yellow respectively in Fig. 3.2, they are tuned to the D_2 lines of each isotope, more specifically to the transition $D_2 : \ F = 3/2 \rightarrow F' = 5/2$ for ^{6}Li and $D_2 : \ F = 2 \rightarrow F' = 3$ for ^{7}Li. The ^{6}Li principal beam also affects the slowing of the ^{7}Li due to the proximity of the D_2 line of the former and the D_1 line of the latter, forcing a trade-off between the loading of the two species in the MOT. The

repumping beams ^{6}Li and ^{7}Li are represented in green and orange respectively in Fig. 3.2, they correspond to the transitions $D_1: \ F = 1/2 \rightarrow F' = 3/2$ and $D_2: \ F = 1 \rightarrow F' = 2$ respectively. The four Zeeman beams are actually detuned from their respective transitions of around 400 MHz to compensate for the Doppler effect taking place at the zero-crossing of the magnetic field.

3.4.3 Magneto-optical trap

The slowed down atoms can now be trapped in the magneto-optical trap where further cooling will also occur. The optical part of the trapping is made with three counterpropagating beams, with a circular polarization, and the magnetic part is a magnetic field gradient of 25 G.cm^{-1} provided by a pair of coils (the MOT coils, in purple with an M on Fig. 3.1). The combination of restoring and friction forces traps the atoms in real and momentum space, in the vicinity of the zero magnetic field region.

Concerning the MOT light, we have again two frequencies for each isotope, a principal and a repumper. The transitions for the principal beams are $D_2: \ F = 3/2 \rightarrow F = 5/2$ and $D_2: \ F = 2 \rightarrow F' = 3$ for ^{6}Li and ^{7}Li respectively and the transitions used for the repumper beams are $D_1: \ F = 1/2 \rightarrow F = 3/2$ and $D_2: \ F = 1 \rightarrow F' = 2$, so very similar to the Zeeman slower beams except for the detunings. Indeed, the detunings are much smaller in the MOT, all beams are red-detuned with detuning of about $\delta_{6P} = -6\Gamma$ and $\delta_{7P} = -7\Gamma$ for the principal beams while we have $\delta_{6R} = -3\Gamma$ and $\delta_{7P} = -5.5\Gamma$ for the repumper beams.

The MOT loading requires about one minute, at which stage we have around 10^9 atoms of ^{7}Li and 10^8 atoms of ^{6}Li at around 3 mK. We then switch off the Feshbach coils (blue coils with an F on Fig. 3.1) that were just applying a bias field to align the center of the magnetic trap with the end of the Zeeman slower and shift the MOT. This is then followed by a CMOT phase where the MOT is compressed and the detunings are set closer to the resonance ($\delta_{6P} = -1.5\Gamma$ and $\delta_{7P} = -5\Gamma$ for the principal beams) while the repumping intensities are ramped down to zero in 8 ms. This increases the atomic density, all pumped in the lowest hyperfine manifold, and decreases the temperature to about $T \simeq 600 \ \mu$K. The temperature is higher than the theoretical Doppler temperature $T_D = \hbar\Gamma/2k_B \simeq 140 \ \mu$K, because the upper hyperfine states are unresolved and, at high density, multiple photon scattering takes place.

The temperature at this stage is too high to have an efficient loading into the final hybrid dipolar-magnetic trap. To reduce the temperature, we will perform an RF evaporative cooling in a magnetic trap, and not in the MOT because it is not a conservative trap due to the constant absorption and reemission of the resonant photons. If we switch off the Zeeman slower, atoms in the MOT are all lost in less than a minute, whereas the RF evaporation lasts around 30 seconds.

3.5 Magnetic trapping

3.5.1 Optical pumping

To load the atoms in the lower magnetic trap, we have to transfer the atoms in a low-field seeking state (the energy increases with the magnetic field) since Maxwell's equation forbid local maxima of magnetic fields. Therefore we perform an optical pumping step where the atoms are transferred into the states $|6_f\rangle = |F = 3/2, \ m_F = 3/2\rangle$ and $|8_b\rangle =$

$|F = 2, m_F = 2\rangle$ of the second lowest manifold. These states are also stable against spin-exchange collisions, a necessary condition for the sequence.

During this step, we use a beam with two frequencies and a σ^+ polarization, as well as a weak magnetic field $B \simeq 10$ G parallel to the axis of the beams. The first beam is tuned to the D_2 : $F = 1 \rightarrow F' = 2$ transition to pump the ^{7}Li atoms to the $F = 2$ manifold. The second beam has two roles: first it transfers the ^{7}Li atoms into the $|F = 2,\ m_F = 2\rangle$ state through the $F' = 2$ state of the D_1 transition to realize the"Zeeman" optical pumping of ^{7}Li; then it also pumps the ^{6}Li atoms from the $F = 1/2$ manifold to the $F' = 3/2$ manifold to realize the ^{6}Li hyperfine pumping. The ^{6}Li gas is not fully polarized in the $|F = 3/2,\ m_F = 3/2\rangle$ state, leading to some losses, but the number of ^{6}Li atoms is not as critical as for ^{7}Li.

3.5.2 Lower magnetic trap and transport

After the optical pumping, a quadrupole trap is turned on by supplying the MOT coils with currents running in opposite directions after a short ramp of 2 ms. The magnetic field gradient in the quadrupole is around 200 G.cm^{-1} for a current of 300 A. The efficiency of the optical pumping and quadrupole loading is around 50% for ^{7}Li and 30% for ^{6}Li, corresponding to $N_f = 7 \times 10^7$ and $N_b = 7 \times 10^8$ trapped atoms at a temperature around $2 - 3$ mK.

The atoms are then transferred in the appendage of the glass cell: we ramp up the current in the Feshbach coils and ramp down the current in the MOT coils at the same time, for a total duration of 500 ms, so that the center of the magnetic trap is progressively moved upwards towards the center of the appendage. At the end of the transfer, the current in the MOT coils is even reversed to give a final push to the atoms. The efficiency of this magnetic transport is around 50%, most of the losses being from the collisions between the peripheral atoms and the walls of the appendage, since the atomic cloud is larger than the appendage and clips on the walls.

3.5.3 Ioffe-Pritchard trap

Atoms are then transferred from the quadrupole trap to a Ioffe-Pritchard trap [214]. This trap consists of four bars parallel to the z direction, represented in Fig. 3.1, that realize a tight radial confinement and a pair of pinch coils (green coils with a P on Fig. 3.1) for the axial confinement by inducing a strong curvature. Another pair of coils, which happen to be the Feshbach coils, are used to implement a bias field strong enough to prevent any Majorana losses [215] but not too strong to maintain a good radial confinement. The bias field can also be finely tuned using the pinch-offset coils, represented in yellow with an O in Fig. 3.1.

On a sidenote, during the course of my PhD, the Ioffe bars started leaking. Unfortunately, they are located very closely to the appendage and inaccessible without taking them out. Temporary solutions were tempted to fix this leak but eventually it appeared to be irreparable. A project has thus been launched to replace them which is being carried out currently. We have taken out the whole structure containing all the coils out of the optical table to replace the bars. At the same time, to avoid the possible future leaks on other coils, all the coils will be replaced following a similar design.

On the contrary, to try to increase the lifetime of the Ioffe bars, which is limited to the appearance of leaks (they were replaced around ten years ago), we changed the general

strategy for their conception. As represented in Fig. 3.1, we can see they have a triangular section. In the former design, they were formed by folding standard cylindrical tubes and crushing them in a press, resulting in the structure fragility. On the contrary, the future bars will be 3D printed directly in the right shape and will be pierced to let water circulate through them, hopefully for a better longevity. On top of that, the future use of a closed loop water circuit should also ensure a much better longevity. A picture of the new bars is given in Fig. 3.6.

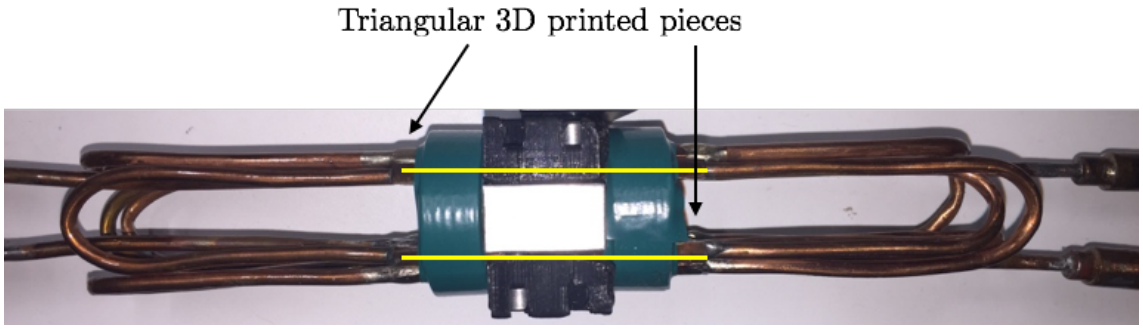

Figure 3.6: Picture of a prototype of the new Ioffe bars. The yellow lines mark the area where the triangular 3D printed bars are located, their extremities can be seen and are pointed out by the arrows. There is a set of three triangular bars on each side of the picture, corresponding to each yellow lines, interconnected at their extremities with cylindrical copper tubes. The soldering used to connect the different Ioffe bars is Silver, which has a lower resistivity than copper. The difficulty resides in the piercing of the bars without breaking the system or creating leaks, which is a work in progress.

3.5.4 Doppler cooling

Back on the experimental sequence, when the atoms are loaded in the Ioffe trap, they have a temperature around 3 mK. The collisional scattering cross-section of ^{7}Li vanishes for a relative collision energy of 6 mK and is still pretty low at 3 mK, therefore the temperature of the gas is still too high to start the evaporative cooling of the cloud. Consequently, we perform a Doppler cooling on ^{7}Li atoms.

A single beam is sent on the atoms, circularly polarized, red-detuned to the transition $D_2 : \ F = 2, m_F = 2 \rightarrow F' = 3, m_{F'} = 3$ to match the corresponding bias field felt by the atom ($\simeq 500$ G). This beam cools down the atoms in one direction and elastic collisions as well as the anharmonicity of the trap enable the thermalization of the cloud after recompression. This step is repeated a second time, with a stronger confinement and smaller detuning. At the end of this step, the temperature is down to 300 μK, with atom losses of only 25%, and the collision rate is multiplied by a factor ~ 16, now enough to perform an evaporative cooling.

3.5.5 RF evaporation

At this stage, the Ioffe-Pritchard trap is highly compressed and a low bias field is maintained ($B \simeq 5$ G) to avoid Majorana losses. Since the bias magnetic field produced by the pinch coils in this phase reaches around 1000 G, compensating this field to reduce it to 5 G while maintaining a good magnetic field stability may seem complicated. However, the

pinch coils and Feshbach coils were designed to have the same characteristic for the bias field ($\simeq 2.3$ G/A) while the curvature produced by the Feshbach coils is small compared to the one from the pinch coils. Hence, they are connected in series during this phase to create a bias field very close to zero, that can be finely tuned with the pinch-offset coils.

The general idea of evaporative cooling is to remove the most energetic atoms from the cloud and letting the rest of the atoms thermalize, so that the mean energy per particle decreases and the phase-space density increases [216]. The strategy used at this step is a radio-frequency (RF) evaporation: it consists in sendind a finely tuned RF signal to transfer the hot atoms from a trapped Zeeman state to an anti-trapped state.

We perform this evaporative cooling only on ^{7}Li atoms and ^{6}Li atoms are cooled sympathetically, by thermalization of the mixture: even if ^{6}Li atoms are fully polarized and cannot scatter through s-waves while higher partial wave channels are already frozen, they can still scatter with ^{7}Li atoms.

An RF signal, blue-detuned with respect to the frequency of the transition $|8_b\rangle \rightarrow |1_b\rangle$ (803 MHz at $B = 0$ G) is sent on the atoms. The blue detuning is then reduced progressively, so that only the hottest atoms are transferred in the $|1_b\rangle$ state which is a high-field seeker state thus anti-trapped.

The RF is decreased exponentially from 1040 MHz to around 840 MHz in about 22 s. The final RF frequency is frequently finely tuned to optimize the atom numbers and temperature of the cloud. At the end of this evaporation, the typical numbers of atoms are down to $N_f = 2 \times 10^6$ for ^{6}Li and $N_b = 6 \times 10^5$ for ^{7}Li, with a typical temperature of $T \simeq 10$ μK, corresponding to a phase-space density of around 10^{-1} for ^{6}Li atoms. After this final step, it is finally possible to load efficiently the atoms in the dipole trap thanks to a good mode matching.

3.6 The final hybrid magnetic-dipolar trap

The final trap is a hybrid magnetic-dipolar trap, produced by a far red-detuned ($\lambda = 1073$ nm), high power, IPG Ytterbium fiber laser for the dipolar part and an axial magnetic field produced by the pinch coils (green coils on Fig. 3.1). A bias field of $800 - 1000$ G can be applied independently using the Feshbach coils, to be close to the Feshbach resonances mentioned in section 3.2.2.

3.6.1 The magnetic-dipolar trap

First, let us recall some basic properties of dipole traps produced by the interaction of an atom with a far detuned light beam. It relies on the dipole force [217], that arises when a far-detuned light beam is sent on the atom clouds. The dominant effect of the laser is an AC Stark shift proportional to the laser's intensity, negative for a red-detuned laser, that makes the atom attracted to the maxima of intensity. Since the fine and hyperfine splitting of the atomic states is negligible compared with the laser detuning to the $2^2S \rightarrow 2^2P$ transition, the potential can be simply described using the expression:

$$V_{\text{dip}}(\boldsymbol{r}) = \frac{3\pi c^2}{2\omega_0^3}\frac{\Gamma}{\Delta} I(\boldsymbol{r}) \tag{3.9}$$

where c is the speed of light in the vacuum, ω_0 the frequency of the atoms' transition with natural linewidth Γ, $\Delta = \omega_L - \omega_0$ is the detuning between the laser pulsation and the

pulsation of the transition, and $I(\boldsymbol{r})$ is the intensity profile of the laser. For our trap, we use a laser in a Gaussian TEM_{00} mode so we have:

$$I(\boldsymbol{r}) = \frac{2P}{\pi w(z)^2} e^{-2r^2/w(z)^2}, \tag{3.10}$$

where P is the total laser power and $w(z)$ is the $1/e^2$ radius of the beam at the position z given by $w(z) = w_0\sqrt{1+(z/z_R)^2}$, with w_0 the beam waist and $z_R = \pi w_0^2/\lambda_L$. For our experiments, $w_0 = 36(3)$ μm and $w_0 = 27(2)$ μm for experiments presented in chapters 4 and 5. Close to the beam focus, for $r \ll w_0$ and $z \ll z_R$, the dipole potential is harmonic. It reads for an atom of mass m:

$$V_{\mathrm{dip}}(\boldsymbol{r}) = -V_0 + \frac{1}{2}m\left(\omega_r^2 r^2 + \omega_z^2 z^2\right) \tag{3.11}$$

where $V_0 = 3c^2\Gamma P/\omega_0^3|\Delta|w_0^2$ is the trap depth, $\omega_r = \sqrt{4V_0/mw_0^2}$ the radial frequency and $\omega_z = \omega_r\lambda_L/\sqrt{2}\pi w_0$ the axial trap frequency. Typical frequencies at the highest power we send on the atoms (7 W) are $\omega_r \simeq 2\pi \times 7$ kHz and $\omega_z \simeq 2\pi \times 40$ Hz. The trap is cigar-shaped, very elongated in the axial direction. In first approximation, both isotopes feel the same trapping so $m_f\omega_f^2 = m_b\omega_b^2$, and $\omega_f/\omega_b \simeq \sqrt{7/6}$.

At low powers, to increase the axial trapping, we add a magnetic curvature using the pinch coils. For low-field seeker states, we implement a magnetic field minimum in the vicinity of the beam waist. For high-field seeker states, a saddle-point is created with a maximum in the axial direction, by combining the action of the pinch coils to impose the curvature and of the Feshbach coils to generate a high, negative, bias magnetic field so that the minimum of the magnetic field becomes negative and a maximum in amplitude. Typical axial trapping frequency provided by the pinch coils is $\omega_z = 2\pi \times 20$ Hz. The radially repulsive potential created in this configuration by the coils can be neglected compared to the radial confinement due to the dipolar trap. This strategy can be used to trap high-field seeking states near the Feshbach resonance of ^{6}Li at 832G.

3.6.2 Loading of the trap

We load the atoms from the Ioffe-Pritchard trap to the hybrid magnetic-dipolar trap at relatively high laser power ($\simeq 7$ W), by simultaneously ramping up the optical trap power and ramping down the current in the Ioffe-Pritchard bars. Since the geometry of both trap are quite similar, the loading efficiency is about 80%.

3.6.3 Mixture preparation

To take advantage of the Feshbach resonance for ^{6}Li, we want to prepare our atoms in the states $|1_f\rangle$ and $|2_f\rangle$ for the fermions and $|2_b\rangle$ for the bosons, as featured in Fig. 3.3. This is done using several RF adiabatic transfers. In a two-level system, this technique consists in dressing the levels by a strong field with Rabi frequency Ω and sweeping the field detuning δ across the resonance, slowly enough so that the atoms follow the dressed state to end up in the other level, having absorbed or emitted a photon of the coherent RF field.

First, we transfer at low field the ^{7}Li atoms from the state $|8_b\rangle$ to $|1_b\rangle$ and the ^{6}Li atoms from the $|6_f\rangle$ state to the $|1_f\rangle$ state, both high-field seeker states. To do so, we send a fixed RF frequency of 827 MHz for the bosons and 240 MHz for the fermions

and we ramp the magnetic bias field from 13 G to 4 G in 50 ms to cross the resonance. Then, we increase the bias magnetic field up to 656 G, before reaching the Feshbach resonance for the bosons at 738 G depicted in purple in Fig. 3.4, and we perform another adiabatic passage by using an RF signal whose frequency is swept in 10 ms from 170.9 MHz to 170.7 MHz to transfer the ^{7}Li atoms from the $|1_b\rangle$ state to the $|2_b\rangle$ state. The typical efficiency of these transfers is about 90%, it is limited by decoherence effects due to atom collisions, trap inhomogeneities or field fluctuations. Remaining atoms in the $|8_b\rangle$ and $|6_f\rangle$ are expelled from the trap which is now set to trap high-field seeking states and remaining bosons in the $|1_b\rangle$ state are lost to three-body collisions when their Feshbach resonance is crossed at 738 G.

Finally, to prepare the ^{6}Li atoms in the desired states, we increase the magnetic field up to 835 G close to the Feshbach resonance at 832 G, by sweeping the frequency of an RF signal from 76.25 MHz to 76.3 MHz. By varying the RF power or the total duration of the sweep, we can adjust the transfer to obtain a mixture in the desired states according to the Landau-Zener formula:

$$P_{\mathrm{tr}} = 1 - e^{-2\pi\Omega^2/\dot{\omega}} \tag{3.12}$$

where P_{tr} is the transition probability, Ω is the Rabi frequency of the RF radiation and $\dot{\omega} = \mathrm{d}\omega/\mathrm{d}t$ is the frequency sweep velocity.

Therefore, we can adjust the parameters of this last sweep to modify the polarization of the Fermi cloud. The transfer efficiency can fluctuate or even drift and needs to be readjusted from time to time to remain in the same polarization conditions.

3.6.4 Final evaporation

The evaporation starts as soon as ^{6}Li atoms are being transferred in the $|2_f\rangle$ state and collisions are activated. The collision rate between $|\uparrow\rangle$ and $|\downarrow\rangle$ fermions is extremely large ($\gamma_{ff} \sim 10$ kHz) thanks to the Feshbach resonance, allowing for an efficient evaporation, whereas the ^{7}Li atoms are sympathetically cooled by the fermions.

We start with typically $N_f = 2 \times 10^6$ fermions and $N_b = 3 \times 10^5$ bosons at a temperature $T = 40$ μK for a trap depth $V_0 = 180$ μK. We then decrease exponentially the laser power to reach trap depths as low as $V_0 = 1.5$ μK. After a waiting around 1 seconds for the atoms to thermalize, we can obtain around $N_f = 3 \times 10^5$ fermions and $N_b = 4 \times 10^4$ bosons for temperatures down to $80 - 100$ nK, ensuring, as we will see later, that both clouds are indeed quantum degenerate.

3.7 Imaging

In the last sections, we saw how we could obtain an ultracold Bose-Fermi mixture by using a succession of traps and evaporative coolings. To analyze these atomic clouds and study their properties, we image them, either while trapped (in-situ) or after a time-of-flight expansion.

3.7.1 Absorption imaging

Absorption imaging consists in sending a resonant probe on the atoms, that will partly absorb it, along a given direction for instance the direction x. Using a CCD camera, we obtain the intensity profile $I(y, z)$ of the probe after passing through the cloud, as can

be seen in Fig. 3.7. To account for inhomogeneities of the probe beam, another picture is taken without the atomic cloud to obtain the intensity profile $I_0(y,z)$ that is needed to deduce properties only related to the atomic cloud. For a probe with a small enough intensity $I \ll I_{\text{sat}}$ where I_{sat} is the saturation intensity for the frequency of the beam[2], the intensity of the probe beam after absorption by the atoms is given by the Beer-Lambert law which reads

$$I(y,z) = I_0(y,z)e^{-\sigma \int \mathrm{d}x n(x,y,z)} \tag{3.13}$$

where n is the density of the cloud and σ is the absorption cross-section. Therefore, the logarithm of the ratio I/I_0 yields the density of the cloud, integrated along the imaging direction.

The absorption cross-section can be expressed simply in the case of a resonant light beam with a narrow linewidth and reads $\sigma = 6\pi(\lambda/2\pi)^2 C$ with C the Clebsh-Gordan coefficient associated with the absorption transition and the light polarization. However, this theoretical value cannot be used exactly in our measurements since many experimental imperfections can reduce drastically this cross-section. Thankfully this problem can be solved after a calibration of the atom numbers, as described in section 3.9, and absorption imaging can very well be used to determine the clouds' properties.

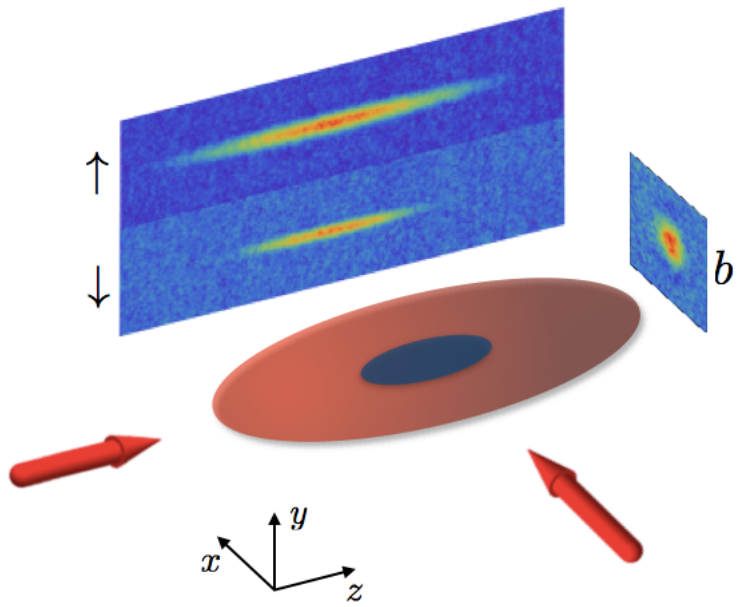

Figure 3.7: Schematics of the bidirectional imaging set-up, featuring real absorption images of the two spin states of a Fermi gas (labeled ↑ and ↓) and the Bose gas (labeled b). The cigar-shaped clouds (blue for the bosons, red for the fermions) can be imaged along the x or the z directions (two red arrows). The absorption images are represented in false colors, with red corresponding to the highest densities and blue to the vacuum background. the bosonic image is taken after a time-of-flight of 4.5 ms while the fermionic ones are taken after a time-of-flight of 0.5 ms, both were taken at 817 G after a full evaporation at 835 G.

[2]The saturation intensity at resonance for the D_1 and D_2 lines of ^{7}Li are respectively $I_{\text{sat}} = 7.6$ mW/cm^2 and $I_{\text{sat}} = 2.5$ mW/cm^2.

3.7.2 Double and Triple imaging

In the appendage, imaging can be done along two directions as depicted in Fig. 3.7: the z direction, corresponding to the axial direction of the trap, and the x direction corresponding to a radial direction of the trap.

Taking images along the z axis requires some time-of-flight to reduce the optical density and because the resolution along this axis is about 10 μm per pixel. However, imaging along this axis enables to detect low number of atoms thanks to the integration along the axial direction of the cigar-shaped cloud.

Along the x axis, images can be taken in-situ or after time-of-flight, the resolution is about 5 μm per pixel thus still not sufficient to resolve along the x direction of the profile. As a consequence, no information is lost after a second integration of the obtained profile along a radial direction and we tend to work with doubly integrated profiles.

For this imaging, we use two PixelFly cameras that can be operated very fast. Each of these cameras can take two images with a time separation as short as 3 μs. This allows us to take quasi-simultaneous images in one direction of one fermionic species and the bosons (double imaging), or of the two fermionic species with the bosons in the other direction (triple imaging).

For the measurements of the oscillations of the fermionic and bosonic cloud performed in Chapter 5, the former strategy was used whereas for the lifetime measurements of Chapter 4 it was the latter. In this case, we imaged the two fermionic species in the x direction and the bosons in the z directions as represented in Fig. 3.7. To avoid heating of the cloud by the imaging beam, we used short 10 μs pulses, separated by 10 μs at low intensities $I/I_{\mathrm{sat}} = 0.06$. Reference images are taken 20 ms later. This short pulse duration combined with a readout noise of 7 electrons RMS yields a not so high signal-to-noise ratio. Typically, at the end stage of the sequence we are able to resolve atom numbers down to 10^3 bosons in the z direction and 2×10^3 fermions per spin state in the x direction. The replacement of the cameras for an Andor one with better quantum efficiency and the installation of a microscope objective for a better resolution are in preparation.

In short, our imaging set-up allows us to obtain the integrated profiles of the three species in our mixture quasi-simultaneously, which gives us many information such as the pressure, the temperature, the number of atoms, ...

3.8 Analysis of the profiles

3.8.1 Degenerate bosons and thermometry

In our experiment, we work with bosons that are interacting weakly and the profiles are rather simple to fit.

For high temperatures, the cloud can be fitted using a Gaussian profile, typical of any thermal cloud. The doubly-integrated profile can thus be written as

$$\overline{n}_b(y) = \overline{n}_b(0) \exp\left(-\frac{y^2}{y_{th}^2}\right) \tag{3.14}$$

where we supposed we integrated along the z and x directions and with y_{th} related to the temperature T by

$$\frac{1}{2} m_b \omega_{b,r}^2 y_{th}^2 = k_B T. \tag{3.15}$$

When the temperature decreases, the profile of the gas changes drastically due to Bose-Einstein condensation. The critical temperature for this phenomenon in a harmonic trap for an ideal gas is given by

$$k_B T_{c,b} = \hbar\overline{\omega}_b (N_b/\zeta(3))^{1/3}. \tag{3.16}$$

Hence, for temperatures $T < T_{c,b}$, the ^{7}Li atoms start forming a BEC. The number of condensed atoms $N_{b,c}$ is related to the temperature by

$$\frac{N_{b,c}}{N_b} = 1 - \left(\frac{T}{T_{c,b}}\right)^3 \tag{3.17}$$

While the non-condensed atoms can still be analyzed using a Gaussian profile, the condensed fraction corresponds to a Thomas-Fermi profile. This can be demonstrated in the Local Density Approximation (LDA). The LDA assumes that at each position $\boldsymbol{r}$ of the system, there exists a mesoscopic volume over which the system is homogeneous and at equilibrium. All those small volumes are in contact and can exchange heat so they are at thermal equilibrium at the temperature T. Likewise, they can exchange particles imposing the constant chemical potential μ_0 over the system. In the LDA, each small local volume is treated as a homogeneous system shifted by the external potential $\mu(\boldsymbol{r}) = \mu_0 - V(\boldsymbol{r})$ with μ_0 the chemical potential at the center of the trap. The LDA can be applied whether the atoms are of bosonic or fermionic nature, or for a mixture of both in which case the chemical potential of a species may depend on the density of the others through the mean-field interaction.

Hence, in the LDA, and using a mean-field approximation to characterize the interactions, we write for the bosons

$$\mu(r) = \mu_b - \frac{1}{2} m_b \sum_i \omega_i^2 r^2 = g_{bb} n(r) \tag{3.18}$$

where the index $i = x, y, z$ corresponds to the three directions of space, g_{bb} is the coupling constant between two bosons and μ_b is the chemical potential at the center of the cloud, which reads

$$\mu_b = \frac{\hbar\overline{\omega}_b}{2} \left(15 N_{b,c} a_{bb} \sqrt{\frac{m_b \overline{\omega}_b}{\hbar}}\right)^{2/5} \tag{3.19}$$

with a_{bb} the boson-boson scattering length and $\overline{\omega}_b = (\omega_{z,b}\omega_{r,b}^2)^{1/3}$ the averaged trapping frequency for the bosons.

The doubly-integrated density can then be written as

$$\overline{n}_b(y) = \overline{n}_b(0) \left(\mu_b - \frac{1}{2} m_b \omega_{r,b}^2 y^2\right)^2 \tag{3.20}$$

Hence, the spatial extent of the cloud along the radial direction is given by the Thomas-Fermi radius

$$R_{TF,z,b} = \sqrt{\frac{2\mu_b}{m_b \omega_{r,b}^2}}. \tag{3.21}$$

A similar formula can be obtained for the axial extent using the axial trapping frequency instead of the radial one.

The double-structure, a Thomas-Fermi profile with thermal gaussian wings can be used to extract a lot of information, in particular the temperature of the gas, which is also the temperature of the whole Bose-Fermi mixture. However, we often need to do the imaging after a certain time-of-flight to reduce the optical density of the cloud, after which the cloud expands and the temperature cannot be deduced directly from the profile. Fortunately, the profile of the cloud after expansion can be connected to the in-situ profile by a simple scaling. The behaviour of the thermal gas and the condensed fraction differ, but, for an elongated cloud, they follow the same scaling in the radial direction and their size grow by a factor $\lambda_r(t) = \sqrt{1 + (\omega_{r,b}t)^2}$ [218, 219]. In our experiment, the expansion is done after turning off the dipolar trap but with the saddle potential of the coils still on, which modifies the previous formula[3]. However, this effect is negligible for small enough time-of-flights, typically a few percents for a 5 ms time-of-flight.

We show in Fig. 3.8 the doubly-integrated profile for a degenerate bosonic cloud obtained at two different temperatures.

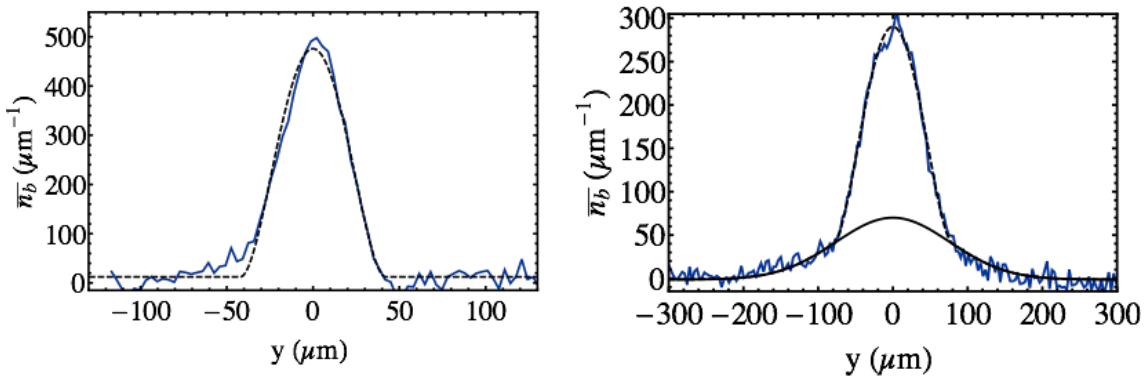

Figure 3.8: Profiles of the Bose gas at different temperatures. Left panel: for very low temperatures, there are no visible thermal wings in the profile (blue solid curve), which is fitted with a Thomas-Fermi profile (gray dashed curve) given in eq. (3.20), to extract a Thomas-Fermi radius of 42 μm after a time-of-flight of 4.5 ms so corresponding to approximately 3 μm in-situ. Right panel: bosonic profile (blue solid curve) at a higher temperature where the thermal wings are visible and fitted with a Gaussian profile (black solid curve). The whole profile is fitted with the sum of a Gaussian function and the Thomas-Fermi profile (gray dashed curve) from eq. (3.20). It corresponds to a temperature of 306 nK, consistent with the temperature $T = 295$ nK obtained using the condensed fraction deduced from the fit. This profile was obtained from an image taken after a time-of-flight of 4 ms.

The first one, on the left-hand panel of Fig. 3.8, has no visible thermal fraction. Typically, this is the case when the condensed fraction represents more than 80% of the cloud[4]. In this case, we can only get an upper bound for the temperature, which for the

[3] In the radial direction, in the limit where the axial trapping is the same before and after the dipolar trap is turned off, the scaling coefficient writes as [219]

$$\lambda_r(t) = \sqrt{\cosh^2\left(\frac{1}{\sqrt{2}}\omega_{z,b}t\right) + \frac{2\omega_{r,b}^2}{\omega_{z,b}^2}\sinh^2\left(\frac{1}{\sqrt{2}}\omega_{r,b}t\right)}. \tag{3.22}$$

[4] Far from the boson-boson resonance, for $a_{bb} \to 0^+$, the condensed fraction can become very small and the thermal wings can remain detectable at lower temperatures.

profile presented in Fig. 3.8 corresponds to $T \simeq 130$ nK.

The second one, on the right-hand panel, presents two distinct features: a Thomas-Fermi peak with thermal wings. From a Gaussian fit to the wings we extract a temperature $T = 306$ nK. From integration of the fits, we obtain a condensed fraction $N_{c,b}/N_b \simeq 0.5$, which can also be used to obtain the temperature with eq (3.17) and yields $T \simeq 295$ nK, in good agreement with the first estimate.

In conclusion, we can fit very precisely the bosonic cloud to extract its characteristics as well as the temperature of our mixture. We are able to reach temperatures low enough to obtain a BEC, that we can distinguish very well using the doubly-integrated profile.

3.8.2 Superfluidity of the fermions

The fermionic profile depends on the interaction strength that we vary by exploring the BEC-BCS crossover. For a Fermi gas in a harmonic trap, the Fermi energy $E_{f,h}$ can be calculated for a two-component ideal gas:

$$E_{f,h} = \hbar\overline{\omega}_f (3N_f)^{1/3} \tag{3.23}$$

with $\overline{\omega}_f$ the trapping frequency averaged over the three directions x, y, z. A Fermi wavevector can be associated with this Fermi energy using $E_{f,h} = \hbar^2 k_{F,h}^2/2m_f$, as well as a harmonic Fermi temperature defined with $k_B T_{F,h} = E_{F,h}$. This "harmonic" Fermi energy is different from the homogeneous, or local Fermi energy E_F which is proportional to $n_f^{2/3}$ and thus vary in the trap. Both definitions of the Fermi energy can be used for a harmonically trapped gas depending on whether the study focuses on local or global properties of the Fermi gas. In this thesis, if the homogeneous Fermi energy/wavevector/temperature is used without precising the position in the trap, it means it corresponds to the value at the center of the cloud.

At zero temperature, the profile depends on the interaction strength $1/k_{F,h}a_{ff}$: far on the BEC side, the profile coincides with the profile of an atomic BEC, whereas at unitarity, or far on the BCS side, the profile corresponds to the Thomas-Fermi profile of a non-interacting gas. For a unitary Fermi gas, the profile is given by the following Thomas-Fermi profile:

$$\overline{n}_f(z) = \overline{n}_f(0) \left(\mu_f - \frac{1}{2} m_f \omega_{z,f}^2 z^2 \right)^{5/2} \tag{3.24}$$

with $\mu_f = \sqrt{\xi} E_{f,h}$. In our experiments, since we mostly work in a domain where $1/k_{F,h}|a_{ff}| < 1$, we use the Thomas-Fermi profile of a unitary Fermi gas to obtain the size of the cloud and the atom numbers.

The spatial extent of the gas is then given by

$$R_{TF,f,z} = \xi^{1/4} \sqrt{\frac{2E_{f,h}}{m_f \omega_{f,z}^2}}. \tag{3.25}$$

Since we only work with very short time-of-flights t for the fermions $\omega_z t \ll 1$, the profile $\overline{n}_f(z,t)$ integrated in both radial directions is always very close to the in-situ one.

The superfluidity of the Fermi gas is not revealed as obviously as the Bose-Einstein condensation of the bosons in the doubly integrated profiles. However, the superfluidity can be inferred in our experiment via two different arguments.

Critical temperature

The superfluid/normal transition of the gas is a phase transition that happens at a certain critical temperature $T_{c,f}$. One simple idea is to measure the temperature of the Fermi gas and to compare it with $T_{c,f}$. However, in the strongly interacting regime, it becomes very complicated to extract the temperature of the Fermi gas. To overcome this hurdle, we use another species as an auxiliary thermometer, in our case the Bose gas, a technique first used in [220, 221]. At the end of the last evaporation stage, we wait about 1 second to ensure the thermalization of the two gases (the classically estimated collision rate is about $10\ \mathrm{s}^{-1}$), and then we extract the temperature of the Fermi gas by analyzing the density profile of the Bose gas.

The critical temperature for superfluidity was measured very precisely at unitarity in MIT [136] with $T_c/T_F = 0.167(13)$ (where T_F is the local Fermi temperature) by observing simultaneously a jump in the compressibility, a jump in the specific heat and the vanishing of the condensed fraction at this temperature. It was also evaluated as $T_c/T_{F,h} = 0.19$ by our group [181], this time using the Fermi temperature in the harmonic potential ($k_B T_{F,h} = E_{F,h}$). Determining the critical temperature for superfluidity in the crossover is a very complicated problem that is still under heavy investigation. Several theories exist that do not agree with each other as can be seen for instance in this recent review of T-matrix approaches [222], but the asymptotic regime is fairly well-known: on the BEC side it should tend to a roughly constant value given by the critical temperature for Bose-Einstein condensation of the dimers and on the BCS side it should decrease exponentially [140]. Some theories predict a maximum near unitarity and some do not, leaving the measurement of T_c in the crossover a burning issue, that has yet to be measured experimentally to confirm or infirm the many predictions. In our experiment, since again we work in the strongly interacting regime ($1/k_F|a_{ff}| < 1$) most of the time, close to unitarity, we use the critical value determined at unitarity as a reference.

For typical fermion numbers $N_f = 3 \times 10^5$, and trapping frequencies $\omega_{z,f} = 2\pi \times 18$ Hz and $\omega_{r,f} = 2\pi \times 500$ Hz, we get a critical temperature of $T_{c,f} = 150$ nK, above the general upper bound temperature determined using the bosonic cloud.

Imbalanced Fermi gas

Another possibility is to look at the profiles of the imbalanced Fermi gas, where the number of fermions in each spin state is not the same. This technique can be used as long as the imbalance is not too high, for polarizations P under the critical polarization P_c over which the superfluid state does not exist anymore, as discussed in the previous chapter.

In addition, as we saw in the previous chapter, for an imbalance below this limit and at low temperatures, the cloud is divided into three layers: a superfluid core where the fermions are fully paired $n_\uparrow(z) = n_\downarrow(z)$; a normal phase containing both spin states with a strong imbalance corresponding to the polaron state detailed in Chapter 2; and a fully polarized phase on the outside where atoms of the majority form an ideal Fermi gas.

This structure can be directly seen on the integrated profiles thanks to a remarkable property of the integrated density. Indeed, under the local density approximation, the pressure of a cylindrically symmetric atomic cloud along its symmetry axis z reads [223]

$$P(z, r = 0, T) = \frac{m\omega_r^2}{2\pi}\overline{n}(z). \tag{3.26}$$

This property was originately used to determine the EoS of the Fermi gas at zero

temperature, but using the Gibbs-Duhem relation $n = \partial P/\partial \mu$, it can be written as

$$n(z, r = 0) = -\frac{\omega_r^2}{\omega_z^2} \frac{1}{2\pi z} \frac{\mathrm{d}\overline{n}}{\mathrm{d}z} \tag{3.27}$$

This property is remarkable since it connects the doubly-integrated density $\overline{n}$ to the 3D density n. Applied to our system, in the superfluid core where $n_\uparrow(z) = n_\downarrow(z)$, we should have

$$\frac{\mathrm{d}}{\mathrm{d}z} \left(\overline{n}_\uparrow(z) - \overline{n}_\downarrow(z)\right) = 0 \tag{3.28}$$

which results in a plateau in the difference of the doubly-integrated profiles of the majority and the minority. This striking feature can be observed in Fig. 3.9, where we see a plateau of $\overline{n}_\uparrow(z) - \overline{n}_\downarrow(z)$ in the center, an outer domain where the difference coincides with the majority profile (fully polarized) and in-between a domain with a strong population imbalance.

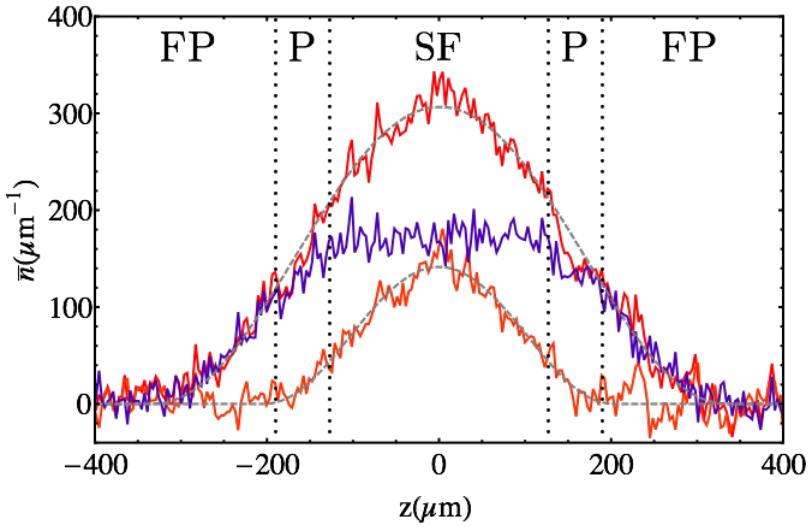

Figure 3.9: Doubly-integrated density profiles of the two spin-states of a Fermi gas. Red curve: majority spin-state (here ↑). Orange curve: minority spin-state (here ↓). Purple curve: difference of the red and orange profiles. The two gray dashed curve are fits to the majority and minority profiles using the Thomas-fermi profile given in eq. 3.24. We also represented the three distinct regions of the Fermi cloud: the superfluid core (SF) where the difference of the majority and minority profiles is constant, the polaron phase (P) where the cloud is strongly polarized and the fully polarized phase (FP) where there are no more minority atoms.

This plateau proves that the fermions are fully paired at the core. The superfluidity of paired atoms was proven by observing the formation of vortices only in the core region of a rotating fermi gas [167]. The presence of this well-defined plateau is a signature that the temperature of the cloud is well below $T_{c,f}$ as superfluids close to the critical temperature are partially polarized at the center, resulting in a more curved central part [224].

In conclusion, we described how we can extract valuable information from the profiles of the Fermi gas using the right fitting functions near unitarity at low temperatures. We also detailed the two criteria we use to assess the superfluidity of the cloud, that can be obtained reliably with our experimental set-up.

3.9 Calibrations

Magnetic field calibration

The magnetic field has to be known precisely for the fine tuning of the various scattering lengths, essential to characterize the interactions. It is determined thanks to the precise knowledge of the magnetic field dependence of the hyperfine transition $|1_b\rangle \rightarrow |2_b\rangle$, by measuring the radio-frequency resonance of the transition. Its typical magnetic field dependence is 40 kHz/G, and we measured transitions frequencies with a typical linewidth of 4 kHz, implying a magnetic field stability of around 0.1 G. This stability is sufficient in our set-up thanks to the broad Feshbach resonances of ^{6}Li and ^{7}Li.

Trapping frequency calibration

The trapping frequency is calibrated by measuring the oscillation frequency of the center of mass motion of the atoms (either bosons or fermions).

For the axial direction, we take advantage of the small shift between the centers of the dipole trap and the magnetic trap. By slowly increasing the laser power, we displace adiabatically the center of the atomic cloud. The laser power is then rapidly put back to its initial value so that the atomic cloud is suddenly not at the center of the trap and starts oscillating. By measuring the position of the center of mass of the cloud, we obtain the axial frequency of the trap.

For the radial direction, we suddenly turn off the dipole trap for a short time (500 μs). The anti-trapping of the magnetic curvature in the axial direction (the magnetic field is like a saddle-point, trapping axially and anti-trapping radially) and the gravity are enough to induce a displacement of the cloud that starts oscillating when the laser is turned back on. Again, the measurement of the position of the center of mass of the cloud over time yields the trapping frequency.

Atom numbers calibration

As stated before, the atom number obtained through the absorption imaging needs to be calibrated. We consider the imaged extent of the cloud to be reliable but not the total count, and we can use the size of the cloud to calibrate the detectivity. Indeed, at low temperatures, interactions provide a relationship between the size of the cloud and the atom numbers as seen with eq. (3.21) for bosons and eq. (3.25) for fermions at unitarity.

The principle of this calibration is to multiply our integrated density by a certain factor κ (κ_6 for fermions and κ_7 for bosons), as shown in Fig. 3.10, so that the size of the cloud remains the same but the number of atoms is adjusted and both quantities can finally coincide. The true number N_{true} is linked to the number obtained through integration of the profiles N_{int} by the simple relation $N_{\mathrm{true}} = \kappa N_{\mathrm{int}}$.

For the fermions, to obtain κ_6, we work at $T = 0$ and at unitarity where their EoS is well known, and the extent of the cloud is given by eq. (3.25). This method gives the calibration factor $\kappa_6 = 1.9(5)$.

For the bosons, this method can also be applied, and gives $\kappa_7 = 2.8(5)$. Another similar method consists in comparing the temperature at the onset of Bose-Einstein condensation with the critical temperature, which gives $\kappa_7 = 2.7(5)$, consistent with the first method.

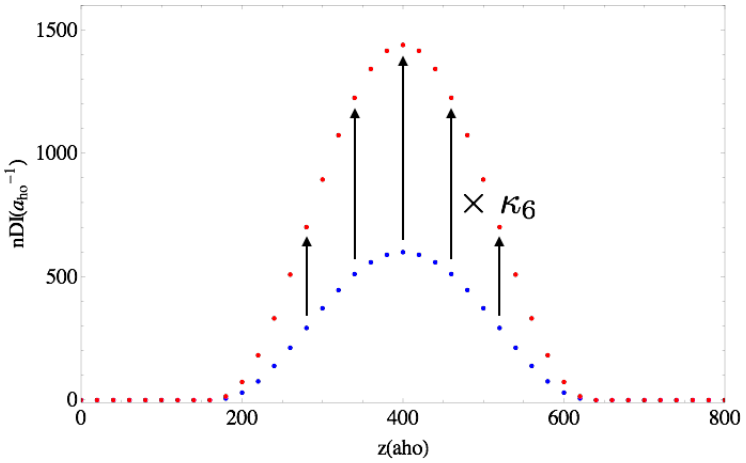

Figure 3.10: Blue: doubly integrated profile of an atomic gas obtained after absorption imaging analysis (simulated). Red: same profile readjusted after calibration: the size of the cloud is not modified, only the corresponding atom number.

The origin of these large calibration factors is not yet fully understood. Due to the finite spectral width of the probe light beams we expect a reduction of detectivity by a factor ≈ 1.7, which is far from the measured calibration factors.

Conclusion

In this chapter, we presented the set-up we use to produce and study Bose-Fermi mixtures from a hot vapor of Lithium, only with the right laser beams and magnetic fields. We presented the different steps needed to produce degenerate gases, using all the classical tools of quantum gases to achieve this goal.

At the end of the last evaporative cooling, the typical numbers we obtain usually verify $N_f \gg N_b$, justifying that we treat most of the time the bosonic gas of ^{7}Li as an impurity immersed in the Fermi superfluid of ^{6}Li. In the next two chapters, we will present the most recent experiments we performed in our lab. First we will study the lifetime of the mixture, and more specifically the three-body losses in the mixture. Then, we will investigate the counterflow of the impurity and the Fermi superfluid. These experiments will not only yield results on the interaction between the Bose and Fermi gases but mainly on the characteristics of the Fermi superfluid itself, as the bosonic impurities act as a probe of the Fermi cloud properties. The physics of the impurity interacting with a Fermi superfluid will be further investigated theoretically in the last chapter, needed to achieve percent-level precision between theory and the experiments we perform.

Chapter 4

Lifetime of an impurity in a two-component Fermi gas

With our setup we are able to produce an ultracold Bose-Fermi mixture. We already discussed in the previous chapter the conditions needed for this mixture to be thermodynamically stable. However, cold atom gases are metastable systems: at the temperature and pressure they reach, the only stable state would be the solid state. Consequently their lifetime must be limited, and since we would like to perform experiments with this mixtures, manipulating it for times up to a few seconds, we need to investigate it.

To go from the gaseous state to the solid state, the atoms need to start binding together, and to release this binding energy they need an impurity to collide with. Due to Pauli blocking, this process is highly suppressed in a two-component Fermi gas, but the ^{7}Li bosons can perfectly play the role of the impurity. When the density becomes large, or the interactions become strong, this three-body recombination can strongly reduce the lifetime of the system.

Although these three-body recombination processes are linked to short-range correlations which are highly non-trivial, especially in the strong interaction regime where many-body effects take place, we will establish in the first section a framework in which they become simple, with all the many-body physics contained in one parameter, the fermionic two-body contact C_2, that we introduced in Chapter 2. It is because of the nature of the system itself, consisting of an impurity immersed in a Fermi gas, that a three-body process is reduced to a two-body parameter.

Therefore, measuring the lifetime of the system is not a mere preliminary testing of its dynamic stability, but it informs us on the properties of the Fermi gas itself. In the last two sections, we will perform such lifetime measurements in various conditions, and we will see how the impurity act as a probe within the Fermi cloud.

4.1 Three-body recombination

4.1.1 General description

When three atoms collide, two of them can form a deeply bound molecule. The released binding energy is converted into kinetic energy: typically around $10^2 - 10^4$ K, orders of magnitude larger than any relevant energy scale in ultracold systems, it is consequently more than enough for the two bodies resulting from this collision to escape the trap. This inelastic process is usually called a three-body recombination event. We character-

ize these three-body recombinations by introducing a three-body loss rate coefficient Γ_3, defined with the following differential equation:

$$\frac{1}{N}\frac{\mathrm{d}N}{\mathrm{d}t} = -\Gamma_3(N). \tag{4.1}$$

The parameter Γ_3 increases with the density of both species, it depends on the interaction between species and other parameters such as the temperature. Moreover, it contains all the non-universal and complicated short-range physics that describe the formation of a molecule when three atoms are close to each other. In the zero-range limit, $a \gg l_{\mathrm{vdW}}$, and assuming perturbative losses, the recombination rate possess universal properties that will depend on the scattering length a and, if the Efimov effect is present, the three-body parameter κ^*. The knowledge of the associated scaling laws enable to predict the lifetime and stability of the gas.

These losses will affect the lifetime of the system, but they can also affect the rest of the gas in several manners, the main one being a source of heating. Indeed, in a non-uniform trap, maxima of densities are associated with minima of the trapping potential, and three-body losses will more likely affect atoms in denser areas. Consequently, they will remove the less energetic atoms and will increase the mean energy of the system.

4.1.2 Expected scalings in our system

We now focus on the losses that can occur for an impurity immersed in a two-component Fermi gas. Several loss processes can take place and limit the lifetime of the system:

- Three-body recombination involving three impurity atoms may happen when they are of bosonic nature. In this case, the losses scale as $\propto a_{bb}^4 n_b^3$ with n_b the boson density and a_{bb} the boson-boson scattering length.

- On the BEC side, the fermions form dimers and dimer-dimer losses can happen, with a scaling as $\propto n_m^2 a_{ff}^{-2.55}$ [130], with n_m the molecule density.

- Finally, three-body recombination between an impurity atom and two fermions of opposite spin can also take place. This is the main process in our system[1] and we will focus on it in the rest of this Chapter. We discuss its expected scalings in the BEC-BCS crossover in the remaining of this paragraph.

On the BEC side of the crossover, fermions form dimers. Hence, the recombination process actually involves one fermionic dimer and one impurity atom, thus the loss rate equation reads as

$$\frac{\mathrm{d}n_i}{\mathrm{d}t} = -L_2 n_i n_m \tag{4.2}$$

where n_i and n_m are the impurity and molecule density respectively.

This recombination process was studied previously in [225] using a mixture of ^{40}K atoms and ^{87}Rb Feshbach molecules, for which the two-body loss rate was shown to scale as $1/a_{ff}$, as predicted in [226].

[1] One could also imagine three-body losses between two impurity atoms and one fermion. As our measurements on a polarized Fermi gas will prove in section 4.2.1, these losses are negligible in our set-up and we will not consider them.

On the BCS side of the crossover, the fermions form loose Cooper pairs, behaving similarly as isolated particles so the recombination process involves three distinguishable particles, one spin-up fermion, two fermions of opposite spins and one impurity atom. The loss rate equation becomes:

$$\frac{\mathrm{d}n_i}{\mathrm{d}t} = -L_3 n_i n_f^2 \tag{4.3}$$

In the case of a weakly coupled impurity, the loss rate scales as a_{ff}^2 [226], leading to vanishing losses in the BCS limit.

The lifetime of an impurity immersed in a two-component Fermi superfluid is here described in the two limits of the BEC/BCS crossover. However, as depicted in Fig. 4.1, these two asymptotic behaviors seem contradictory when we consider them at unitarity: the lifetime vanishes on the BCS side and diverges on the BEC side.

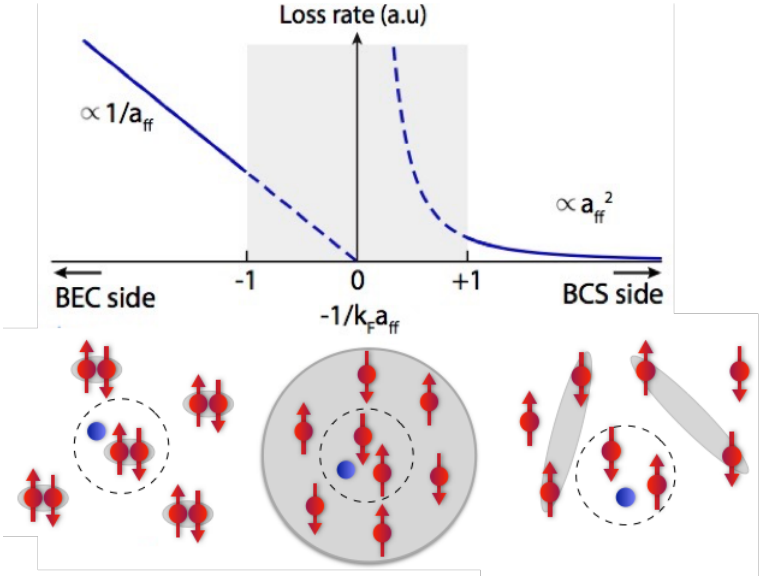

Figure 4.1: Inelastic loss rate asymptotic behavior on the BEC side and the BCS side. On the BEC side, up and down fermions form tightly bound dimers and the decay mechanism can be described by a two body process between the impurity (green disk) and a dimer. On the BCS side, the losses occur through a three-body process. The extrapolations of these two asymptotic behaviors (dashed parts) towards the strongly correlated regime (grey area) seems to yield contradictory results.

At unitarity, the only remaining length scale is given by $n_f^{-1/3}$, and if we replace a_{ff} in the expressions of the loss rate on both the BEC and BCS side we get $\dot{n}_i \propto n_i n_f^{4/3}$. This dimensional argument would yield a finite loss rate with an unusual fractional exponent on the fermion density.[2]

4.1.3 From the three-body loss rate to the two-body contact

The formation of deeply-bound molecules requires the three atoms to be close enough, within a typical distance R_*, the size of the bound states. In our case, we are interested

[2] In the case of three bosons, this dimensional argument would lead to losses at unitarity proportional to $n_b^{5/3}$, once again with a fractional exponent, and was confirmed experimentally [227].

in the three-body recombination process that involves two resonant fermions of opposite spins and an impurity atom as it is represented in Fig. 4.2. Indeed, since we have around ten times more fermions than bosons at the final stage of our experiment, the bosons can be seen as impurities.

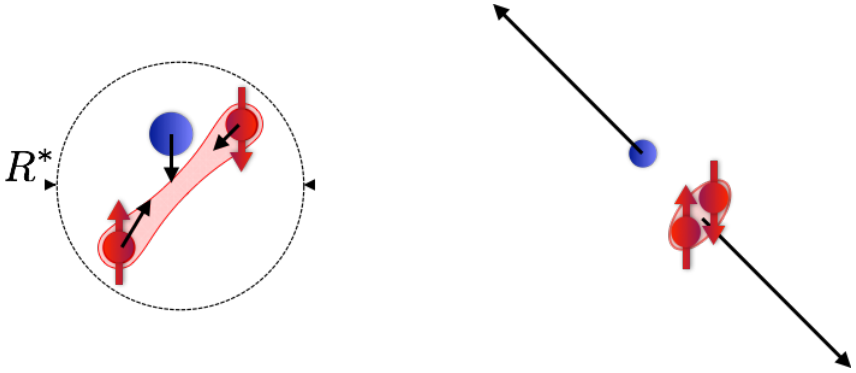

Figure 4.2: Sketch showing the process of three-body recombination. First, on the left-hand side, the three atoms (here two fermions of opposite spins in red and a boson in blue) have to get close enough, within R^*. Then, a deeply bound molecule may be formed between the two highly interacting fermions. Finally, on the right-hand side, the large binding energy is released as kinetic energy and the two resulting bodies can escape the trap. The deeply bound molecule and the boson have very large, opposite momenta (black arrows), independent from the initial momenta of the particles since the binding energy is very large compared to all the other energy scales. Here we did not represent the many-body system which is nevertheless present in the background and affects the probability to have the three particles within R^*.

Since the binding energy is orders of magnitude beyond any other energy scale in the system, the final state of the three-body system is completely decoupled from the momenta of the initial incoming particles. In addition, the final state does not depend on the external magnetic field anymore: the deeply-bound state that is formed is no longer resonant and its distance to the continuum varies very slowly with the magnetic field. Therefore, we can say in a good approximation that the recombination rate is simply proportional to the probability of having the three different particles within a distance R_* [83]:

$$\Gamma_3 N_M \propto \int_{R<R_*} \mathrm{d}^3 r_1 \mathrm{d}^3 r_2 \mathrm{d}^3 r_3 \langle \widehat{\psi}_1^\dagger(r_1)\widehat{\psi}_2^\dagger(r_2)\widehat{\psi}_3^\dagger(r_3)\widehat{\psi}_3(r_3)\widehat{\psi}_2(r_2)\widehat{\psi}_1(r_1)\rangle \tag{4.4}$$

with N_M the number of molecules formed in this process, R is the hyperradius associated with the three particules, $\widehat{\psi}_\alpha$ are the field operators for the atoms ($\alpha = 1, 2, 3$) and the proportionality constant only depends on short-range physics.

This shows that three-body losses are probing the few-body short-range correlations of the system. In our experiment, we study the three-body recombination with an impurity interacting weakly with a two-component Fermi superfluid. In the case of a weakly interacting impurity, here corresponding to $\alpha = 3$, the probability distribution of the fermions and the impurity become independent and can be factorized. By isolating the terms corresponding to the impurity we obtain:

$$\Gamma_3 n_M \propto n_i \int\limits_{R<R_*} \mathrm{d}^3 r_1 \mathrm{d}^3 r_2 \langle \widehat{\psi}_1^\dagger(r_1)\widehat{\psi}_2^\dagger(r_2)\widehat{\psi}_2(r_2)\widehat{\psi}_1(r_1)\rangle \tag{4.5}$$

$$\Gamma_3 n_M \propto n_i \int\limits_{R<R_*} \mathrm{d}^3 r \; G^{(2)}(\mathbf{r}) \tag{4.6}$$

where n_i is the impurity density and where we introduced $G^{(2)}(\mathbf{r})$ the probability density of finding two particles within $\mathbf{r}$.

As we saw in Chapter 2, in the limit $r \to 0$, this probability density is given by [144, 146]:

$$G^{(2)}(\mathbf{r}) \underset{r\to 0}{\sim} \frac{C_2}{(4\pi r)^2} \tag{4.7}$$

where C_2 is Tan's contact for two fermions.

This shows that the three-body loss rate Γ_3 is directly proportional to the fermionic two-body contact C_2. The contact C_2 encompasses all the effects of resonant interactions between the fermions, which are decoupled from the short-range physics included in the proportionality constant. All the dependence of the three-body loss rate on the system parameter T, n, a, and the three body parameter is encapsulated in the contact parameter. The differential equations describing the losses for a weakly interacting impurity writes as

$$\frac{\mathrm{d}n_i}{\mathrm{d}t} = -\gamma n_i \mathcal{C}_2 \tag{4.8}$$

with γ a numerical constant containing all the short-range physics that does not depend on external parameters such as the magnetic field or the temperature in first approximation, and $\mathcal{C}_2 = C_2/V$ the two-body contact density.

The scalings of the fermionic two-body contact in the BEC-BCS crossover is known and was detailed in Chapter 2. We give them again in Table 4.1 along the expected losses scalings: we then see that the contact scalings match exactly the loss rate scalings we gave in section 4.1.2. Furthermore, the dependence of the loss rate on the density at unitarity, that was only obtained using a dimensional argument, is consistent with the density dependence of the contact. As the contact is continuous at unitarity, we expect no divergence in the loss rate in the crossover, and the asymptotic regimes given in Fig. 4.1 have to be reconciled in the strongly interacting regime.

	BEC	Unitarity	BCS
$\frac{\dot{n_i}}{n_i}$	$\propto \frac{n_m}{a_{ff}}$	$\propto n_f^{4/3}$	$\propto n_f^2 a_{ff}^2$
$\frac{C_2}{V}$	$8\pi \frac{n_m}{a_{ff}}$	$\frac{2\zeta}{5\pi} k_F^4$	$4\pi^2 a_{ff}^2 n_f^2$

Table 4.1: Scalings for the loss rate and Tan's contact

In short, we have shown that the three-body loss rate associated with an impurity in a Fermi superfluid is proportional to the two-body fermionic contact. Therefore, measuring

the lifetime of a weakly interacting impurity in a Fermi superfluid not only informs us on the dynamic stability of the system but also allows us to probe the properties of the many-body fermionic background.

4.2 Lifetime measurements

In our set-up we have a Fermi superfluid of ^{6}Li and the impurity corresponds to ^{7}Li atoms. We will thus use the index b instead of the index i to characterize the impurity. The ^{6}Li atoms are prepared in a mixture of $\uparrow$ and $\downarrow$ states corresponding to the states $|1_f\rangle$ and $|2_f\rangle$, and the ^{7}Li atoms are in the state $|2_b\rangle$. The atoms are confined in a hybrid magnetic-optical trap, they are evaporated at the ^{6}Li Feshbach resonance. We ramp the magnetic field to the wanted value in 200 ms and wait for a time t. We then measure the atom numbers of the two species by in situ imaging or after time of flight. We repeat this sequence for various wait times t and we get the number of atoms for each species as a function of t.

In the following, we will present experiments performed in different magnetic field and temperature conditions:

- First, we conducted some experiments on the BEC side at relatively high temperatures $T/T_F \simeq 0.75$. This was done for two main reasons. First, at higher temperatures the gases are less dense which maintains the losses low enough to be measured using reasonable waiting times. Second, at high temperatures, there is no phase separation between the bosons and fermions, as it was mentioned in Chapter 3, which allows us to go to magnetic fields as low as 680 G, far on the BEC side. In these conditions, we performed experiments to confirm the nature of the losses (section 4.2.1) and to extract the proportionality constant γ between the contact C_2 and the loss rate (section 4.2.2).

- Then, we measured the lifetime of the mixture at unitarity at $T = 0$. Since γ does not depend on the temperature nor the magnetic field, we can use its value to measure the contact at unitarity and more specifically its density dependence (section 4.2.3).

4.2.1 Investigating the nature of the losses

To investigate the origin of the boson losses, we compared the decay of bosons in the presence of spin balanced and spin polarized Fermi gases. The comparison between those two decays is done by measuring the total number of atoms at a time $t_i = 0$ and the remaining number of atoms after a waiting time $t_f - t_i = 1$ s for balanced fermions and $t = 1.5$ s for spin-polarized fermions with 90% polarization. For each value of the magnetic field, we record 3 to 5 images for each waiting time to determine the remaining fraction of atoms $N(t_f)/N(t_i)$. These measurements are displayed in Fig. 4.3.

We see that the boson losses in the presence of a polarized Fermi gas are highly suppressed: both spin states are needed to allow for boson decay. This is consistent with having three-body recombination between two fermions of opposite spin and a boson. We also observe that in this domain the three-body recombination between three bosons is negligible: this is due to the fact that the associated loss rate follows the scaling $L_3 \propto a_{bb}^4$ and a_{bb} remains small in the magnetic field domain we explored.

Furthermore, we see that for both fermions and bosons the losses increase drastically the further we go on the BEC side. This is due to the scaling of the three-body loss-rate

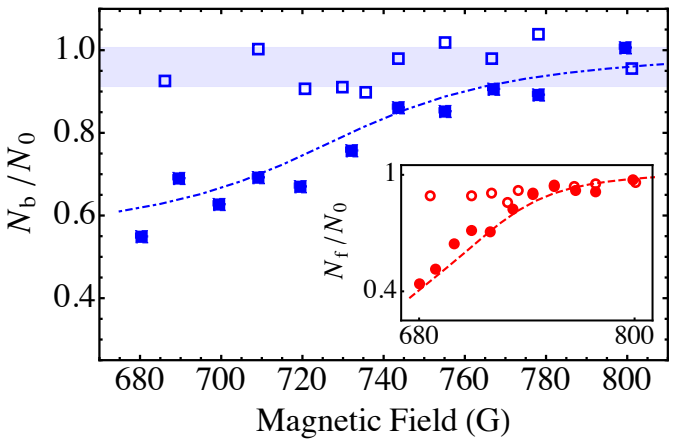

Figure 4.3: Remaining fraction of bosons (blue squares) and fermions (red circles, inset), when the Fermi gas is polarized (empty) or balanced (solid), in the BEC domain of the crossover. For a polarized Fermi gas, the losses are highly suppressed. The blue shaded area corresponds to the 1σ fluctuations for the remaining fraction of bosons in presence of a polarized Fermi gas. The blue dash-dotted curve (red dashed in the inset) is a coupled loss model taking into account the boson-dimer losses and the dimer-dimer losses [130].

$\dot{n}/n \propto 1/a_{ff}$ as well as the scaling of the dimer-dimer losses $\propto a_{ff}^{-2.55}$ (for the fermions only).

4.2.2 Losses on the BEC side

For our measurements on the BEC side, we worked with approximately $N_f \simeq 300 \times 10^3$ fermions and $N_b \simeq 150 \times 10^3$ bosons, with trapping frequencies of $\omega_z = 2\pi \times 26$ Hz and $\omega_r = 2\pi \times 2.0$ kHz, at a temperature $T \simeq 1.6$ μK, corresponding to $T/T_{F,h} \simeq 0.75$ where $k_B T_{F,h}$ is the Fermi energy in the harmonic trap (not local).

On the BEC side, Eq. (4.8) becomes for our system:

$$\frac{\mathrm{d}n_b}{\mathrm{d}t} = -\gamma \frac{8\pi}{a_{ff}} n_m n_b \tag{4.9}$$

with n_b the density of the Bose gas. The goal is to confirm this relation and to extract the coefficient γ that will be used for our measurements at unitarity.

Extraction of a loss rate

Since these measurements are performed in a nearly thermal regime ($T/T_{F,h} \gtrsim 0.75$), we can make the approximation that the Bose and Fermi gases are thermal clouds, that we will describe simply with a Gaussian density profiles.[3] In Fig. 4.4, we show a typical measurement, done at $B = 720$ G. Each point is the average of several data points, the limit being the presence of long term drifts in the atom numbers.

[3]The density profiles read as

$$n_b(\mathbf{r}) = N_b \frac{\overline{\omega}_b^3}{(2\pi k_B T/m_b)^{3/2}} e^{-\frac{m_b}{2k_B T}(\omega_{r,b}^2 r^2 + \omega_{z,b}^2 z^2)} \tag{4.10}$$

The bosonic loss equation, after integration over the trap, becomes

$$\dot{N}_b = -L_{bf}\langle n_f\rangle_{\rm b} N_b - \Gamma_v N_b \tag{4.12}$$

where $\langle n_f\rangle_{\rm b}$ is the averaged fermion density in the trap in presence of bosons[4], L_{bf} is the constant we want to determine and Γ_v is the one-body residual gas loss rate (0.015 s^{-1}) measured independently.

We extract the loss rate by fitting the boson atom numbers with the solution of this differential equation. We do not try to obtain it from the fermion numbers: several processes can contribute to the fermionic losses such as the Bose-Fermi losses of course but also dimer-dimer losses or residual evaporation. We simply use an ad-hoc two-body decay function for the fermions:

$$N_f(t) = \frac{N_0}{1 + t/\tau} \tag{4.14}$$

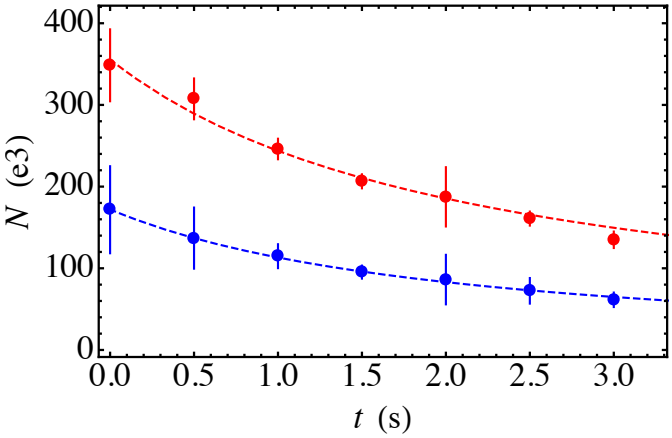

Figure 4.4: Bosonic (blue solid circles) and fermionic (red solid circles) losses at $B = 720$ G for a non-degenerate mixture at $T = 1.25$ μK. Each point is the average of 3 to 5 data points. The red dashed curve is a fit to the fermion decay using an ad-hoc function described in Eq. (4.14) to determine $n_f(t)$. The blue dashed curve is a fit to the boson decay using the solution of Eq. (4.12) and the previously fitted $n_f(t)$ to extract the loss rate.

Therefore, we can extract a loss rate but eq. (4.9) involves directly the density of molecules n_m, which is not as simple as $n_f/2$ at finite temperature.

and assuming all the fermions are bound into molecules

$$n_f(\mathbf{r}) = N_f \frac{\overline{\omega}_f^3}{(\pi k_B T/m_f)^{3/2}} e^{-\frac{m_f}{k_B T}(\omega_{r,f}^2 r^2 + \omega_{z,f}^2 z^2)} \tag{4.11}$$

with $\overline{\omega} = (\omega_z \omega_r^2)^{1/3}$

[4]Using the gaussian density profiles and the approximation $m_f\omega_f^2 = m_b\omega_b^2$ for the three trapping directions, we get

$$\langle n_f(t)\rangle_{\rm b} = \frac{\int {\rm d}^3\boldsymbol{r} n_b(\boldsymbol{r}) n_f(\boldsymbol{r})}{N_b} = N_f(t)\left(\frac{m_f\overline{\omega}_f^2}{3\pi k_B T}\right)^{3/2}. \tag{4.13}$$

Molecular aspect of the losses

The number of dimers in the Fermi gas is not directly accessible, though in the weakly interacting regime ($n_f a_{ff}^3 \ll 1$), the molecular fraction $\eta_m = 2N_m/(N_{\text{free}} + 2N_m)$, where N_m is the number of molecules and N_{free} the number of free fermions, can be estimated using a mass-action law [228]. To apply this law, we consider the Fermi gas to be a mixture of non-interacting molecules and free-atoms at chemical equilibrium, which is justified by the high formation rate of halo-dimers $\propto \hbar a_{ff}^4/m_f$ [229]. The chemical equilibrium condition can be written as

$$N_{\text{free}} = 2\left(\frac{k_B T}{\hbar\overline{\omega}}\right)^3 \text{Li}_3(z) \tag{4.15}$$

$$N_m = \left(\frac{k_B T}{\hbar\overline{\omega}}\right)^3 \text{Li}_3(z^2 e^{-E_b/k_B T}) \tag{4.16}$$

with $\overline{\omega}$ the average trapping frequency, $z = e^{\mu/k_B T}$ the fugacity and $E_b = -\hbar^2/m_f a_{ff}^2$ the binding energy of the dimers. The fugacity is imposed by the total number of fermions $N_f = N_{\text{free}} + 2N_m$.

In Fig. 4.5, we represent the estimated molecular fraction in the BEC domain for a temperature $T \simeq 1.6\,\mu$K. We see that $\eta \simeq 1$ in the deep BEC domain: all fermions pair up to form molecules. Alongside this graph, we plotted the measured loss rate L_{bf} as a function of the molecular fraction η_m. To obtain this curve, we measured the losses at a magnetic field of 720 G, at different temperatures ranging from 1 μK to 4 μK and different ^{6}Li densities from 0.2×10^{13} cm^{-3} to 1×10^{13} cm^{-3} in order to vary η_m. These temperature and density variations are obtained experimentally by performing different evaporation ramps and trap recompressions. From these measurements, we see that the loss rate is proportional to the molecular fraction, showing that the losses are indeed between a boson and a dimer on the BEC side.

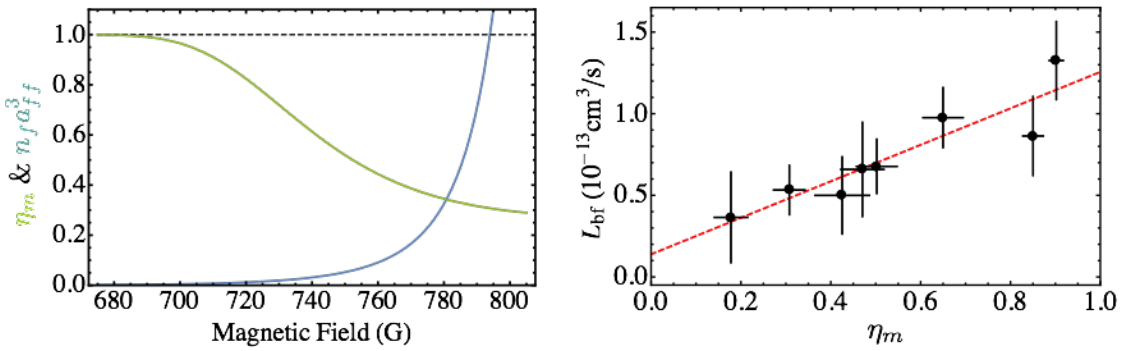

Figure 4.5: Left-hand panel: Molecular fraction η_m (green) and $n_f a_{ff}^3$ (blue) versus magnetic field in the BEC domain. The model used to estimate η_m is valid for $n_f a_{ff}^3 \ll 1$. Right-hand panel: Three-body loss rate L_{bf} as a function of the molecular fraction η_m (black circles). A linear fit (red dashed line) yields the dependence $L_{bf} = (1.12(21)\eta_m + 0.14(13)) \times 10^{13}$ cm^3/s.

As a consequence, we can introduce the constant L_{bm}, defined by $L_{bm}\langle n_m\rangle_{\text{b}} = L_{bf}\langle n_f\rangle_{\text{b}}$, and expect L_{bm} to be directly proportional to $1/a_{ff}$ whereas L_{bf} also contained the dependence from the molecular fraction.

Extracting the coefficient γ

We measure the boson and fermion decay for several value of the magnetic field, at a temperature $T \simeq 1.6\,\mu$K and we extract a loss rate $L_{bm}\langle n_m\rangle_{\rm b}$. Thanks to the molecular fraction and eq. (4.13), we can deduce L_{bm} that we plot against $1/a_{ff}$ in Figure 4.6.

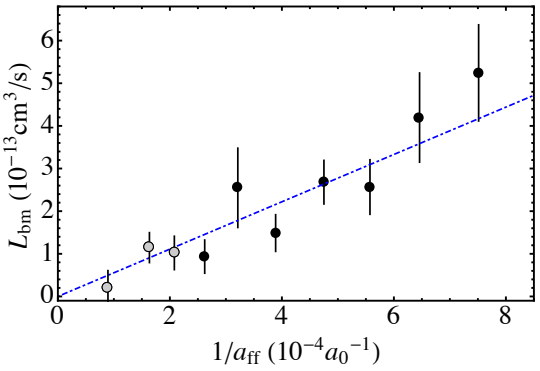

Figure 4.6: Boson-dimer loss rate with respect to inverse scattering length. The blue dashed line is a linear fit to the data with $k_F a_{ff} < 1$ (black solid circles), yielding $\gamma = 1.17(11) \times 10^{-27}$ m^4.s^{-1}.

From Fig. 4.6, we recover that the loss rate is proportional to $1/a_{ff}$ as expected. We can use the slope from the linear fit performed on the data points for which interaction effects were negligible ($k_F a_{ff} < 1$) to deduce the value of the parameter $\gamma \simeq 1.17(11) \times 10^{-27}$ m^4.s^{-1}. Since γ does not depend on the magnetic field nor the temperature, we will use this value for any case, especially at unitarity at $T = 0$.

4.2.3 Losses at unitarity

In this paragraph, we focus on the strongly interacting regime, where the quantum correlations between nearby particles become very important, making three-body recombination a many-body process. Using the relation between the loss rate and the contact, and using the expression of the contact at unitarity, we expect a loss rate equation for the impurity of the form:

$$\frac{{\rm d}n_b}{{\rm d}t} = -\gamma \frac{2\zeta}{5\pi}(3\pi^2 n_f)^{4/3} n_b \tag{4.17}$$

Consequently, we measure the boson decay rate at unitarity ($B = 832$ G) at low temperatures $T/T_F \simeq 0.1$. In this regime, the density of fermions can be easily deduced from the total fermion number N_f and the trap frequencies[5], and the bosons are condensed in a Bose-Einstein condensate, so they probe the contact locally, at the center of the fermionic cloud, instead of averaging it over the whole Fermi cloud. The Bose-Fermi mixture is initially composed of about $N_b = 30 \times 10^3$ fully condensed bosons and $N_f = 150 \times 10^3$ spin-balanced fermions.

[5]We have at unitarity and at $T = 0$:

$$n_f(0) = \frac{8\sqrt{N_f}}{\pi^2 \xi^{3/4}\sqrt{24}} \frac{1}{a_{ho}^3} \tag{4.18}$$

where $a_{ho} = \sqrt{\hbar/m_f \bar{\omega}_f}$ is the typical length of the harmonic oscillator.

At this value of the magnetic field, we are closer to the Feshbach resonance of the boson-boson interaction (located at $B = 845.5$ G), so we have to take into account three-body losses among the bosonic cloud itself, and the loss rate equation for the bosons becomes[6]

$$\dot{N_b} = -L_b \langle n_b^2 \rangle N_b - \Gamma_{bf} N_b - \Gamma_v N_b \tag{4.20}$$

where this time Γ_{bf} includes the dependence in n_f.

For our experimental conditions, with the Bose-Fermi mixture, the difficulty is to measure Γ_{bf} while the majority of the losses (around 80%) are due to three-body recombinations among the bosons themselves.

Consequently, we first need to determine the three-body bosonic loss rate L_b, by doing loss measurements on a ^{7}Li BEC alone, without any fermions, over wait times for which we do not have a visible thermal fraction surrounding the BEC. We get $L_b = 0.11(1) \times 10^{26}$ cm^6.s^{-1}, consistent with [230] and corresponding to typical lifetimes of the cloud of $2.5 - 10$ seconds. This is extracted from the data plotted in green in Fig 4.7.

We can see how important the three-body losses between three bosons are compared to the three-body losses between a boson and two fermions by looking at the blue curves of Fig 4.7: the light blue curve corresponds to the losses we would get without the fermions, using the value of L_b determined with the bosons alone (green curve), whereas the darker blue curve corresponds to a fit to the data points with all the terms of Eq. (4.20) including the one containing the Bose-Fermi three-body recombinations. The two curves are close but are still sufficiently distinguishable to extract a Bose-Fermi loss rate Γ_{bf}.

We can also note that the fermion numbers vary far less (compared to the measurements on the BEC side) over the period of time chosen, with a decrease of about 10%, and we still do not use them to determine Γ_{bf} because of larger number fluctuations and additional decaying channels such as evaporative losses which are complicated to estimate.

Repeating this method for different initial fermion densities n_f, by acting on either the trap confinement or the initial fermion numbers, we can test the expected $n_f^{4/3}$ density dependence of the Bose-Fermi loss rate at unitarity (Table 4.1). During these loss rate measurements, we restrict ourselves to wait times where the fermion numbers do not vary much (see Fig 4.7), and since $n_f \propto \sqrt{N_f}$ at unitarity and $T = 0$, we assume Γ_{bf} to be constant for each measurement.

We get the data points shown in Fig. 4.8. We can fit our data points with a power-law fit of the type An_f^p to extract an exponent $p = 1.36(15)$ perfectly compatible with the predicted exponent of $4/3$ presented in Table 4.1. As stated before, during these measurements the bosons remain condensed so that we probe the local contact, at the center of the cloud, where the fermion density is $n_f(0)$. However, the bosonic cloud has a finite size so there is some averaging of the contact over the bosonic cloud, which implies a correcting factor is required to obtain the local contact. We write the correction as:

$$\frac{\Gamma_{bf}/\gamma}{\mathcal{C}_2(0)} = \frac{\langle n_f^{4/3} \rangle_{\text{bosons}}}{n_f^{4/3}(0)} = \frac{\int \mathrm{d}^3\boldsymbol{r}\, n_b(\boldsymbol{r}) n_f(\boldsymbol{r})^{4/3}}{n_f(0)^{4/3} \int \mathrm{d}^3\boldsymbol{r}\, n_b(\boldsymbol{r})} = 1 - \frac{6}{7}\rho^2 + \frac{5}{21}\rho^4 + ... \tag{4.21}$$

[6]Using a Thomas-Fermi profile for the bosons, we have:

$$\langle n_b^2 \rangle = \frac{1}{N_b} \int \mathrm{d}^3\boldsymbol{r} n_b(\boldsymbol{r})^2 = \frac{7}{6} \left(\frac{15^{2/5}}{14\pi} \right)^2 \left(\frac{m_b \overline{\omega}_b}{\hbar \sqrt{a_{bb}}} \right)^{12/5} N_b^{4/5} \tag{4.19}$$

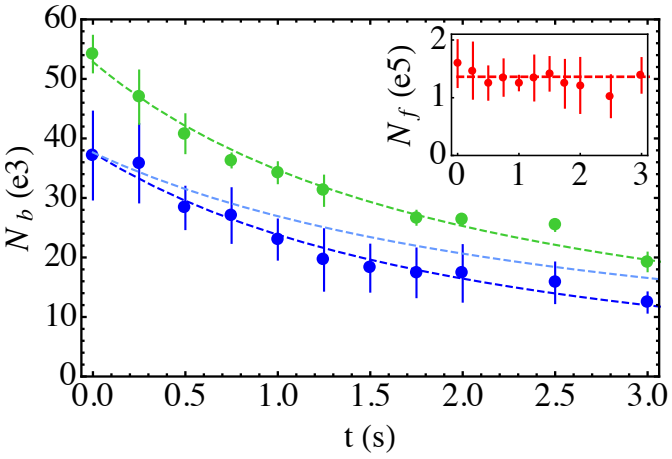

Figure 4.7: Atom numbers with respect to time at unitarity in the dual superfluid regime. Green points: boson numbers taken with condensed bosons alone. Blue Points: boson numbers taken in presence of a two-component Fermi superfluid. Green dashed curve: fit to the green data points using Eq. 4.20 with $\Gamma_{bf} = 0$ (no fermions) in order to determine L_b. Light blue dashed curve: fit to the data using the same L_b and also $\Gamma_{bf} = 0$, showing that the three-body recombination processes between bosons in the BEC are not enough to explain the totality of the boson losses in the mixture. Darker blue curve: Fit to the data using the previous value of L_b and leaving Γ_{bf} as an adjustable parameter. It yields $\Gamma_{bf} = 0.14(4)$ s^{-1}. Inset: fermion numbers for the same duration (data points). The red-dashed curve is the mean value of these data points, used to compute the peak density of the fermionic cloud during this measurement.

with $\rho \simeq 0.35(5)$ the ratio of the Thomas-Fermi radii for bosons and fermions, $\mathcal{C}_2(0) = \frac{2\zeta}{5\pi}(3\pi^2 n_f(0))^{4/3}$ the contact density at the center of the Fermi cloud. We can estimate the correction factor around $0.89(3)$.

The prediction of Eq. (4.17), with the correction factor given by eq. (4.21), is plotted as a red line in Fig 4.8: it matches very well with the data points without any adjustable parameters. Finally, we can also fit our data points with a function $An_f^{4/3}$, fixing the exponent to the theoretical value $4/3$ in order to determine the experimental value of the prefactor A. This gives a value for the homogeneous dimensionless contact $\zeta \simeq 0.82(9)$ in good agreement with previous measurements, for instance $\zeta = 0.87(3)$ [150].

In conclusion, we showed that we could connect the inelastic losses in our Bose-Fermi mixture to the fermions two-body contact both in weakly and strongly interacting regimes. We determined that the lifetime of the mixture is connected to short-range correlations in a many-body system. In particular, we observed the peculiar $n_f^{4/3}$ dependence, signature of non-trivial many-body effects in the system. Consequently, we developed a new technique to probe locally the two-body contact, using the losses between the bosonic impurity and the fermionic superfluid. We will see in the next section how we can further this study by looking into the temperature dependence of the contact, throughout the BEC-BCS crossover.

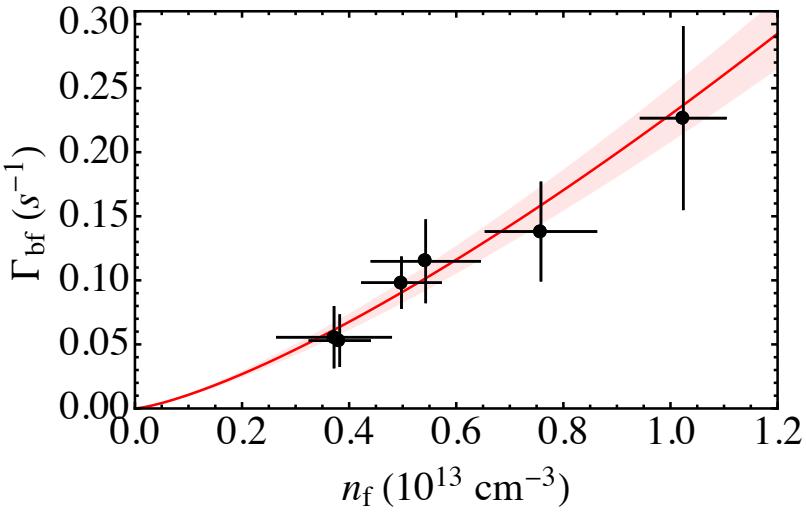

Figure 4.8: Boson loss rate with respect to the fermion peak density at unitarity, $n_f = n_f(0)$. The black circles are the experimental data. The red line is the prediction of Eq. (4.21) without any adjustable parameter. The red shaded area represents the 1 σ uncertainty coming from the value of γ.

4.3 Lifetime at finite temperatures

In this section, we are interested in the contact at finite temperature. We already obtained measurements of the contact at a relatively high temperature in the previous section, but here we will be particularly interested in its behavior around the superfluid transition. The principle of the measurement of the contact at finite temperature is exactly the same. We measure the losses in our Bose-Fermi mixtures at a give temperature, and thanks to the knowledge of γ, which does not depend on the temperature in first approximation, we can deduce the contact. To control the temperature we adjust the optical power at the end of the last evaporative cooling step of our experimental sequence and we measure the temperature using the bosons as an auxiliary thermometer.

This may seem simple, but in order to get a value for the local contact that does not depend on the number of atoms and that can be compared to other experiments, we need to determine the density (not the integrated density) of the Fermi gas at the center of the cloud (also called fermionic peak density), which can be tricky. At $T = 0$ and at unitarity, we had an explicit formula giving the peak density of the Fermi cloud, only knowing the number of atoms and the trap frequencies. At high temperatures, we modeled our thermal gases with simple Gaussian profiles, and the peak density was also simply known. At intermediate regimes, there is no such explicit formula. We detail thoroughly our method to determine the fermionic density in the appendix A. This method, relying on the curvature of the doubly-integrated profile does not require specific knowledge of the profile, works when there is also a Bose gas, at any temperature and for any interaction.

In this section, we will first present some theoretical considerations and experimental results on the contact at unitarity, and then we will detail our preliminary measurements on the unitary contact at finite temperature.

4.3.1 Previous results on the unitary contact

At unitarity, the system is universal. At finite temperature, it is described with two energy scales: the Fermi energy E_F and the thermal energy $k_B T$. A dimensionless contact such as C_2/Nk_F is only a function of T/T_F.

At high temperatures, for $T/T_F \gg 1$, the scalings of the contact correspond to the one of an ideal gas. We expect $C_2 \propto n_f^2$, similar to the scaling we gave on the far BCS side where the interactions tends to zero, which translates in terms of losses as standard three-body losses between two fermions and an impurity. As for the temperature dependence, at high temperature the contact should reflect the inverse mean free path l^* in the gas, thus we expect $C_2 \propto 1/l^* \propto 1/T$.

For lower temperatures, in particular near $T_{c,f}$ the critical temperature for superfluidity, theoretical predictions on the contact vary widely. In particular, some theories predict a discontinuity in the contact or its derivative [231,232] though it seems to be an artifact of numerical calculations for the contact should be continuous at the transition. Indeed, we can describe the temperature dependence of the contact near the transition by the use of a critical exponent. We introduce the critical exponent α, defined by $C_V \underset{T\to T_{c,f}}{\propto} |T-T_{c,f}|^{-\alpha}$, where C_V is the heat capacity at constant volume. In the canonical ensemble, we have

$$C_V = -T \left.\frac{\partial^2 F}{\partial T^2}\right|_{V,N}. \tag{4.22}$$

Close to the superfluid transition, this yields

$$F = f_0 + f_1 |T - T_{c,f}(N, 1/a_{ff})|^{2-\alpha} \tag{4.23}$$

$$C_2 \propto \frac{\partial F}{\partial(1/a_{ff})} \Rightarrow C_2 = c_0 + c_1 |T - T_{c,f}(N, 1/a_{ff})|^{1-\alpha} \tag{4.24}$$

where f_0, f_1, c_0 and c_1 are quantities that do not depend on the temperature.

The superfluid transition for a 3D system is a $U(1)$ transition, which belongs to the 3D XY or O(2) university class, where $\alpha \simeq -0.0151(3)$ [233]. Therefore, the temperature dependence of the contact near the transition should be as $|T - T_{c,f}|^{1,0151}$ so it should be continuous.

Finally, at very low temperatures $T \ll T_{c,f}$, the remaining excitations correspond probably to phonons, and are expect to follow a Stefan law thus contributing to the contact with a scaling as T^4 [234].

Very recently (2019), the contact was measured in MIT as a function of the temperature at unitarity using RF spectroscopy [235] and in Swinburne University with the measurement of structure factors via Bragg spectroscopy [236]. We represent in Fig. 4.9 the measurements realized in [235] in comparison with many numerical predictions and previous experimental results obtained at JILA [237]. Close to $T = 0$, they agree well with the contact we measured using the three-body losses, and above $T_{c,f}$ they match well with the predictions made with bold-diagrammatic Monte-Carlo calculations [238]. The experimental results from [235, 236] do not suggest any discontinuity close to the superfluid transition, though they show a significant decrease around $T = T_{c,f}$.

Hence, there seems to be a clear signature of the superfluid transition in the contact dependence on the temperature at unitarity. If we assume that this signature is still present everywhere else, the contact measurements may be used to determine the critical temperature in the crossover. Measuring the contact at finite temperature in the whole BEC-BCS

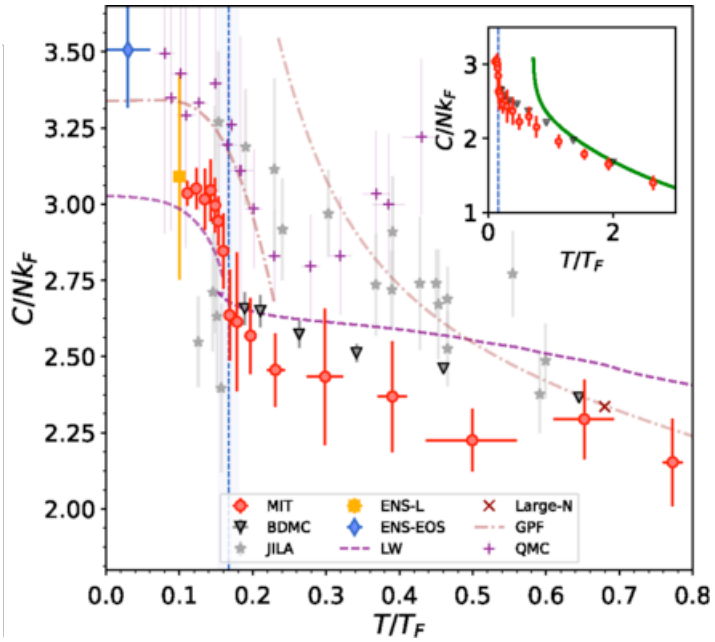

Figure 4.9: Dimensionless local contact C/Nk_F versus the T/T_F. Red dots: experimental data measured in [235]. They are compared with several theoretical calculations: Bold-Diagrammatic Monte Carlo (BDMC) [238], QMC [239], Luttinger-Ward (L-W) [240], Large-N [241], and Gaussian pair fluctuations (GPF) [231]. There is also the contact we obtained (ENS) [83] and whose measurement we will detail in the next chapter, from Bragg spectroscopy by the CQOS group [150], and using rf spectoscopy by the JILA group across a range of temperatures [237]. The vertical blue dashed line corresponds to the critical temperature $T_{c,f}/T_F = 0.167(13)$ measured previously in [136]. The inset shows the temperature dependence over a wider range and the agreement with third order virial expansion (green line) [242].

crossover could very well give us $T_{c,f}(1/k_F a_{ff})$, a very complicated problem still under heavy investigation, as we mentioned it in Chapter 3.

4.3.2 Lifetime measurements at finite temperature (preliminary)

With our set-up, we performed a preliminary series of losses measurements at finite temperature, with typically $N_f \simeq 200 \times 10^3$ fermions, $N_b \simeq 50 \times 10^3$ bosons, and trapping frequencies after recompression to prevent further evaporation of $\omega_z = 2\pi \times 21$ Hz and $\omega_r = 2\pi \times 1.6$ kHz. For these measurements, we had a temperature $T \simeq 800$ nK, corresponding to $T/T_{c,b} \simeq 1.2$, so we will consider the bosonic gas to be a thermal gas. We also evaluated a mean peak density for the Fermi gas $n_f^{\text{exp}}(0) = 0.7(1) \times 10^{19}$ m^{-3} from which we deduce a mean $T/T_F = 0.6(1)$. We did not observe a particular time-dependence of these parameters, so they will be assumed to be constant.

We give the equation describing the bosonic losses in presence of the Fermi gas, considering the bosonic gas as a thermal gas[7]

$$\dot{N}_b = -\tilde{L}_b N_b^3 - \Gamma_{bf} N_b - \Gamma_v N_b \tag{4.25}$$

[7]Here, we have $\tilde{L}_b N_b^2 = L_b \langle n_b^2 \rangle$. Since the Bose gas is considered to have a Gaussian profile, $\langle n_b^2 \rangle \propto N_b^2$ and the constant $\tilde{L}_b$ we defined does not depend on N_b.

Similarly as we did at zero-temperature, we first determine the constant $\tilde{L}_b$ looking at the losses of bosons alone and then we determine Γ_{bf}. The corresponding curves are presented in Fig. 4.10.

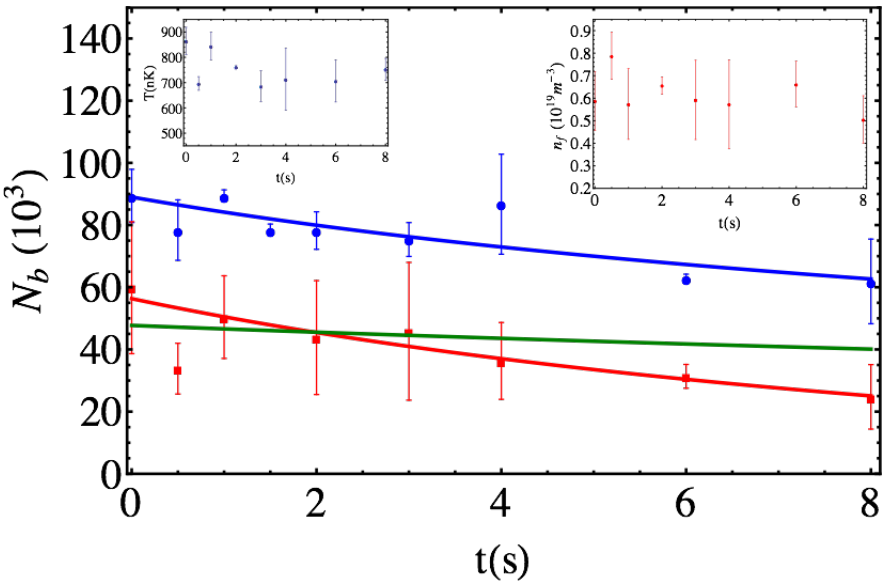

Figure 4.10: Blue points and blue curve: Three-body losses between bosons. Red points and red curve: data points and fit to the data using Eq. 4.25. Green curve : Fit to the data without any boson-fermions losses and using the three-body bosonic losses coefficient determined thanks to the blue data. It shows the introduction of Γ_{bf} is necessary to explain the losses.

The fit to the data, using the solution of eq. 4.25, gives us $\Gamma_{bf} \simeq 0.074(029)$ s^{-1}. From this value, we would like to obtain the dimensionless contact and compare it to the measurements plotted in 4.9. However, this measurement cannot be directly used because at this temperature, the Bose gas has a spatial extent comparable to the Fermi gas thus we do not probe the contact locally. The loss rate Γ_{bf} that we obtained is related to the value of the contact averaged over the Bose gas:

$$\Gamma_{bf} = \gamma \langle \mathcal{C}_2 \rangle_{\mathrm{b}} \tag{4.26}$$

with γ the proportionality factor between the loss rate and the contact that was determined in Section 4.2.2 and amounts to $\gamma = 1.17 \times 10^{-27}$ m^4.s^{-1}.

This averaging makes the comparison with the measurements from MIT and Swinburne University complicated, but at least we know it should be lower than the local contact. We define $\varrho = \langle \mathcal{C}_2 \rangle_{\mathrm{b}} / \mathcal{C}_2(0)$ the ratio between the averaged contact and the local contact $\mathcal{C}_2(0)$. To obtain a value of the local contact from the dimensionless contact C_2/Nk_F measured by the teams from MIT and Swinburne University, we use the equation

$$\mathcal{C}_2(0) = \left(\frac{C_2}{Nk_F} \right) (3\pi^2)^{1/3} n_f^{4/3}(0) \tag{4.27}$$

where $n_f^{4/3}(0)$ is the fermion peak density we obtain in our experiment with the method described in Appendix A.

From this last equation, we get a ratio $\varrho = 0.7(3)$, indeed inferior to one. In the following section, we will assess quantitatively the effect of the averaging.

4.3.3 Effect of the finite size of the impurity cloud

At high temperatures, for $T \gg T_F$, we can evaluate the correcting factor due to the size of the Bose gas rather simply. In this regime, both the Fermi and the Bose gas are thermal gases, their density follow the equation $n_\alpha = n_\alpha(0)e^{-\beta V(r)}$ with the index $\alpha = b, f$ distinguishing the two species, $\beta = 1/k_B T$ and $V(r)$ the trapping potential which is the same for each species. Using the fact that $C_2 \propto n_f^2$ at high temperatures, we get

$$\varrho_{\text{ideal}} \underset{T\gg T_F}{=} \frac{\langle n_f^2\rangle_{\text{b}}}{n_f^2(0)} = \frac{\int \mathrm{d}^3\boldsymbol{r} e^{-3\beta V(r)}}{\int \mathrm{d}^3\boldsymbol{r} e^{-\beta V(r)}} = \frac{1}{3\sqrt{3}} \simeq 0,19. \tag{4.28}$$

For temperatures $T \gtrsim T_F$, we can use the third virial expansion of the contact. It is an expansion in powers of the fugacity $e^{\beta\mu}$ that is explained in many details in [242], and represented in the inset of Fig. 4.9. This expansion reads

$$\frac{C_2}{V} = \frac{16\pi^2}{\lambda_{\text{th}}^4}\left(c_2 e^{2\beta\mu} + c_3 e^{3\beta\mu} + ...\right) \tag{4.29}$$

with $\lambda_{\text{th}} = \sqrt{2\pi\hbar^2/mk_BT}$ the thermal de Broglie wavelength. We see that the k_F^4 dependence at $T = 0$ has been replaced here by $1/\lambda_{\text{th}}^4$, signature of this expansion at finite temperature. The coefficients c_i can be deduced from the usual virial coefficients b_i through a derivative with respect to $\lambda_{\text{th}}/a_{ff}$, which explains why there is no first order term in fugacity since b_1 is constant. Their numerical values are given by $c_2 = 1/\pi$ and $c_3 = -0.141$ [242].

To obtain, $\mathcal{C}_2(\boldsymbol{r})$, we use the LDA for which $\mu(\boldsymbol{r}) = \mu_0 - V(\boldsymbol{r})$ with μ_0 the chemical potential at the center of the trap. After integration over the Bose gas treated as a thermal gas ($T \simeq 1.2\,T_{c,b}$), we obtain

$$\varrho_{\text{virial}} = \frac{1}{3\sqrt{3}}\frac{c_2}{c_2 + c_3 e^{\beta\mu_0}} + \frac{1}{8}\frac{c_3 e^{\beta\mu_0}}{c_2 + c_3 e^{\beta\mu_0}} \tag{4.30}$$

Thanks to the EoS of the unitary Fermi gas [136] that we detail in the appendix A, we have $\beta\mu_0$ as a function of $n_f\lambda_{\text{th}}^3 \propto (T/T_F)^{-3/2}$, hence we plot ϱ_{virial} as a function of T/T_F in Fig. 4.11. We can see it remains close to the value of the correction factor for high temperatures until it diverges around $T/T_F \simeq 0.4$, due to the limitations of this expansion. Since we obtained the loss rate near $T/T_F \simeq 0.6(1)$, the third virial expansion is not valid and it is not surprising that the correction factor this expansion yields ($\varrho_{\text{virial}}(0.6) \simeq 0.25$) is different from the one we obtained experimentally ($\varrho_{exp} = 0.7(3)$). However, the discrepancy between the two values is particularly important thus it may require further investigation in the future.

The error bars are quite important due to shot-to-shot number fluctuations, that affect at the same time the density, the Fermi temperature, and the determination of the loss rate. This preliminary work on the temperature dependence of the contact will likely be furthered in the future, but is currently stopped because we are replacing the leaking Ioffe bars (see Chapter 3), so our dataset was rather limited (only 40 points for the losses measurements) which is the main explanation for the important error bars. These error bars could be reduced vertically by obtaining experimentally larger datasets and horizontally by doing a post-selection on the temperature, assuming it does not vary significantly during the timescale of the loss measurements.

At $T = 0$, we had an expression of the correction factor as a function of the relative size of the Bose and Fermi gases, that was given in eq. (4.21), and gave a correction factor

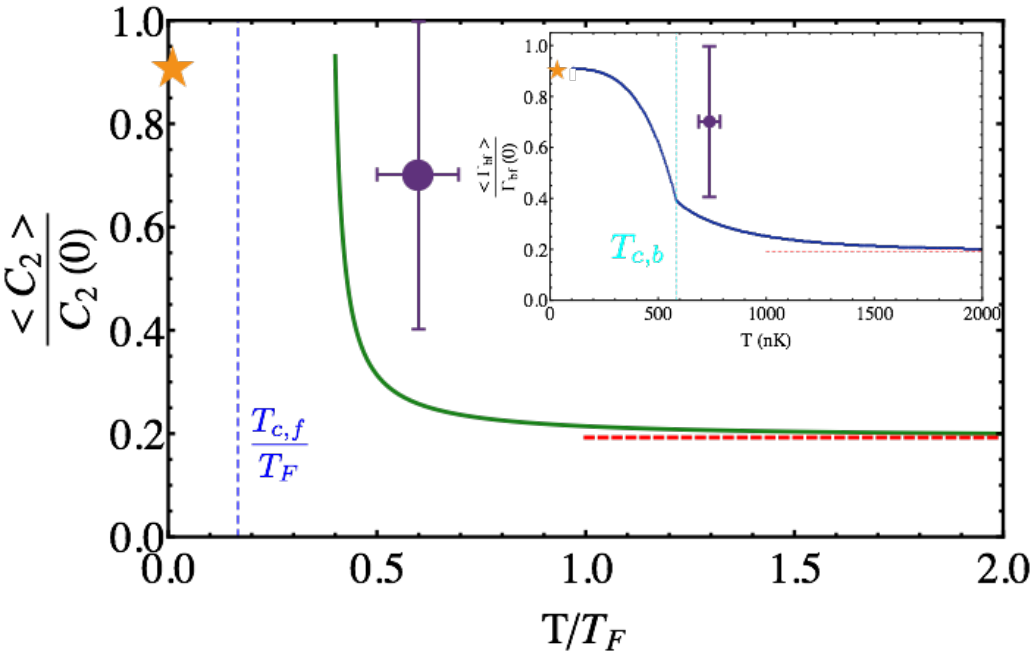

Figure 4.11: Ratio ϱ of the averaged contact C_2 due to the finite size of the impurity and the contact at the center. A ratio of 1 means the measurement yields the local contact at the center of the cloud. Green solid line: Calculation of ϱ using the third virial expansion of the contact, valid for $T/T_F \gtrsim 1$, where it remains quite close to the high temperature limit, corresponding to the red dashed curve. The purple solid circle is our experimental point. The dashed blue vertical line marks the critical temperature for the Fermi gas superfluidity $T_{c,f}/T_F = 0.167(3)$ [136]. The orange star corresponds to the ratio close to $T = 0$, evaluated in the previous section. Inset: A similar curve (solid dark blue) obtained numerically for the averaging of a loss rate Γ_{bf} by considering the Fermi gas as an ideal gas, as well as the thermal part of the Bose gas (their density profile are a Polylog function [219]). For the condensate fraction of the bosons we took a Thomas-Fermi profile. In this hypothesis, the loss rate has been taken $\Gamma_{bf} \propto n_f^2$ (ideal gases). At high temperatures, this correction factor tends towards the correction obtained in the high temperature limit (red dashed curve) while at low temperatures it converges towards the value we obtained at $T = 0$ (orange star). A vertical dashed cyan line marks the critical temperature for the condensation of the bosons $T_{c,b}$. Once again, the purple solid circle is our experimental point which falls far from the curve. This is not a curve giving the expected correction for the contact as a function of T but merely a way to show the contribution to the averaging that comes solely from the BEC transition of the bosons. It connects nicely the regimes of low-temperature and high-temperature but the intermediate regime may not reflect the behavior of ϱ.

$\varrho \simeq 0.9$. As a consequence, ϱ must go from 0.9 at $T = 0$ to the values obtained with the third virial expansion (which remain close to 0.2) near $T = T_F$. Unfortunately, it does not seem possible to evaluate the correction factor ϱ in the intermediate regime since we do not know the precise density dependence (or fugacity dependence) of the contact for these low temperatures.

Hence, in order to obtain local measurements of the contact, we should restrict ourselves to a temperature domain in which most of the bosons are in the condensed fraction,

which is generally the case around the critical temperature of the Fermi gas[8]. Therefore, we can still use our lifetime measurements to determine the local fermionic two-body contact, as long as we remain at temperatures not too high above $T_{c,f}$, which is not really a drawback since it is the regime we were interested in anyway.

To conclude, our method could very well be used to determine the critical temperature for superfluidity in the crossover, assuming there is a signature in the temperature-dependence of the contact at the superfluid transition in the whole crossover. Furthermore, to our knowledge this is the only method that can be used to measure the contact at finite temperature in the whole crossover. Indeed, the MIT group currently needs to stay at unitarity to determine the temperature of their Fermi gas because they use the EoS of the unitary Fermi gas. Thus, they cannot determine the temperature anywhere else in the crossover whereas it is not an issue for us since we have the Bose gas as an auxiliary thermometer.

Conclusion

In this chapter, we studied the lifetime of a an impurity immersed in a Fermi superfluid in the BEC-BCS crossover. Beyond the fact that knowing this lifetime informs us on the dynamic stability of the system, we highlighted the connection between this lifetime and the properties of the Fermi superfluid. Thus, we noted that the three-body losses between two fermions of opposite spin and a weakly interacting impurity atom give us a measurement of the fermionic two-body contact C_2.

Using our Bose gas as the impurity, we were able to measure the contact on the BEC side where we showed that $C_2 \propto n_m/a_{ff}$. At unitarity and at $T = 0$, since the BEC of ^{7}Li is much smaller than the Fermi cloud, it acts as a local probe for the measurement of C_2 at the center of the Fermi cloud. Hence we measured the local contact at unitarity, for which we demonstrated a peculiar density dependence $C_2 \propto n_f^{4/3}$ where the fractional exponent $4/3$ is the signature of many-body effects.

Finally, we presented a preliminary work on the contact at finite temperature. Our method of measurement using the losses between an impurity and a two-component Fermi gas can very well be used at finite temperature and anywhere in the crossover. We saw that in order to measure the local contact we needed to remain at temperatures for which most of the bosons are condensed, which is generally the case around $T_{c,f}$ allowing for a measurement of the local contact at the superfluid transition. This could lead us to determining $T_{c,f}(1/k_F a_{ff})$ if the signature of the transition that was observed at unitarity is present everywhere in the crossover.

Another perspective would be the measurement of the contact of a polarized Fermi cloud, which is also possible with our lifetime measurements, and in particular to observe the transition between the Fermi polaron and the molecular state we evoked in Chapter 2, for which we expect a discontinuity or at least a jump in the contact [164].

In the next chapter, we will present another experiment that was performed in our group, where we produced a counterflow of the impurity and the Fermi superfluid. We

[8]It is not simple to give estimations, because the critical temperature for the condensation of the bosons $T_{c,b}$ depends on the frequencies of the trap, and to fix a given temperature we act on these frequencies. So, as we increase T/T_F, we also increase $T_{c,b}$. To give a typical value anyway, for $T = T_{c,f}$, we have generally $T/T_{c,b} \simeq 0.6$ which corresponds to a condensed fraction of $N_c/N_0 \simeq 80\%$, so the probing remains local.

will show how this experiment informs us on the interaction between the impurity and the superfluid as well as the properties of the superfluid itself once again.

Chapter 5

Counterflow of a dual Bose-Fermi superfluid

Superfluidity was discovered in ^{4}He in 1938 when two teams in Oxford [4] and Moscow [3] reported the anomalous hydrodynamic behaviour of liquid ^{4}He, and later observed in ^{3}He in 1970 [5]. Since the Bose and Fermi superfluids were only observed separately, getting a mixture combining both superfluid has since been coveted [243, 244]. However, for ^{3}He and ^{4}He, the strong interactions between both species prevents from getting this dual superfluid: such a mixture contains a very small fraction of ^{3}He (around 6%), thus decreasing drastically its density and lowering its critical temperature for superfluidity under any temperature reachable yet with liquid Helium [210, 211].

Although getting a Bose-Fermi mixture with both species in the superfluid state has not be obtained with Helium, the advent of ultracold atom gases has made it theoretically possible: as we saw in Chapter 3 the much lower interspecies interactions in gases involve a better stability of the mixture. Mixtures of degenerate gases were produced with Bose-Bose superfluid mixtures [245], or Bose-Einstein condensates immersed in a Fermi sea [246]. Bose-Fermi mixtures of many kinds have been obtained, to cite a few: ^{23}Na-^{6}Li [247], ^{87}Rb-^{40}K [248], ^{87}Rb-^{6}Li [249], ^{174}Yb-^{6}Li [250, 251], ^{162}Dy-^{161}Dy [252], ^{133}Cs-^{6}Li [253], ^{87}Rb-^{171}Yb [254] or ^{41}K-^{6}Li [255]. However, it is in our group, in 2014, that a dual superfluid Bose-Fermi mixture was first obtained. Two years later, three other group have obtained another such mixture and found similar properties: in Seattle with ^{174}Yb and ^{6}Li [256], in Shanghai with ^{41}K and ^{6}Li [257], and in Tokyo with ^{6}Li and ^{7}Li [258].

In this chapter, we will study the interactions between the Bose and the Fermi superfluids. The low Bose-Fermi interactions ensures the stability of the mixture of the two superfluids in a large range of external magnetic fields, which is at the same time a blessing and a curse since it also means that it is harder to observe the effects of the interactions between the two gases. In order to observe them, we perform a counterflow experiment: we create a relative motion between the bosonic and the fermionic superfluid, an experimental technique previously used for the study of mixtures of Bose-Einstein condensates [259, 260], mixtures of Bose-Einstein condensates and spin-polarized Fermi sea [261], spin diffusion in Fermi gases [262] or integrability in one-dimensional systems [263]. This work was presented in [84, 264] and also throughly described in [265, 266]. We will here sum up the main results and show how this counterflow experiment enables to use the bosonic impurities as probes for the interactions between the two species as well as the EoS of the Fermi superfluid.

5.1 Dipole mode excitations

We prepare a Bose-Fermi mixture in the internal states described in Chapter 3, with balanced spin population for the Fermi gas. We have typically $N_b = 30 \times 10^3$ bosons and $N_f = 300 \times 10^3$ fermions, the trapping frequencies are typically $\omega_z = 2\pi \times 16$ Hz and $\omega_r = 2\pi \times 550$ Hz, with at temperature $T/T_F \lesssim 0.1$ ensuring both gases are superfluid.

5.1.1 Creating the counterflow

We create this relative motion between the Bose and Fermi clouds by taking advantage of the fact that the center of the magnetic trap does not totally coincide with the center of the dipolar trap. When the YAG laser is working at low powers, the axial trapping is mainly due to the magnetic confinement and the two clouds lie at its center. Since we work at high external magnetic fields, both isotopes are in the Paschen-Back regime, thus all particles have the same energy dependence with magnetic field and they feel the same trapping in the axial direction ie $m_f\omega_f^2 = m_b\omega_b^2$.

When the power of the laser is increased, both cloud centers are displaced along the z direction: we can ramp up slowly the power of the laser so that both clouds move adiabatically in the axial direction then decrease quickly the power back to its original value so that both clouds lie away from the center of the axial trapping and therefore will start oscillating in the harmonic trap as shown in Fig 5.1. The first step needs to be done slowly compared to the trap oscillation period (typically we have $t_{\text{up}} = 150$ ms, to compare with the radial and axial frequencies) so that both clouds follow the displacement of the center of the axial trap.

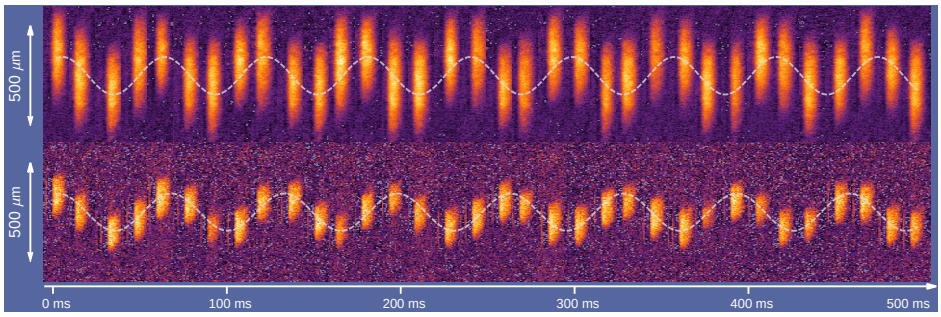

Figure 5.1: The fermionic cloud (top) and the bosonic cloud (down) oscillate in the axial direction simultaneously. Here we can see the absorption images of both clouds and the sinusoidal motion of their center of mass at two different frequencies taken at different times and then all gathered in this picture.

These oscillations constitute excitations of the dipole modes of the two clouds. To ensure we are not exciting radial modes, the duration of the ramp of the laser power down to low values has to be slow compared to the radial oscillation periods, but still fast compared to the axial oscillation period, conditions that are satisfied for $t_{\text{down}} = 20$ ms. With this process, quadrupole axial modes can still be excited but thanks to the small compression of the trap, the Thomas-Fermi radius of the two clouds vary by less than 10%, so we will neglect them in first approximation, as well as higher order excitation modes.

Since both clouds feel the same trapping and the two isotopes do not have the same mass, they will oscillate at different frequencies, typically $\omega_b = 2\pi \times 17$ Hz and $\omega_b = 2\pi \times 15$ Hz in the axial direction[1]. Consequently, they will not be synchronized and will acquire a relative motion, having opposite phases for the first time after approximately 4.5 periods. The clouds positions are then monitored for durations up to 4 s, as seen in Fig. 5.1 so that we can determine precisely the frequencies of oscillation.

5.1.2 Uncoupled oscillations

First, we study the oscillations of the Bose and Fermi clouds when they are alone. We obtain the oscillations frequencies of the bosons $\omega_b = 2\pi \times 15.68(10)$ Hz and the fermions $\omega_f = 2\pi \times 17.14(10)$ Hz, with a ratio $\omega_f/\omega_b = 1.09 \simeq \sqrt{7/6}$, in agreement with the expected ratio. The bosonic oscillations are presented in Fig. 5.2. The decay time of the oscillations is $\tau \gtrsim 20$ s, yielding a quality factor $Q = \omega\tau/2 \gtrsim 1500$, showing that the axial trapping is harmonic in a very good approximation. This is due to the fact that the axial confinement is mainly due to the magnetic confinement which is produced with coils whose size is much bigger than the amplitude of the oscillations of the clouds.

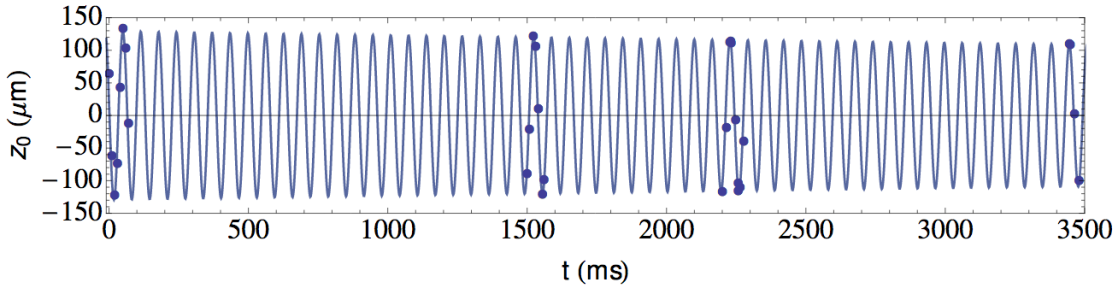

Figure 5.2: Position of the center of mass of the Bose gas when oscillating alone in the trap versus time, for an external magnetic field of $B = 832$ G, corresponding to the Feshbach resonance of the fermions. The oscillations have a very long time of life confirming the very good harmonicity of the trap. We can measure an oscillating frequency $\omega_b = 2\pi \times 15.27(1)$ Hz.

For the rest of the chapter, we will study the oscillations when both clouds are present to retrieve information on the interactions. This will be presented in the next two sections: the first one corresponds to the case of nearly undamped, long-term oscillations, whereas the second one will be focused on the study of the damping.

5.2 Long-lived oscillations: probing the interactions between the impurities and the superfluid

5.2.1 Effect of the Fermi superfluid on the impurities oscillations

At low temperatures, when both species are superfluid, and for small amplitudes of oscillation (typically ≤ 100 μm, we observe long-term oscillations of the bosonic impurities

[1]The ratio $\sqrt{7/6}$ between the two frequencies is due to the relation $m_f\omega_f^2 = m_b\omega_b^2$.

and the Fermi superfluid, see Fig. 5.3, and the measurement is only limited by the lifetime of the mixture (cf section 4.2.2).

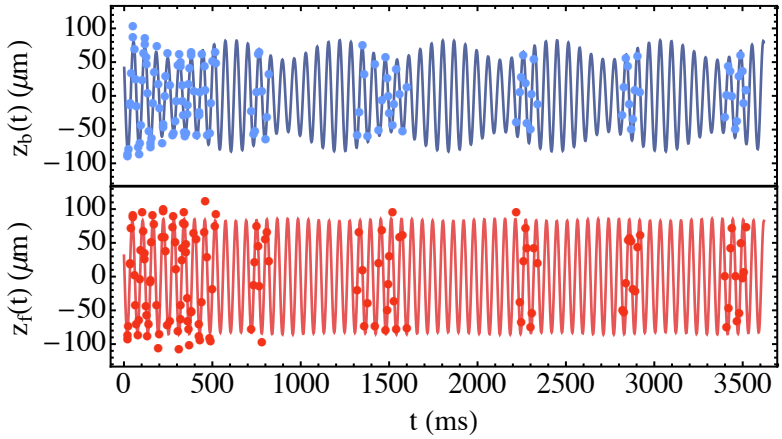

Figure 5.3: Position of the center of mass of the bosonic cloud (top) and the fermionic cloud (down) versus time taken at unitarity ($B = 832$ G). The Fermi cloud oscillates with almost no beating, at the frequency $\tilde{\omega}_f \simeq \omega_f = 2\pi \times 16.80(2)$ Hz. The bosonic cloud's motion reveals a beating feature, between the pulsations $\tilde{\omega}_f$ and $\tilde{\omega}_b = 2\pi \times 15.00(1)$ Hz, revealing a frequency shift of around 1.8% on the bosonic frequency.

From Fig. 5.3, we can make two observations. Firstly, there is an amplitude modulation, mainly on the bosonic oscillations. Secondly, we can measure the oscillation frequency of the Bose gas $\tilde{\omega}_b = 2\pi \times 15.00(1)$ Hz, which is downshifted of about 1.8% from the bare frequency ω_b obtained when it is alone, whereas the oscillating frequency of the fermions barely changes *ie* $\tilde{\omega}_f \simeq \omega_f = 2\pi \times 16.80(2)$. Moreover, a measurement of the pulsation of the amplitude modulations gives $\omega_{\text{mod}} \simeq \tilde{\omega}_f - \tilde{\omega}_b$.

The first feature corresponds to a coherent energy exchange between the two superfluids: the modulation comes from a beating between the two dipole modes dressed by the coupling. It is also present on the fermions but is way smaller due to a larger inertia $N_f m_f \gg N_b m_b$. A phenomenological model of coupled oscillators can be used to recover the equations of motion of the two clouds [267] which are given below:

$$z_f(t) = d\left[(1 - \epsilon_m \rho)\cos(\tilde{\omega}_f t) + \rho \epsilon_m \cos(\tilde{\omega}_b t)\right] \tag{5.1}$$
$$z_b(t) = d\left[-\epsilon_m \cos(\tilde{\omega}_f t) + (1 + \epsilon_m)\cos(\tilde{\omega}_b t)\right] \tag{5.2}$$

with $\rho = N_b/N_f \simeq 1/10$, and $\epsilon_m = \frac{2m_b}{m_f - m_b}\frac{\omega_b - \tilde{\omega}_b}{\omega_b} \approx 0.25$ at unitarity. The small value for ρ explains why the beating is barely present in the Fermi gas oscillations, whereas the not so negligible value of ϵ_m makes it very visible in the bosonic ones.

The second feature, the frequency shift, will be discussed in more details in the following section.

5.2.2 Frequency shift through the BEC-BCS crossover

Theoretical expression

We now focus on the calculation of the frequency shift of the bosons. The bosons feel an effective potential which is the sum of the trapping potential $V(\mathbf{r})$ and the interaction energy $E_{bf}(n_f(\mathbf{r}))$. In first approximation, we neglect the back-action of the bosons on the fermions, considering them as impurities in the Fermi superfluid, so the density of the fermion is given simply, in the local-density approximation, by $n_f(\mathbf{r}) = n_f(\mu_f^0 - V(\mathbf{r}))$ with μ_f^0 the chemical potential at the center of the cloud. Since the extension of the bosonic cloud is much smaller than the Fermi gas ($R_{TF,b} \simeq 0.35 R_{TF,f}$), it remains mainly at the center of the Fermi cloud. Therefore, we perform an expansion of the effective potential seen by the impurities near the center of the cloud:

$$V_{eff} = V(r) + E_{bf}\left[n_f(\mu_f^0) - \left.\frac{\mathrm{d}n_f}{\mathrm{d}\mu_f}\right|_0 V(r)\right] \tag{5.3}$$

$$V_{eff} = V(r) + E_{bf}(n_f(\mu_f^0)) - \left.\frac{\mathrm{d}n_f}{\mathrm{d}\mu_f}\right|_0 V(r)\frac{\mathrm{d}E_{bf}}{\mathrm{d}n_f} \tag{5.4}$$

$$V_{eff} = E_{bf}(n_f(\mu_f^0)) + V(r)\left[1 - \frac{\mathrm{d}E_{bf}}{\mathrm{d}n_f}\left.\frac{\mathrm{d}n_f}{\mathrm{d}\mu_f}\right|_0\right] \tag{5.5}$$

By writing $V_{eff}(r) = \frac{1}{2} m_b \tilde{\omega}_b^2 r^2$, we obtain the expression of $\tilde{\omega}_b$. In the mean-field approximation, we have $E_{bf}(n_f(\mathbf{r})) = g_{bf} n_f(\mathbf{r})$, so we can simplify the last expression as:

$$\tilde{\omega}_b = \omega_b \left[1 - \frac{1}{2} g_{bf} \left.\frac{\mathrm{d}n_f}{\mathrm{d}\mu_f}\right|_0\right] \tag{5.6}$$

or again, by writing $\delta\omega_b = \omega_b - \tilde{\omega}_b$:

$$\frac{\delta\omega_b}{\omega_b} = \frac{1}{2} g_{bf} \left.\frac{\mathrm{d}n_f}{\mathrm{d}\mu_f}\right|_0 \tag{5.7}$$

This expression can also be obtained within a fully quantum formalism through a sum-rule approach (see [267], Supplementary material).

Universal expression of the shift

To compare this prediction with this experiment, we need to determine $\left.\frac{\mathrm{d}n_f}{\mathrm{d}\mu_f}\right|_0$ throughout the BEC-BCS crossover. It can be estimated by using the EoS of the Fermi gas, measured in our group [137] and presented in Chapter 2. However, this quantity depends not only on the interaction strength but also on the atom numbers, leading to complicated dependencies. Fortunately, one can also show that the frequency shift obeys a universal scaling:

$$\frac{\delta\omega_b}{\omega_b} = k_{F,h} a_{bf} f\left(\frac{1}{k_{F,h} a_{ff}}\right) \tag{5.8}$$

with $k_{F,h} = \sqrt{2 m_f \overline{\omega}_f (3N_f)^{1/3}/\hbar}$ the Fermi wavevector of the trapped Fermi gas.

We can retrieve the expression of the function f in several asymptotic regimes:

- First, in the deep BCS regime, we have $\mu_f \simeq E_F = \frac{\hbar}{2m_f}(3\pi^2 n_f)^{2/3}$ the derivative can be computed easily, and we obtain:

$$f\left(\frac{1}{k_{F,h} a_{ff}}\right) \underset{\frac{1}{k_{F,h} a_{ff}} \to 0^-}{\sim} \frac{13}{7\pi} \tag{5.9}$$

- In the far BEC limit, the Fermi gas forms a molecular BEC and the expression of the chemical potential reads in the mean-field regime $\mu_d = g_{dd}n_d + g_{bd}n_b$ as seen in section 3.2.3. Using this expression, we obtain:

$$f\left(\frac{1}{k_{F,h}a_{ff}}\right) \underset{\frac{1}{k_{F,h}a_{ff}}\to 0^+}{\sim} 6.19 \times \frac{1}{k_{F,h}a_{ff}} \tag{5.10}$$

- Finally, at unitarity, where $1/k_{F,h}a_{ff} \to 0$, we have $\mu_f = \xi E_F$, similar to the BCS limit, and we get:

$$f(0) = \frac{13}{7\pi\xi^{5/4}} \tag{5.11}$$

Comparison to experimental data

To verify the expression of the frequency shift throughout the BEC-BCS crossover, we performed counterflow experiments for different magnetic fields, ranging from 780 G to 860 G corresponding to values of $1/k_{F,h}a_{ff}$ from -0.4 to 0.8. The comparison of the curve calculated using eq. (5.7) and the EoS measured in [137] with the experimental data is presented in Fig. 5.4.

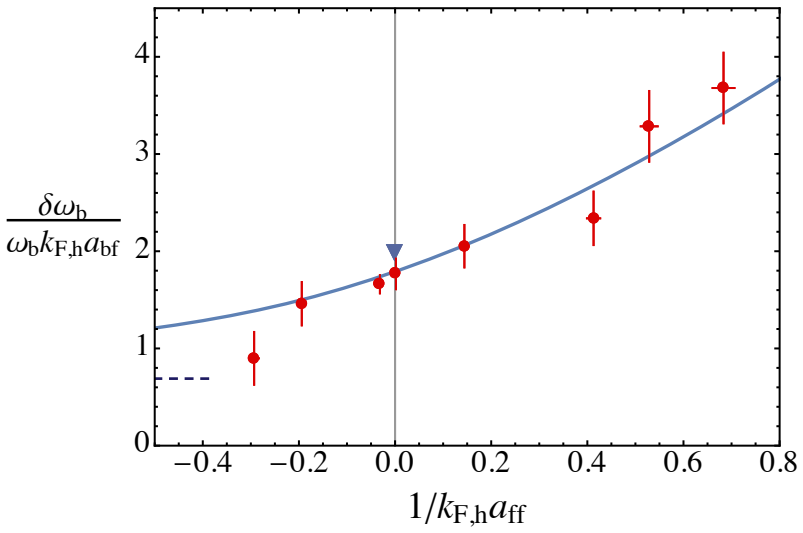

Figure 5.4: Frequency shift across the BEC-BCS crossover renormalized to have a universal scaling in $1/k_{F,h}a_{ff}$. The red points are the data points, the horizontal uncertainty comes from the atom number fluctuations and the vertical uncertainty comes from both number fluctuations and the frequency shift measurement. The blue solid curve is computed using the EoS measured in [137]. The blue triangle at unitarity is the value obtained using eq. (5.11) and the Bertsh parameter measured in [136]. The black dashed curve is the asymptotic value of the frequency shift on the BCS side predicted in eq. (5.9).

The experimental data matches very well with the calculated curve, showing that the collective dipole modes of the Bose gas are an accurate probe to the equation of state of the Fermi gas, revealing the properties of a quantum many-body system, as it did in a different way in Chapter 4. Yet, we must notice that, at unitarity, our experimental point matches with the theoretical curve obtained from our measurement of the Equation of State but is

shifted from the theoretical point we would obtain using the value of the Bertsh parameter measured at MIT [136], taken to be more precise. This (small) discrepancy between our data point and this theoretical value may find an explanation in the last chapter, after calculating the shift beyond a mean-field approach.

5.3 Damping of the oscillations

In the former section, we saw that at low temperatures and low amplitudes, the oscillations of the two clouds were long-lived, with no visible damping, as expected from a superfluid with no viscosity. However, when we deviate from these conditions, damping may appear. The damping of the oscillations of the two clouds can appear in two different conditions. On the one hand, damping appears when the amplitude of the oscillations increases. On the other hand, damping appears when the temperature of the clouds increases and the two gases are no longer superfluid.

The damping of the oscillations can be interpreted as the finite lifetime of the elementary excitations in the Fermi gas that are created by the counterflow. The finite lifetime of these excitations, seen as phonons, is explained by the different scattering processes they can undergo. In the case of the counterflow of an impurity and a Fermi superfluid, in order to provide a hand waving interpretation for the two different origins of the damping we observed, we consider two simplified scattering processes expressed in the referential of the superfluid and adapted from the scattering processes that may occur in a superfluid with no impurity [268]. First, there is the Beliaev process [269, 270] where an impurity of momentum $\boldsymbol{p}$ releases a phonon of momentum $\hbar\boldsymbol{q}$ and ends up with a decreased momentum $\boldsymbol{p}'$. Then, a Landau-Khalatnikov process [268] where an impurity interacts with a phonon, which may modify its impulsion and the energy of the phonon. Those two processes are represented in Fig 5.5.

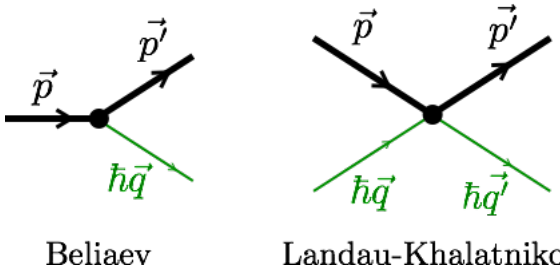

Figure 5.5: Schematics of the two scattering processes we considered for the excitations in our system. We represented the Beliaev process on the left-hand side and the Landau-Khalatnikov process on the right-hand side. The black solid lines correspond to the impurity and the green lines to the phonons.

The Landau-Khalatnikov process requires an incoming phonon, thus is more likely at finite temperature where thermal excitations exist. The Beliaev process will be the dominant process at low temperature [271] and, as we will see in the next paragraph, it exists only above a given critical velocity of the impurity, so for oscillations with high amplitudes.

In order to distinguish both mechanisms of dissipation, we will first study oscillations with high amplitude and low temperature and then oscillations with low amplitude and higher temperatures.

5.3.1 Higher amplitudes: critical velocity

Experimental observations

In this regime, the damping of the oscillations is very peculiar: at first, the amplitude is rather important and some damping occurs, then the amplitude decreases until it reaches a certain value at which the damping stops, finally leading to long-lived oscillations at this new, lower amplitude. These experimental behaviors are plotted in Fig. 5.6.

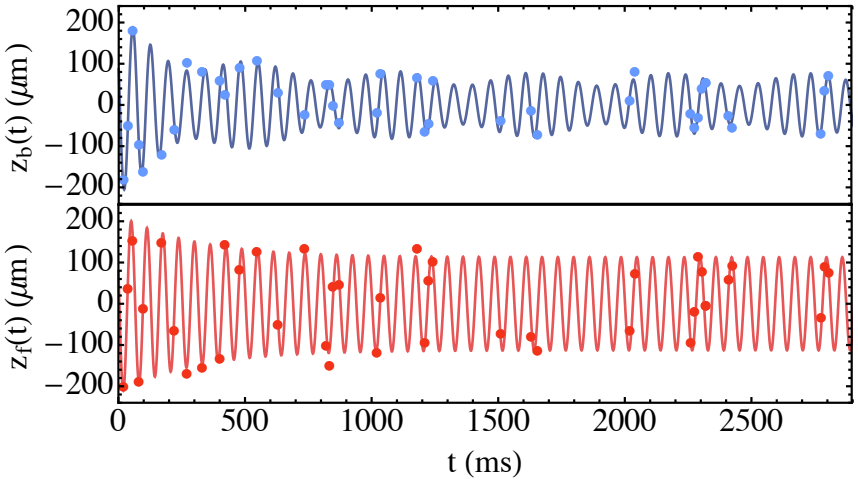

Figure 5.6: Position of the center of mass of the bosonic impurity (top) and the fermionic cloud (bottom) versus time at unitarity, taken with a starting amplitude of $z_0 \simeq 200$ μm. The oscillations are first damped until the amplitude of the fermionic cloud reaches $z_0 \simeq 120$ μm at which point the damping stops. The beating in the bosonic motion is still very observable.

From these curves, we can extract a damping rate using a phenomenological model where we replace the constant amplitude in eq. 5.1 and 5.2 with a time-dependent one:

$$d_f(t) = d(1 + \delta_f e^{-\gamma_f t}) \tag{5.12}$$
$$d_b(t) = d(1 + \delta_b e^{-\gamma_b t}) \tag{5.13}$$

At a given magnetic field, we can repeat the experiment for several initial displacements and extract a damping rate for each one, and find out their dependency. However, it is not the amplitude but rather the relative velocity that is the relevant parameter as we will see later. Anyway, increasing the amplitude amounts to increasing the relative velocity, so the former remarks still hold. In Fig. 5.7, we plot the damping rate as a function of the maximal relative velocity, for three different magnetic fields: one on the BEC side, another at unitarity and the last one on the BCS side.

We see that, for each curve there is a velocity threshold under which the damping rate is close to zero, and above which the damping rate starts rising. To extract the critical velocity corresponding to this threshold, we use another phenomenological model to account for this behavior:

$$\gamma = \gamma_0 \Theta(v - v_c)((v - v_c)/v_F)^p \tag{5.14}$$

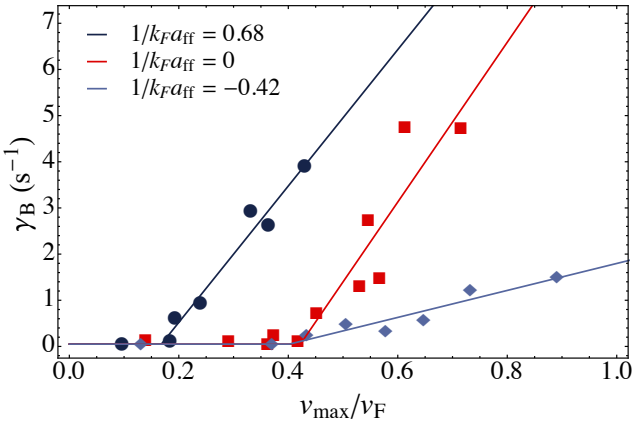

Figure 5.7: Damping rate versus the maximum relative velocity between the two clouds for three different magnetic fields. Dark blue circles: on the BEC side ($B = 780$ G). Red squares: at unitarity ($B = 832$ G). Light blue diamonds: on the BCS side ($B = 880$ G). The solid curves are fits to the data using the function from eq. (5.14) and $p = 1$.

with Θ the Heaviside function and $v_F = \hbar k_{F,h}/m_f$ the Fermi velocity.

The best fits, using χ^2 as a criterion, give out $p \simeq 1$ so we will retain this value for the exponent. Using this fit, we can extract the critical velocity for different values of the magnetic field, throughout the BEC-BCS crossover. The critical velocities corresponding to the three curves plotted in Fig. 5.7 are:

- At $1/k_{F,h}a_{ff} = 0.68$: $v_c = 0.17^{+0.06}_{-0.10} v_F$,
- At $1/k_{F,h}a_{ff} = 0$: $v_c = 0.42^{+0.08}_{-0.14} v_F$,
- At $1/k_{F,h}a_{ff} = -0.42$: $v_c = 0.40^{+0.10}_{-0.20} v_F$,

with the uncertainty coming from the exploration of the exponent p around 1.

Landau's criterion for superfluidity

The presence of a critical velocity in superfluids was predicted first by Landau in 1941 [272]. Landau described the case of a microscopic impurity of mass m moving through a homogeneous superfluid at constant speed. In order to have dissipation, the impurity must generate an elementary excitation in the superfluid, and we will see that due to energy and momentum conservation, it will lead to the appearance of a critical velocity. For a Beliaev scattering process (see Fig. 5.5), the initial and final momentum and energy of the system {impurity + excitation} in the frame of the superfluid read as

$$E_i = \frac{mv^2}{2}, \qquad \boldsymbol{p}_i = m\boldsymbol{v} \tag{5.15}$$

$$E_f = \frac{mv'^2}{2} + \varepsilon(\boldsymbol{p}), \quad \boldsymbol{p}_f = m\boldsymbol{v}' + \boldsymbol{p} \tag{5.16}$$

where $\epsilon(\boldsymbol{p})$ is the energy of the excitation with $\boldsymbol{p}$ is its momentum. The conservation of momentum and energy yield:

$$\frac{p^2}{2m} + \varepsilon(\boldsymbol{p}) = \boldsymbol{p}.\boldsymbol{v} \leq p \times v \tag{5.17}$$

leading to the following criterion:

$$v \geq v_c = \underset{\mathbf{p}}{\mathrm{Min}} \left[\frac{\epsilon(\mathbf{p}) + \frac{p^2}{2m}}{p} \right] \tag{5.18}$$

For an impurity with a very lage mass $m \to \infty$, the criterion is simplified into:

$$v_{c1} = \underset{\mathbf{p}}{\mathrm{Min}} \left[\frac{\epsilon(\mathbf{p})}{p} \right]. \tag{5.19}$$

In a Fermi gas, there are actually two excitations branches:

- The first one corresponds to bosonic collective excitations *ie* phonons with bosonic statistics [273]. We write the critical velocity associated with this phononic branch as v_p. The dispersion relation of this branch is linear at low momenta:

  $$\epsilon(\mathbf{p}) \underset{p \to 0}{=} p \times c_f \tag{5.20}$$

  with c_f the sound velocity in the Fermi superfluid, given by

  $$c_f = \sqrt{\frac{n_f}{m_f} \frac{\partial \mu_f}{\partial n_f}} \tag{5.21}$$

  and can be calculated through the BEC-BCS crossover using the EoS (similarly at what was done to compute the frequency shift).

  The dispersion relation from eq. (5.20) is only valid in the limit $k \to 0$, and the critical velocity obtained with eq. (5.19) will depend on the concavity/convexity of the dispersion relation. The dispersion relation of the low-energy excitations in a Fermi superfluid changes from convex to concave in the BEC-BCS crossover, close to the strongly interacting limit [274, 275]. On the BEC side, the dimers condense to form a BEC and the dispersion relation can be described with the Bogoliubov form

  $$\epsilon^{\mathrm{BEC}}(\boldsymbol{p}) = \sqrt{\frac{p^2}{2m} \left(\frac{p^2}{2m} + 2\mu_d \right)} \tag{5.22}$$

  with μ_d the chemical potential of dimers. This expression of the dispersion relation is essentially convex, so in the BEC limit, the critical velocity associated with the phononic branch corresponds to the sound velocity.

  On the BCS side, the presence of the pair-breaking continuum can bend downwards the dispersion relation of the phonons, implying a concave dispersion relation. The dispersion relation is actually concave for $1/k_F a_{ff} \lesssim 0.14$ [268]. In this case, the critical velocity does not correspond necessarily to sound velocity and its determination requires the precise knowledge of the dispersion relation.

- The second excitation branch corresponds to the breaking of Cooper pairs [276]. In BCS theory, the critical velocity due to the pair-breaking v_{pb} can be expressed as[2]

  $$v_{pb} = \sqrt{\frac{1}{m_f} \left(\sqrt{\Delta^2 + \mu_f^2} - \mu_f \right)} \tag{5.23}$$

[2]The energy of the elementary excitations due to pair-breaking in BCS theory corresponds to $E_k = \sqrt{(\varepsilon_k^{(f)} - \mu_f)^2 + \Delta^2}$ as seen in Appendix B. The expression of the critical velocity is obtained by looking for the minimum of E_k/k. The search for a minimum leads to eq. (5.23) for the critical velocity, realized for $k = \sqrt{2m_f/\hbar^2}(\Delta^2 + \mu_f^2)^{1/4}$.

where Δ is the gap parameter that can also be computed throughout the BEC-BCS crossover (see Appendix B). For this calculation, we also have simplified the problem a bit since two elementary excitations are actually created by a pair-breaking in the Fermi superfluid, the detailed calculation is described in [277].

The critical velocity in the Fermi superfluid is then $v_c = \mathrm{Min}(v_p, v_{pb})$. The critical velocity on the BEC side corresponds more to the one obtained with the phononic branch whereas on the BCS side it is rather the one due to the pair-breaking. The precise domains where the critical velocity is due to a given branch can be found in [277].

However, in our experiment, the impurity is played by the bosons that condense into a BEC. We may wonder if the BEC can be treated as a rigid impurity or if we have to take into account its collective behaviors, in particular the possible creation of excitations within the BEC. To account for this, the Landau's criterion was adapted to counterflowing superfluids in [277]. The minimal process for dissipation is the creation of an elementary excitation in each superfluid with opposite momenta (or two in the Fermi superfluid in the case of pair-breaking excitations). Energy and momentum conservation lead to

$$\epsilon_f(\boldsymbol{p}) + \epsilon_b(-\boldsymbol{p}) + \boldsymbol{p}.\boldsymbol{v} = 0 \tag{5.24}$$

with $\epsilon_f(\boldsymbol{p})$ the energy of the excitation in the Fermi superfluid and $\epsilon_b(\boldsymbol{p})$ the energy of the excitation in the Bose superfluid. We then obtain the critical velocity:

$$v_{c2} = \underset{\mathbf{p}}{\mathrm{Min}} \left[\frac{\epsilon_f(\mathbf{p}) + \epsilon_b(\mathbf{p})}{p} \right]. \tag{5.25}$$

In the bosonic superfluid, the excitations are phonons so $\epsilon_b(\mathbf{p}) = p \times c_b$ at low momenta with c_b the sound velocity in the bosonic superfluid[3] and the dispersion relation is convex. Consequently, we see that the critical velocity given by eq. 5.25 is essentially the same as the one given by eq. 5.19, only shifted by c_b.

In order to distinguish if the collective behavior of the Bose gas plays a role in the dissipation process, we have to compare our experimental measurements of the critical velocity to the theoretical values v_{c1} and v_{c2} obtained using the standard Landau criterion and the extended Landau criterion to counterflowing superfluids respectively.

Comparison between theory and experiments

In Fig. 5.8, the critical velocity obtained from the experiment is plotted along with $\overline{v}_{c1}$, the theoretical critical velocities obtained from eq. (5.19) , $\overline{v}_{c2}$, the one from 5.25, and the sound velocity in the Bose gas $\overline{c}_b$, all of them integrated over the transverse density profile of the cloud.

Even though it is plotted against $1/k_{F,h}a_{ff}$, $\overline{c}_b$ actually does not depend directly on this parameter but rather the external magnetic field and the bosons number. It is small compared to the experimental values, so it is excluded as a candidate for the critical velocity. On the other hand, the experimental data is consistent with either $\overline{v}_{c1}$ and $\overline{v}_{c2}$, confirming

[3]The sound velocity in the Bose gas has the same definition as in the Fermi gas. It is given by:

$$c_b = \sqrt{g n_b / m_b} \tag{5.26}$$

where n_b is the boson density and m_b their mass.

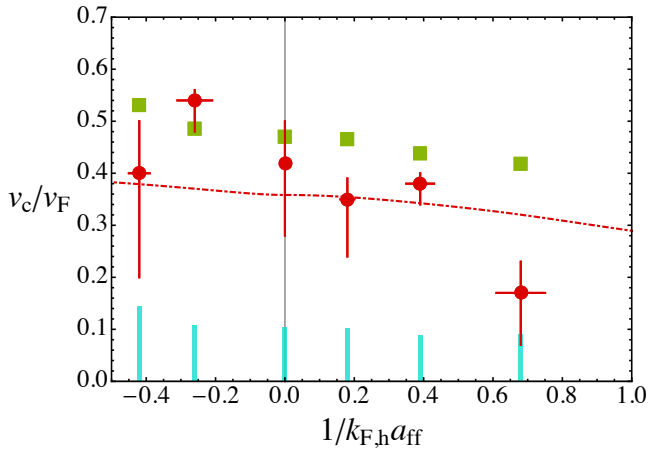

Figure 5.8: Critical velocity, normalized by the Fermi velocity, versus $1/k_{F,h}a_{ff}$. Red circles: data points measured across the BEC-BCS crossover, the vertical uncertainty mainly comes from the uncertainty on the value of the critical velocity from the fit, obtained by varying the p coefficient in Eq. 5.14. Red line: theoretical critical velocity v_{c1} obtained with eq. (5.19) derived from Landau's criterion. Blue bars: calculated sound velocity in the bosonic impurity, with the uncertainty corresponding to the fluctuations on the bosons numbers. Green squares: theoretical critical velocity v_{c2} obtained using the extension of Landau's criterion from eq. 5.25. The data points matches with both v_{c1} and v_{c2}, not allowing to choose one over the other.

the nature of the dissipation, but not enabling to distinguish between the model corresponding to the original Landau criterion (with a "rigid" impurity) and the one from the adapted criterion (with a BEC).

The drop on the last value of the experimental critical velocity, near $1/k_{F,h}a_{ff} = 0.7$, the furthest value taken on the BEC side has yet to be explained. A first explanation could come from the interaction between the two clouds that modifies the expression of the sound velocities. As detailed in [278], the critical velocity has to be corrected to take into account the interactions between the clouds, with a correcting factor A_c writing as

$$A_c = \sqrt{1 - \frac{\frac{\partial \mu_f}{\partial n_b}\frac{\partial \mu_b}{\partial n_f}}{\frac{\partial \mu_f}{\partial n_f}\frac{\partial \mu_b}{\partial n_b}}}. \tag{5.27}$$

This correction factor drops to zero when the condition

$$\frac{\partial \mu_f}{\partial n_b}\frac{\partial \mu_b}{\partial n_f} - \frac{\partial \mu_f}{\partial n_f}\frac{\partial \mu_b}{\partial n_b} = 0 \tag{5.28}$$

is realized. It corresponds to exactly the same condition as the one for phase separation described in section 3.2.3, so it implies that the correction factor is close to one in most of the crossover and will drop to zero on the BEC side around $B = 730$ G corresponding to $1/k_{F,h}a_{ff} \simeq 1.6$. On a side-note, it shows that phase separation can be determined by looking for a drop in the critical velocity.

For $1/k_{F,h}a_{ff} = 0.7$, the correction factor can be evaluated around 0.8 inducing a 20% correction on the critical velocity, not enough to explain the discrepancy with the

theoretical value. Other effects, such as a back bending of the dispersion relation due to radial confinement [279, 280], blurring of the threshold due to oscillatory motion of the impurity [281, 282] or finally thermal fluctuations which can also reduce the apparent critical velocity [281], and are more prone to happen far on the BEC side where inelastic losses (three body recombination or dimer-dimer losses as detailed in chapter 4) are enhanced. In retrospect, our measurement of the critical velocity is surprisingly close to the theoretical values in most of the crossover despite these different effects, and compared to previous experiments on Bose superfluids [283–285] and Fermi superfluids [282, 286].

5.3.2 Higher temperatures: out of the superfluid phase

At finite temperatures, over the critical temperatures for superfluidity of the two species, the oscillations of both clouds are damped down to zero amplitude. This can be explained by the fact that the clouds are no longer superfluid and frictionless movement no longer occurs. More strikingly, the friction becomes so strong that the two clouds start oscillating in phase, at almost the same frequency, the fermionic frequency, as can be seen in Fig. 5.9.

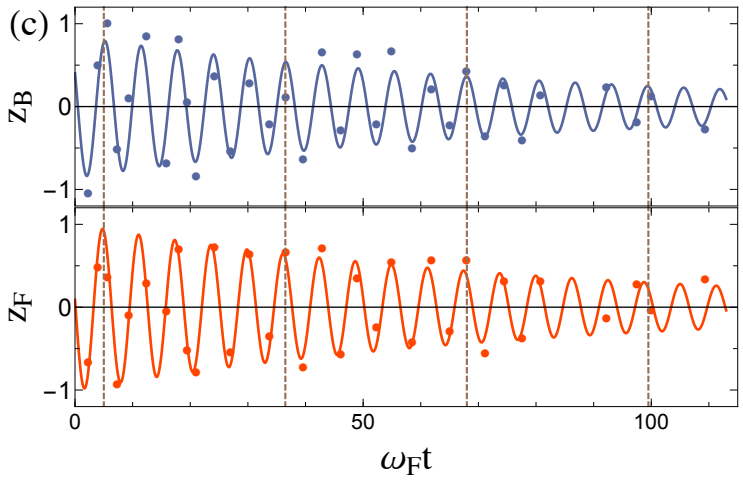

Figure 5.9: Position of the center of mass of the bosonic impurity (top) and the fermionic cloud (bottom) versus time, taken at unitarity at $T = 0.4T_F$, above the critical threshold for both gases. Amplitudes are both damped towards zero and the two clouds are locked in phase at the fermionic frequency (see dashed lines to observe the synchronization).

As stated before, the significantly less massive impurity is dragged by the fermionic cloud when the friction becomes very high, making it oscillate in phase with the Fermi cloud. To study this effect, the frequency of oscillation of the bosons is plotted against the temperature in Fig. 5.10. We see that the frequency locking occurs when the temperatures reaches the critical temperature for the Bose-Einstein condensation $T_{c,b}$, way after the critical temperature for the superfluidity of the fermions has been reached. This can be explained by the fact that the thermal fraction of the impurity oscillates at ω_f while the remaining condensed fraction keep oscillating at $\tilde{\omega}_b$ as was proven through separate spectral analysis of the condensed fraction and the thermal part of the cloud in [265].

This shows that in this context, the collective behavior of the Bose gas cannot be neglected as long as it remains superfluid, limiting the damping of the oscillations even when

the Fermi gas is no longer superfluid, whereas the thermal Bose gas is simply dragged by the Fermi gas and behaves as an ensemble of impurities.

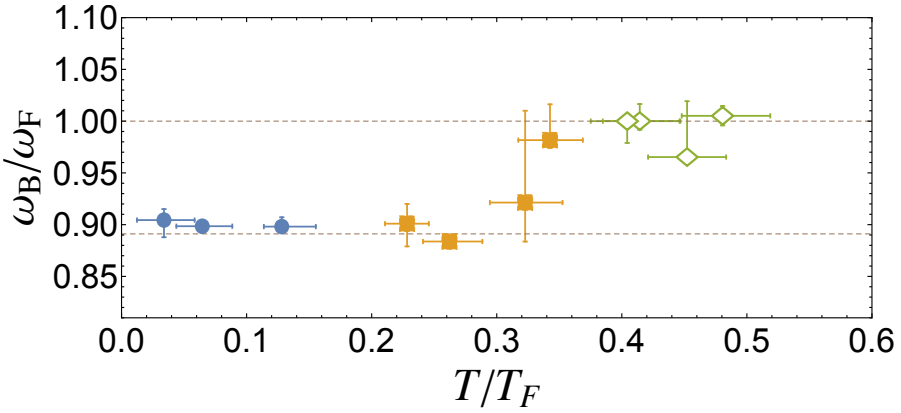

Figure 5.10: Frequency of oscillation of the bosonic cloud versus temperature. Blue circles correspond to temperatures beneath both critical thresholds for superfluidity. Yellow squares correspond to temperatures where the Fermi cloud is in the normal phase while part of the bosonic cloud remains condensed. Green empty diamonds correspond to temperatures where both clouds are not superfluid anymore. The phase-lock between the clouds happen near the critical threshold for superfluidity of the bosonic impurity.

On a side-note, the frequency locking happens at $T = T_{c,b}$, in the experimental conditions we described at the beginning of the Chapter for which we have $T_{c,f} < T_{c,b}$. One may wonder what would happen if we prepared the atoms in specific conditions such that $T_{c,f} > T_{c,b}$, which can be realized by increasing even more the ratio N_f/N_b. We could expect the frequency locking to happen near $T = T_{c,f}$, where there can be friction between the thermal Bose gas and the no longer superfluid Fermi gas, which could give a new means to determine $T_{c,f}$ in the crossover, in addition to the measurement of the contact we explained in section 4.3, though it would be very challenging experimentally[4].

5.4 Conclusion

In this chapter, we detailed experimental results on the counterflow of a cloud of bosonic impurities in a Fermi superfluid. For small oscillation amplitudes, the two cloud flow with no visible damping, despite being quickly out-of-phase since they oscillate at different frequencies, confirming the superfluidity of the Fermi gas. We observed a shift in the oscillating frequency of the Bose gas whether it was alone or in presence of the Fermi superfluid. We were able to explain this shift by the interaction between both clouds using a mean-field calculation.

In a second part, we presented results concerning the damping of the counterflow. First, when increasing the oscillation amplitude and with it the relative velocity between the two cloud, we saw that the oscillations where damped right until the amplitude was

[4]At unitarity, where we know $T_{c,f}$, we can evaluate that in order to have $T_{c,b} < T_{c,f}$, we would need to have $N_f \gtrsim 27 N_b$, requiring $N_b < 10\,000$ since the total number of fermions at low temperatures is limited at around $N_f \approx 300\,000$ in our experimental set-up. This very low number of bosons is at the limit of detectivity in our set-up and would be subjected to high shot-to-shot fluctuations, limiting the precise measurement of the oscillation frequency.

low enough. This was consistent with the presence of a critical velocity, explainable with Landau's criterion for superfluidity or its extension for the counterflow of two superfluids, whose experimental values across the BEC-BCS crossover were measured and found out to be compatible with both models. Then, in the case of counterflow at finite temperature, the two clouds were no longer superfluid and we found that the bosonic impurity was phase-locked with the Fermi gas due to the high friction between them. This last experiment showed the limit of the treatment of the bosons as mere impurities since their collective behavior *ie* their superfluidity ensured oscillations with limited damping despite being at temperatures where the Fermi gas was no longer superfluid.

In the next chapter, we will see how we can treat theoretically the interactions between an impurity and the Fermi superfluid beyond mean-field calculations, taking into account the many-body effects in the strongly interacting regime, ultimately coming back to the calculations of the frequency shift, which may explain for instance the discrepancy between our experimental point and the point calculated using the MIT data at unitarity in Fig. 5.4.

Chapter 6

The 2N+1 body problem

In the previous chapter, we studied the oscillations of an impurity in a Fermi superfluid. In this experiment, the polaron was weakly coupled to the background Fermi gas and we were able to interpret the frequency shift of the impurity oscillations using a mean-field approximation for the impurity-fermion interaction. The case of an impurity interacting strongly with the Fermi superfluid was studied theoretically [117, 287] but by using a mean-field theory to describe the fermionic many-body ensemble, revealing the role of Efimov physics for the system and as a consequence the existence of unphysical ultraviolet divergences in some results. Our objective is to study the interaction between an impurity and a many-body ensemble, beyond the mean-field approach for the impurity-fermion interaction and without making assumptions on the Fermi superfluid.

In our experiment, the impurity is the Bose gas of ^{7}Li, though the exact nature of the impurity does not matter in this problem. For the sake of generality and simplicity, we will now write a the scattering length for the interaction between two fermions and a' the scattering length for the interaction between an impurity and a fermion, assuming the interaction between the impurity and the fermions is the same for both spin states, as it is in our set-up. Moreover, g and g' will be the associated coupling constants with $g = 4\pi\hbar^2 a/m_f$ and $g' = 2\pi\hbar^2 a'/m_r$, with m_r the reduced mass between the impurity and a fermion.

Concerning our specific problem, different phenomena arise depending on the interactions. In the case of small, negative values of a', as we saw in Chapter 2, the impurity can be seen as a polaronic quasi-particle: we will refer to this phase as the polaron phase. For small, positive values of a', the impurity atoms can form molecules with fermions from the many-body background: we will call them dimerons, to differentiate them from the dimers that can form between two fermions on the BEC side of the Feshbach resonance. Finally, for strong interactions, when $1/a' \to 0$, Efimov physics have to be taken into account and the impurity atoms can form trimers with a Cooper pair made of two fermions of opposite spin: we will call them trimerons. Consequently, the phase diagram of the impurity will be separated into those three phases, depending on the strength of impurity/fermion interactions.

In Fig. 6.1, we see the typical shape of the energy curve of the three possible states. This is a representation for a given a. By increasing $1/a'$ all the way from the negative values, it shows the transition from the polaron state to the trimeron state, which is actually expected to be merely a smooth crossover due to earlier variational calculations [117,287], to eventually the dimeron state.

In the appendix C, we describe how we can build a phase diagram by comparing the

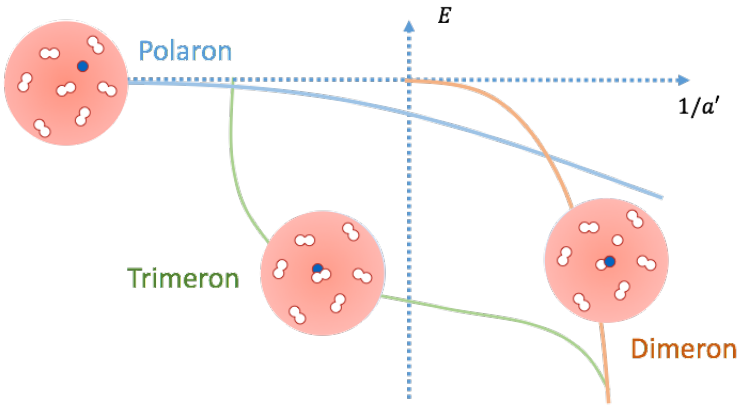

Figure 6.1: Sketch of the energy branches of an impurity (red dot) immersed in an ensemble of Cooper-paired fermions when the impurity/fermion scattering length a' is varied. Blue: polaronic branch. Green: Trimeronic branch. Orange: Dimeronic branch. According to mean-field calculations [117, 287], the polaron/trimeron transition is actually a smooth crossover, which should correspond to an avoided crossing between the two branches.

energy of these three phases. For this phase diagram, the relevant parameters are not only the two scattering lengths a and a' but also the resonance range R_e introduced in Chapter 1, since we use a similar two-channel model to describe the trimeron and the dimeron.

Since the size of the ground-state of the trimeron is typically much smaller than the distance between particles (see section 1.3), its binding energy is much larger than the Fermi energy of the fermionic background, or than the energy of the polaron which is a correction to the Fermi energy. Consequently, the internal structure of the trimer is only weakly affected by the many-body background, except when the Efimov trimer becomes resonant with the atomic continuum and its binding energy tends to zero. Likewise, the dimeron state is very weakly affected by the many-body background. The calculation of their energy can be done using few-body physics and is presented in the appendix C. The phase diagram we obtained is given in Fig. 6.2.

Since the trimeron and dimeron states can be essentially described using few-body physics, we will now study the polaronic branch, which is much more affected by the many-body background, in particular in the regime $|a'| \lesssim R_e$ which is compatible with our experimental conditions that correspond to $|a'| \simeq R_e$. When the fermion-fermion interaction is varied in the BCS-BEC crossover, from a weakly attractive interaction on the BCS side of the crossover where fermions form loose Cooper pairs to a strongly attractive interaction on the BEC side where the Fermi gas condensates in a BEC of tightly bound dimers, the polaronic state switches from a Fermi polaron on the BCS side to a Bose polaron on the BEC side. Our objective is to determine the energy of the polaron in this crossover between the Fermi polaron and the Bose Polaron, for small fermion-impurity interactions and with a given value of R_e/a', thus exploring horizontally the phase diagram.

In the first section, we will start with a perturbative expansion of the polaron energy for small fermion-impurity interactions, and we will see that a logarithmic divergence arises already in the second order term of the expansion. The following sections will treat the regularization of this many-body problem using few-body physics in order to

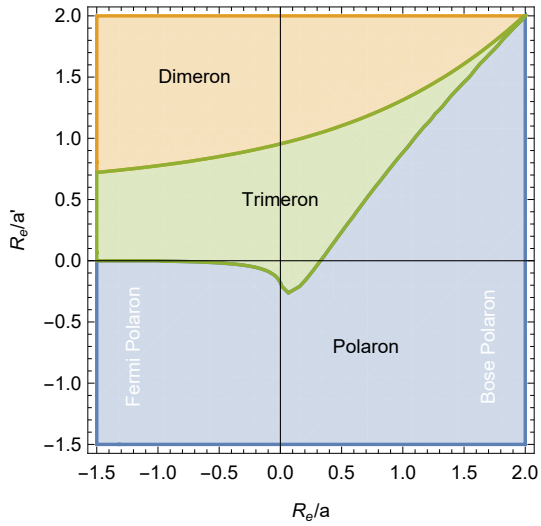

Figure 6.2: Phase diagram of an impurity immersed in a two-component Fermi superfluid.

obtain an expression of the polaron energy in the crossover. Finally, we will come back to the counterflow experiments, where we will see how this polaronic energy can affect the theoretical curve of the frequency shift that was compared to the experimental data in the previous chapter.

6.1 Perturbative expansion of the polaron energy

6.1.1 Theoretical framework

We consider an impurity of mass m_i immersed in a many-body ensemble of spin $1/2$ fermions of mass m_f. We write the Hamiltonian of the system as

$$\widehat{H} = \widehat{H}_{\text{imp}} + \widehat{H}_{\text{mb}} + \widehat{H}_{\text{int}}, \tag{6.1}$$

where $\widehat{H}_{\text{imp}}$ (resp. $\widehat{H}_{\text{mb}}$) is the Hamiltonian of the impurity (resp. many-body background) alone, and $\widehat{H}_{\text{int}}$ describes the interaction between the impurity and the fermions. We label the eigenstates of the impurity by their momentum $\mathbf{q}$ and energy $\varepsilon_q^{(i)} = \hbar^2 q^2/2m_i$. The eigenstates and eigenvalues of $\widehat{H}_{mb}$ are noted $|\alpha\rangle$ and E_α, where $\alpha = 0$ corresponds to the ground state of the fermionic background.

We consider a contact interaction between the impurity and the fermions, so the interaction Hamiltonian reads

$$\widehat{H}_{\text{int}} = g_0' \sum_{\sigma=\uparrow,\downarrow} \int d^3\boldsymbol{r}\, \widehat{\psi}_\sigma^\dagger(\boldsymbol{r})\widehat{\psi}_\sigma(\boldsymbol{r})\widehat{\phi}^\dagger(\boldsymbol{r})\widehat{\phi}(\boldsymbol{r}), \tag{6.2}$$

where $\widehat{\psi}_\sigma$ and $\widehat{\phi}$ are the field operators for spin σ particles of the fermionic superfluid and of the impurity respectively. We used the bare coupling constant g_0' between the impurity and the fermions, defined in Chapter 1, linked to the physical coupling constant[1]

[1]We recall $g' = 2\pi\hbar^2 a'/m_r$ with m_r the reduced mass of the impurity and the fermions: $m_r = m_i m_f/(m_i + m_f)$.

g', through the equation:

$$\frac{1}{g'_0} = \frac{1}{g'} - \frac{1}{\Omega}\sum_{k<\Lambda}\frac{1}{\varepsilon_k^{(\mathrm{r})}}, \tag{6.3}$$

with Ω the quantization volume, Λ an ultraviolet cut-off and $\varepsilon_k^{(r)} = \hbar^2k^2/2m_r$, m_r being the impurity-fermion reduced mass. Assuming the contact interaction can be treated perturbatively, in the limit $\Lambda a' \ll 1$, we can expand eq. (6.3) up to second order into

$$g'_0 = g' + \frac{g'^2}{\Omega}\sum_{k<\Lambda}\frac{1}{\varepsilon_k^{(\mathrm{r})}} + o(g'^2). \tag{6.4}$$

Calculating perturbatively the energy of the polaron ΔE_{pert} beyond the mean-field term, we get

$$\Delta E_{\mathrm{pert}} = \langle 0,0|\widehat{H}_{\mathrm{int}}|0,0\rangle + \sum_{\alpha,\boldsymbol{q}}\frac{\left|\langle\alpha,\boldsymbol{q}|\widehat{H}_{\mathrm{int}}|0,0\rangle\right|^2}{E_0 - E_\alpha - \varepsilon_q^{(i)}} \tag{6.5}$$

After expanding the bosonic wavefunctions $\widehat{\phi}$ over plane-wave field-operators, the bosonic part of the equation simplifies into an exponential and the whole expression can be recast as

$$\Delta E_{\mathrm{pert}} = g'n + \frac{g'^2n}{\Omega}\sum_q\frac{1}{\varepsilon_q^{(r)}} + \frac{g'^2}{\Omega^2}\sum_{\alpha,\boldsymbol{q}}\frac{\left|\langle\alpha|\sum_\sigma\int d^3\boldsymbol{r}\widehat{\psi}^\dagger_\sigma(\boldsymbol{r})\widehat{\psi}_\sigma(\boldsymbol{r})e^{-i\boldsymbol{q}\cdot\boldsymbol{r}}|0\rangle\right|^2}{E_0 - E_\alpha - \varepsilon_q^{(i)}}, \tag{6.6}$$

where n is the particle density in the many-body medium.

We define:

$$\rho_{-\mathbf{q}} = \sum_\sigma\int d^3\boldsymbol{r}\widehat{\psi}^\dagger_\sigma(\boldsymbol{r})\widehat{\psi}_\sigma(\boldsymbol{r})e^{-i\boldsymbol{q}\cdot\boldsymbol{r}} \tag{6.7}$$

the Fourier transform of the density operator and also the response function χ:

$$\chi(\boldsymbol{q},E) = \frac{1}{N}\sum_\alpha\frac{|\langle\alpha|\widehat{\rho}_{-\boldsymbol{q}}|0\rangle|^2}{E_\alpha - E_0 + E}. \tag{6.8}$$

The density response function is actually a complex function and contains a $+i0^+$ at its denominator. The real and imaginary parts should satisfy Kramers-Kronig relations.

Using these functions, we can write the energy as

$$\Delta E_{\mathrm{pert}} = g'n + \frac{g'^2n}{\Omega}\sum_{\boldsymbol{q}}\left[\frac{1}{\varepsilon_q^{(\mathrm{r})}} - \chi(\boldsymbol{q},\varepsilon_q^{(\mathrm{i})})\right]. \tag{6.9}$$

6.1.2 Asymptotic limit and structure factor

To get a first glimpse of the behavior of this expression, we study the asymptotic regime of χ for $q \to \infty$. In this limit, the function χ must have a $1/q^2$ dependence to cancel out the one found in the $1/\varepsilon_q^{(r)}$ term.

For large momenta q, the eigenstates of the many-body Hamiltonian excited by the operator $\widehat{\rho}_{\boldsymbol{q}}$ correspond to free-particle excitations of momentum $\boldsymbol{q}$ and energy $\varepsilon_q^{(f)} = \hbar^2q^2/2m_f$. For an ideal Fermi gas, the response function then simplifies into

$$\chi(\boldsymbol{q},E) \simeq \left(\frac{1}{\varepsilon_q^{(f)} + E}\right)\frac{1}{N}\sum_\alpha|\langle\alpha|\widehat{\rho}_{-\boldsymbol{q}}|0\rangle|^2. \tag{6.10}$$

for $q \gg k_F$.

Since we are here interested in a semi-quantitative argument to obtain an asymptotic behaviour of χ, we will extend this expression to the case of an interacting gas, neglecting the fact that the energy of the final state can no longer be considered as fixed but should depend on the interactions.

Let us introduce the static structure factor $S(q)$, defined by

$$S(q) = \frac{1}{N} \sum_{\alpha} |\langle \alpha | \widehat{\rho}_{\boldsymbol{q}} | 0 \rangle|^2 \tag{6.11}$$

The static structure factor characterize two-body correlations of interacting systems. Indeed, in condensed matter systems, it enters in many relations for thermodynamic functions and kinetic coefficients, and more importantly it constitutes a mathematical description of the scattering from a disordered system of neutrons, electrons, photons,... and is thus directly measurable [288, 289]. The static structure factor is linked to the Fourier transform of the density-density response function in the long-wave limit [290], and thanks to the works of Tan giving us the expression for this response function [145], we have an expression of the static structure factor in this limit [158]:

$$S(q) = 1 + \frac{C_2}{4Nq} + o\left(\frac{1}{q}\right), \tag{6.12}$$

with C_2 Tan's contact for two fermions, already introduced in chapter 4, coming from the density-density response function. Hence

$$\chi(\boldsymbol{q}, \varepsilon_q^{(i)}) \underset{q\to\infty}{\simeq} \frac{S(q)}{\varepsilon_q^{(f)} + \varepsilon_q^{(i)}} \simeq \frac{1}{\varepsilon_q^{(r)}} + \frac{C_2}{4Nq\varepsilon_q^{(r)}} + o\left(\frac{1}{q^3}\right). \tag{6.13}$$

The first term in the expansion cancels out with the $1/\varepsilon_q^{(r)}$ coming from the expression of the bare coupling constant, and this should remain true even without making any assumptions on the interactions in the Fermi cloud. Finally, the term inside the sum in the expression of the polaron energy from eq. (6.9) behaves as

$$\frac{1}{\varepsilon_q^{(\mathrm{r})}} - \chi(\boldsymbol{q}, \varepsilon_q^{(\mathrm{i})}) \propto \frac{C_2}{Nq^3}. \tag{6.14}$$

This subdominant term in the expression of χ is only an approximation, and we cannot use the prefactor we would obtain through this calculation, however we consider the general behaviour to be correct, as confirmed by the calculations present in the following sections. As a consequence, the correction to the polaron energy still presents a logarithmic UV-divergence, meaning the regularization of the coupling constant was not enough.

This logarithmic divergence is typical of a singularity in the three-body problem for particles with contact interactions. This characteristic was first discovered by Wu [116] for a system of three bosons and was also investigated in the context of nuclear physics [75] or more recently with cold atoms [117–120]. Therefore, we will now work on the three-body problem to find a solution to renormalize this energy and see how few-body physics will help us regularize this many-body problem.

6.2 Regularization of the three-body scattering amplitude

The general idea is to introduce a three-body interaction to cure the divergence of the perturbative expansion of the polaron energy. In order to do that, one could try calculating the function χ directly and deduce the energy of the polaron. This can be done within the framework of BCS theory for instance as presented in Appendix B, but in the very general case it is much more challenging. Instead, we are going to calculate the three-body scattering amplitude of an impurity and two fermions of opposite spins, which will also lead us to the determination of $g_3(\Lambda)$.

We consider a system of three particles, an $\uparrow$ fermion, a $\downarrow$ fermion and an impurity that we will label as 1, 2 and 3 respectively. The interaction potential $\widehat{V}$ of this system can be written as $\widehat{V} = \widehat{V}_1 + \widehat{V}_2 + \widehat{V}_3$ with $\widehat{V}_i$ the two-body interaction potential between the two particles other than i. Before introducing a three-body interaction, we will first calculate the T-matrix of this system and watch out for logarithmic divergences.

6.2.1 T-matrix in Faddeev's formalism

The T-matrix is a mathematical tool of in scattering theory we introduced in Chapter 1 for a two-body interaction. A three-body T-matrix can also be defined similarly for the three-body scattering problem. Similarly as the two-body T-matrix, it follows the Dyson equation we gave in Chapter 1:

$$\widehat{T} = \widehat{V} + \widehat{V}\widehat{G}_0\widehat{T} \tag{6.15}$$

where $\widehat{V}$ is the potential of interaction for the three bodies and $\widehat{G}_0(z) = (z - \widehat{H}_0)^{-1}$ the resolvent operator for the Hamiltonian $\widehat{H}_0$ of the free particles, with $z = E_0 + i\epsilon$ where E_0 corresponds to the total energy of the three particles, conserved during the scattering process.

Since it obeys this self-consistent equation, the T-matrix can thus be calculated perturbatively writing $\widehat{T} = \widehat{V} + \widehat{V}\widehat{G}_0\widehat{V} + ...$ The goal would then be to obtain the matrix elements to resolve the three-body scattering problem. To simplify this study, we will work within Faddeev's formalism [291]. The principle of this formalism is to write the three-body T-matrix as the sum of three contributions $\widehat{T}_1$, $\widehat{T}_2$ and $\widehat{T}_3$ solutions of the set of coupled equations:

$$\begin{pmatrix} \widehat{T}_1 \\ \widehat{T}_2 \\ \widehat{T}_3 \end{pmatrix} = \begin{pmatrix} \widehat{t}_1 \\ \widehat{t}_2 \\ \widehat{t}_3 \end{pmatrix} + \begin{pmatrix} 0 & \widehat{t}_1 & \widehat{t}_1 \\ \widehat{t}_2 & 0 & \widehat{t}_2 \\ \widehat{t}_3 & \widehat{t}_3 & 0 \end{pmatrix} \widehat{G}_0 \begin{pmatrix} \widehat{T}_1 \\ \widehat{T}_2 \\ \widehat{T}_3 \end{pmatrix} \tag{6.16}$$

where $\widehat{t}_i$ is the two-body T-matrix leaving the particle i unaffected. We will choose for convention that the particles 1, 2 and 3 correspond to the spin-up fermion, the spin-down fermion and the impurity respectively.

By using this formalism, we essentially reduce a three-body problem to a sum of two-body problems. Indeed, we can expand perturbatively the operator $\widehat{T}_1 = \widehat{t}_1 + \widehat{t}_1\widehat{G}_0\widehat{t}_2 + \widehat{t}_1\widehat{G}_0\widehat{t}_3 + ...$ which now only involves the two-body operators $\widehat{t}_i$. This is the same for the three operators $\widehat{T}_i$ and for $\widehat{T} = \widehat{T}_1 + \widehat{T}_2 + \widehat{T}_3$. Each of the terms involved in these expansions can be interpreted as a succession of two-body interactions $\widehat{t}_i$ separated by the free propagation of the particles as in $\widehat{G}_0$. We can note that the contribution $\widehat{T}_i$ to the

T-matrix correspond to the sum of all the terms starting by t_i: it encapsulates all series of interaction/propagation starting with an interaction leaving the particle i unaffected.

Furthermore, Faddeev's formalism also includes a resummation: by construction, the term $\widehat{t}_i\widehat{G}_0\widehat{t}_i$ never appears in the expansions because all the consecutive $\widehat{t}_i$ interactions have been added together. This is actually very important because otherwise these terms would lead to singularities (delta functions), a major issue out of Faddeev's framework.

6.2.2 Diagrammatic representation of the solutions

In the expansion of the T-matrix, we have many terms of the form $\widehat{t}_i$, $\widehat{t}_i\widehat{G}_0\widehat{t}_j$, $\widehat{t}_i\widehat{G}_0\widehat{t}_j\widehat{G}_0\widehat{t}_k$, ... In order to make the resolution more efficient, we represent these different terms as diagrams.

On Fig. 6.3, we show a diagram corresponding to the term $\widehat{t}_1\widehat{G}_0\widehat{t}_3\widehat{G}_0\widehat{t}_2\widehat{G}_0\widehat{t}_3$.

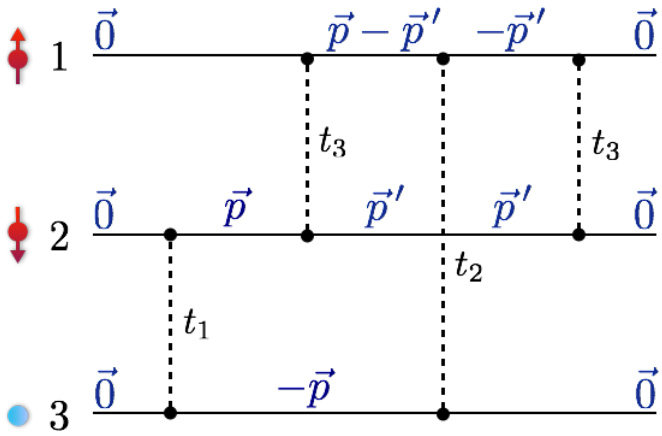

Figure 6.3: Diagrammatic representation of the matrix element $\langle 0|\widehat{t}_1\widehat{G}_0\widehat{t}_3\widehat{G}_0\widehat{t}_2\widehat{G}_0\widehat{t}_3|0\rangle$. Each horizontal solid line corresponds to one of the three particles, each dashed vertical line corresponds to an interaction between the two particles having a black solid circle on their line. The possible momenta are written over the particle lines, we set the initial and final state to zero. Taking into account the boundary conditions, we have here to introduce two independent momenta $\boldsymbol{p}$ and $\boldsymbol{p}'$ over which we need to sum in order to calculate the matrix element.

In this representation, each line corresponds to a particle, here we placed the two fermionic spin states at the top two lines and the impurity at the bottom line. In these diagrams, we will go to the low energy limit where the energy of the initial and final states goes to zero, thus setting their momenta to zero as we did in Fig. 6.3. The different interactions are symbolized by a dashed line with black circles to specify exactly which particles are involved in the interaction. Each time there is an interaction between two particles, momentum is transferred between the two partners, whereas the remaining particle has its momentum unchanged.

To account for this effect while respecting the boundary conditions, we had to introduce two independent momenta $\boldsymbol{p}$ and $\boldsymbol{p}'$ in Fig. 6.3. They can take any value so the term corresponding to this diagram is the sum over these two momenta of the matrix elements

of the operators involved. The entire expression reads

$$\begin{aligned}\langle 0|\widehat{t}_1\widehat{G}_0\widehat{t}_3\widehat{G}_0\widehat{t}_2\widehat{G}_0\widehat{t}_3|0\rangle = \sum_{\boldsymbol{p},\boldsymbol{p}'}\Big[&\langle 0|\widehat{t}_1|\mathbf{0},\boldsymbol{p},-\boldsymbol{p}\rangle\langle \mathbf{0},\boldsymbol{p},-\boldsymbol{p}|G_0(z)|\mathbf{0},\boldsymbol{p},-\boldsymbol{p}\rangle\\ &\langle \mathbf{0},\boldsymbol{p},-\boldsymbol{p}|\widehat{t}_3|\boldsymbol{p}-\boldsymbol{p}',\boldsymbol{p}',-\boldsymbol{p}\rangle\langle \boldsymbol{p}-\boldsymbol{p}',\boldsymbol{p}',-\boldsymbol{p}|\widehat{G}_0(z)|\boldsymbol{p}-\boldsymbol{p}',\boldsymbol{p}',-\boldsymbol{p}\rangle\\ &\langle \boldsymbol{p}-\boldsymbol{p}',\boldsymbol{p}',-\boldsymbol{p}|\widehat{t}_2|-\boldsymbol{p}',\boldsymbol{p}',\mathbf{0}\rangle\langle -\boldsymbol{p}',\boldsymbol{p}',\mathbf{0}|\widehat{G}_0(z)|-\boldsymbol{p}',\boldsymbol{p}',\mathbf{0}\rangle\langle -\boldsymbol{p}',\boldsymbol{p}',\mathbf{0}|\widehat{t}_3|0\rangle\Big]\end{aligned} \tag{6.17}$$

where $|0\rangle$ is the state where the three particle each have a null momentum, corresponding to the limit of low energy, and a state $|\boldsymbol{k}_1,\boldsymbol{k}_2,\boldsymbol{k}_3\rangle$ is a state where particle i has a momentum $\boldsymbol{k}_i$ for $i=1,2,3$. In the remainder of this thesis, we will write $t_1G_0t_3G_0t_2G_0t_1 = \langle 0|\widehat{t}_1\widehat{G}_0\widehat{t}_3\widehat{G}_0\widehat{t}_2\widehat{G}_0\widehat{t}_1|0\rangle$ to lighten slightly the expressions.

This notation is very cumbersome hence the use of diagrams to clarify it. This shows that we have to calculate many matrix elements involving the operator $\widehat{G}_0$ and the operators t_i. For the former, the matrix elements can be written very simply:

$$\langle \boldsymbol{k}_1,\boldsymbol{k}_2,\boldsymbol{k}_3|\widehat{G}_0(z)|\boldsymbol{k}_1,\boldsymbol{k}_2,\boldsymbol{k}_3\rangle = \frac{1}{z-\varepsilon^{(f)}_{k_1}-\varepsilon^{(f)}_{k_2}-\varepsilon^{(i)}_{k_3}} \tag{6.18}$$

On the other hand, for the $\widehat{t}_i$ operators, it is more complicated. We already gave their expression in the first chapter of this thesis in the center-of-frame of the two interacting particles but here we are working in the center-of-mass frame of the three particles. This distinction may appear subtle but requires careful treatment to avoid mistakes.

6.2.3 Calculation of t_i

In Chapter 1, section 1.1.5, we already obtained an expression of its matrix elements $\langle \boldsymbol{k}|\widehat{t}_i|\boldsymbol{k}\rangle$, with $\boldsymbol{k}$ the relative momentum of the two particles in the center-of-mass frame of the two particles.

In this section, we will calculate for instance the matrix elements of the operator $\widehat{t}_1$, leaving particle 1 (corresponding in our convention to the spin-up fermion) unaffected, this time in the center-of-mass frame of the three particles. The calculation method is very much the same as in Chapter 1, since the operator $\widehat{t}_1$ obeys the Dyson equation, involving the interaction potential $\widehat{V}_1$.

To address the difference in reference frame from Chapter 1, we have to describe precisely the quantum states of the particles in the center-of-mass frame of the three particles. The initial state is characterized by the momenta $\boldsymbol{k}_1$, $\boldsymbol{k}_2$ and $\boldsymbol{k}_3$ for the particles 1, 2 and 3 and for the final state we include the symbol ' in the notation. We write $\boldsymbol{K} = \boldsymbol{k}_2 + \boldsymbol{k}_3$ the momentum of the center of mass of particles 2 and 3, conserved during the collision, and $\boldsymbol{k} = \boldsymbol{k}_2 - \boldsymbol{k}_3$ the relative momentum of the two particles. The momentum of particle 1 is also conserved as it is not affected. With these notations, calculating the matrix element $\langle \boldsymbol{k}'_1,\boldsymbol{k}'_2,\boldsymbol{k}'_3|\widehat{t}_1|\boldsymbol{k}_1,\boldsymbol{k}_2,\boldsymbol{k}_3\rangle$ boils down to computing $\langle \boldsymbol{k}_1,\boldsymbol{K},\boldsymbol{k}'|\widehat{t}_1|\boldsymbol{k}_1,\boldsymbol{K},\boldsymbol{k}\rangle$.

The difference of reference frame is solely critical in the calculation of the matrix elements of the propagator $\widehat{G}_0(z)$ of the three particles. The relevant matrix elements of $\widehat{G}_0(z)$ read in this reference frame:

$$\langle \boldsymbol{k}_1,\boldsymbol{K},\boldsymbol{k}''|\widehat{G}_0(z)|\boldsymbol{k}_1,\boldsymbol{K},\boldsymbol{k}''\rangle = \frac{1}{z-E_{\mathrm{cm}}-E_{\mathrm{non}}-\varepsilon^{(r)}_{k''}}, \tag{6.19}$$

where $E_{cm} = \hbar^2 K^2/2(m_i + m_f)$ is the energy of the center of mass of the two interacting particles and $E_{\rm non} = \varepsilon_{k_1}^{(f)}$ is the energy of the non-interacting particle, a fermion in this example.

Finally, after following the same reasoning as in section 1.1.5, we obtain the expression

$$\langle \boldsymbol{k}_1, \boldsymbol{K}, \boldsymbol{k}'|\widehat{t}_1|\boldsymbol{k}_1, \boldsymbol{K}, \boldsymbol{k}\rangle = \frac{g'/\Omega}{1 + ia'\sqrt{\frac{2m_r}{\hbar^2}(z - E_{\rm cm} - E_{\rm non})} + a'^2 \frac{R_e}{a'}\frac{2m_r}{\hbar^2}(z - E_{\rm cm} - E_{\rm non})}. \tag{6.20}$$

where we also included a term involving the resonance range $R_e > 0$.

This expression is the same as the one found in Chapter 1, except for the fact that the total energy of the particles z has to be shifted by the energy of the non-participating particle ($E_{\rm non}$) and the energy of the center-of-mass of the two interacting particles ($E_{\rm cm}$). In the following, we will consider the limit of low energies, which means $\mathrm{Re}(z) \to 0$ but not necessarily the two energies mentioned just before since they are associated with relative momenta in the center-of-mass frame thus can take any value.

By using the exact same reasoning, we can show that $\widehat{t}_2$ is essentially the same as $\widehat{t}_1$ because the interaction between the impurity and the fermions is not spin-dependent and calculate t_3 where we would obtain the same expression but with a, g and m_f instead of a', g' and $2m_r$.

6.2.4 Power counting

The main idea now is to see if some of the diagrams have a logarithmic divergence, similar to the one we found in section 6.1 with our perturbative expansion of the energy.

If we calculate the diagrams using eq. (6.20) for the expression of the $\widehat{t}_i$ operators, there is no divergence. However, this is not in contradiction with the logarithmic divergence we found in the polaron energy in section 6.1 because the divergence appeared when it was calculated perturbatively at the order two in g'. Consequently, we will do the same expansions with the $\widehat{t}_i$ operators for $i = 1, 2$, which writes for $i = 1$ as[2]

$$\langle \boldsymbol{k}_1, \boldsymbol{K}, \boldsymbol{k}'|\widehat{t}_1|\boldsymbol{k}_1, \boldsymbol{K}, \boldsymbol{k}\rangle = \frac{g'}{\Omega}\left(1 - ia'\sqrt{\frac{2m_r}{\hbar^2}(z - E_{\rm cm} - E_{\rm non})} + O(a'^2)\right). \tag{6.21}$$

On the other hand, we keep the full expression for the $\widehat{t}_3$ operators.

Since we want an expansion up to order two in g', we will restrict ourselves to diagrams containing one or two $\widehat{t}_1$ or $\widehat{t}_2$ operators (the operators containing a fermion-impurity interaction). To look for the diverging terms we want to find if some of the diagrams in this Born expansion have the typical behavior $\int \mathrm{d}p/p$.

Let us analyze the general structure of the diagram:

- On the sides, where the momenta of each particle are set to zero, the interaction terms are reduced to a constant since $E_{\rm cm} = E_{\rm non} = 0$.
- Between two successive interactions, we have a propagation term associated with the operator $\widehat{G}_0$ with a general dependence $1/p^2$. If we call N the number of these propagation terms, the total contribution of these terms will be of the order $1/p^{2N}$.

[2] In this expansion, we consider $a' \to 0$ while R_e/a' remains constant, so the term in $a'^2(R_e/a')$ is considered of the order two and does not appear in the expansion of $\widehat{t}_1$ since it would be a third-order term after multiplication by g'.

- The operator $\widehat{t}_3$, if located between two other operators, has a general behavior in $1/p$ due to the term $\sqrt{z - E_{\text{cm}} - E_{\text{non}}}$ at the denominator. If we write k the number of occurrences of these specific terms, their total contribution amounts to $1/p^k$.

- If we have $N + 1$ interactions, thus N propagation terms, we have to introduce in total $N - 1$ different momenta, so the integration is over $\mathrm{d}^{3(N-1)}p \to p^{3N-4}\mathrm{d}p$.

Taking everything into consideration, the term corresponding to a diagram has the asympotic behavior $\int \mathrm{d}p p^{N-4-k}$. The general illustration of this reasoning has been applied to the particular diagram introduced with Fig. 6.3, and it is represented in Fig. 6.4, where we see that the corresponding term was convergent.

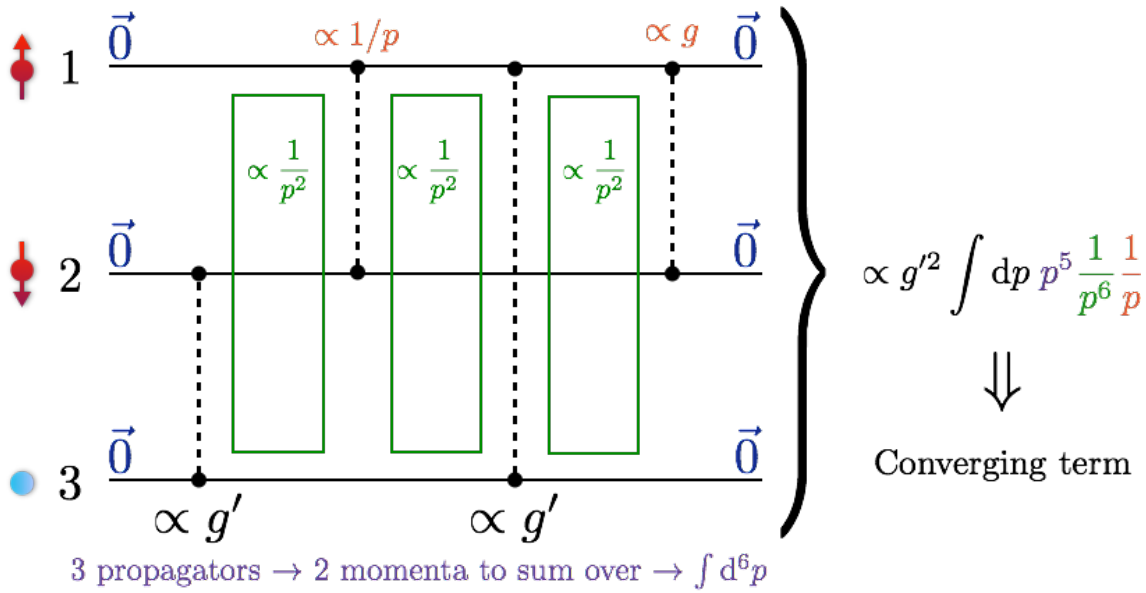

Figure 6.4: Analysis of the convergence of a diagram. In green are given the contributions of the propagators $\widehat{G}_0$, in orange the contributions of the $\widehat{t}_3$ interactions, and in purple the contribution due to the number of independent momenta to sum over. The resulting analysis shows that it is a second order term in g', with no logarithmic divergence.

We first consider the case of a single fermion-impurity interaction, where $\widehat{t}_{1-2}$ is expanded up to order 2 in g'. If it is on the edge, the expansion will only be of the order 1 in g' so it must be in the middle where its contribution to the integral is of the order p. Keeping the same reasoning as before, we must have $N - 4 - k + 1 = -1$ so $N - 2 = k$. With only one fermion-impurity interaction, we must have $k = 0$ so it imposes $N = 2$. This yields two equivalent diagrams, corresponding to the term $\widehat{t}_3\widehat{G}_0\widehat{t}_{1-2}\widehat{G}_0\widehat{t}_3$. Their sum will be written $\widehat{t}_3\widehat{\Gamma}_{\text{I}}\widehat{t}_3$.

In the case of two fermion-impurity interactions, the contribution of the operators $\widehat{t}_{1-2}$ amounts to a constant so in order to have a term that diverges logarithmically, we must have $N - 4 - k = -1$ or again $k = N - 3$. Since the number k' of interactions between fermions and impurity has been set to 2, we can have a maximum of 3 interactions (counting the ones on the sides of the diagram) between two fermions since they cannot be consecutive. This means that the total number of interactions $N + 1$ cannot exceed 5 so $N \leq 4$.

This gives two possibilities: $N = 3$ and $k = 0$ or $N = 4$ and $k = 1$. They correspond to two types of diagrams:

- In the first case, there is a total of four interactions with no fermion-fermion interaction in the center of the diagram. This imposes to have two fermion-impurity interactions at the center and two fermion-fermion interactions on the sides for a total of two equivalent diagrams: $\widehat{t}_3\widehat{G}_0\widehat{t}_{1/2}\widehat{G}_0\widehat{t}_{2/1}\widehat{G}_0\widehat{t}_3$. The total contribution is written $\widehat{t}_3\widehat{\Gamma}_{\mathrm{II}}\widehat{t}_3$.
- In the second case, there are five interactions in total. Since we only consider the case of two fermion-impurity interactions, there are three fermion-fermion interactions. Considering they cannot be consecutive, this yields the only possible sequence: $\widehat{t}_3\widehat{G}_0\widehat{t}_{1-2}\widehat{G}_0\widehat{t}_3\widehat{G}_0\widehat{t}_{1-2}\widehat{G}_0\widehat{t}_3$ corresponding to four equivalent diagrams. Their sum is written $\widehat{t}_3\widehat{\Gamma}_{\mathrm{III}}\widehat{t}_3$

In Fig. 6.5, we represent one example of diagram for each type of diverging term.

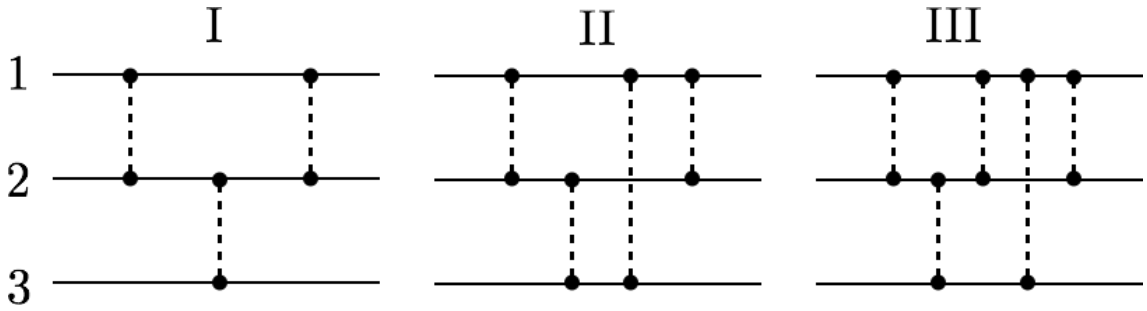

Figure 6.5: Representation of an example of diagram associated with each type of diverging term (I, II and III). Starting from the top, the first line correspond to the $\uparrow$ fermion, the second line to the $\downarrow$ fermion and the last line to the impurity atom. As before, the dashed vertical lines are interactions between the two particles that have a black solid circle on their line.

It can be shown using this line of reasoning that every diagram at the order 2 in g' is not diverging more than logarithmically, which is due to the Faddeev resummation which prevents from having two consecutive interactions that would otherwise lead to strongly diverging terms. We notice that all the diverging terms begin and end with an operator $\widehat{t}_3$, and we write their total contribution as $\widehat{t}_3\widehat{\Gamma}\widehat{t}_3$.

Before going on, we have to remember that Γ is only diverging when we treat the two-body T-matrices perturbatively. We will actually use the notation Γ^{Born} to designate the term calculated at the second order in g' while we will use $\Gamma^{\mathrm{Faddeev}}$ to designate the term corresponding to the same diagrams calculated with the full expression of $\widehat{t}_i$ operators.

6.2.5 Calculation of the diverging term

In this section we will focus on the calculation of $\widehat{\Gamma}$. We can start by expressing the energies E_{cm} and E_{non} that appear in the expression of the t_i matrix elements. For the diagrams we want to calculate, those energies always take the same form because the fermion-impurity interaction always happen right before or right after a fermion-fermion interaction located on the edge of the diagram. Consequently, we only have to consider

the case where the fermions have momenta of $\boldsymbol{p}$ and $-\boldsymbol{p}$ and the impurity has a momentum equal to zero (cf Fig. 6.5). This leads to:

$$E_{\rm non} = \frac{\hbar p^2}{2m_f}, \quad E_{\rm cm} = \frac{p^2}{2(m_f+m_i)} \tag{6.22}$$

$$\frac{2m_r}{\hbar^2}(E_{\rm cm}+E_{\rm non}) = p^2\frac{\eta(2+\eta)}{(1+\eta)^2} \tag{6.23}$$

with $\eta = m_i/m_f$.

Finally, we can write $\widehat{t}_1$ or $\widehat{t}_2$ for the three types of diagram we consider as:

$$\widehat{t}_{1-2} = \frac{g'/\Omega}{1-\sqrt{\frac{\eta(2+\eta)}{(1+\eta)^2}}a'p - \frac{\eta(2+\eta)}{(1+\eta)^2}(\frac{R_e}{a'})(a'p)^2} = \frac{g'}{\Omega}t(p) \tag{6.24}$$

Then, we can write below the expressions corresponding to each of the diverging terms.

$$\Gamma_{\rm I} = 2\frac{m_f^2}{\hbar^4}\frac{g'}{\Omega}\sum_{\boldsymbol{p}}\frac{1}{p^4}t(p) \tag{6.25}$$

$$\Gamma_{\rm II} = -2\frac{m_f^3}{\hbar^6}\frac{g'^2}{\Omega^2}\sum_{\boldsymbol{p_1},\boldsymbol{p_2}}\frac{1}{p_1^2p_2^2}\frac{t(p_1)t(p_2)}{(p_1^2+p_2^2)(\frac{\eta+1}{2\eta})-\frac{1}{\eta}\vec{p_1}.\vec{p_2}} \tag{6.26}$$

$$\Gamma_{\rm III} = 4\frac{m_f^3}{\hbar^6}\frac{g'^2}{\Omega^3}\sum_{\boldsymbol{p_1},\boldsymbol{p_2},\boldsymbol{p_3}}\left[\frac{1}{p_1^2p_3^2}\frac{4\pi}{1/a-p_2\sqrt{\frac{\eta+2}{4\eta}}}\frac{t(p_1)}{p_1^2+p_2^2(\frac{\eta+1}{2\eta})-\vec{p_1}.\vec{p_2}}\frac{t(p_3)}{p_3^2+p_2^2(\frac{\eta+1}{2\eta})-\vec{p_3}.\vec{p_2}}\right] \tag{6.27}$$

To calculate the Faddeev term for Γ, one has to use the full expression of $t(p)$ that was given in eq. (6.24). Concerning the Born term, one has to expand the expression of $t(p)$ up to first order in a' for $\Gamma_{\rm I}$ and just replace it by 1 for the other two components, so that all three components of Γ are expanded up to order two in a'. Besides, for the term $\Gamma^{\rm III}$, we calculate the sum in the limit $1/a \ll 1/a'$ (strongly interacting fermions), in which case the difference between the Faddeev term and the Born term does not depend on a.

To calculate these different sums we go the continuous limit and replace the sums by integrals. We write these integrals in the case of the Born approximation, the idea will be exactly the same for the Faddeev terms.

$$\Gamma_{\rm I}^{\rm Born} = 2\frac{m_f^2}{\hbar^4}g'\int\frac{{\rm d}^3p}{(2\pi)^3}\frac{1}{p^4}(1+a'\sqrt{\frac{\eta(2+\eta)}{(1+\eta)^2}}p) = {\rm Cst} + \frac{m_f^3}{\hbar^6}g'^2\kappa_{\rm I}(\eta)\int\frac{{\rm d}p}{p} \tag{6.28}$$

$$\Gamma_{\rm II}^{\rm Born} = -\frac{m_f^3}{\hbar^6}g'^2\frac{\eta}{8\pi^4}\int\frac{{\rm d}p_1}{p_1}\int\frac{{\rm d}p_2}{p_2}\ln\left(\frac{(p_1^2+p_2^2)(\frac{\eta+1}{2\eta})+\frac{1}{\eta}p_1p_2}{(p_1^2+p_2^2)(\frac{\eta+1}{2\eta})-\frac{1}{\eta}p_1p_2}\right) \tag{6.29}$$

$$\Gamma_{\rm III}^{\rm Born} = -\frac{m_f^3}{\hbar^6}g'^2\frac{1}{2\pi^5}\sqrt{\frac{4\eta}{2+\eta}}\int\frac{{\rm d}p_2}{p_2}\left[\int\frac{{\rm d}p_1}{p_1}\ln\left(\frac{p_1^2+p_2^2(\frac{\eta+1}{2\eta})+p_1p_2}{p_1^2+p_2^2(\frac{\eta+1}{2\eta})-p_1p_2}\right)\right]^2 \tag{6.30}$$

where we performed the angular integrations (yielding the logarithms). The last term involves the square of an integral because the integrals over the momentum p_1 and p_3 are exactly the same.

From these equations, we conclude readily that all three terms diverge logarithmically and we can write

$$\Gamma^{\mathrm{Born}} \underset{\Lambda\to\infty}{\sim} \frac{m_f^3}{\hbar^6} g'^2 \kappa(\eta) \ln\Lambda \tag{6.31}$$

where $\kappa(\eta)$ is a constant, sum of the contributions of the three terms constituting Γ^{Born}, which reads

$$\kappa(\eta) = \frac{\sqrt{\eta^3(\eta+2)}}{2\pi^3(\eta+1)^2} - \frac{\eta}{2\pi^3}\arctan\left(\frac{1}{\sqrt{\eta(\eta+2)}}\right) - \frac{4}{\pi^3}\sqrt{\frac{\eta}{\eta+2}}\arctan\left(\sqrt{\frac{\eta}{\eta+2}}\right)^2. \tag{6.32}$$

For an impurity as massive as the fermions ($\eta = 1$), we obtain

$$\kappa(1) = \frac{\sqrt{3}}{8\pi^3} - \frac{1}{12\pi^2} - \frac{1}{9\pi\sqrt{3}} \simeq -0.0219, \tag{6.33}$$

and for a ^{6}Li-^{7}Li Bose-Fermi mixture, we have $\kappa(7/6) \simeq -0.025$.

Since $\Gamma^{\mathrm{Faddeev}}$ does not diverge at all, we can introduce a three-body characteristic length R_3 defined by

$$\Gamma^{\mathrm{Born}} - \Gamma^{\mathrm{Faddeev}} \underset{\Lambda\to\infty}{=} \frac{m_f^3}{\hbar^6} g'^2 \kappa(\eta) \ln(\Lambda R_3) + o(1), \tag{6.34}$$

One could notice that the integrals we gave for the different terms of Γ^{Born} were divergent in $p = 0$. The integrals for $\Gamma^{\mathrm{Faddeev}}$ actually present the exact same divergences so we can calculate numerically the difference between the two terms without any problem, which allows us to get the value of R_3 (see appendix D). In this perturbative approach, R_3/a' only depends on the mass ratio η and R_e/a'.

6.2.6 Three-body contact interaction

To cure the divergence of Born's expansion, we now introduce a three-body hamiltonian $\widehat{H}_{3b}$ containing a three-body contact interaction that will contribute to the total energy of the polaron and regularize it. It reads in the most general way

$$\widehat{H}_{3b} = g_3(\Lambda) \int d^3\boldsymbol{r}\, \widehat{\psi}_1^\dagger(\boldsymbol{r})\widehat{\psi}_2^\dagger(\boldsymbol{r})\widehat{\psi}_3^\dagger(\boldsymbol{r})\widehat{\psi}_3(\boldsymbol{r})\widehat{\psi}_2(\boldsymbol{r})\widehat{\psi}_1(\boldsymbol{r}), \tag{6.35}$$

This technique follows the effective field theory approach discussed in [120].

The diagram corresponding to the three-body interaction is given in Fig. 6.6: it is built similarly as the other ones, beginning and ending with a fermion-fermion interaction, with a three-body contact interaction in-between.

Following the calculation principles laid out in the previous paragraph, the diagram can be written as $t_3\Gamma^{3b}t_3$ with

$$\Gamma^{3b} = \frac{1}{\Omega^2}\sum_{\boldsymbol{p},\boldsymbol{p}'} \frac{-1}{2\varepsilon_p^{(f)}}\frac{-1}{2\varepsilon_{p'}^{(f)}} g_3(\Lambda) = g_3(\Lambda)\left(\frac{1}{\Omega}\sum_{\boldsymbol{p}}\frac{1}{2\varepsilon_p^{(f)}}\right)^2 \tag{6.36}$$

In this expression, we have the square of a highly divergent sum[3] contained by its prefactor $g_3(\Lambda)$.

[3] This also shows what would happen if we had terms with the same interaction successively: we would get the same divergent sums but without the factor $g_3(\Lambda)$ to tame them.

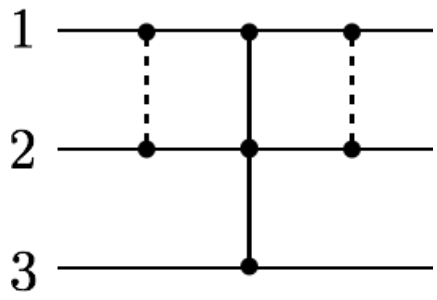

Figure 6.6: Diagram containing the three-body contact interaction where the three particle lines cross at the same point. The fermions correspond again to the top two lines and the impurity to the bottom line.

Using this three-body interaction to regularize the logarithmic divergence in Γ^{Born}, we must have $\Gamma^{\mathrm{Born}} + \Gamma^{3b} = \Gamma^{\mathrm{Faddeev}}$. Combining this equation with eq. (6.34) yields:

$$g_3(\Lambda)\left(\frac{1}{\Omega}\sum_{\boldsymbol{p}}\frac{1}{2\varepsilon_p^{(f)}}\right)^2 = -\frac{m_f^3}{\hbar^6}g'^2\kappa(\eta)\ln(\Lambda R_3). \tag{6.37}$$

6.3 Renormalization of the polaron energy

6.3.1 Expression of the polaron energy

We can now evaluate the contribution ΔE_{3b} to the energy of the polaron. This first-order (in $g_3(\Lambda)$) perturbative expansion of this three-body energy reads

$$\Delta E_{3b} = \langle 0, \mathbf{0}|\widehat{H}_{3b}|0, \mathbf{0}\rangle = \frac{g_3(\Lambda)}{\Omega}\langle 0|\int d^3\boldsymbol{r}\ \widehat{\psi}_\uparrow^\dagger(\boldsymbol{r})\widehat{\psi}_\downarrow^\dagger(\boldsymbol{r})\widehat{\psi}_\downarrow(\boldsymbol{r})\widehat{\psi}_\uparrow(\boldsymbol{r})|0\rangle \tag{6.38}$$

where we labeled $|0, \mathbf{0}\rangle$ the state where the impurity is in the state $\boldsymbol{k} = \mathbf{0}$ and the fermions are in their ground state. The right hand side term can also be written with the hamiltonian of the many-body background. Indeed,

$$\langle 0|\int d^3\boldsymbol{r}\ \widehat{\psi}_\uparrow^\dagger(\boldsymbol{r})\widehat{\psi}_\downarrow^\dagger(\boldsymbol{r})\widehat{\psi}_\downarrow(\boldsymbol{r})\widehat{\psi}_\uparrow(\boldsymbol{r})|0\rangle = \langle 0|\frac{\partial \widehat{H}_{mb}}{\partial g_0}|0\rangle \tag{6.39}$$

where g_0 is the bare coupling constant for the fermion-fermion interaction.

Using Hellman-Feynman's theorem, and noting E_0 the energy of the ground state of the Fermi ensemble, we can write:

$$\Delta E_{3b} = \frac{g_3(\Lambda)}{\Omega}\frac{\partial E_0}{\partial g_0} = \frac{g_3(\Lambda)}{\Omega}\frac{1}{g_0^2}\frac{\partial E_0}{\partial(1/g_0)} \tag{6.40}$$

$$\Delta E_{3b} \simeq \frac{g_3(\Lambda)}{\Omega}\left(\frac{1}{\Omega}\sum_{k<\Lambda}\frac{1}{2\varepsilon_k^{(f)}}\right)^2\frac{\partial E_0}{\partial(1/g)} \tag{6.41}$$

where we used the relation between the bare coupling g_0 and the physical coupling g, equivalent to (eq. 6.3), and the fact that E_0 only depends on g and not g_0. By using eq.

(6.37), as well as the adiabatic sweep theorem we presented in Chapter 2, we can finally write

$$\Delta E_{3b} = -\frac{m_f C_2}{\hbar^2 \Omega} g'^2 \kappa(\eta) \ln(\Lambda R_3) \tag{6.42}$$

We now add this term to the energy $\Delta E_{\rm pert}$ calculated perturbatively, which yields the energy ΔE of the polaron

$$\Delta E = g' n \left[1 + k_F a' F\left(\frac{1}{k_F a}\right) - 2\pi \frac{m_{\rm f}}{m_{\rm r}} \kappa(\eta) \frac{a' C_2}{N} \ln(k_F R_3) + ... \right], \tag{6.43}$$

with

$$F\left(\frac{1}{k_F a}\right) \underset{\Lambda\to\infty}{=} \frac{2\pi}{k_F} \left[\frac{\hbar^2}{m_{\rm r}} \int_{q<\Lambda} \frac{d^3\boldsymbol{q}}{(2\pi)^3} \left(\frac{1}{\varepsilon_q^{(\rm r)}} - \chi(q, \varepsilon_q^{(\rm i)}) \right) - \frac{m_{\rm f}}{m_{\rm r}} \kappa(\eta) \frac{C_2}{N} \ln(\Lambda / k_F) \right]. \tag{6.44}$$

Since we work in a regime where the polaron is the ground state and there are no Efimov trimers, this regularization scheme is sufficient and we do not need to use non-perturbative approaches involving Efimov physics, that would otherwise lead to a log-periodic dependence of the three-body observables of the system [292].

The last two equations show that the second order correction to the polaron energy can be written as the sum of two contributions: a first term which is regular and characterized by the function F defined in eq. (6.44) and a second term, involving the logarithm of R_3 and proportional to the contact C_2. This expression bridges between the Fermi polaron on the BCS side and the Bose polaron on the BEC side, on the condition of knowing the F function, which is investigated in the next paragraph.

6.3.2 The F function: Asymptotic expansions

On the BCS limit, when the fermions are weakly interacting, we have to recover the Fermi polaron problem that was investigated in Chapter 2, section 2.5.2, with a factor 2 due to the two spin states. In this limit, $C_2 \propto a^2 \to 0$, so the only term from eq. (6.44) that remains is the one with the F function. For the case $\eta = 1$, we can deduce

$$F\left(\frac{1}{k_F a} \to -\infty\right) = \frac{3}{2\pi} \tag{6.45}$$

Far in the BEC domain, the fermions pair up to form dimers and condense into a weakly interacting BEC. The polaron energy must take the mean-field form $\Delta E_{\rm BEC} = g_{ad} n/2$ where g_{ad} is the impurity-dimer s-wave coupling constant and $n/2$ the dimer density. In particular, the expression of the energy does not depend directly on k_F. Since in the BEC limit, the contact reads $C_2/N = 4\pi/a$, we must have

$$F\left(\frac{1}{k_F a}\right) \underset{a\to 0^+}{=} 8\pi^2 \kappa(\eta) \frac{m_f}{m_r} \frac{1}{k_F a} \left(\ln(k_F a) + C_{ad} \right) + ... \tag{6.46}$$

with then

$$g_{ad} = 2g' \left[1 - 8\pi^2 \kappa(\eta) \frac{m_f}{m_r} \frac{a'}{a} \left(\ln(R_3/a) + C_{ad} \right) + ... \right] \tag{6.47}$$

where C_{ad} is a constant that depends on the mass ratio η, which can be obtained from the analysis of the atom-dimer scattering problem (see Appendix D).

This equation also sheds new light on the range of validity of our perturbative expansion: in addition to the diluteness assumption $k_F|a'| \ll 1$ and the condition $|a'| \lesssim R_e$, our expansion is only valid for $|a'|/a \ll 1$ when $a > 0$. It may seem odd that this condition only appears on the BEC side ($a > 0$), but it is due to the fact that the energy of the Fermi gas on the BCS side converges towards a constant in this limit (and the contact vanishes), whereas it becomes increasingly important as we go in the BEC limit (also true for the contact), so there is no need for such a condition on the BCS side. Under this assumption, the atom-dimer coupling given in eq. (6.47) does not diverge when $a \to 0$ since $|a'|/a$ remains small.

The result we obtained in Eq. (6.43) for the energy of the polaron can be used to benchmark approximation schemes addressing this problem. We will present a few of them in the next section.

6.3.3 Comparison with other theories

Polaron problem within BCS theory framework

Using a standard BCS approach, we obtain the same form for the energy of the polaron, but with a different prefactor κ (see Appendix B). Indeed, the value κ^{MF} obtained with BCS theory corresponds to the first two terms of the true constant κ, excluding the contribution from diagrams with a fermion-fermion in the middle. This can be perfectly understood since BCS theory excludes interactions between the Bogoliubov excitations of the superfluid which only appeared in the third type of diagrams. For $\eta = 1$, we have $\kappa/\kappa^{\mathrm{MF}} \simeq 15$, showing that BCS theory fails to evaluate those beyond mean-field corrections.

It is easy to compute the F function with BCS theory and our numerical calculations are represented in Fig. 6.7. We recover the expected BCS limit while on the BEC side we get a logarithmic behaviour with the wrong prefactor.

6.3.4 The atom-dimer scattering problem

Our work also gives a value for the impurity-dimer scattering length a_{ad}. It can be obtained from g_{ad} using the formula $g_{ad} = 2\pi\hbar^2 a_{ad}/m_{ad}$ with $m_{ad} = m_f(2\eta/\eta + 2)$ the impurity-dimer reduced mass. This yields the result

$$a_{ad} = a_{\mathrm{Born}} \left(1 - 8\pi^2 \kappa(\eta) \frac{m_f}{m_r} \frac{a'}{a} \left(\ln(R_3/a) + C_{ad} \right) + ... \right) \tag{6.48}$$

with $a_{\mathrm{Born}}/a' = 4(1+\eta)/(2+\eta)$.

This was compared directly to numerical calculation reported in [293] where the authors solved Skorniakov-Ter Markirosian's equations for this problem. The comparison between numerics and our analytical results are shown in Fig. 6.8, where we see that the two are indeed in very good agreement. The small discrepancy (there is a maximum of 15% difference on an already small ($\sim 10\%$) correction) can be explained due to the fact that in [293] a UV cutoff Λ was used to regularize the equations with Λ between $2/a'$ and $8/a'$, rather different from our method. This cutoff could be somehow compared to the inverse range $1/R_e$ in our calculations but there is actually no direct quantitative way to compare our regularization schemes, so we simply decided to take $R_e = 0$ for the curves in Fig. 6.8.

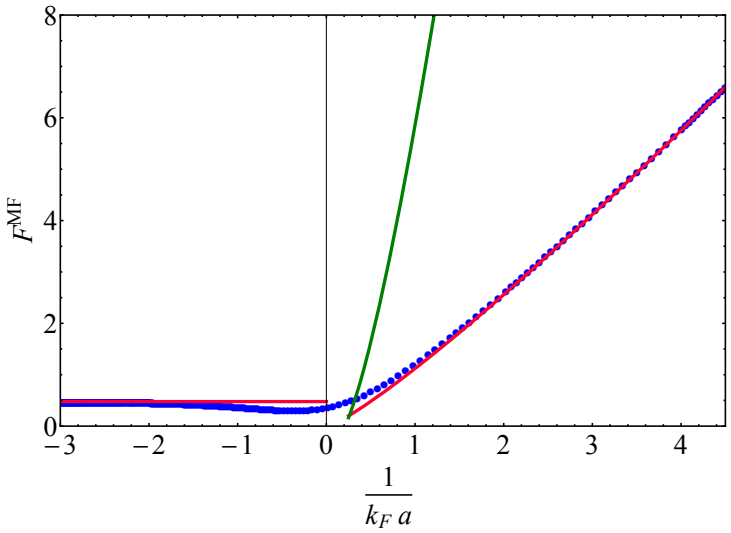

Figure 6.7: Representation of the F function calculated numerically using BCS Theory. Blue circles: numerical data points. Red curve on the negative side: BCS limit with $F(-\infty) = 3/2\pi$. Red curve on the positive side: BEC limit given by eq. (6.46) with κ^{MF} as the proportionality constant. Green curve: same limit but using the real κ constant instead. We see that BCS theory fails to give a quantitative result for the F function on the BEC side but gives the right qualitative behavior.

6.3.5 Infinite-mass impurity

When m_i goes to infinity, $\varepsilon_q^{(i)} \to 0$ and $\chi(\boldsymbol{q}, \varepsilon_q^{(i)}) = \chi(\boldsymbol{q}, 0)$ is given directly by the static response of the superfluid. In our case, we do not have an exact expression of χ but for equation (6.44) to actually converge, it must have the asymptotic behavior:

$$\chi(\boldsymbol{q}, \varepsilon_q^{(i)}) = \frac{1}{\varepsilon_q^{(r)}} \left[1 - \pi^2 \kappa(\eta) \frac{m_f}{m_r} \frac{C_2}{Nq} \right] \tag{6.49}$$

In the case where $m_i \to +\infty$, we have $m_r \to m_f$ and $\eta \to \infty$. Using the full expression of κ, we also have $\kappa(\infty) = -1/4\pi$. This gives the equation:

$$\chi(\boldsymbol{q}, 0) = \frac{1}{\varepsilon_q^{(f)}} \left[1 + \frac{\pi}{4} \frac{C_2}{Nq} \right] \tag{6.50}$$

This result is in total agreement with the expression derived in [294] using operator product expansion. We can also notice that the BCS theory would not have agreed with this independent result since $\kappa^{\mathrm{MF}}(\infty) = 0$.

To sum up, our beyond mean-field correction of the polaron energy is confirmed by independent theoretical approaches. In the last paragraph, we will apply these corrections to the problem we studied in the previous chapter and see how our correction can help us get percent-level agreement between experiment and theory.

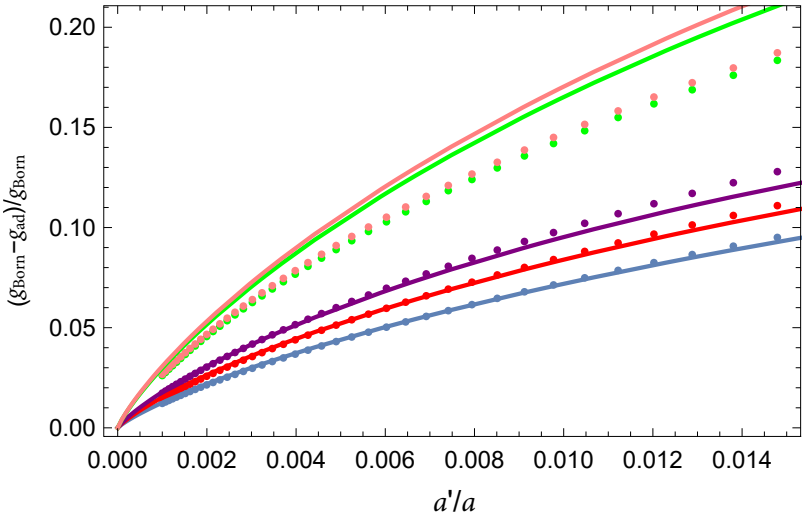

Figure 6.8: Representation of the correction to the atom-dimer coupling constant beyond Born's approximation, as a function of a'/a, for different mass ratios, compared to the results given in [293]. Data points: numerical calculations from [293]. The colors correspond to different experimentally relevant mass ratios, from bottom to top: $\eta = 7/40$ (blue), $\eta = 23/40$ (red), $\eta = 7/6$ (purple), $\eta = 87/6$ (green), $\eta = 133/6$ (orange). Solid curves: asymptotic results from eq. (6.47), where R_3 and C_{ad} are computed numerically and given in appendix D, in the case $R_e = 0$. The small discrepancy at large η is probably due to the finite range $R_e \lesssim a'$ used in [293] to regularize the three-body problem.

6.4 Consequences on the experiment: frequency shift corrections

In this section, we study the effect of this energy correction on the frequency shift measured in the counterflow experiment in the previous chapter.

First, we have to address a major difference between the situation in our experiment and the problem that was studied in this chapter. Indeed, in our experiment we do have $|a'| \ll a$ but $a' > 0$. According to the phase diagram, we should be in the dimeron phase where dimers made of an impurity atom and a fermion should form. However, in Chapter 5, we detected no such dimeron; instead we observed the counterflow of the impurity and the Fermi superfluid. This means that in our set-up, the system is not in its ground state (dimeron phase) but more so in an excited state, such as the repulsive branch of the polaronic state that was introduced in Chapter 2.

We will then make the assumption that the asymptotic behavior ($|a'| \to 0$) of the attractive branch $a' < 0$ is the same as that of the repulsive branch ($a' > 0$), and use the same expansion of the polaron energy, simply with $a' > 0$.

We recall that the formula giving the frequency shift in the counterflow experiment reads

$$\frac{\delta\omega_b}{\omega_b} = -\frac{1}{2}\frac{\mathrm{d}E_{bf}}{\mathrm{d}n_f}\left.\frac{\mathrm{d}n_f}{\mathrm{d}\mu_f}\right|_0 . \tag{6.51}$$

In the mean-field approximation, we simply took $E_{bf} = g_{bf}n_f$ which gave the theoretical curve we presented in section 5.2.2. We will discuss in this section the effect of the beyond mean-field terms. Other corrections to this formula have also been evaluated

such as the back-action of the impurity on the fermions or the second-order term of the expansion used to obtain eq. 6.51, but they were both assessed to be under 1% of the shift value, negligible compared to the corrections we are going to present. We are going to evaluate

$$\beta = \frac{(\delta\omega_b/\omega_b) - (\delta\omega_b/\omega_b)^{\mathrm{MF}}}{(\delta\omega_b/\omega_b)^{\mathrm{MF}}} \tag{6.52}$$

the correction to the mean-field relative shift noted $(\delta\omega_b/\omega_b)^{\mathrm{MF}}$.

6.4.1 BCS side

Far on the BCS side, we have $C_2 \propto a^2 \to 0$, and the function F converges to the constant value $3/2\pi$, and $F'(-\infty) = 0$. The correction then corresponds to the already known Fermi polaron correction, which reads here

$$\beta = \frac{3}{2\pi} k_F a' \tag{6.53}$$

Using this equation we get $\beta(-\infty) \simeq +0.5\%$, too small to be measured with our current set-up.

6.4.2 BEC side: corrections to the atom-dimer scattering length

On the far BEC side, fermions form dimers and the energy takes the form $\Delta E_{\mathrm{BEC}} = g_{ad} n/2$. In the mean-field approximation, we have $g_{ad} n/2 = g' n$ and we recover the usual result. Here, we obtained a beyond mean-field correction to g_{ad}, which can be used to obtain

$$\beta = -8\pi^2 \kappa(\eta) \frac{m_f}{m_r} \frac{a'}{a} \left(\ln(R_3/a) + C_{ad}\right) + ... \tag{6.54}$$

We cannot really use our data points to confirm this formula because the furthest we went on the BEC side was about $1/k_{F,h}|a| = 0.7$ with $k_{F,h}$ the Fermi wavevector calculated in the harmonic trap (defined in section 3.8.2). If that formula was correct for this data point, we would get a correction of $\beta \simeq -5\%$ which remains within the error bars of this data point. We took $R_e = a'$ for this evaluation.

If we managed to take data points further on the BEC side, for instance on the theoretical phase separation limit (see Chapter 3), we would have $1/k_{F,h}|a| = 1.6$, $a'/a \simeq 0.016$, so we would be in the right regime and the correction would be of the order $\beta \simeq -9\%$.

6.4.3 Unitarity: interactions with the many-body background

At unitarity, we have to use the full expression of the energy ΔE we gave in eq. (6.43). After some straightforward calculation, we obtain

$$\beta = \frac{4}{3} k_F a' \left(F(0) - 2\pi\kappa(\eta) \frac{m_f}{m_r} \frac{6\pi\zeta_c}{5} \left(\ln(k_F R_3) + \frac{1}{4} \right) \right). \tag{6.55}$$

However, we do not know the F function at unitarity. To get an estimation nevertheless, we can use the value obtained with BCS theory, corresponding to the function represented in Fig. 6.7. This value gives $F(0) = 0.4$ which is negligible compared to the other term containing the logarithm. Considering that it is still the case with the real

expression of F, we can estimate a correction of $\beta = -5\%$ on the value of the frequency shift.

This is interesting because in the previous chapter, in section 5.2.2, we had two calculated results at unitarity. The first one corresponded to the equation of state (solid curve) measured in our lab but which gives a value for the Bertsh parameter of $\xi \simeq 0.41$ higher than the more accepted value measured at MIT of $\xi = 0.376$ corresponding to the second theoretical comparison made, represented by the triangle.

Our data point at unitarity matches very well with our measurement of the EoS but was not matching within error bars with the theoretical point using MIT data. If we apply this -5% correction to each theory, they both match with the data point within error bars.

Conclusion

In this chapter, we have studied the physics of an impurity immersed in a Fermi superfluid. After discussing the three possible phases of this system, we focused on the polaron phase, more affected by many-body physics. We evaluated the polaron energy up to second order in g', the impurity-fermion coupling constant, and revealed a logarithmic singularity that we regularized by encapsulating three-body interactions within a field theoretical approach. This work unifies the framework between the Fermi polaron and the Bose polaron, in particular with the F function from eq. (6.44) that encompasses the physics of this crossover. Finally, we compared our theory to independent theoretical studies, confirming our results, and we also evaluated the impact of these corrections to the interaction energy on the counterflow experiment performed in this group.

To observe stronger experimental effects of this correction with our experimental set-up, we have essentially two possibilities.

The first one is to go as far as possible on the BEC side to increase the ratio a'/a by decreasing a. This is challenging experimentally, because the further we go on the BEC side, with $a \to 0$, the stronger the dimer-dimer losses become ($\gamma \propto a^{-2.55}$ [130]) and it becomes harder to maintain a Fermi superfluid.

A second option would be to simply increase a' to enhance the impact of the corrective term across the whole crossover. In order to do that, we would need to use different internal states for our atoms, so that we get a Feshbach resonance between the impurity and the fermions. While it may rise new questions such as having two different values of a' for the interaction with each spin state, this would be a very interesting study to conduct with our set-up.

A theoretical extent of this work would be to obtain a correction valid for $a' \gtrsim a$, to be able to explore further on the BEC side, where dimers are tightly bound.

In our approach, we regularize the three-body problem by looking at the perturbative expansion of the polaron energy (or equivalently the parameter Γ) and by using it to deduce $g_3(\Lambda)$. Once we obtained $g_3(\Lambda)$, we derived the renormalization of the energy and the atom-dimer scattering length, using that we should have $E = g_{ad} n_d$ on the BEC side. A consequence of our regularization scheme is that this approach is limited to values $|a'| \ll a$ when $a > 0$, as we explained in section 6.4.2.

However, instead of regularizing the problem using the polaron energy, we could use the atom-dimer scattering length. Assuming we would have calculated a_{ad} (or equivalently g_{ad}) independently, we would obtain another expression for $g_3(\Lambda)$. The polaron

energy would then be deduced from the regularized $g_{ad}n_d$. This would then be valid as long as we have dimers, meaning for $a > 0$. This second method for regularization would then extend our calculation of the polaron energy for $a' \gtrsim a$.

The validity domain for these two approaches are represented in Fig. 6.9. We can see that they have an area of validity in common over which both expression of $g_3(\Lambda)$ must have the same asymptotic behavior.

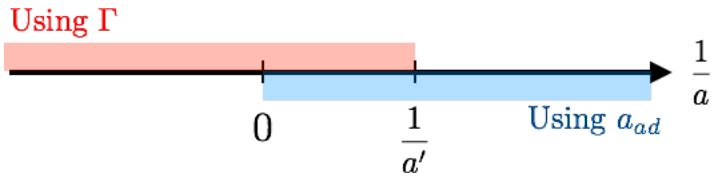

Figure 6.9: Validity domains of two possible regularization approaches to determine g_3. Red: validity domain for a regularization using Γ calculated perturbatively, as it was performed in this thesis. Blue: validity domain for a regularization using a_{ad}

In the regime of deeply bound dimers, this problem could become similar to that of an impurity interacting with two bosons (each boson corresponding to a dimer) that has been studied in [195] where a logarithmic singularity was also observed. Comparing our problem to this one would give yet another confirmation of our theory, and it may be further studied by our group in the future.

Conclusion

Summary

In this thesis, we studied experimentally and theoretically the physics of an impurity immersed in a Fermi superfluid, in the BEC-BCS crossover. A common feature of these investigations is that they are always twofold: while we uncover the properties of the impurity and its interactions with the many-body background, the impurity probes the properties of the many-body background itself, sometimes inaccessible to other investigation methods.

In Chapter 4, the measurement of the lifetime of the impurity acted as a probe of short range correlations of the medium and gave us access to the contact parameter. Our measurement of the two-body fermionic contact at unitarity showed a $n^{4/3}$ dependence, whose fractional exponent is a signature of many-body effects.

In Chapter 5, the measurement of the frequency shift of the oscillations of the impurity informed us on the interactions between the impurity and the superfluid and provided a check on the Equation of State of the Fermi gas in the crossover at the same time. Furthermore, for oscillations at high amplitudes, we observed a damping that can be explained by introducing the notion of critical velocity, whose value is related to the dispersion relation of the elementary excitations of the system.

Finally, in Chapter 6, we studied the system of an impurity immersed in a Fermi superfluid and we calculated perturbatively its energy beyond the mean-field approximation that was used in the previous chapters. After regularizing the second-order term by introducing a three-body interaction, we obtained an expression of the energy bridging between the Fermi polaron on the BCS side and the Bose polaron on the BEC side. This expression of the energy can be used to refine the quantitative analyses of our experimental results: for instance, in the measurement of the frequency shift, due to this calculation we expect a 5% shift at unitarity, which is measurable experimentally. Consequently, this beyond mean-field calculation is needed to achieve percent-level agreement between experiment and theory, sought in many-body physics.

Theoretical extensions

Calculations beyond our approximations

The second-order perturbative calculation of the polaron energy we presented is valid under a few assumptions, all regarding the impurity-fermion interaction. Indeed, we must have $|a'| \ll a$, $a' \ll R_e$ and $k_F a' \ll 1$.

Concerning the first approximation we listed, a first theoretical extension we can consider is the one we already discussed in the conclusion of the former chapter: regularizing

the divergence of the polaron energy by using the atom-dimer problem in order to have an expression valid for all values of $a > 0$, and connect with the calculations made in [195] for three bosons.

When $a' \gtrsim R_e$, there is the polaron/trimeron transition, expected to be a smooth crossover [287]. To address it, we would need to come up with a variational scheme including Efimov physics and independent of assumptions made on the many-body background, which constitutes a great theoretical challenge.

Finally, in order to go beyond the perturbative approach in general, we would need to calculate the many-body diagrams of the system instead of three-body diagrams. This is a current project led by X. Leyronas. Another possibility is to evaluate the dynamical response function $\chi(\boldsymbol{q}, \omega)$, as it was done using Random Phase Approximation in [273].

Interactions between polarons

In our experiment, we cannot have only one impurity atom immersed in a Fermi sea as we considered in our theoretical calculations, but we always have a cloud with many impurities. Hence, the importance of the interactions between impurities and more generally the collective behaviour of the bosons sometimes had to be taken into account to interpret our experimental results. For instance, in Chapter 5, in order to evaluate the critical velocity we considered a model taking into account the excitations that can arise in the Bose gas, and the superfluidity of the Bose gas was necessary to explain the low damping of the oscillations for temperatures at which the Fermi gas was no longer superfluid. Therefore, an extension of our calculation of the polaron energy would be to include the case of multiple impurities, taking into account the possible interaction between polarons.

In the case of two impurities in a Bose-Einstein condensate, the two polarons can bind together and form a Bipolaron [295]. For more impurities in a Fermi sea, we already presented in chapter 2 the theory of the partially polarized Fermi gas, interpreted as a gas of polarons. We also gave the EoS of this system:

$$E = \frac{3}{5} N_\uparrow E_{F_\uparrow} \left[1 - \frac{5}{3} A x + \frac{m}{m^*} x^{5/3} + F x^2 + ... \right] \tag{6.56}$$

where the term Fx^2 accounts for the interaction between polarons. The interactions between polarons will depend on the interactions between the fermions of the background, and bridging between the Fermi polaron and the Bose polaron will be once again required.

The study of many impurities immersed in a Fermi sea would enable us to have a full description of our experimental system, and constitutes a great challenge.

In the last section, we discuss the possible experimental extensions of this thesis.

Experimental outlook

The first experimental extension of this thesis is the one we already evoked in quite some depth in Chapter 4. In that chapter, we presented some preliminary results on the contact at finite temperature. A natural extension would be to complete these measurements, at unitarity and in the rest of the crossover. In addition to a measurement of the contact, this could lead to a determination of the critical temperature in the crossover, if the jump at $T_{c,f}$ that was observed at unitarity is present in the whole crossover.

We will now focus on two possible experimental extensions that would enable to verify experimentally our calculation of the polaron energy beyond mean-field approximation. Though it is within the reach of our experimental capabilities, this correction on the energy of the polaron remains small with our experimental parameters (less than 10%), but in specific conditions this corrective term can be enhanced. We will here present two such examples: the first one concerns the frequency shift of the bosonic cloud we measured in Chapter 5, and the second one deals with the location of the Bose-Fermi phase separation we discussed in Chapter 3.

Oscillations

We already evaluated in Chapter 6 the consequences of the beyond mean-field term of the polaron energy on the frequency shift measured in Chapter 5. We will focus in this section on the precise ways to increase the effect of this beyond mean-field term. In the previous chapter, we evoked two possibilities concerning our experiment:

- The first one is to go deeper on the BEC side, where the correction is proportional to a'/a. At the theoretical limit for the stability of the mixture we discussed in Chapter 3, it would correspond to a ratio $a'/a \simeq 0.016$ and a correction of the order of 9%.
- The second one is to use different internal states, and take advantage of a Bose-Fermi Feshbach resonance.

Let us discuss this second option in more details. The new internal states must be compatible with having a stable BEC of ^{7}Li near the Feshbach resonance of interest, and the resonance must be sufficiently broad to enable a precise control of the Bose-Fermi interactions. Moreover, we would need to be on the BCS side of the crossover for the fermions, or at least not too far on the BEC side so that our calculations are valid.

In a private discussion with our group, Eite Tiesinga from NIST suggested a combination of internal states that could fit the different criteria. For fermions in the states $|1_f\rangle$, and bosons in the state $|6_b\rangle$, Tiesinga predicts an adequate Feshbach resonance near $B = 740$ G. For the second fermionic species, the state $|2_f\rangle$ could be used but the Fermi gas would be far on the BEC side, in a limit $|a'| > a$ for which our calculations are not valid anymore, so we would use instead the state $|3_f\rangle$, for which a characterization of the Feshbach resonance can be found in [207] and predicts a broad resonance at $B_0 = 689.68(8)$ G, meaning the Fermi gas would be strongly interacting on the BCS side. In this case, near the ^{6}Li-^{7}Li Feshbach resonance, the BEC would be stable and the fermions would be strongly interacting on the BCS side of the crossover, which seems like good conditions to test the validity of our perturbative expansion and even determine experimentally the F function. However, another issue would arise in that the fermionic states considered are low-field seekers whereas the bosonic state is a high-field seeker. Therefore, trapping both states at the same time would require to use an all-optic final trap, or at least a trap where the axial confinement is dominated by an optical confinement, using two crossed beams for instance, which is not a project at the time but could still be implemented in the future.

Finally, we can consider another possibility: performing the conterflow experiment with a different mass ratio between the impurity and the fermions, thus using different species. This is obviously not possible with our current experimental set-up but the counterflow experiment could be done in the other experiments which obtained a dual super-

fluid Bose-Fermi mixture [256–258]. The constant $\kappa(\eta)$ increases with η and saturates at $-1/4\pi \simeq 3 \times \kappa(7/6)$. We represent it in Fig. 6.10, along with dashed line corresponding to the mass ratio of the species used in [256–258]. For instance, the experiment in Seattle using ^{174}Yb and ^{6}Li [256], would have a factor of 3 on their coefficient κ compared to us, which would make that much more impactful the second-order term of the polaron energy.

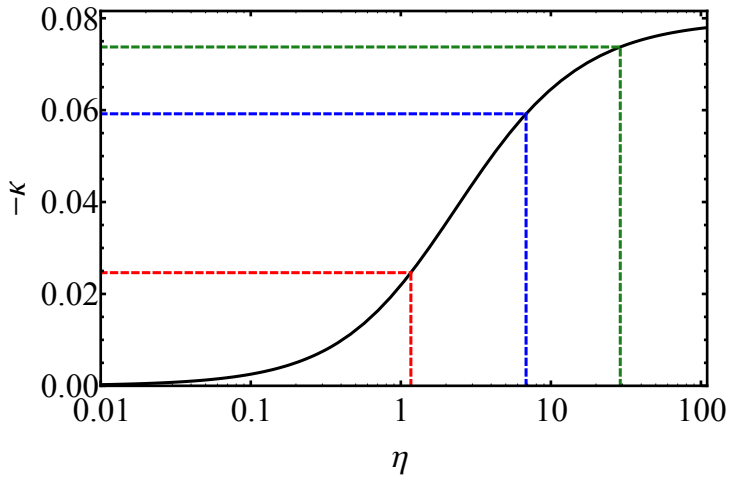

Figure 6.10: Black solid curve: coefficient $-\kappa$ with respect to the mass ratio of the impurity and the fermions η, with a logarithmic scale for the X-axis. Red-dashed curve: value corresponding to a ^{7}Li-^{6}Li mixture (our group and [258]). Blue-dashed curve: value corresponding to a ^{41}K-^{6}Li mixture [257]. Green-dashed curve: value corresponding to a ^{174}Yb-^{6}Li mixture [256].

Phase separation of the mixture

Another example that can be affected by our calculations is the critical threshold for phase separation of the Bose-Fermi mixture. We evaluated in Chapter 3, two cases where the mixture becomes unstable: one on the BCS side close to a Feshbach resonance for the bosons, and one on the BEC side where the Bose-Fermi interaction becomes less and less negligible compared to the boson-boson and fermion-fermion interaction. We will focus on the latter, for which we obtained the value of a critical magnetic field $B_{c0} \simeq 730$ G under which phase separation of the Bose-Fermi mixture occurs. To obtain this value, we used a mean-field approximation to characterize the atom-dimer interaction. Using the expression we obtain in Chapter 6 with eq. (6.47), we have a correction for the critical magnetic field which now corresponds to $B_{c0} \simeq 740$ G (the atom-dimer interaction is increased compared to the mean-field evaluation so the phase separation occurs less far in the BEC domain).

However, we also have to consider the effect of finite temperatures. Above the critical temperatures of the two species, the densities become lower, and the thermal excitations dominate the mean-field interaction terms, so the mixture is expected to be stable for temperatures $T \gtrsim T_c$, with T_c the highest of the two critical temperatures of the Bose and Fermi gases. This was observed in our group, for instance in the conditions described in Chapter 4, section 4.2.2, where we had a stable mixture at magnetic fields well beyond

B_{c0} at a temperature $T > T_c$. At finite temperature, under T_c, the effect of the temperature is non trivial. This was investigated recently in [296] with a new approach, based on a generalization of Popov theory [297–299] to obtain the energy at finite temperature. In this paper is studied the case of a mixture of two Bose gases, with identical bosons in two different internal states, where both species are condensed thus for $T < T_c$. This does not correspond exactly to our situation where we have a mixture of a BEC of ^{7}Li and a BEC of dimers of ^{6}Li, but is sufficiently close to share the same qualititative behavior. In this framework, it was found that there is a magnetic phase transition occurring at $T^* < T_c$ characterized by a phase separation of the system for $T > T^*$, with T^* depending on the different interactions between bosons in the same or different internal states. This unstability is revealed by the negative sign of the magnetic susceptibility[4] of the system for $T > T^*$. This prediction, applied to our system, corresponds to the following behavior:

- For $B < B_{c0}$, we expect the mixture to be always unstable for $T \lesssim T_c$.
- For $B > B_{c0}$, we expect the mixture to be stable for $T < T^*$ and unstable against phase separation for $T^* < T < T_c$.

Using the equations of [296], we can for instance evaluate the onset of phase separation at $T = T_c/2$ to be around $B \simeq 50$ G. Of course, this evaluation is only correct when the two bosonic species have the same mass which is not the case in our experiment ($m_d/m_b = 12/7$).

To check our beyond mean-field predictions and the prediction of phase separation at finite temperature, the phase separation has to be located experimentally. In order to do so, several methods could be used. A first possibility is to measure the critical velocity of the counterflow of the two dimers, since we noted in Chapter 5 that the critical velocity goes to zero at the same time there is a phase separation, as it was done in [278]. Another possibility is to look at the boson losses: near $B = B_{c0}$, we are far from the Feshbach resonance for the boson-boson interaction so the bosonic losses will be completely dominated by the three-body recombination between two fermions and a boson as studied in Chapter 4. If the two superfluid clouds were separated, these losses would disappear, and we would be able to notice a significant drop in the bosonic loss rate. This method has been used in [300] with a Bose-Fermi mixture of ^{41}K and ^{6}Li. The three-body losses in their system mainly involved recombination between two bosons and a fermion. They found that the drop in the loss rate was not sharp but rather smooth due to residual overlap of the two clouds and kinetic energy terms in the total energy, but it was nevertheless a signature of the demixing of the two clouds.

However, whatever the method considered, this study requires to maintain a dual superfluid on the far BEC side, where dimer-dimer losses in the Fermi gas become notably strong, which constitutes an experimental challenge that has yet to be overcome, mainly due to the dimer-dimer losses which are proportional to $a_{ff}^{-2.55}$ and become very important this deep on the BEC side. An alternative would be to use different internal states such as the one we described in the previous section as a way to increase a'. In this case we

[4]The magnetic susceptibility κ_M is defined by:

$$\left.\frac{\partial^2 F/V}{\partial m^2}\right|_{m=0} \tag{6.57}$$

with $m = n_1 - n_2$ the magnetization density, difference of the density of each species (labeled here by the indexes 1 and 2).

would be close to a Feshbach transition for the Bose-Fermi mixture so phase separation could also be observed, though this time the fermions on the BCS side of the crossover thus corresponding to a very different situation than the one we described.

Appendix A

Determination of the fermionic peak density

In order to obtain a dimensionless contact we can compare with other experiments, we need to be able to determine the fermionic peak density at finite temperature, which is not trivial for a harmonically trapped gas. In this appendix, we present a method to evaluate this peak density that can be used for any temperature, everywhere in the BEC-BCS crossover.

A.1 The inverse Abel transformation

We give in Fig. A.1 an example of a typical doubly-integrated profile from which we want to extract the peak 3D density.

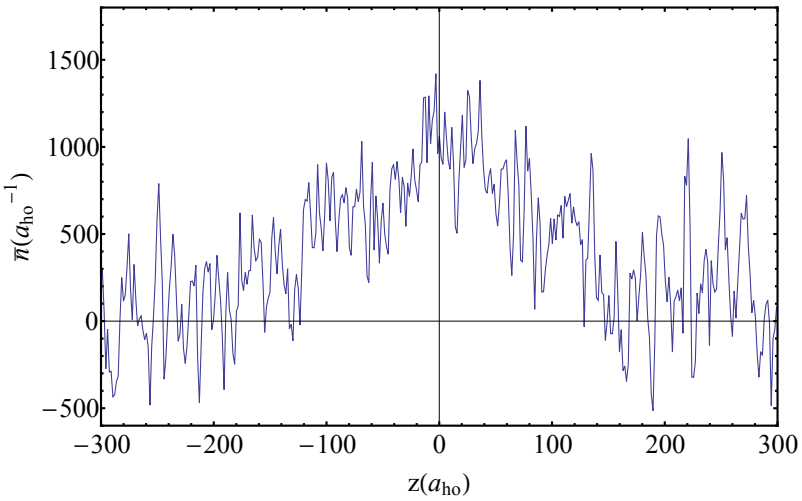

Figure A.1: Typical doubly integrated density profile obtained at relatively high temperature, after summation of the integrated density profiles of the two spin states, given in units of the harmonic oscillator length $a_{ho} = \sqrt{\hbar/m_f\overline{\omega}_f}$. This corresponds to a total number of fermions $N_f \simeq 200 \times 10^3$. The corresponding absorption image was taken in the presence of approximately $N_b \simeq 30 \times 10^3$ bosons. Measuring the temperature thanks to the bosons, we obtain $T \simeq 800$ nK, above the critical threshold for the condensation of the Bose gas and corresponding to $T/T_F \simeq 0.6$.

A first method that can be used to determine the peak density of an atomic cloud is

the inverse Abel transformation. This method was used for instance to determine the 3D density for the measurement of the EoS of the unitary Fermi gas in [136, 176, 224, 301], or the measurement of the unitary contact [235, 236]. It can be applied not only at unitary but actually anywhere in the BEC-BCS crossover, as long as the trap has a cylindrical symmetry. However, we will see that for a noisy profile such as the one in Fig. A.1, this method cannot be used.

The Abel transformation corresponds physically to the integration of an axially symmetric image along one direction. The inverse Abel transform consists in reversing this process to obtain the 3D density from the 2D integrated density. Since in our set-up the pictures of the Fermi gas are not radially resolved (see Chapter 3), we actually have to apply this process twice to get the 3D density from the 1D doubly-integrated density.

In the case of a spherical potential, the inverse Abel transformation would read:

$$n_{3D}(\rho = \sqrt{x^2 + y^2}, z) = -\frac{1}{\pi} \int_{\rho}^{\infty} \frac{\mathrm{d}\tilde{n}_{2D}(y, z)}{\mathrm{d}y} \frac{\mathrm{d}y}{\sqrt{y^2 - \rho^2}} \tag{A.1}$$

$$\tilde{n}_{2D}(R = \sqrt{y^2 + z^2}) = -\frac{1}{\pi} \int_{R}^{\infty} \frac{\mathrm{d}\overline{n}_{1D}(z)}{\mathrm{d}z} \frac{\mathrm{d}z}{\sqrt{z^2 - R^2}} \tag{A.2}$$

whereas for an ellipsoidal cloud we just need to change the scaling of the z axis with a factor ω_z/ω_r to be able to use these transformations.

These transformations are exact, however we have two main issues arising from them: we need to use the second derivative of a very noisy density profile (the noise is even more important at finite temperature than at $T = 0$) and the divisions by the factors such as $\sqrt{z^2 - R^2}$ make the final profile especially noisy at the center. In conclusion, we cannot apply this method directly to our data to get the peak density without pre-processing it (artificial smoothing, high-order polynomial fits) and we do not want to resort to this.

A.2 Peak density of the unitary fermi gas

At unitarity, we can actually take advantage of the fact that an EoS has been measured in other groups to determine the peak density in our cloud.

A.2.1 The EoS of the Unitary Fermi gas

The Fermi gas at finite temperature has been studied experimentally extensively [181], and the EoS of the Fermi gas was measured experimentally with high precision in [136] at Unitarity. The corresponding EoS is represented in Fig. A.2, where they showed the pression and the density as functions of the temperature, it is in very good agreement with diagrammatic Monte-Carlo theory [302]. To obtain their EoS, the MIT team measured the pressure using the integrated density as described before, and obtained the non-integrated density through the inverse Abel transformation of the column density. From these measurements, the critical temperature for superfluidity was evaluated at $T_c/T_F = 0.167(13)$ (with T_F the local Fermi temperature) by observing simultaneously a jump in the compressibility, a jump in the specific heat and the vanishing of the condensed fraction at this temperature.

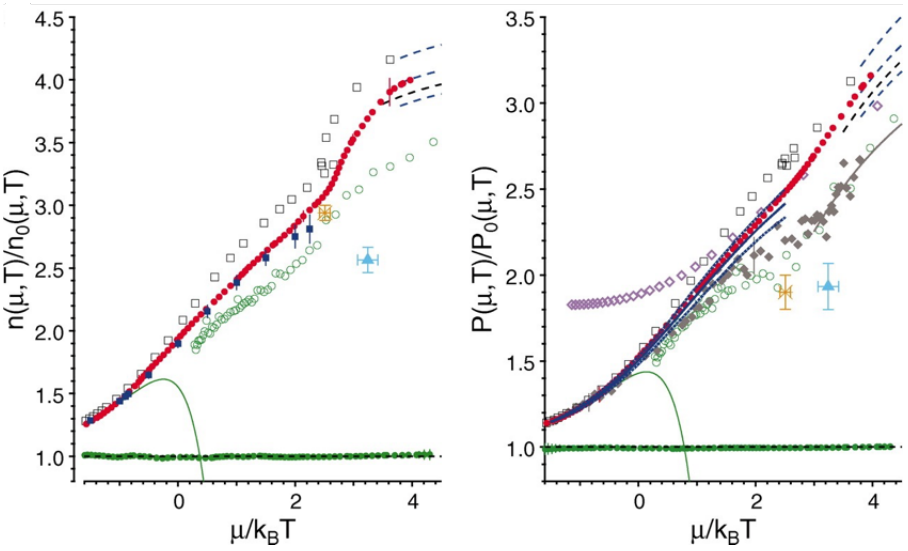

Figure A.2: Density (left panel) and pressure (right panel) of a unitary Fermi gas versus μ/k_BT, normalized respectively by the density and pressure of a noninteracting Fermi gas at the same chemical potential μ and temperature T. Red solid circles: data points measured in [136]. Blue dashed curves: low-temperature behavior with $\xi = 0.364$ (upper), 0.376 (middle), and 0.388 (lower). Black dashed curve: low-temperature behavior with ξ at upper bound of 0.383 from [303]. It is compared to three theoretical calculations of the EoS: diagrammatic Monte Carlo calculation [302] for density / pressure (blue solid squares / blue curve, with blue dashed curves denoting the uncertainty bands), self-consistent T-matrix calculation [140] (open black squares) and lattice calculation [304] (open green circles). The solid green line on each panel corresponds to the third-order Virial expansion, it is correct at high temperatures but fails as expected as the temperature decreases. The orange star and blue triangle on the right panel correspond to the critical point from the Monte Carlo calculations, [305] and [306] respectively. The MIT data is also compared to previous experimental data [181] (solid diamonds) and [307] (purple open diamonds). At the bottom of each panel the experimental/theoretical data from MIT for the ideal gas can be seen (green solid circles / black fine dashed line).

More recent theoretical works relying on Feynman diagrammatic calculations [308] have been performed, agreeing very well with the experimental data. Thanks to F. Werner who contributed to this paper, I had access to their data for the normalized pressure $\mathcal{P}$ and the normalized density Υ, defined by

$$\mathcal{P}(\beta\mu) = P(\mu, T)\beta\lambda_{\text{th}}^3 \tag{A.3}$$
$$\Upsilon(\beta\mu) = n_{3D}(\mu, T)\lambda_{\text{th}}^3 \tag{A.4}$$

where $\lambda_{\text{th}} = \sqrt{2\pi\hbar^2/mk_BT}$ is the thermal de Broglie wavelength and $\beta = 1/k_BT$.

A.2.2 Using the EoS to determine the peak density

We start with a doubly-integrated profile, such as the one that was given in Fig. A.1.

We recall that thanks to the doubly-integrated density, we have directly access to the

pressure in our Femi gas, using

$$P(\mu(z), T) = \frac{m_f \omega_{\mathrm{rad}}^2}{2\pi} \overline{n}(z) \tag{A.5}$$

By writing the reverse of the $\mathcal{P}$ function as $\mathcal{P}^{-1}$, we have :

$$\beta\mu(z) = \mathcal{P}^{-1}\left(\beta\lambda_{\mathrm{th}}^3 \frac{m_f \omega_{\mathrm{rad}}^2}{2\pi} \overline{n}(z)\right) \tag{A.6}$$

Since we have numerical data points for $\mathcal{P}$, we have easily access to $\mathcal{P}^{-1}$. In order to apply this last transformation, we need to interpolate the data points. Since there are many data points and no sudden variations in the EoS, we consider this interpolation to be of high fidelity. In addition, we need the value of the temperature that we obtain thanks to the bosonic gas.

Using the LDA approximation, we then have:

$$\beta\mu(z) = \beta \times \left(\mu_0 - \frac{m_f \omega_z^2 z^2}{2} - g_{bf} n_b(z)\right) \tag{A.7}$$

with the last term accounting for mean-field boson-fermion interactions, negligible in our case.

By applying the $\mathcal{P}^{-1}$ function to our profile (multiplied by the right quantity) as in Eq. A.6, we obtain a parabola (corrected by the bosonic mean-field term) which contains all the information that we need. The offset term of the parabola gives us the fugacity at the center of the cloud whereas the term of degree 2 gives us a confirmation on the temperature obtained through the bosonic profile. Unfortunately, seeing the noise we have on our profiles (see Fig. A.3), it is not reasonable to retrieve the term of degree 2: the standard deviation for this term is estimated to be over 300%. The offset term, however, can be determined quite precisely, with a set of basic constant fits $f(z) = A_0$ performed around the maximum. We do several fits because we vary the window Δ of values over which the fit is performed (*ie* for a window Δ we only use the part of the profile with $|z| < \Delta$ to do the fit) with $0.1 \leq \Delta/R \leq 0.2$, where R is the spatial extent of the cloud in the z direction. This window was optimized by performing a series of fits on simulated noisy parabolic profiles, with a noise chosen to be similar to the one we have in our data. We average the value A_0 obtained by this different fits to obtain the fugacity at the center of the cloud. We expect a systematic error of around 3% for this fit (due to the window) that we take into account for determining the density.

Once we obtain the value $\beta\mu(0)$, we can use the other part of the equation of state to obtain the density by using $\Upsilon(\beta\mu(0))$. In the example of Fig. A.3, we obtain a peak density of $n_{3D}(0) = 0.8 \times 10^{13}$ cm^{-3}.

This method can be applied at unitarity, for any temperature that falls in the range of the experimental and theoretical data that was taken. This typically fails for very low temperatures but can be used around the critical temperature for superfluidity and above. However, this method does not work for data taken anywhere else in the BEC-BCS crossover, so we came up with an alternate method.

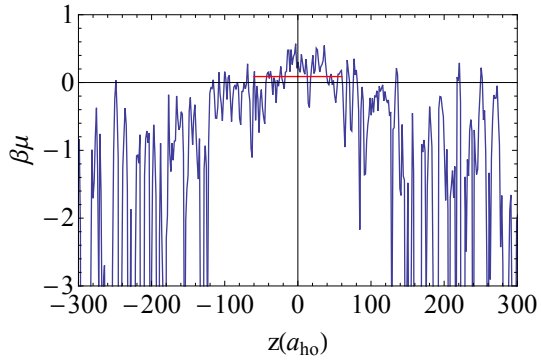

Figure A.3: Representation of the fugacity $\beta\mu$ along z, centered in 0, obtained from the doubly-integrated profile given in Fig. A.1. The red line corresponds to the fit of the maximum of the parabola, taken with a window of $0.2R$. As soon as $|z| > 100a_{ho}$, the profile cannot be used because values of the fugacity below -1.5 correspond to extrapolations of the equation of state (thus the very small signal-to-noise ratio in this domain).

A.3 A new method: using the curvature of the integrated profile

A.3.1 Principle of the method

In order to determine the density at the center of the cloud and the local Fermi temperature, we can use the doubly integrated profiles that we normally get for image analysis.

We consider a doubly integrated profile obtained after a time of flight t, integrated along the x and y directions as it is the case for our Fermi gas:

$$\overline{n}(z) = \int\int \mathrm{d}x\mathrm{d}y\; n\left(\sqrt{\frac{x^2}{R_x^2}+\frac{y^2}{R_y^2}+\frac{z^2}{R_z^2}}, t\right) \tag{A.8}$$

with R_i for $i = x, y, z$ the respective sizes of the cloud in each direction which also depend on t.

We make a first variable change $\rho = \sqrt{\frac{x^2}{R_x^2}+\frac{y^2}{R_y^2}}$ and $\tilde{z} = z/R_z$ and rewrite the integrated density as:

$$\overline{n}(z) = 2\pi R_x R_y \int \mathrm{d}\rho\; n\left(\sqrt{\tilde{z}^2+\rho^2}, t\right) \tag{A.9}$$

We finally make the variable change $s = \rho^2 + \tilde{z}^2$ and we can write:

$$\overline{n}(z) = 2\pi R_x R_y \int_{\tilde{z}^2}^{\infty} \mathrm{d}s\; n\left(\sqrt{s}, t\right) \tag{A.10}$$

Then,

$$\frac{\mathrm{d}\overline{n}}{\mathrm{d}(z^2)} = -\pi R_x R_y \frac{n(z/R_z, t)}{R_z^2} \tag{A.11}$$

$$\frac{1}{z}\frac{\mathrm{d}\overline{n}}{\mathrm{d}z} = -2\pi \frac{R_x R_y}{R_z^2} n(z/R_z, t) \tag{A.12}$$

We are only interested at the density at the center and at $t = 0$, so we introduce the expansion factors λ_i of the cloud along the direction $i = x, y, z$ after a time of flight t.

$$\frac{1}{z}\frac{\mathrm{d}\overline{n}}{\mathrm{d}z}\bigg|_0 = -2\pi\frac{R_x(0)R_y(0)}{R_z^2(0)}\frac{\lambda_x\lambda_y}{\lambda_z^2}\frac{n(0,t=0)}{\lambda_x\lambda_y\lambda_z} \tag{A.13}$$

$$\frac{1}{z}\frac{\mathrm{d}\overline{n}}{\mathrm{d}z}\bigg|_0 = -2\pi\frac{\omega_z^2}{\omega_r^2}n(0)\frac{1}{\lambda_z^3} \tag{A.14}$$

with ω_i the trapping frequency along direction i before the release of the trap.

This last expression yields the peak density of the Fermi gas:

$$n_f(0) = -\frac{1}{2\pi}\lambda_z^3\frac{\omega_\mathrm{r}^2}{\omega_z^2}\,\frac{1}{z}\frac{\mathrm{d}\overline{n}}{\mathrm{d}z}\bigg|_0 \tag{A.15}$$

The time of flight for fermions is typically $\tau_f = 0.4$ ms, so we are in the limit $\tau_f\omega_z \ll 1$ and we can write simply $\lambda_z = \sqrt{1+\omega_z^2\tau_f^2} \simeq 1$.

Therefore, we have to calculate the quantity $C = \frac{1}{z}\frac{\mathrm{d}\overline{n}}{\mathrm{d}z}\big|_0$ which in the case of a maximum coincides with the second derivative as well as the curvature of the integrated density taken at its center, in order to determine the peak density of the cloud.

To evaluate this curvature, we first do some tests on data taken at $T = 0$ to calibrate our method and then we apply it to determine the contact at higher temperatures.

A.3.2 Calibration at T=0

In our experiment, as we explained in Chapter 3, we need to calibrate the number of atoms obtained from the integrated profiles. We detailed the method used for calibration, where we consider the spatial extent of the profile to be reliable but not the total count, so we multiply our integrated density by a factor κ_6 so that the size of the cloud remains the same but the number of atoms is adjusted and both quantities can finally coincide. The true number N_true is linked to the number obtained through integration of the profiles N_int by the simple relation $N_\mathrm{true} = \kappa_6 N_\mathrm{int}$. However, the spatial extent of the gaz, given by the Thomas-Fermi radius at $T = 0$ has the dependence $R_\mathrm{TF} \propto N_\mathrm{true}^{1/6}$, which is not the best to determine the calibration factor with precision.

Since the set of data we used is relatively older than the one used to determine the values of the calibration factor determined in Chapter 3, not knowing what might affect it, we decided to perform a new calibration, using the curvature C. The principle is basically the same but there is a subtlety as the curvature obtained from the profile changes if we multiply it by κ_6, contrary to the Thomas-Fermi radius. Indeed, for a fixed Thomas-Fermi radius, we understand that multiplying the profile by κ_6 will multiply the curvature by the same factor. Let us write C_exp the curvature obtained with the Thomas-Fermi fit to the non-modified doubly integrated profile after a fit using a Thomas-Fermi profile and C_true the "true" curvature. If κ_6 is well determined then

$$C_\mathrm{true} = \kappa_6 C_\mathrm{exp}. \tag{A.16}$$

The peak density of a unitary Fermi gas containing N_f atoms at $T = 0$ is given by the equation:

$$n_f(0) = \frac{8\sqrt{N_f}}{\pi^2\xi^{3/4}\sqrt{24}}\frac{1}{a_\mathrm{ho}^3} \tag{A.17}$$

with a_{ho} the typical size of the harmonic oscillator. We can then given an expression of the theoretical curvature in respect with the number of fermions:

$$C_{\rm true}(N_f) = -\frac{\omega_z^2}{\omega_r^2}\frac{4\sqrt{N_f}}{\pi^3\xi^{3/4}\sqrt{24}}\frac{1}{a_{\rm ho}^3} \tag{A.18}$$

Therefore, the true curvature can be written as

$$C_{\rm true} = C_{\rm th}(N_{\rm true}) = \sqrt{\kappa_6}C_{\rm th}(N_{\rm int}) \tag{A.19}$$

.

Finally, we can use eq. (A.16) and (A.19) to obtain the calibration factor as:

$$\kappa_6 = \left(\frac{C_{\rm th}(N_{\rm int})}{C_{\rm exp}}\right)^2 \tag{A.20}$$

The big advantage of this method is that the curvature depends on $N^{1/2}$, which is far more sensitive than $N^{1/6}$, hence more reliable. This calibration method can be used if there are bosons present but with adjustments on the theoretical formula for the central density. After analysis of several set of data with different trapping frequencies, we obtained a calibration factor $\kappa_6 = 2.4(5)$, compatible with the former value within error bars. By construction, by using this calibration factor the relation between the corrected curvature and the peak density is always verified.

While it was important to determine this calibration factor, the main interest of calibrating at zero-temperature is to test a method to determine the curvature that does not rely on the precise knowledge of the shape of the integrated profile. At high temperature at unitarity, even if the shape of the profile is known, it involves the ratio of two Polylog functions [1], and the fits to our noisy profiles are not reliable and anywhere else in the BEC-BCS crossover, the shape of the profile is not precisely known at finite temperature anyway.

To this purpose, we test the measurement of the curvature using a polynomial fit. To perform these fits, we have to consider two parameters. The first one is the degree of this polynom: since it is a symmetric profile, we expect an expansion with only even terms: $\overline{n}(z) \underset{z\approx 0}{\simeq} A_0 + A_2 z^2 + A_4 z^4 + A_6 z^6 + ...$ The other one is the extent of the profile over which we want to perform this fit, what we call the window Δ. To decide which of these parameters we want to chose, we tested fits of a simulated noisy Thomas-Fermi profile with different windows and for the polynomial degrees up to 6. The results are presented in Fig. A.4.

We see from Fig. A.4 that the best choice is a polynom of degree 4 for a window $\Delta/R_{\rm TF}$ between 0.8 and 0.9. We will calculate the curvature for several Δ corresponding to this domain and then take the mean as the curvature. We can note that the difference between the curvature calculated with this polynomial profile and the real one for this window is expected to be about 3 % (due to the divergence from the polynomial expansion).

[1] At higher temperatures, the general expression for the doubly-integrated profile can be expressed as :

$$\overline{n}(z) = \overline{n}(0)\frac{\mathrm{Li}_{5/2}\left(-\exp\left[\mathrm{q} - \frac{\mathrm{z}^2}{\mathrm{R}_\mathrm{z}^2}\mathrm{f}(\mathrm{e}^\mathrm{q})\right]\right)}{\mathrm{Li}_{5/2}(-\mathrm{e}^\mathrm{q})} \tag{A.21}$$

with $f(q) = \frac{1+q}{q}\ln(1+q)$ and $q = \beta\mu$ the fugacity and Li the PolyLog function.

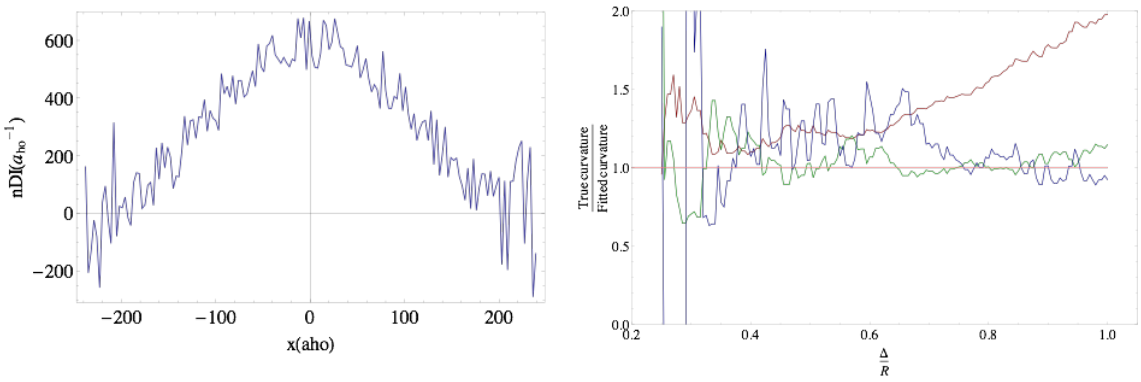

Figure A.4: Left: Simulated noisy Thomas-Fermi profile. The random noise is chosen to have an amplitude of 20% of the max value at the center and 50 % for the background, to reproduce more closely the experimental profiles. Right: Ratio of the "true" curvature (calculated from the non-noisy profile) over the fitted curvature, depending on the window Δ over the Thomas-Fermi radius of the profile R. This ratio is best when equal to one, corresponding to the pink straight line. The red curve corresponds to a polynom of degree 2 : the area where the fit would be optimal is dominated by the noise, this choice is not reliable. The blue curve corresponds to a polynom of degree 6 : even if we tend approximately to the right curvature, the standard deviation remains quite high, because the fit tries too hard to follow irrelevant noise fluctuations. Finally, the green curve corresponds to a polynom of degree 4: it is the best choice, for a window Δ/R between 0.8 and 0.9, for which the ratio is reliably steady and close to 1.

On Fig. A.5, we show an example of the determination of the calibration factor and the peak density using these two methods on a doubly-integrated density profile obtained experimentally.

To confirm the validity of this method, we compared the peak density determined using the curvature calculated from the Thomas-Fermi fit and the polynomial fit on the sets of data that were used to determine the calibration factor. By compiling all the results ($\simeq 150$ images), the mean ratio of the central density obtained through a Thomas-Fermi fit and a polynomial fit is : $\frac{n_{\mathrm{TF}}}{n_{\mathrm{poly}}} \simeq 1.04(05)$, consistent with the estimations made on simulated profiles, confirming the validity of this alternate method.

A.3.3 Measurements at finite temperature

At higher temperatures, we only use polynomial fits to determine the curvature. Similarly as in the previous section, we generated simulated noisy profiles using eq. (A.21), for several values of the fugacity contained in a reasonable range, and determined that the best window to perform the fit was again $\Delta/R \simeq 0.8 - 0.9$, and that we would in this case systematically underestimate the curvature by around 4%, a correction that we will apply to our calculations.

A typical profile is given in Fig. A.6, along with a curve giving the density for several windows. We see that the value of the central density is indeed stable in the domain $\Delta/R \simeq 0.8 - 0.9$, and the final value of the central density will be taken as a mean of the density values obtained in this range.

We can then use this method for our whole data set at finite temperature and compare it to the first method. This is gathered in Fig. A.7. We see that we have a very good

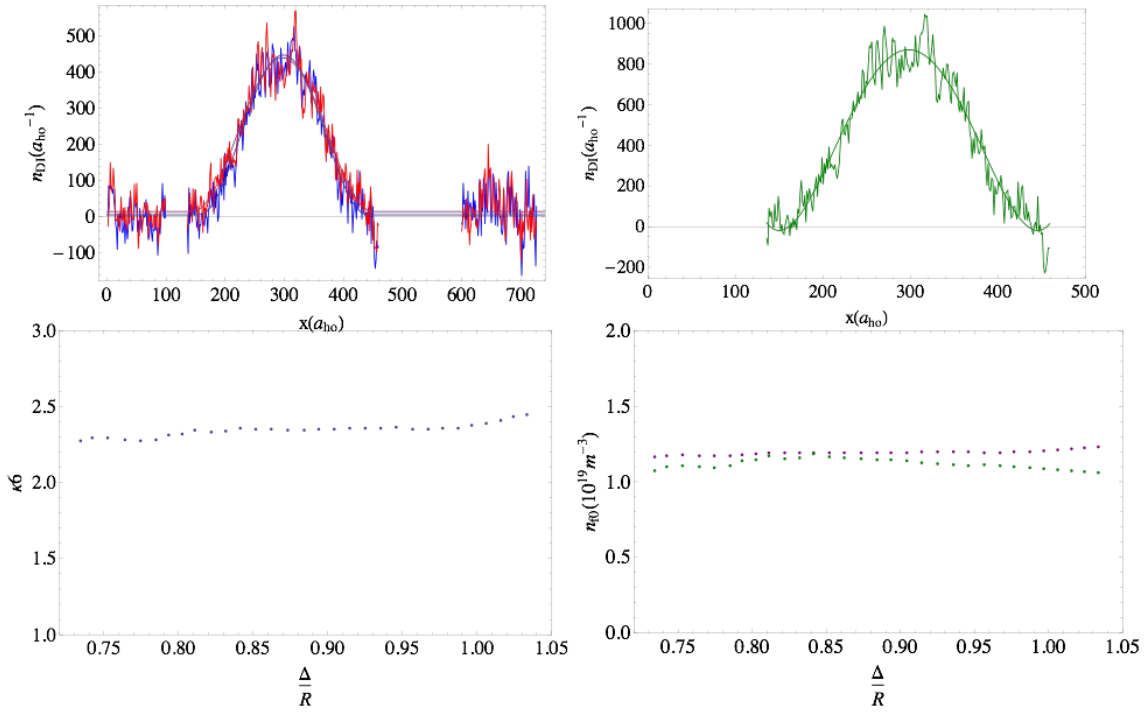

Figure A.5: Top left: doubly integrated profiles for the top (blue) and bottom (red) fermions, fitted with a Thomas-Fermi profile. We also use a window for the fit but we always keep points corresponding to the background in order to have a well-defined baseline. Top right: total (top + bottom) doubly-integrated density fitted with a polynomial fit. Bottom left : calibration factor according to the window taken to perform the Thomas-Fermi fit, we see it is not sensitive to the window. Bottom right: densities obtained with the Thomas-Fermi fit (purple) and the polynomial fit (green), according to the window of the fit. The two fits give out approximately the same result in the range $\Delta/R \simeq 0.8 - 0.9$.

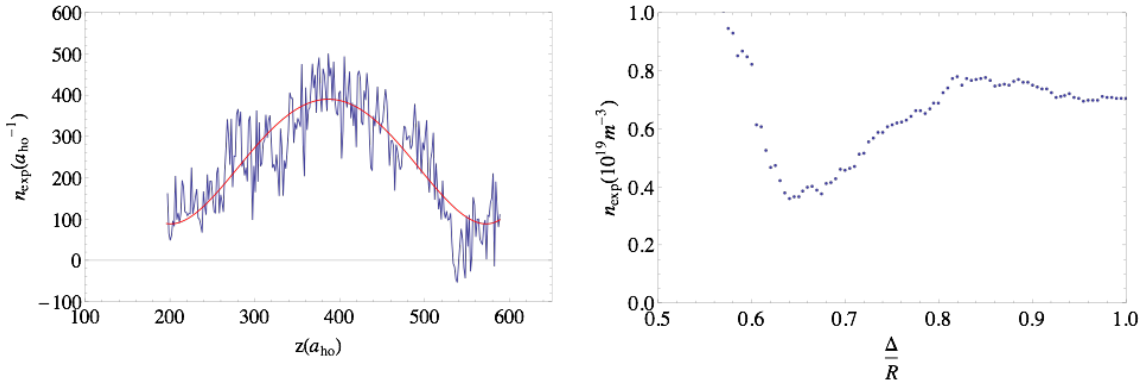

Figure A.6: Left: typical density profile (blue) with a polynomial fit (red) taken with a window $\Delta/R = 1$, which is outside the range we consider to determine the curvature. Right: Calculated central density in respect with the window taken to perform the fit. We see that the value becomes stable in the range mentioned in the text.

correspondence between the two methods which strongly reinforces our confidence in the use of polynomial fits to determine the curvature, the only method that can be used in any condition (for any temperature, through the BEC-BCS crossover or for any boson-fermion interaction).

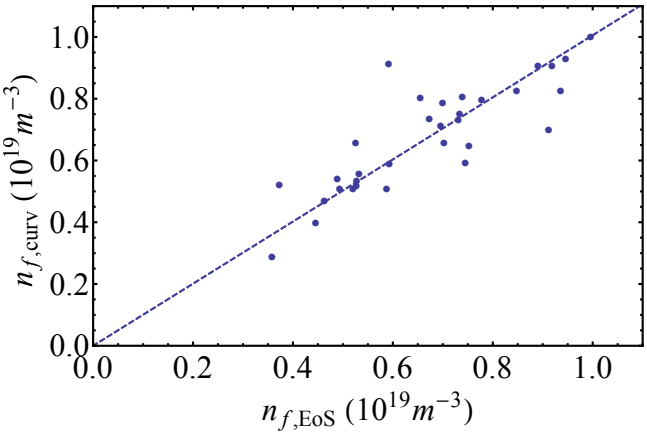

Figure A.7: Comparison of the density obtained through the equation of state (X axis) and the curvature measurements (Y axis). We fit with a linear curve and obtain a slope of $1.00(02)$, showing the two methods give consistent results.

Conclusion

We have detailed here a method to determine the fermionic peak density at finite temperature, in the BEC-BCS crossover, in presence or not of a Bose gas, by measuring the curvature of the integrated profiles. We compared it to a method relying on the EoS of the unitary gas and concluded that they were consistent, confirming the robustness of our method.

Appendix B

BCS Theory

In this appendix, we present some elements of BCS theory relevant to this thesis. We start by introducing the BCS model and then we focus on the determination of the response function described in Chapter 6 and obtaining the polaron energy up to second order using BCS theory.

B.1 Elements of BCS Theory

We consider a two-component Fermi gas of spin $1/2$ fermions of mass m_f, with equal populations in each spin state, with a scattering length a. Within BCS theory, the fermionic medium is described by the mean-field Hamiltonian:

$$\widehat{H}_{\mathrm{mb}} = \sum_{\boldsymbol{k},\sigma} \xi_k \widehat{c}^{\dagger}_{\boldsymbol{k}\sigma} \widehat{c}_{\boldsymbol{k}\sigma} + \Delta^* \sum_{\boldsymbol{k}} \widehat{c}_{\boldsymbol{k}\uparrow} \widehat{c}_{-\boldsymbol{k}\downarrow} + \mathrm{h.c.} \tag{B.1}$$

with $\xi_k = \epsilon_k^{(\mathrm{f})} - \mu$, μ is the chemical potential, and the gap Δ is defined by

$$\Delta = \frac{g}{\Omega} \sum_{\boldsymbol{k}} \langle \widehat{c}_{-\boldsymbol{k}\downarrow} \widehat{c}_{\boldsymbol{k}\uparrow} \rangle \tag{B.2}$$

with $g_{ff} = 4\pi\hbar^2 a/m_f$ the coupling constant in the mean-field approximation.

To diagonalize the Hamiltonian, we introduce the Bogoliubov operators $\widehat{\gamma}_{\boldsymbol{k}\pm}$ defined by:

$$\widehat{c}_{\boldsymbol{k}\uparrow} = u_k \widehat{\gamma}_{\boldsymbol{k}+} - v_k \widehat{\gamma}_{-\boldsymbol{k}-} \tag{B.3}$$

$$\widehat{c}_{\boldsymbol{k}\downarrow} = u_k \widehat{\gamma}_{\boldsymbol{k}-} + v_k \widehat{\gamma}_{-\boldsymbol{k}+}, \tag{B.4}$$

with

$$u_k = \sqrt{\frac{1}{2}\left(1 + \frac{\xi_k}{E_k}\right)}, \quad v_k = \sqrt{\frac{1}{2}\left(1 - \frac{\xi_k}{E_k}\right)} \tag{B.5}$$

and $E_k = \sqrt{\xi_k^2 + |\Delta|^2}$.

In this representation we have the diagonalized Hamiltonian $\widehat{H}_{\mathrm{mb}} = \sum_{\boldsymbol{k},\pm} E_k \widehat{\gamma}^{\dagger}_{\boldsymbol{k}\pm} \widehat{\gamma}_{\boldsymbol{k}\pm}$. We see that E_k corresponds to the energy of the excited states, always greater than the gap Δ, the minimum energy needed to break a pair.

Two parameters have yet to be determined, the gap Δ and the chemical potential μ, so we need two equations. The first one is the gap equation, that can be written as

$$\Delta = \frac{g_0}{\Omega} \sum_{\boldsymbol{k}} u_k v_k \tag{B.6}$$

The second one is the equation giving the total number of atoms, given by

$$N_f = \frac{1}{\Omega} \sum_{\boldsymbol{k}} 2v_k^2 \tag{B.7}$$

Using these two equations, we obtain Δ and μ that we represent in Fig. B.1.

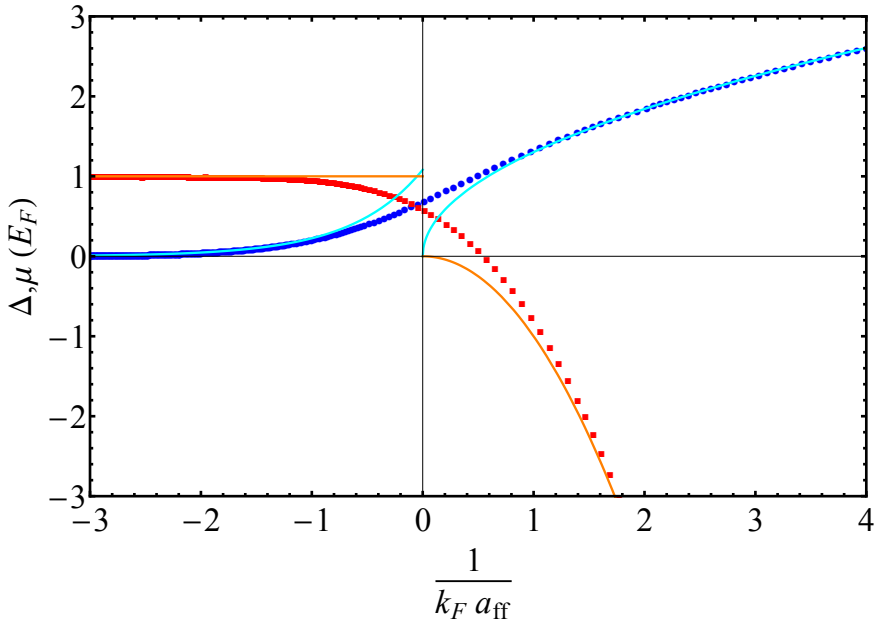

Figure B.1: BCS parameters μ (red squares) and Δ (blue circles) in the BEC-BCS crossover, calculated using eq. (B.6) and (B.7). Solid orange curves (Solid cyan curves) correspond to the asymptotic behavior of the chemical potential (gap) in the BCS and BEC limits.

On Fig. B.1, we also represented the asymptotic behaviors of the chemical potential and the gap in the BCS limit and the BEC limit that we list below [47, 309]:

- BCS limit: $\mu_f \approx E_F$ and $\Delta \sim E_F \times 8e^{-2} \exp(-\pi/2k_F|a|)$. The chemical potential corresponds to the Fermi energy and the gap decreases exponentially to zero, which coincides with the ideal Fermi gas.
- BEC limit: $\mu_f \approx -\hbar^2/ma^2$, corresponding to the binding energy of the dimers and

$$\Delta \sim \sqrt{\frac{16}{3\pi}} \frac{E_F}{\sqrt{k_F a}}. \tag{B.8}$$

B.2 Perturbative expansion of the polaron energy within BCS Theory

This section presents a derivation of the results presented in Chapter 6 within the simplified framework of BCS mean-field theory. We first determine the response function χ,

then the F function and finally we compare it to the exact expressions obtained in this thesis.

With BCS theory, we do not expect to obtain quantitatively correct results but only a qualitative check of the behavior of the different relevant functions. Therefore, we only consider the simple case $m_f = m_i = m$, corresponding to $\eta = 1$, a ratio close to the mass ratio we have with our Lithium experiment $(7/6)$. We also write a' the scattering length associated to the impurity-fermion interaction.

B.2.1 Mean-field compressibility

As described in Chapter 6, second order perturbation theory connects the polaron energy shift to the fermionic superfluid dynamical response function $\chi(\boldsymbol{q}, E)$ defined by

$$\chi(\boldsymbol{q}, E) = \frac{1}{N} \sum_{\alpha} \frac{|\langle \alpha | \widehat{\rho}_{-\boldsymbol{q}} | 0 \rangle|^2}{E_\alpha - E_0 + E}. \tag{B.9}$$

To derive the BCS expression of the response function, we express the matrix elements appearing in the response function

$$\langle \alpha | \widehat{\rho}_{-\boldsymbol{q}} | 0 \rangle = \sum_{\sigma} \langle \alpha | \widehat{c}^\dagger_{\boldsymbol{k}-\boldsymbol{q},\sigma} \widehat{c}_{\boldsymbol{k},\sigma} | 0 \rangle \tag{B.10}$$

using the Bogoliubov creation and annihilation operators. We obtain readily

$$\chi^{\mathrm{MF}}(\boldsymbol{q}, E) = \frac{1}{N} \sum_{\boldsymbol{k}} \frac{2u^2_{k-q} v^2_k + 2u_k v_k u_{k-q} v_{k-q}}{E_k + E_{k-q} + E}, \tag{B.11}$$

where we have used the fact that the excited states $|\alpha\rangle$ correspond to pairs of Bogoliubov excitations, hence $E_\alpha - E_0 = E_k + E_{k-q}$. We use the notation MF to signify that this result is only valid in BCS theory, a mean-field theory.

B.2.2 Perturbative calculation of the energy

In order to calculate the polaron energy shift, we need to consider the perturbative development we obtained in Chapter 6, adapted to BCS theory:

$$\Delta E^{\mathrm{MF}}_{\mathrm{pert}} = \left[g' n + \frac{g'^2 n}{\Omega} \sum_{\boldsymbol{q}} \left(\frac{1}{\varepsilon^{(\mathrm{r})}_q} - \chi^{\mathrm{MF}}(\boldsymbol{q}, \varepsilon^{(\mathrm{i})}_q) \right) \right] \tag{B.12}$$

After converting sums into integrals and performing the angular integrations, this expression becomes

$$\begin{aligned} \Delta E^{\mathrm{MF}}_{\mathrm{pert}} = g' n + \frac{g'^2}{8\pi^4} \frac{m}{\hbar^2} \int k^2 \mathrm{d}k \int q^2 \mathrm{d}q \Bigg[\frac{4 v_k^2}{q^2} - \\ \frac{2u_q^2 {v_k}^2 + 2u_k v_k u_q v_q}{kq} \ln \left(\frac{E_k + E_q + \frac{\hbar^2 (k+q)^2}{2m}}{E_k + E_q + \frac{\hbar^2 (k-q)^2}{2m}} \right) \Bigg] \end{aligned} \tag{B.13}$$

In order to describe the behavior of these integrals for high momentum k, we perform the variable change $k \to u = (k/k_F)/\sqrt{|\Delta|/E_F}$, $q \to v = (q/k_F)/\sqrt{|\Delta|/E_F}$ and we get

$$\Delta E^{\mathrm{MF}}_{\mathrm{pert}} = g'n \left[1 + k_F a' \frac{3}{2\pi} \left|\frac{\Delta}{E_F}\right|^2 I(\Lambda/k_F)\right] \tag{B.14}$$

with I corresponding to the integral left to calculate in Eq. (B.13) that depends on the cut-off Λ and also on the ratio $\mu/|\Delta|$.

In the limit $u,\, v \gg 1$, we can simplify greatly the expression of the integral I. First, we can see that the terms u_k^2 and v_k^2 can be rewritten, in this limit:

$$u_k^2 \sim 1, \quad v_k^2 \sim \frac{1}{4}\frac{|\Delta|^2}{\xi_k^2} \to \frac{1}{4u^4} \tag{B.15}$$

From this last expression, we can also get the fermionic two-body contact C_2 in BCS theory. Indeed, using the property of momentum distribution [145]:

$$n_\uparrow(k) \underset{k\to\infty}{\sim} n_\downarrow(k) \underset{k\to\infty}{\sim} \frac{C_2}{k^4} \tag{B.16}$$

and knowing that in BCS theory we have $n(k) = n_\uparrow(k) + n_\downarrow(k) = 2v_k^2\Omega$, we see that we have the right dependence for the momentum distribution and we can extract the contact

$$\frac{C_2}{N} = \frac{3\pi^2}{4}\left|\frac{\Delta}{E_F}\right|^2 k_F. \tag{B.17}$$

In the high momentum limit, using the simplified expressions of u_k and v_k derived in eq. (B.15), we obtain for I:

$$I(\Lambda/k_F) = \int \frac{\mathrm{d}u}{u} \int \frac{\mathrm{d}v}{u} \left[1 - \frac{1}{2}\left(\frac{v}{u} + \frac{u}{v}\right) \ln\left(\frac{1 + v/u + (v/u)^2}{1 - v/u + (v/u)^2}\right)\right]. \tag{B.18}$$

The second integral (over v/u) converges towards $2\pi^4\kappa^{\mathrm{MF}}$ and the first integral (over u) gives the logarithmic divergence:

$$I = 2\pi^4\kappa^{\mathrm{MF}}(\ln(\Lambda/k_F) + ...) \tag{B.19}$$

with κ^{MF}:

$$\kappa^{\mathrm{MF}} = \frac{\sqrt{3}}{8\pi^3} - \frac{1}{12\pi^2}. \tag{B.20}$$

In Chapter 6, we found:

$$\kappa(1) = \frac{\sqrt{3}}{8\pi^3} - \frac{1}{12\pi^2} - \frac{1}{9\pi\sqrt{3}}. \tag{B.21}$$

The two results are very similar except for the last term of $\kappa(1)$ which does not appear in the mean-field approach because BCS theory does not account for interactions between excitations of the superfluid, whereas the missing term corresponds to the third diagram in Fig. 6.5 from Chapter 6, which is the only diagram that features an interaction between two fermionic excited states. This missing term is actually the most important one in κ, which is why we get a ratio $\kappa(1)/\kappa^{\mathrm{MF}} \simeq 15$.

B.2.3 The F function

We demonstrated analytically that there is again a logarithmic divergence of the second order term of the expansion of the polaron energy. By combining equations (B.14), (B.17) and (B.19), we get the expression of the energy calculated up to second order in perturbation using BCS theory :

$$\Delta E^{\mathrm{MF}}_{\mathrm{pert}} = g'n \left[1 + k_F a' F^{\mathrm{MF}} \left(\frac{1}{k_F a} \right) + 4\pi \kappa^{\mathrm{MF}} a' \frac{C_2}{N} \ln(\Lambda / k_F) \right] \tag{B.22}$$

with F^{MF} a function that can be computed numerically throughout the BEC-BCS crossover by calculating the difference between the exact expression of the integral I defined in Eq. (B.13) and the logarithmic term we obtained in Eq. (B.19). In particular, these numerical calculations show that this function does not depend on the cut-off but only on the parameter $1/(k_F a)$.

Then, if we introduce a renormalization with a three-body interactions, similarly as what was done in Chapter 6, the energy reads

$$\Delta E^{\mathrm{MF}} = g'n \left[1 + k_F a' F^{\mathrm{MF}} \left(\frac{1}{k_F a} \right) - 4\pi \kappa^{\mathrm{MF}} \frac{a' C_2}{N} \ln(k_F R_3) + ... \right], \tag{B.23}$$

We get a very similar expression to the one we found in Chapter 6, only we replace F and $\kappa(1)$ by F^{MF} and κ^{MF}.

The function F^{MF} is represented in Fig. B.2, and we can observe the two asymptotic behaviors on the BCS and BEC sides:

- In the BCS limit we recover once again the Fermi-polaron, hence $F^{\mathrm{MF}}(-\infty) = 3/2\pi$ for $\eta = 1$.
- In the BEC limit, we get a behavior consistent with the energy of the Bose polaron $g_{ad} n$ that does not depend on k_F:

$$F^{\mathrm{MF}} \left(\frac{1}{k_F a} \right) = 16\pi^2 \kappa^{\mathrm{MF}} \frac{\ln(k_F a)}{k_F a} + ... \tag{B.24}$$

Since the value we get for the F^{MF} function at unitarity does not deviate much from the values on the BCS side (see Fig. B.2) which have the same asymptotic behavior as F in Chapter 6, we used in a first approximation the value of $F^{\mathrm{MF}}(0)$ at unitarity instead of the (unknown) value $F(0)$ in the calculation of the frequency shift at unitarity in section 6.4.

In conclusion, BCS theory predicts the correct qualitative behavior for the polaron energy shift but is quantitatively wrong. The discrepancies between the BCS calculations and the calculations led in Chapter 6 can be explained by the absence of interactions between the excitations of the superfluid in BCS theory.

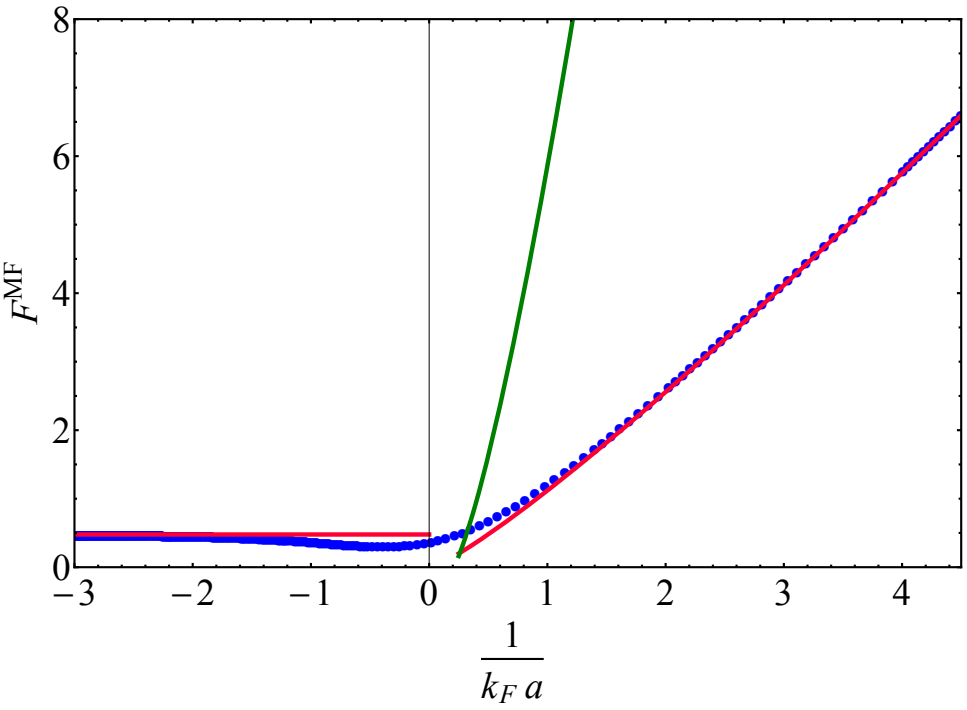

Figure B.2: Blue dots: Representation of the function F^{MF} through the crossover for $\eta = 1$. Red curves: Asymptotic behaviors described in the text on the BCS side: $F^{\mathrm{MF}}(-\infty) = \frac{3}{2\pi}$, and the BEC Side : $F^{\mathrm{MF}}(X) \simeq 16\pi^2\kappa^{\mathrm{MF}} X \ln(1/X) + A_0 X$ with A_0 an adjustable parameter found out to be, after optimization, $A_0 \simeq 1.1$. Green curve: asymptotic behavior on the BEC side using the true value of κ, C_{ad} and R_3 (the last two are given in Appendix D).

Appendix C

Phase diagram of an impurity immersed in a Fermi superfluid

We detail in this appendix the construction of the phase diagram of an impurity immersed in a Fermi superfluid, depending on the interaction between the impurity and the fermions of the superfluid (chracterized by the scattering length a') and the interaction between two fermions of the superfluid (characterized by the scatering length a). We consider our system to be in the vicinity of narrow Feshbach resonances of resonance range $R_e > 0$ for the fermion-impurity interaction and the fermion-fermion interaction. To simplify the study we consider that the fermions and the impurity all have the same mass m.

We recall the three possible phases of the system: for $a'/R_e \to 0^-$ we have the polaron phase, for $a'/R_e \to 0^+$ it is the dimeron phase (impurity atom + fermion) and the domain $R_e/a' \to 0$ corresponds to the trimeron phase (impurity atom + $\uparrow$ fermion + $\downarrow$ fermion).

To build the phase diagram, we will first study each phase separately before discussing the equation of the different frontiers separating the different phases. The energy of the dimeron and the trimeron will be evaluated by an analysis of the two-body and the three-body problems respectively since their binding energy is much bigger than the Fermi energy in each case (as discussed in the introduction of Chapter 6). This treatment is valid as long as they are not resonant with the atomic continuum, when their structure is not really affected by the many-body background.

The boundaries of the phase diagram that we will determine are only semi-quantitative and model-dependent, but still constitute a pedagogical discussion of the general behavior of the system.

C.1 Polaron

In the case of an impurity immersed in a two-component Fermi gas, the nature of the polaron quasiparticle depends on the interactions between the fermions of the superfluid. As long as this interaction remains weak, which is the case in our experiment $a_{bf} \ll a_{ff}$, we can use a mean-field approximation to determine the energy of the polaron E_P. We can write in two particular cases:

- BCS side, Fermi polaron: $E_P = E_{SF} + g'n$ with E_{SF} the ground state energy of the superfluid without the impurity and n the density of fermions.
- BEC side, Bose polaron: $E_P = E_{SF} + g_{ad}n/2$ with E_{SF} with g_{ad} the coupling constant between an impurity atom and a dimer of two fermions.

This stops being valid when a' becomes stronger, but since we expect the transition between the polaron and the trimeron to be a mere crossover, its exact position is not relevant experimentally, so we will remain within the hypothesis that the energy of the system in the polaron phase is solely a mean-field correction to the energy of ground state of the superfluid alone.

C.2 Dimeron

In the case of a narrow Feshbach resonance, in the dilute limit $na'^3 \ll 1$, the energy E_2' of a dimeron can be written in general as [310]:

$$E_2' = \frac{-\hbar^2}{m}\left(\frac{-1+\sqrt{1+4R_e/a'}}{2R_e}\right)^2 . \tag{C.1}$$

Close to the Feshbach resonance, in the limit $R_e/a' \ll 1$, we recover the universal result $E_2' = \hbar^2/ma'^2$ with this expression, corresponding to the energy of a shallow dimer, strongly dressed by the open channel of the resonance. For $R_e/a' \gg 1$, we obtain $E_2' = \hbar^2/mR_e a'$, corresponding to the result we obtained in Chapter 1 in this limit.

The energy of fermion-fermion dimers follows the same expression, written as $E_2(R_e, a)$, corresponding to the expression of E_2' where a' is replaced by a.

To form a dimeron, one has to extract a Cooper pair from the superfluid, break it and pair one of the fermions with the impurity. The energy needed to extract the two fermions from the background is $2\mu_F$ which value depends on where we stand on the fermion BEC-BCS crossover: on the BCS side, we have $\mu_F \simeq E_F$, at unitarity $\mu_F = \xi E_F$ and on the BEC side it is dominated by the binding energy of the fermion dimers $2\mu_F \simeq E_2$.

On top of that, we have to add the mean-field energy between the dimeron, the remaining fermion and the particles of the superfluid. The total energy reads as:

- On the BCS side: $E_{SF} - 2\mu_F + E_2' + g_{ad}'n + gn$ with g_{ad}' the coupling constant between a dimeron and a fermion of the superfluid.

- On the BEC side: $E_{SF} - 2\mu_F + E_2' + g_{dd}'n + g_{ad}n$ with g_{dd}' the coupling constant between a dimeron and a dimer from the superfluid.

C.3 Trimeron

Two-channel model

Here we want to determine the energy E_3 of a trimer made of an impurity atom and two fermions of opposite spins, focusing only on three-body physics. To study this problem, we adapt the limited-range two channel model, previously used to determine the Efimov spectrum of three identical bosons [94, 311], that we presented in Chapter 1. The open channel is characterized by atomic annihilation operators $\widehat{a}_{\mathbf{k},\sigma}$ with $\sigma = 1, 2, 3$ designating one of the three distinguishable particles. The closed channel is represented by the operators $\widehat{b}_{\mathbf{K},\sigma}$ describing a dimer of two particles not involving the particle σ. The Hamiltonian reads:

$$\begin{aligned}\widehat{H} = &\sum_{\mathbf{k},\sigma} \epsilon_k \widehat{a}^\dagger_{\mathbf{k},\sigma}\widehat{a}_{\mathbf{k},\sigma} + \sum_{\mathbf{K},\sigma}(E_{\sigma,0}+\epsilon_k/2)\widehat{b}^\dagger_{\mathbf{K},\sigma}\widehat{b}_{\mathbf{K},\sigma} \\ &+ \frac{\hbar^2}{2m}\sqrt{\frac{2\pi}{R_e}} \sum_{\substack{\mathbf{K},\mathbf{k},k<\Lambda \\ \sigma_1\neq\sigma_2\neq\sigma_3}} (\widehat{b}^\dagger_{\mathbf{K},\sigma_1}\widehat{a}_{\mathbf{k}+\mathbf{K}/2\sigma_2}\widehat{a}_{-\mathbf{k}+\mathbf{K}/2,\sigma_3} + \text{H.c.}).\end{aligned} \tag{C.2}$$

where Λ is a UV momentum cut-off.

In this model we make the assumption that the atom-dimer coupling is the same for all three-species. However, the atom-atom scattering lengths are controlled independently by the bare molecular binding energies $E_{\sigma,0}$. We can determine their expression by solving the two-body problem. The atomic scattering length a_σ between two atoms $(\sigma_1,\sigma_2)\neq\sigma$ is given by:

$$\frac{1}{a_\sigma} = \frac{2}{\pi}\Lambda - \frac{R_e m E_{\sigma,0}}{\hbar^2}. \tag{C.3}$$

To solve the three-body problem, we introduce an ansatz of the three-body bound states:

$$|\psi\rangle = \sum_{\boldsymbol{k}_1,\boldsymbol{k}_2}\beta(\boldsymbol{k}_1,\boldsymbol{k}_2)\widehat{a}^\dagger_{\boldsymbol{k}_1,1}\widehat{a}^\dagger_{\boldsymbol{k}_2,2}\widehat{a}^\dagger_{-\boldsymbol{k}_1-\boldsymbol{k}_2,3}|0\rangle + \sum_{\sigma,\boldsymbol{k}}\frac{\alpha_\sigma(\boldsymbol{k})}{k}\widehat{a}^\dagger_{-\boldsymbol{k},\sigma}\widehat{b}^\dagger_{\boldsymbol{k},\sigma}|0\rangle. \tag{C.4}$$

where $|0\rangle$ is the vacuum. The first term corresponds to three atoms in the open channel and the second one to a molecule in the closed channel with the third atom being in the open channel.

To determine the energy $E_3 = -\hbar^2\kappa^2/m$ of the trimer, we calculate $\langle\psi|\widehat{H}|\psi\rangle$ and we obtain a set of three equations:

$$\begin{aligned}&\left[\sqrt{1+3p^2/4}+\kappa R_e(1+3p^2/4)-\frac{1}{\kappa a_\sigma}\right]\alpha_\sigma(p) \\ &= \frac{1}{\pi}\int_0^\infty dq\ln\left(\frac{p^2+q^2+pq+1}{p^2+q^2-pq+1}\right)\left[\sum_{\sigma'\neq\sigma}\alpha_{\sigma'}(q)\right],\end{aligned} \tag{C.5}$$

An example of solution

To see an example on how to resolve this problem, we will the study the particular case where $a = a'$. In this case, all three equations defined by eq. (C.6) are the same and we have $\alpha_1(p) = \alpha_2(p) = \alpha_3(p)$. The equation to solve is then:

$$\left[\sqrt{1+3p^2/4}+\kappa R_e(1+3p^2/4)-\frac{1}{\kappa a}\right]\alpha(p) = \frac{2}{\pi}\int_0^\infty dq\ln\left(\frac{p^2+q^2+pq+1}{p^2+q^2-pq+1}\right)\alpha(q) \tag{C.6}$$

To solve it, we write $x = \kappa R_e$, considered as a given parameter, and we discretize the integral to transform this equation into an eigenproblem, where the eigenvalue to find is $1/\kappa a$. Since we are looking for the fundamental state, we want the eigenvalue maximizing κ so the minimal eigenvalue. We represent in Fig. C.1 κR_e as a function of R_e/a, and we compare it to the equivalent of κ in the case of the trimeron. We see that in this particular case we do not get a clear transition between the two states, which will reflect on the phase diagram given in Fig. C.2.

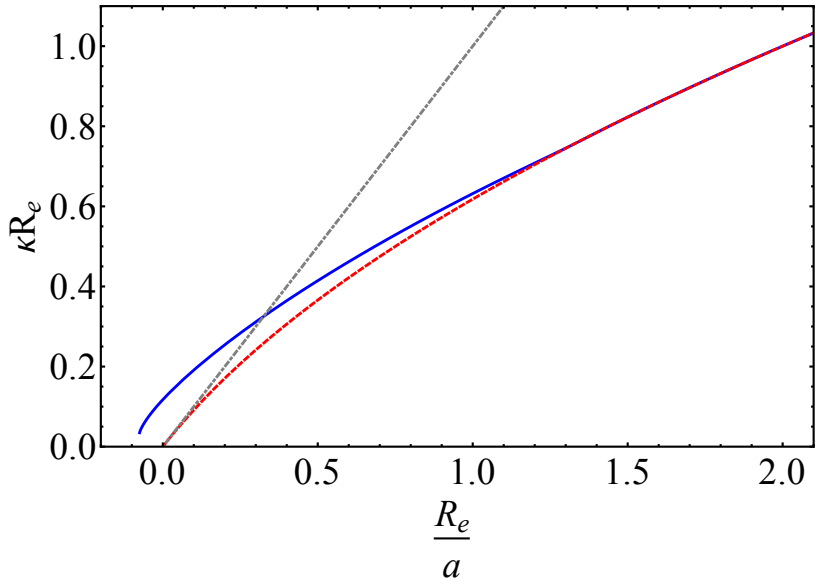

Figure C.1: Representation of κR_e versus R_e/a calculated in the case $a = a'$, and its equivalent for the dimeron. Blue solid curve: trimeron, we see that the start of the Efimov spectrum is at $a_- \simeq -11R_e$, consistent with the "universal" value $a_- \simeq -9.1 l_{VdW}$. Red dashed curve: dimeron, where we took $\kappa = \sqrt{m|E_2'|/\hbar^2}$. When the red curve surpasses the blue one, the dimeron state becomes more stable, in this particular case it actually leads to a triple point as will be seen in the phase diagram presented in the following section. Grey dot-dashed curve: dimeron, where we took the simpler expression $\kappa = 1/a$ corresponding to the limit $R_e/a \ll 1$. The intersection with the trimeron energy curve is neater in this case and is more representative of what happens away from the triple point.

We then repeat this method for several values of R_e/a and R_e/a' to get the energy of the trimer E_3 for all the conditions possible, though the calculations are not as straightforward.

To form a trimeron, one has again to extract a Cooper pair from the superfluid and break it. Taking also the mean-field energies into account, we get the energy $E_{SF} - 2\mu_F + E_3 + g_t n$ with g_t the coupling constant between the trimeron and fermions (or dimers) from the superfluid.

C.4 Building the diagram

The full phase diagram is represented in Fig. C.2.

In experiments, R_e is small compared to the interparticle distance, corresponding roughly to k_F^{-1}, where we defined the Fermi wavevector $k_F = (3\pi^2 n)^{1/3}$, hence $k_F R_e \ll 1$. We work generally in a domain where $-1 \lesssim 1/k_F a \lesssim 1$, so with $R_e/|a| = k_F R_e \times 1/k_F a \ll 1$. Consequently, the crossover region of the superfluid is actually located in a very narrow region around the y-axis. The consequence of this separation of scales is that outside of this narrow region, fermions form very loose Cooper pairs on the BCS side and weakly interacting tightly-bound dimers on the BEC side. This region is reprensented by a gray band on the phase diagram in Fig. C.2.

Concerning the impurity-fermion interaction, we have $k_F a' = (R_e/a')^{-1} \times k_F R_e$, so except in a narrow region around the x-axis where R_e/a' is small, we have $k_F a' \ll 1$,

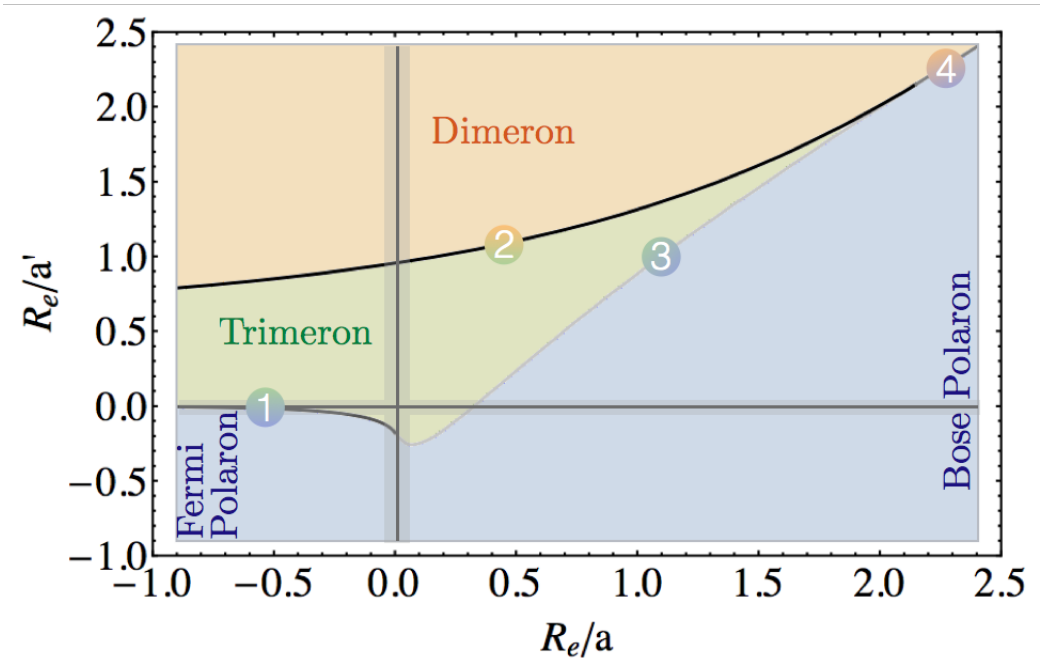

Figure C.2: Phase diagram of the system, for $m_i = m_f$. Variational approaches based on a mean-field description of the background superfluid suggest that the polaron/trimeron transition is a crossover [287]. The domain limits are calculated as explained in this section, the numbers correspond to the one in the text. We see that the trimeron/dimeron transition line is tangent to the line $a = a'$, a consequence of what was seen in Fig. C.1. The grey bands correspond to the parameter range where many-body effects affect few-body physics for a typical value $k_F R_e = 5 \times 10^{-2}$.

corresponding to the conditions of our experiment.

Depending on the different parameters, we determine which state has the lowest energy to determine the most stable one. In the dilute limit where n, k_F, E_f go to zero, we can neglect some of the terms (including the mean-field terms) and simplify all the expressions of the energies. Those are gathered in Table C.1.

	BCS limit	BEC limit
Dimeron	$E_{SF} + E_2'$	$E_{SF} - E_2 + E_2'$
Trimeron	$E_{SF} + E_3$	$E_{SF} - E_2 + E_3$
Polaron	E_{SF}	E_{SF}

Table C.1: Energy of the system in the different phases

Below, we list the equation of the different lines separating the stability domains of each phase, each number corresponding to the one on Fig. C.2 where we represented the

phase diagram of the system.

1. Fermi polaron ($R_e/a < 0$) vs trimeron: $E_3(R_e, a, a') = 0$.
2. Dimeron vs trimeron: $E_3(R_e, a, a') = E_2'(R_e, a')$.
3. Bose polaron ($R_e/a > 0$) vs trimeron: $E_3(R_e, a, a') = E_2(R_e, a)$.
4. Bose polaron vs dimeron: $E_2(R_e, a) = E_2'(R_e, a')$, which coincides with $a = a'$ so it is included in the first bisector of Fig. C.2.

Finally, we can notice in Fig. C.2 that the Fermi polaron/trimeron separation line (corresponding to the number 1) approaches the x-axis for $Re/a' \to -\infty$. In this region, the calculation is not controlled since k_F is not negligible anymore. However, since the polaron/trimeron is a crossover [287], the transition line cannot be defined precisely anyway. Furthermore, for $a = a'$, our results are consistent with the ones reported in [310] for three-component color Fermi gases.

Appendix D

Determination of the R_3 and C_{ad} constants

We present in the section our numerical evaluations of the constants R_3 and C_{ad} that we introduced in Chapter 6. We first go back to the evaluation of the three-body T-matrix to get R_3 and then study the atom-dimer T-matrix to obtain C_{ad}.

D.1 Calculating R_3

The parameter R_3 is defined by the relation

$$\Gamma^{\text{Born}} - \Gamma^{\text{Faddeev}} \underset{\Lambda\to\infty}{=} g'^2 \kappa(\eta) \ln(\Lambda R_3) + o(1). \tag{D.1}$$

Consequently, we can obtain R_3 by calculating numerically the difference between Γ^{Born} and Γ^{Faddeev}. In our framework, R_3/a' only depends on the ratio R_e/a' and the mass ratio η. The general scheme of the calculation of these terms has already been detailed in Chapter 6, so here we will directly give the results of the numerical calculations.

In Fig. D.1, we represent the numerical calculations of the difference $\Gamma_{\text{Born}} - \Gamma_{\text{Faddeev}}$ for the mass ratio $\eta = 7/6$ and $R_e/|a'| = 1$. We see that we indeed get the logarithmic behavior for this difference, with $\kappa(7/6)$ as the proportionality constant.

We show in Fig. D.2 the dimensionless parameter $R_3/|a'|$ for different values of the ratio $R_e/|a'|$ and for a mass ratio $\eta = 7/6$. For $R_e/|a'| \ll 1$, we get the asymptotic behavior $R_3 \simeq 1.50|a'|$. For $R_e/|a'| \gg 1$, we see that R_3 increases exponentially:

$$R_3 \underset{\frac{R_e}{|a'|}\gg 1}{\propto} \sqrt{R_e|a'|} \exp\left(\frac{\sqrt{3}}{16\pi^2|\kappa(7/6)|}\sqrt{\frac{R_e}{|a'|}}\right). \tag{D.2}$$

At this stage, we recall that in Chapter 6, in the perturbative expansion in a' for the polaron energy, we consider expansions for $\Lambda|a'| \ll 1$ but with $R_e/|a'|$ as an independent parameter with a given value. Consequently, we consider this exponential term as a constant included in R_3 in our perturbative calculations, and it does not affect the perturbative expansion.

The dependence on the mass ratio η is given in Table D.1 which lists numerical values of the parameter R_3 for experimentally relevant mass ratios and $R_e = 0$. For $\eta \gtrsim 0.5$ the value of R_3 is approximately constant with less than 10% variations, but it decreases significantly for smaller values.

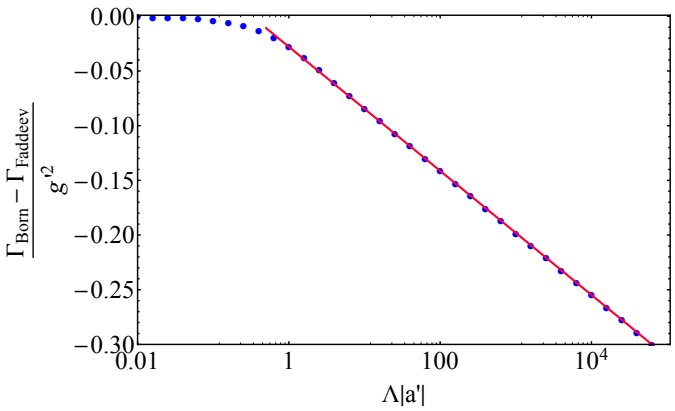

Figure D.1: Blue dots: numerical calculations of $(\Gamma_{\rm Born} - \Gamma_{\rm Faddeev})/g'^2$, for $\eta = 7/6$ and $R_e = |a'|$. Red curve: fitting curve of the blue dots in the limit $\Lambda|a'| \gg 1$. We fit the data for $\Lambda|a'| \gg 1$ with the function $\kappa(7/6)\ln(X \times A_0)$ with A_0 a fitting parameter. The parameter A_0 gives us the value of $R_3/|a'|$: we obtain for this curve $A_0 \simeq 3.10$.

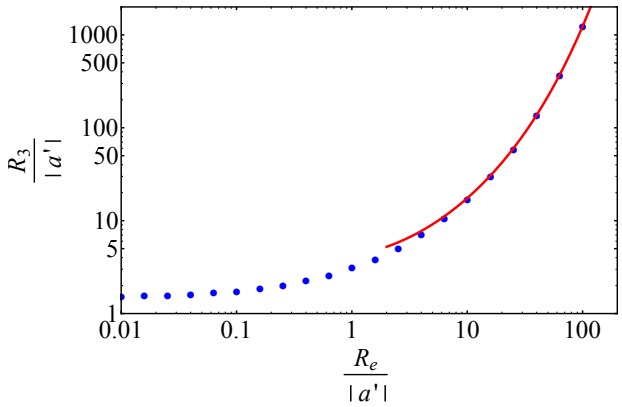

Figure D.2: Blue dots: numerical calculations of $R_3/|a'|$ for different $R_e/|a'|$ ratios and $\eta = 7/6$. Red curve: fit for $R_e/|a'| \gg 1$ using a function $A\sqrt{X}\exp\left(\frac{\sqrt{3}}{16\pi^2|\kappa(7/6)|}\sqrt{X}\right)$, with A an adjustable parameter. $A \simeq 0.8$ after optimization.

D.2 Atom-dimer scattering

In order to determine the constant C_{ad} that appears in Chapter 6 concerning the BEC side of the crossover, we study the atom-dimer problem, for fermions are tightly bound into halo-dimers in this regime.

The atom-dimer T-matrix can be computed similarly as the three-body T-matrix. Indeed, in the BEC domain the fermions are asymptotically bound, so we can treat the impurity-fermion interaction as a perturbation. This T-matrix can also be transcribed into diagrams. The initial and final states are taken with a fermion-fermion dimer and an impurity with momenta taken equal to zero. Since we want to decompose the atom-dimer interaction into a sequence of two-body interactions, all diagrams have to start and finish by a fermion-fermion interaction to "open" the molecule to enable isolated impurity-fermion interactions. A typical diagram is represented in Fig. D.3.

As all diagrams have to start and end with a fermion-fermion interaction, we have to consider the same diagrams as in the three-body scattering problem. As a consequence,

η	7/40	23/40	7/6	87/6	133/6
R_3/a'	1.03	1.41	1.50	1.46	1.46

Table D.1: Dimensionless parameter characterizing the Born expansion of the three-body scattering amplitude (Eq. (D.1)) for $R_e = 0$.

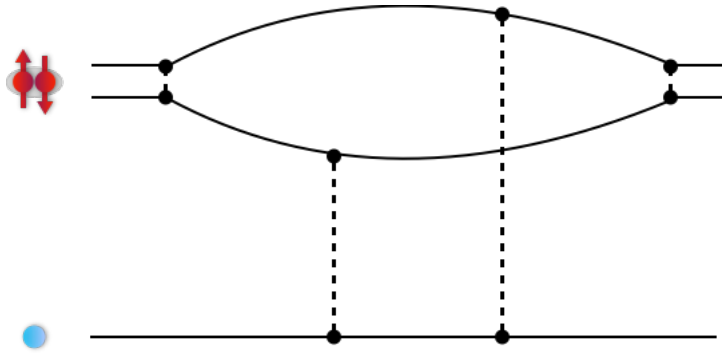

Figure D.3: Example of diagram considered for the study of atom-dimer scattering. In the initial and final state there is a dimer and an impurity atom. With the same dimensional analysis as in Chapter 6, we see that it corresponds to a logarithmically divergent term.

the atom-dimer scattering length presents the same logarithmic divergence when the range of the potential vanishes. For large Λ, the atom-dimer T-matrix scales as

$$T_{\rm ad}^{\rm div} = \frac{2g'}{\Omega}\left[1 + 8\pi^2 \frac{m_f}{m_r}\kappa(\eta)\frac{a'}{a}\left(\ln(\Lambda a) + C_{\rm ad} + ...\right)\right] \tag{D.3}$$

where the constant $C_{\rm ad}$ is computed numerically and is given in Table D.2 for experimentally relevant values of the mass ratio η. Contrary to the three-body diagrams, there is no divergence for $k \to 0$ because the binding energy of the dimer acts as a low momentum cutoff (hence the Λa in the logarithm).

η	7/40	23/40	7/6	87/6	133/6
$C_{\rm ad}$	1.52	1.59	1.56	1.37	1.36

Table D.2: Dimensionless parameter characterizing the Born expansion of the atom-dimer scattering amplitude (Eq. (D.3)) for $R_e = 0$.

Once again, the logarithmic divergence is regularized by introducing the three-body interaction. Its contribution to the atom-dimer T-matrix is computed using the renormalized expression of $g_3(\Lambda)$. It reads

$$T_{\rm ad}^{3b} = -\frac{16\pi^2 g'}{\Omega}\frac{m_f}{m_r}\kappa(\eta)\frac{a'}{a}\ln(\Lambda R_3). \tag{D.4}$$

By combining equations (D.3) and (D.4), we obtain the regularized atom-dimer T-matrix:

$$T_{\rm ad} = T_{\rm ad}^{\rm div} + T_{\rm ad}^{3b} = T_{\rm ad,Born}\left[1 - 8\pi^2 \frac{m_f}{m_r}\kappa(\eta)\frac{a'}{a}\left(\ln(R_3/a) + C_{\rm ad} + ...\right)\right] \tag{D.5}$$

where $T_{\mathrm{ad,Born}} = 2g'/\Omega$ corresponds to an atom-dimer scattering length obtained in the mean-field approximation, *ie* $a_{\mathrm{ad,Born}}/a' = 4(1+\eta)/(2+\eta)$. We can note that this expression is consistent with the asymptotic expression of g_{ad} we obtained in Chapter 6. As pointed out in Chapter 1 and [312], in the Efimovian regime $R_e \ll |a'|$ not considered here, T_{ad} should acquire a log-periodic dependence in a'.

List of publications

- "A mixture of Bose and Fermi superfluids"
  Igor Ferrier-Barbut, Marion Delehaye, Sébastien Laurent, Andrew T. Grier, Matthieu Pierce, Benno S. Rem, Frédéric Chevy, and Christophe Salomon
  Science, **345**, 1035-1038 (2014)

- "Connecting few-body inelastic decay to quantum correlations in a many-body system: a weakly coupled impurity in a resonant Fermi gas"
  Sébastien Laurent, Matthieu Pierce, Marion Delehaye, Tarik Yefsah, Frédéric Chevy, and Christophe Salomon
  Physical Review Letters, **118**, 103403 (2017)

- "Few vs many-body physics of an impurity immersed in a superfluid of spin $1/2$ attractive fermions"
  Matthieu Pierce, Wavier Leyronas, Frédéric Chevy
  arXiv:1903.01108v1

A mixture of Bose and Fermi superfluids

Igor Ferrier-Barbut, Marion Delehaye, Sébastien Laurent, Andrew T. Grier, Matthieu Pierce, Benno S. Rem, Frédéric Chevy, and Christophe Salomon

Science, **345**, 1035-1038 (2014)

collisions. An analysis with some similarities to ours for the bright debris disk of HD 172555 (*20*) found that dust created in a hypervelocity impact will have a size slope of ~ –4, in agreement with the fits of (*10*) to the IR spectrum of ID8.

After the exponential decay is removed from the data ("detrending"), the light curves at both wavelengths appear to be quasi-periodic. The regular recovery of the disk flux and lack of extraordinary stellar activity essentially eliminate coronal mass ejection (*21*) as a possible driver of the disk variability. We employed the SigSpec algorithm (*22*) to search for complex patterns in the detrended, post-impact 2013 light curve. The analysis identified two significant frequencies with comparable amplitudes, whose periods are P_1 = 25.4 ± 1.1 days and P_2 = 34.0 ± 1.5 days (Fig. 3A) and are sufficient to qualitatively reproduce most of the observed light curve features (Fig. 3B). The quoted uncertainties (*23*) do not account for systematic effects due to the detrending and thus are lower limits to the real errors. Other peaks with longer periods in the periodogram are aliases or possibly reflect long-term deviation from the exponential decay. These artifacts make it difficult to determine whether there are weak real signals near those frequencies.

We now describe the most plausible interpretation of this light curve that we have found. The two identified periods have a peak-to-peak amplitude of ~6×10^{-3} in fractional luminosity, which provides a critical constraint for models of the ID8 disk. In terms of sky coverage at the disk distance inferred from the IR SED, such an amplitude requires the disappearance and reappearance every ~30 days of the equivalent of an opaque, stellar-facing "dust panel" of radius ~110 Jupiter radii. One possibility is that the disk flux periodicity arises from recurring geometry that changes the amount of dust that we can see. At the time of the impact, fragments get a range of kick velocities when escaping into interplanetary space. This will cause Keplerian shear of the cloud (*24*), leading to an expanding debris concentration along the original orbit (supplementary text). If the ID8 planetary system is roughly edge-on, the longest dimension of the concentration will be parallel to our line of sight at the greatest elongations and orthogonal to the line of sight near conjunctions to the star. This would cause the optical depth of the debris to vary within an orbital period, in a range on the order of 1 to 10 according to the estimated disk mass and particle sizes. Our numerical simulations of such dust concentrations on moderately eccentric orbits are able to produce periodic light curves with strong overtones. P_2 and P_1 should have a 3:2 ratio if they are the first- and second-order overtones of a fundamental, which is consistent with the measurements within the expected larger errors (<2σ or better). In this case, the genuine period should be 70.8 ± 5.2 days (lower-limit errors), a value where it may have been submerged in the periodogram artifacts. This period corresponds to a semimajor axis of ~0.33 astronomical units, which is consistent with the temperature and distance suggested by the spectral models (*10*).

Despite the peculiarities of ID8, it is not a unique system. In 2012 and 2013, we monitored four other "extreme debris disks" (with disk fractional luminosity ≥10^{-2}) around solar-like stars with ages of 10 to 120 My. Various degrees of IR variations were detected in all of them. The specific characteristics of ID8 in the time domain, including the yearly exponential decay, additional more rapid weekly to monthly changes, and color variations, are also seen in other systems. This opens up the time domain as a new dimension for the study of terrestrial planet formation and collisions outside the solar system. The variability of many extreme debris disks in the era of the final buildup of terrestrial planets may provide new possibilities for understanding the early solar system and the formation of habitable planets (*25*).

REFERENCES AND NOTES

1. R. Helled *et al.*, in *Protostars and Planets VI*, H. Beuther, R. Klessen, C. Dullemond, T. Henning, Eds. (Univ. of Arizona Press, Tucson, AZ, 2014), in press; available at http://arxiv.org/abs/1311.1142.
2. M. C. Wyatt, *Annu. Rev. Astron. Astrophys.* **46**, 339–383 (2008).
3. K. Righter, D. P. O'Brien, *Proc. Natl. Acad. Sci. U.S.A.* **108**, 19165–19170 (2011).
4. S. N. Raymond, E. Kokubo, A. Morbidelli, R. Morishima, K. J. Walsh, in *Protostars and Planets VI*, H. Beuther, R. Klessen, C. Dullemond, T. Henning, Eds. (Univ. of Arizona Press, Tucson, AZ, 2014), in press; available at http://arxiv.org/abs/1312.1689.
5. R. M. Canup, *Annu. Rev. Astron. Astrophys.* **42**, 441–475 (2004).
6. M. Ćuk, S. T. Stewart, *Science* **338**, 1047–1052 (2012).
7. R. M. Canup, *Science* **338**, 1052–1055 (2012).
8. H. Y. A. Meng *et al.*, *Astrophys. J.* **751**, L17–L21 (2012).
9. D. R. Soderblom, L. A. Hillenbrand, R. D. Jeffries, E. E. Mamajek, T. Naylor, in *Protostars and Planets VI*, H. Beuther, R. Klessen, C. Dullemond, T. Henning, Eds. (Univ. of Arizona Press, Tucson, AZ, 2014), in press; available at http://arxiv.org/abs/1311.7024.
10. J. Olofsson *et al.*, *Astron. Astrophys.* **542**, 90–115 (2012).
11. P. Artymowicz, *Astrophys. J.* **335**, L79–L82 (1988).
12. G. G. Fazio *et al.*, *Astrophys. J. Suppl. Ser.* **154**, 10–17 (2004).
13. D. Jewitt, H. Matthews, *Astron. J.* **117**, 1056–1062 (1999).
14. J. A. M. McDonnell *et al.*, *Nature* **321**, 338–341 (1986).
15. D. Perez-Becker, E. Chiang, *Mon. Not. R. Astron. Soc.* **433**, 2294–2309 (2013).
16. P. H. Warren, *Geochim. Cosmochim. Acta* **72**, 3562–3585 (2008).
17. B. C. Johnson, H. J. Melosh, *Icarus* **217**, 416–430 (2012).
18. M. C. Wyatt, W. R. F. Dent, *Mon. Not. R. Astron. Soc.* **334**, 589–607 (2002).
19. B. Zuckerman, I. Song, *Astrophys. J.* **758**, 77–86 (2012).
20. B. C. Johnson *et al.*, *Astrophys. J.* **761**, 45–57 (2012).
21. R. Osten *et al.*, *Astrophys. J.* **765**, L44–L46 (2013).
22. P. Reegen, *Astron. Astrophys.* **467**, 1353–1371 (2007).
23. T. Kallinger, P. Reegen, W. W. Weiss, *Astron. Astrophys.* **481**, 571–574 (2008).
24. S. J. Kenyon, B. C. Bromley, *Astron. J.* **130**, 269–279 (2005).
25. S. Elser, B. Moore, J. Stadel, R. Morishima, *Icarus* **214**, 357–365 (2011).
26. T. Naylor *et al.*, *Mon. Not. R. Astron. Soc.* **335**, 291–310 (2002).
27. R. D. Jeffries, T. Naylor, C. R. Devey, E. J. Totten, *Mon. Not. R. Astron. Soc.* **351**, 1401–1422 (2004).

ACKNOWLEDGMENTS

H.Y.A.M, K.Y.L.S., and G.H.R. thank R. Malhotra and A. Gáspár for valuable discussions. This work is based on observations made with the Spitzer Space Telescope, which is operated by the Jet Propulsion Laboratory (JPL), California Institute of Technology, under a contract with NASA. Support for this work was provided by NASA through an award issued by JPL/Caltech and by NASA grant NNX13AE74G. All data are publicly available through the NASA/IPAC Infrared Science Archive.

SUPPLEMENTARY MATERIALS

www.sciencemag.org/content/345/6200/1032/suppl/DC1
Supplementary Text
Figs. S1 to S4
References (*28*–*45*)

23 April 2014; accepted 15 July 2014
10.1126/science.1255153

SUPERFLUIDITY

A mixture of Bose and Fermi superfluids

I. Ferrier-Barbut,* M. Delehaye, S. Laurent, A. T. Grier,† M. Pierce, B. S. Rem,‡ F. Chevy, C. Salomon

Superconductivity and superfluidity of fermionic and bosonic systems are remarkable many-body quantum phenomena. In liquid helium and dilute gases, Bose and Fermi superfluidity has been observed separately, but producing a mixture in which both the fermionic and the bosonic components are superfluid is challenging. Here we report on the observation of such a mixture with dilute gases of two lithium isotopes, lithium-6 and lithium-7. We probe the collective dynamics of this system by exciting center-of-mass oscillations that exhibit extremely low damping below a certain critical velocity. Using high-precision spectroscopy of these modes, we observe coherent energy exchange and measure the coupling between the two superfluids. Our observations can be captured theoretically using a sum-rule approach that we interpret in terms of two coupled oscillators.

In recent years, ultracold atoms have emerged as a unique tool to engineer and study quantum many-body systems. Examples include weakly interacting Bose-Einstein condensates (*1*, *2*), two-dimensional gases (*3*), and the superfluid-Mott insulator transition (*4*) in the case of bosonic atoms, and the crossover between Bose-Einstein condensation (BEC) and fermionic superfluidity described by the the theory of Bardeen, Cooper, and Schrieffer (BCS) for fermionic atoms (*5*). Mixtures of Bose-Einstein condensates were produced shortly after the observation of BEC (*2*), and a BEC mixed with a single-spin state Fermi sea was originally observed in (*6*, *7*). However, realizing a mixture in which both fermionic and bosonic species are superfluid has been experimentally challenging. This has also been a long-sought goal in liquid helium, where superfluidity was achieved separately in both bosonic ^{4}He and fermionic ^{3}He. The double superfluid should undergo a transition

between s-wave and p-wave Cooper pairs as the ^{3}He dilution is varied (*8*). However, because of strong interactions between the two isotopes, ^{3}He-^{4}He mixtures contain only a small fraction of ^{3}He (typically 6%) which, so far, has prevented attainment of simultaneous superfluidity for the two species (*8*, *9*).

Here we report on the production of a Bose-Fermi mixture of quantum gases in which both species are superfluid. Our system is an ultracold gas of fermionic ^{6}Li in two spin states mixed with ^{7}Li bosons and confined in an optical dipole trap. Using radio-frequency pulses, we prepare ^{6}Li atoms in their two lowest hyperfine states $|1_f\rangle$ and $|2_f\rangle$, whereas ^{7}Li is spin polarized in the second-to-lowest state $|2_b\rangle$ (*10*). For this combination of states, in the vicinity of the ^{6}Li Feshbach resonance at a magnetic field of 832 G (*11*), the scattering length of the bosonic isotope $a_b = 70a_0$ (a_0 is the Bohr radius) is positive, preventing collapse of the BEC. The boson-fermion interaction is characterized by a scattering length $a_{bf} = 40.8a_0$ that does not depend on magnetic field in the parameter range studied here. At resonance, the Fermi gas exhibits a unitary limited collision rate, and lowering the optical dipole trap depth leads to extremely efficient evaporation. Owing to a large excess of ^{6}Li atoms with respect to ^{7}Li, the Bose gas is sympathetically driven to quantum degeneracy.

The two clouds reach the superfluid regime after a 4-s evaporation ramp (*10*). As the ^{7}Li Bose gas is weakly interacting, the onset of BEC is detected by the growth of a narrow peak in the density profile of the cloud. From previous studies on atomic Bose-Einstein condensates, we conclude that the ^{7}Li BEC is in a superfluid phase. Superfluidity in a unitary Fermi gas is notoriously more difficult to detect because of the absence of any qualitative modification of the density profile at the phase transition. To demonstrate the superfluidity of the fermionic component of the cloud, we slightly imbalance the two spin populations. In an imbalanced gas, the cloud is organized in concentric layers, with a fully paired superfluid region at its center, where Cooper pairing maintains equal spin populations. This ^{6}Li superfluid core can be detected by the presence of a plateau in the doubly integrated density difference (*12*). Examples of density profiles of the bosonic and fermionic superfluids are shown in Fig. 1, where both the Bose-Einstein condensate (blue circles) and the plateau (black diamonds in the inset) are clearly visible. Our coldest samples contain $N_b = 4 \times 10^4$ ^{7}Li atoms and $N_f = 3.5 \times 10^5$ ^{6}Li atoms. The absence of a thermal fraction in the bosonic cloud indicates a temperature below $0.5T_{c,b}$, where $k_B T_{c,b} = 0.94\hbar\bar{\omega}_b N_b^{1/3}$ is the critical temperature of the ^{7}Li bosons, and $\bar{\omega}_b$ ($\bar{\omega}_f$) is the geometric mean trapping frequency for ^{7}Li (^{6}Li). Combined with the observation of the ^{6}Li plateau, this implies that the Fermi cloud is also superfluid with a temperature below $0.8T_{c,f}$. Here, $T_{c,f}$ is the critical temperature for superfluidity of a spin-balanced, harmonically trapped Fermi gas at unitarity, $T_{c,f} = 0.19T_F$ (*13*), and $k_B T_F = \hbar\bar{\omega}_f(3N_f)^{1/3}$ is the Fermi temperature. The superfluid mixture is very stable, with a lifetime exceeding 7 s for our coldest samples.

As seen in Fig. 1, the Bose-Fermi interaction is too weak to alter significantly the density profiles of the two species (*14*). To probe the interaction between the two superfluids, we study the dynamics of the mass centers of the two isotopes (dipole modes), a scheme used previously for the study of mixtures of Bose-Einstein condensates (*15*, *16*), mixtures of Bose-Einstein condensates and spin-polarized Fermi seas (*17*), spin diffusion in Fermi gases (*18*), or integrability in one-dimensional systems (*19*). In a purely harmonic trap and in the absence of interspecies interactions, the dipole mode of each species is undamped and can therefore be measured over long time spans to achieve a high-frequency resolution and detect small perturbations of the system. We excite the dipole modes by shifting the initial position of the ^{6}Li and ^{7}Li clouds by a displacement d along the weak direction z of the trap (*10*). We then release them and let them evolve during a variable time t, after which we measure their positions. By monitoring the cloud oscillations during up to 4 s, we determine their frequencies with high precision ($\frac{\Delta\omega}{\omega} \lesssim 2 \times 10^{-3}$). In the absence of the other species, the oscillation frequencies of ^{6}Li and ^{7}Li are, respectively, $\omega_f = 2\pi \times 16.80(2)$ Hz and $\omega_b = 2\pi \times 15.27(1)$ Hz. In the axial direction, the confinement is mostly magnetic, and at high magnetic field, both species are in the Paschen-Back regime, where the electronic and nuclear spin degrees of freedom are decoupled. In this regime, the magnetic confinement mostly results from the electronic spin and is therefore almost identical for the two isotopes. The ratio ω_f/ω_b is then very close to the expected value $\sqrt{7/6} \simeq 1.08$ based on the ratio of the atomic masses (*20*).

Contrary to the large damping observed in the Bose-Bose mixtures (*15*), we observe long-lived oscillations of the Bose-Fermi superfluid mixture at frequencies ($\tilde{\omega}_b$, $\tilde{\omega}_f$). These oscillations extend over more than 4 s with undetectable damping (Fig. 2 and fig. S2). This very weak dissipation is only observed when the initial displacement d is below 100 μm, corresponding to a maximum relative velocity $v_{max} = (\tilde{\omega}_b + \tilde{\omega}_f)d$ below 18 mm/s $\simeq 0.4\ v_F$, where $v_F = \sqrt{2k_B T_F/m_f}$. In this situation, the BEC explores only the central part of the much broader Fermi cloud. When $v_{max} > v_c = 0.42^{+0.05}_{-0.11} v_F = 20^{+2}_{-5}$ mm/s, we observe a sharp onset of damping and heating of the BEC compatible with the Landau criterion for breakdown of superfluidity (Fig. 2C) (*10*). For comparison, the sound velocity of an elongated Fermi gas at its center is $v_s' = \xi^{1/4} v_F/\sqrt{5} = 17$ mm/s (*21*), where $\xi = 0.38$ is the Bertsch parameter (*5*, *13*). The measured critical velocity v_c is very close to v_s' and is clearly above the BEC sound velocity of ≃5 mm/s at its center.

Two striking phenomena are furthermore observed. First, whereas the frequency $\tilde{\omega}_f$ of ^{6}Li oscillations is almost unchanged from the value in the absence of ^{7}Li, that of ^{7}Li is downshifted

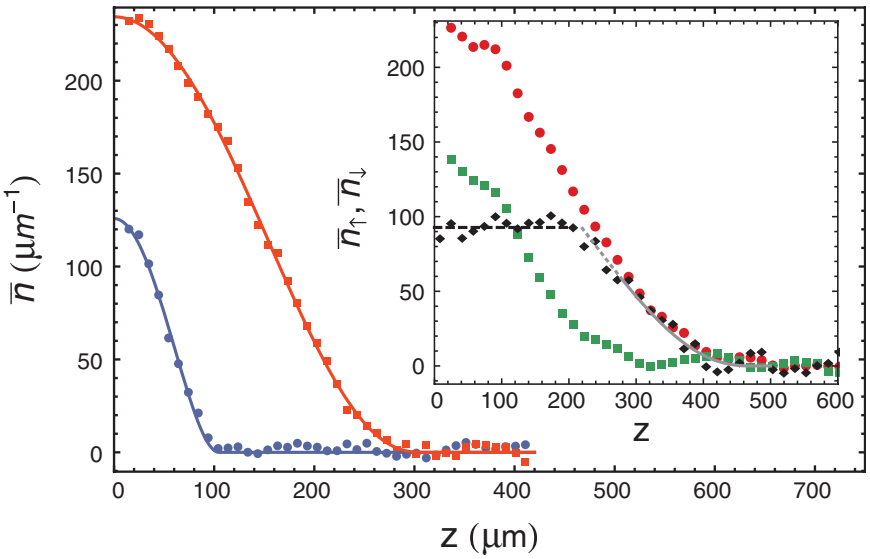

Fig. 1. Density profiles in the double superfluid regime. $N_b = 4 \times 10^4$ ^{7}Li atoms and $N_f = 3.5 \times 10^5$ ^{6}Li atoms are confined in a trap at a temperature below 130 nK. The density profiles $\bar{n}_b$ (blue circles) and $\bar{n}_{f,\uparrow}$ (red squares) are doubly integrated over the two transverse directions. The blue (red) solid line is a fit to the ^{7}Li (^{6}Li) distribution by a mean-field (unitary Fermi gas) EoS in the Thomas-Fermi approximation. Inset: Spin-imbalanced Fermi gas ($N_{f,\uparrow} = 2 \times 10^5$, $N_{f,\downarrow} = 8 \times 10^4$) in thermal equilibrium with a BEC. Red circles: $\bar{n}_{f,\uparrow}$; green squares: $\bar{n}_{f,\downarrow}$; black diamonds: difference $\bar{n}_{f,\uparrow} - \bar{n}_{f,\downarrow}$. The plateau (black dashed line) indicates superfluid pairing (*12*). Gray solid line: Thomas-Fermi profile of a noninteracting Fermi gas for the fully spin-polarized outer shell prolonged by the partially polarized normal phase (gray dashed line).

Laboratoire Kastler-Brossel, École Normale Supérieure, Collège de France, CNRS and UPMC, 24 rue Lhomond, 75005 Paris, France.
***Corresponding author. E-mail: iferrier@lkb.ens.fr** †Present address: Van Swinderen Institute, University of Groningen, Faculty of Mathematics and Natural Sciences, Zernikelaan 25, 9747 AA Groningen, Netherlands. ‡Present address: Institut für Laserphysik, Universität Hamburg, Luruper Chaussee 149, Building 69, D-22761 Hamburg, Germany.

to $\tilde{\omega}_b = 2\pi \times 15.00(2)$ Hz. Second, the amplitude of oscillations of the bosonic species displays a beat at a frequency $\simeq(\tilde{\omega}_f - \tilde{\omega}_b)/(2\pi)$, revealing coherent energy transfer between the two clouds (Fig. 2B). To interpret the frequency shift of the ^{7}Li atoms, we note that $N_b \ll N_f$, which allows us to treat the BEC as a mesoscopic impurity immersed in a Fermi superfluid. Similarly to the Fermi polaron case (*22*), the effective potential seen by the bosons is the sum of the trapping potential $V(r)$ and the mean-field interaction $g_{bf}n_f(r)$, where n_f is the total fermion density, $g_{bf} = 2\pi\hbar^2 a_{bf}/m_{bf}$, and $m_{bf} = \frac{m_b m_f}{m_b+m_f}$ is the ^{6}Li/^{7}Li reduced mass. Neglecting at first the back-action of the bosons on the fermions, we can assume that n_f is given by the local-density-approximation result $n_f(r) = n_f^{(0)}(\mu_f^0 - V(r))$, where $n_f^{(0)}(\mu)$ is the stationary equation of state (EoS) of the Fermi gas. Because the Bose-Einstein condensate is much smaller than the Fermi cloud (Fig. 2A), $V(r)$ is smaller than μ_f^0 over the BEC volume. We can thus expand $n_f^{(0)}$, and we get

$$V_{eff}(r) = g_{bf}n_f(0) + V(r)\left[1 - g_{bf}\left(\frac{dn_f^{(0)}}{d\mu_f}\right)_{r=0}\right] \quad (1)$$

We observe that the effective potential is still harmonic and the rescaled frequency is given by

$$\tilde{\omega}_b \simeq \omega_b\left(1 - \frac{1}{2}g_{bf}\left(\frac{dn_f^{(0)}}{d\mu_f}\right)_{r=0}\right) \quad (2)$$

For a unitary Fermi gas, the chemical potential is related to the density by $\mu_f = \xi\hbar^2(3\pi^2 n_f)^{2/3}/2m_f$. In the weakly coupled limit, we get $\frac{\delta\omega_b}{\omega_b} = \frac{\omega_b - \tilde{\omega}_b}{\omega_b} = \frac{13k_F a_{bf}}{7\pi\xi^{5/4}}$, where $\hbar k_F = \sqrt{2\hbar m_f \bar{\omega}_f (3N_f)^{1/3}}$ is the Fermi momentum of a noninteracting harmonically trapped Fermi gas. Using our experimental parameters $k_F = 4.6 \times 10^6$ m^{-1}, we predict a value $\tilde{\omega}_b \simeq 2\pi \times 14.97$ Hz, in very good agreement with the observed value 15.00(2)Hz.

To understand the amplitude modulation, we now take into account the back-action on the fermions. A fully quantum formalism using a sum-rule approach (*23*–*25*) leads to a coupled oscillator model in which the positions of the two clouds obey the following equations (*10*)

$$M_f\ddot{z}_f = -K_f z_f - K_{bf}(z_f - z_b) \quad (3)$$

$$M_b\ddot{z}_b = -K_b z_b - K_{bf}(z_b - z_f) \quad (4)$$

where $M_b = N_b m_b$ ($M_f = N_f m_f$) is the total mass of the ^{7}Li (^{6}Li) cloud, $K_b = M_b\omega_b^2$ ($K_f = M_f\omega_f^2$) is the spring constant of the axial magnetic confinement, and K_{bf} is a phenomenological (weak) coupling constant describing the mean-field interaction between the two isotopes. To recover the correct frequency shift (Eq. 2), we take $K_{bf} = 2K_b\frac{\delta\omega_b}{\omega_b}$. Solving these equations with the initial condition $z_f(0) = z_b(0) = d$, and defining $\rho = N_b/N_f$ and $\varepsilon = \frac{2m_b}{m_b - m_f}\left(\frac{\tilde{\omega}_b - \omega_b}{\omega_b}\right)$, in the limit $\rho, \varepsilon \ll 1$ we get

$$z_f = d[(1 - \varepsilon\rho)\cos(\tilde{\omega}_f t) + \varepsilon\rho\cos(\tilde{\omega}_b t)] \quad (5)$$

$$z_b = d[-\varepsilon\cos(\tilde{\omega}_f t) + (1 + \varepsilon)\cos(\tilde{\omega}_b t)] \quad (6)$$

The predictions of Eqs. 5 and 6 agree well with experiment (Fig. 2B). Interestingly, the peak-to-peak modulation of the amplitude of ^{7}Li is much larger than the relative frequency shift, a consequence of the almost exact tuning of the two oscillators (up to a factor $\sqrt{6/7}$). Thus, the mass prefactor in the expression for ε is large (=14) and leads to $\varepsilon \simeq 0.25$ at unitarity. This results in efficient energy transfer between the two modes despite their weak coupling, as observed.

We now extend our study of the Bose-Fermi superfluid mixture to the BEC-BCS crossover by tuning the magnetic field away from the resonance value $B_f = 832$ G. We explore a region from 860 G down to 780 G where $1/k_F a_f$ spans the interval $[-0.4, +0.8]$. In this whole domain, except in a narrow region between 845 and 850 G where the boson-boson scattering length

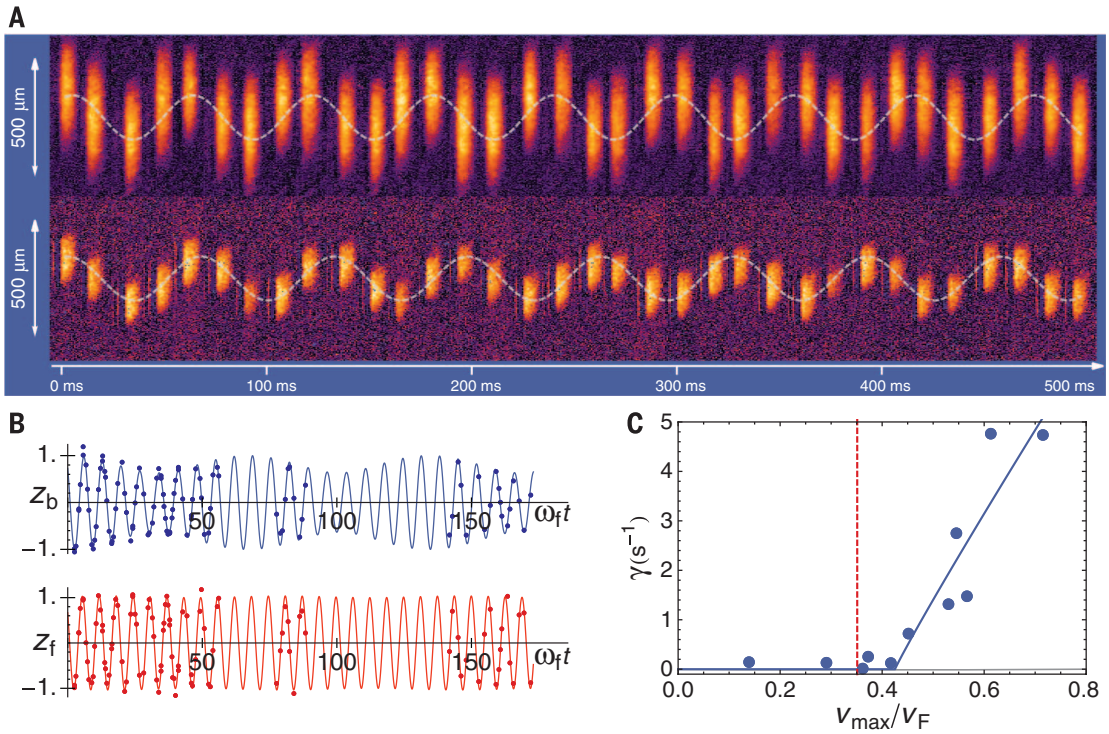

Fig. 2. Coupled oscillations of the superfluid mixture. (**A**) Center-of-mass oscillations. The oscillations are shown over the first 500 ms at a magnetic field of 835 G for a Fermi superfluid (top) and a Bose superfluid (bottom).The oscillation period of ^{6}Li (^{7}Li) is 59.7(1) ms [66.6(1) ms], leading to a dephasing of π near 300 ms. These oscillations persist for more than 4 s with no visible damping. The maximum relative velocity between the two clouds is 1.8 cm/s. (**B**) Coupled oscillations. Symbols: Center-of-mass oscillation of ^{7}Li (top) and ^{6}Li (bottom) displaying coherent energy exchange between both superfluids. Solid lines: Theory for an initial displacement d of 100 µm at a magnetic field of 835 G; see text. (**C**) Critical damping. Symbols: Damping rate (blue circles) of the amplitude of the center-of-mass oscillations of the ^{7}Li BEC as a function of the maximal relative velocity between the two superfluids normalized to the Fermi velocity of the ^{6}Li gas. Data taken at 832 G. From these data and using a fit function given in (*10*) (solid line), we extract $v_c = 0.42^{+0.05}_{-0.11}v_F$. The red dashed line shows the speed of sound of an elongated unitary Fermi superfluid $v_s' = \xi^{1/4}v_F/\sqrt{5} = 0.35v_F$ (*20*).

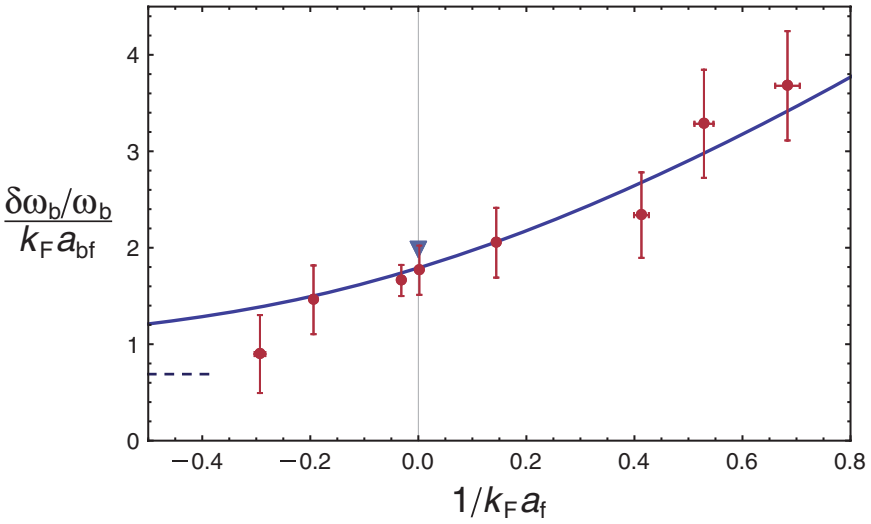

Fig. 3. Dipole mode frequency shift in the BEC-BCS crossover. Red circles: Experiment. Blue line: zero-temperature prediction from the equation of state of (*26*); dashed line: ideal Fermi gas. Blue triangle: prediction from (*13*). Error bars include systematic and statistical errors at 1 SD.

is negative, the mixture is stable and the damping extremely small.

The frequency shift of the BEC (Eq. 2) now probes the derivative of the EoS $n_f(\mu_f)$ in the BEC-BCS crossover. In the zero-temperature limit and under the local density approximation, Eq. 2 obeys the universal scaling $\frac{\delta\omega_b}{\omega_b} = k_F a_{bf} f\left(\frac{1}{k_F a_f}\right)$

In Fig. 3, we compare our measurements to the prediction for the function f obtained from the zero-temperature EoS measured in (*26*). On the BCS side, $(1/k_F a_f < 0)$, the frequency shift is reduced and tends to that of a noninteracting Fermi gas. Far on the BEC side $(1/k_F a_f \gg 1)$, we can compute the frequency shift using the EoS of a weakly interacting gas of dimers. Within the mean-field approximation, we have $\frac{dn_f}{d\mu_f} = \frac{2m_f}{\pi\hbar^2 a_{dd}}$, where $a_{dd} = 0.6a_f$ is the dimer-dimer scattering length. This expression explains the increase in the frequency shift when a_f is reduced, i.e., moving toward the BEC side [see (*10*) for the effect of Lee-Huang-Yang quantum correction].

The excellent agreement between experiment and our model confirms that precision measurements of collective modes are a sensitive dynamical probe of equilibrium properties of many-body quantum systems (*27*). Our approach can be extended to the study of higher-order excitations. In particular, although there are two first sound modes, one for each atomic species, we expect only one second sound for the superfluid mixture (*28*) if cross-thermalization is fast enough. In addition, the origin of the critical velocity for the relative motion of Bose and Fermi superfluids is an intriguing question that can be further explored in our system. Finally, a richer phase diagram may be revealed when N_b/N_f is increased (*29*) or when the superfluid mixture is loaded in an optical lattice (*30*).

REFERENCES AND NOTES

1. W. Ketterle, *Rev. Mod. Phys.* **74**, 1131–1151 (2002).
2. E. A. Cornell, C. E. Wieman, *Rev. Mod. Phys.* **74**, 875–893 (2002).
3. Z. Hadzibabic, P. Krüger, M. Cheneau, B. Battelier, J. Dalibard, *Nature* **441**, 1118–1121 (2006).
4. M. Greiner, O. Mandel, T. Esslinger, T. W. Hänsch, I. Bloch, *Nature* **415**, 39–44 (2002).
5. W. Zwerger, Ed., *The BCS-BEC Crossover and the Unitary Fermi Gas*, vol. 836 of *Lecture Notes in Physics* (Springer, Berlin, 2012).
6. F. Schreck *et al.*, *Phys. Rev. Lett.* **87**, 080403 (2001).
7. A. G. Truscott, K. E. Strecker, W. I. McAlexander, G. B. Partridge, R. G. Hulet, *Science* **291**, 2570–2572 (2001).
8. J. Rysti, J. Tuoriniemi, A. Salmela, *Phys. Rev. B* **85**, 134529 (2012).
9. J. Tuoriniemi *et al.*, *J. Low Temp. Phys.* **129**, 531–545 (2002).
10. See supplementary materials on *Science* Online.
11. G. Zürn *et al.*, *Phys. Rev. Lett.* **110**, 135301 (2013).
12. T. De Silva, E. Mueller, *Phys. Rev. A* **73**, 051602 (2006).
13. M. J. H. Ku, A. T. Sommer, L. W. Cheuk, M. W. Zwierlein, *Science* **335**, 563–567 (2012).
14. K. Mølmer, *Phys. Rev. Lett.* **80**, 1804–1807 (1998).
15. D. S. Hall, M. R. Matthews, J. R. Ensher, C. E. Wieman, E. A. Cornell, *Phys. Rev. Lett.* **81**, 1539–1542 (1998).
16. P. Maddaloni, M. Modugno, C. Fort, F. Minardi, M. Inguscio, *Phys. Rev. Lett.* **85**, 2413–2417 (2000).
17. F. Ferlaino *et al.*, *J. Opt. B Quantum Semiclassical Opt.* **5**, S3–S8 (2003).
18. A. Sommer, M. Ku, G. Roati, M. W. Zwierlein, *Nature* **472**, 201–204 (2011).
19. T. Kinoshita, T. Wenger, D. S. Weiss, *Nature* **440**, 900–903 (2006).
20. Because of a slight deviation from the Paschen-Back regime for ^{7}Li, this ratio is 1.1 instead of 1.08.
21. Y. Hou, L. Pitaevskii, S. Stringari, *Phys. Rev. A* **88**, 043630 (2013).
22. C. Lobo, A. Recati, S. Giorgini, S. Stringari, *Phys. Rev. Lett.* **97**, 200403 (2006).
23. S. Stringari, *J. Phys. IV France* **116**, 47–66 (2004).
24. T. Miyakawa, T. Suzuki, H. Yabu, *Phys. Rev. A* **62**, 063613 (2000).
25. A. Banerjee, *Phys. Rev. A* **76**, 023611 (2007).
26. N. Navon, S. Nascimbène, F. Chevy, C. Salomon, *Science* **328**, 729–732 (2010).
27. M. K. Tey *et al.*, *Phys. Rev. Lett.* **110**, 055303 (2013).
28. G. Volovik, V. Mineev, I. Khalatnikov, *Sov. Phys. JETP* **69**, 675 (1975).
29. T. Ozawa, A. Recati, S. Stringari, http://arxiv.org/abs/1405.7187 (2014).
30. A. B. Kuklov, B. V. Svistunov, *Phys. Rev. Lett.* **90**, 100401 (2003).

ACKNOWLEDGMENTS

We thank S. Stringari and Y. Castin for fruitful discussions and S. Balibar, J. Dalibard, F. Gerbier, S. Nascimbène, C. Cohen-Tannoudji, and M. Schleier-Smith for critical reading of the manuscript. We acknowledge support from the European Research Council Ferlodim and Thermodynamix, the Ile de France Nano-K (contract Atomix), and Institut de France Louis D. Prize.

SUPPLEMENTARY MATERIALS

www.sciencemag.org/content/345/6200/1035/suppl/DC1
Materials and Methods
Figs. S1 to S4
References (*31*–*34*)

29 April 2014; accepted 30 June 2014
Published online 17 July 2014;
10.1126/science.1255380

EARTHQUAKE DYNAMICS

Strength of stick-slip and creeping subduction megathrusts from heat flow observations

Xiang Gao[1] and Kelin Wang[2,3]*

Subduction faults, called megathrusts, can generate large and hazardous earthquakes. The mode of slip and seismicity of a megathrust is controlled by the structural complexity of the fault zone. However, the relative strength of a megathrust based on the mode of slip is far from clear. The fault strength affects surface heat flow by frictional heating during slip. We model heat-flow data for a number of subduction zones to determine the fault strength. We find that smooth megathrusts that produce great earthquakes tend to be weaker and therefore dissipate less heat than geometrically rough megathrusts that slip mainly by creeping.

Subduction megathrusts that primarily exhibit stick-slip behavior can produce great earthquakes, but some megathrusts are observed to creep while producing small and moderate-size earthquakes. The relationship between seismogenesis and strength of subduction megathrust is far from clear. Faults that produce great earthquakes are commonly thought of as being stronger than those that creep (*1*). Megathrusts that are presently locked to build up stress for future great earthquakes are thus described as being "strongly coupled." However, some studies have proposed strong creeping megathrusts because of the geometric irregularities of very rugged subducted sea floor (*2*, *3*).

Contrary to a widely held belief, geodetic and seismic evidence shows that very rough subducting sea floor promotes megathrust creep (*2*). All

Connecting few-body inelastic decay to quantum correlations in a many-body system: a weakly coupled impurity in a resonant Fermi gas

Sébastien Laurent, Matthieu Pierce, Marion Delehaye, Tarik Yefsah, Frédéric Chevy, and Christophe Salomon

Physical Review Letters, **118**, 103403 (2017)

Connecting Few-Body Inelastic Decay to Quantum Correlations in a Many-Body System: A Weakly Coupled Impurity in a Resonant Fermi Gas

Sébastien Laurent,* Matthieu Pierce, Marion Delehaye,† Tarik Yefsah, Frédéric Chevy, and Christophe Salomon
Laboratoire Kastler Brossel, ENS-PSL Research University, CNRS, UPMC-Sorbonne Universités, Collège de France, 24 rue Lhomond, 75005 Paris, France
(Received 22 December 2016; published 10 March 2017)

We study three-body recombination in an ultracold Bose-Fermi mixture. We first show theoretically that, for weak interspecies coupling, the loss rate is proportional to Tan's contact. Second, using a ^{7}Li/^{6}Li mixture we probe the recombination rate in both the thermal and dual superfluid regimes. We find excellent agreement with our model in the BEC-BCS crossover. At unitarity where the fermion-fermion scattering length diverges, we show that the loss rate is proportional to $n_f^{4/3}$, where n_f is the fermionic density. This unusual exponent signals nontrivial two-body correlations in the system. Our results demonstrate that few-body losses can be used as a quantitative probe of quantum correlations in many-body ensembles.

DOI: 10.1103/PhysRevLett.118.103403

Understanding strongly correlated quantum many-body systems is one of the most daunting challenges in modern physics. Thanks to a high degree of control and tunability, quantum gases have emerged as a versatile platform for the exploration of a broad variety of many-body phenomena [1], such as the crossover from Bose-Einstein condensation (BEC) to Bardeen-Cooper-Schrieffer (BCS) superfluidity [2], quantum magnetism [3], or many-body localization [4]. At ultralow temperatures, atomic vapors are metastable systems and are plagued by three-body recombination which represents a severe limitation for the study of some dense interacting systems. A prominent example is the strongly correlated Bose gas [5,6] that bears the prospect of bridging the gap between dilute quantum gases and liquid helium. However, inelastic losses can also be turned into an advantage. For instance, they can be used to control the state of a system through the Zeno effect [7–9], or serve as a probe of nontrivial few-body states, as demonstrated by the observation of Efimov trimers, originally predicted in nuclear physics, but observed for the first time in Bose gases as resonances in three-body loss spectra [10].

In this Letter, we study inelastic losses in a mixture of spinless bosons and spin 1/2 fermions with tunable interaction. We show that when the Bose-Fermi coupling is weak, the loss rate can be related to the fermionic contact parameter, a universal quantity overarching between microscopic and macroscopic properties of a many-body system with zero-range interactions [11–19]. We first check our prediction on the strongly attractive side of the fermionic Feshbach resonance, where we recover known results on atom-dimer inelastic scattering. We then turn to the unitary limit where the fermion-fermion scattering length is infinite. We demonstrate both theoretically and experimentally—with a ^{6}Li/^{7}Li Fermi-Bose mixture—that the bosons decay at a rate proportional to $n_f^{4/3}$, where n_f is the fermion density. The unusual fractional exponent results from nontrivial quantum correlations in the resonant gas. Our method offers a new way to measure the two-body contact of the homogeneous Fermi gas. More generally, our work shows that the decay of an impurity immersed in a strongly correlated many-body system is a quantitative probe of its quantum correlations.

Inelastic decay of an impurity inside a two-component Fermi gas has been studied previously both in the weakly

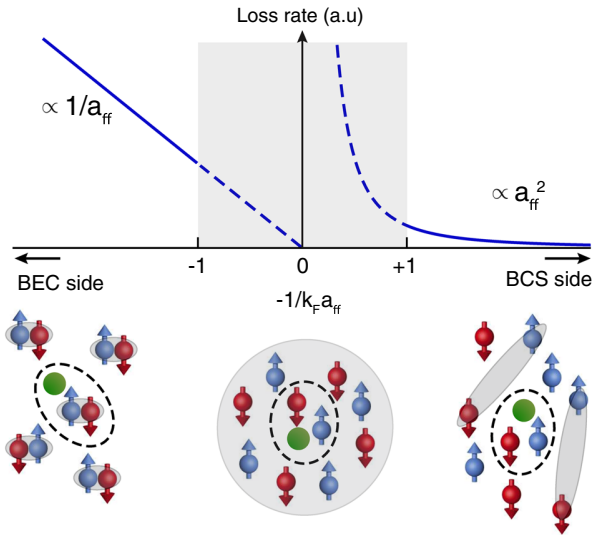

FIG. 1. Sketch of inelastic decay of an impurity immersed in a tunable Fermi gas. On the BEC side, ↑ and ↓ fermions are paired in tightly bound molecules and the decay mechanism is a two-body process involving the impurity (green disk) and a molecule. The loss rate scales as $1/a_{ff}$ [20,24]. On the BCS side, the loss occurs through a three-body process and it scales as a_{ff}^2 in the mean-field limit [20]. The extrapolation of these two asymptotic behaviors towards the strongly correlated regime yields contradictory results (grey area).

TABLE I. Scaling of the boson-fermion mixture loss rate and of Tan's contact [11], C_2, in the BEC-BCS crossover. Both scalings are identical in the weakly and strongly attractive limits. As $k_F = (3\pi^2 n_f)^{1/3}$, at unitarity C_2 scales as $n_f^{4/3}$. ζ is a dimensionless constant, $\zeta = 0.87(3)$ [17,25].

	BEC	Unitary	BCS
$(\dot{n}_b/n_b)$	$\propto (n_m/a_{ff})$ [20]	$\propto n_f^{4/3}$	$\propto a_{ff}^2 n_f^2$ [20]
C_2	$8\pi(n_m/a_{ff})$	$(2\zeta/5\pi)k_F^4$	$4\pi^2 a_{ff}^2 n_f^2$

and strongly attractive limits of the BEC-BCS crossover [20–23], see Fig. 1 and Table I. When the fermion-fermion interaction is weak, the fermions behave almost as isolated particles and the recombination can be described as a three-body process involving one spin-up (↑), one spin-down (↓) fermion and the impurity (a boson in our experiments). In this case, the impurity or boson density n_b follows a rate equation $\dot{n}_b = -L_3 n_f^2 n_b$, with $L_3 \propto a_{ff}^2$, where a_{ff} is the fermion-fermion scattering length [20,22,24]. In contrast, on the strongly attractive side of the Feshbach resonance, the fermions form halo dimers of size $\simeq a_{ff}$ and the relaxation occurs through two-body processes between one such molecule and one boson. In this case the rate equation for bosons reads $\dot{n}_b = -L_2 n_m n_b$, where $n_m = n_f/2$ is the molecule density. Far from the Feshbach resonance, the two-body loss rate scales as $1/a_{ff}$ as a consequence of the enhanced overlap of the halo dimer wave function with the deeply bound product molecules [20,24]. However, these two scalings give rise to a paradox in the central region of the BEC-BCS crossover. Indeed, as depicted in Fig. 1, the extrapolation towards unitarity leads to contradictory results depending on whether we approach the resonance from the BEC or the BCS side. In the former case, one would predict an increasingly long lifetime at unitarity while it tends to a vanishingly small value in the latter case. This paradox has a fundamental origin: these two scalings are obtained in the dilute limit where the recombination can be described by a well-defined few-body process, whereas this hypothesis fails in the strongly correlated regime where $n_f|a_{ff}|^3 \gg 1$. There, it is not possible to single out two fermions from the whole many-body system. Instead, the inelastic loss involving a boson and two fermions is tied to the correlations of the whole ensemble. A first hint towards reconciling these two behaviors near unitarity is to assume that they saturate for $a_{ff} \simeq n_f^{-1/3}$, yielding the same scaling $\dot{n}_b \propto n_f^{4/3} n_b$.

The three asymptotic regimes—BEC, BCS, and unitary—were obtained using different theoretical approaches and we now show that, using Tan's contact, they can be unified within the same framework. The recombination rate is proportional to the probability of having the three particles within a distance b from each other, where b is the typical size of the deeply bound molecule formed during the collision [26–28]. Take $\rho_3(\boldsymbol{r}_\uparrow, \boldsymbol{r}_\downarrow, \boldsymbol{r}_b)$ the three-body probability distribution of the system. When the bosons are weakly coupled to the fermions, we can factor it as $\rho_3(\boldsymbol{r}_\uparrow, \boldsymbol{r}_\downarrow, \boldsymbol{r}_b) = \rho_f(\boldsymbol{r}_\uparrow, \boldsymbol{r}_\downarrow)\rho_b(\boldsymbol{r}_b)$. Integrating over the positions of the three atoms we readily see that the three-body loss rate is proportional to Tan's contact parameter C_2 of the fermions that gives the probability of having two fermions close to each other [11]. C_2 is calculated using the equation of state of the system thanks to the adiabatic-sweep theorem

$$C_2 = -\frac{4\pi m_f}{\hbar^2}\frac{\partial F}{\partial(1/a_{ff})}, \tag{1}$$

where m_f is the fermion mass and F is the free-energy of the fermionic gas per unit-volume [12,13]. The asymptotic expressions of C_2 in the BEC, BCS and unitary regimes are listed in Table I. In the deep BEC limit, the free energy is dominated by the binding energy of the molecules $\hbar^2/m_f a_{ff}^2$; in the BCS regime C_2 is derived using the mean-field approximation [11]. At unitary, the expression of the contact stems from the absence of any length scale other than the interparticle distance. The dimensionless parameter $\zeta = 0.87(3)$ was determined both theoretically [29] and experimentally [14–19]. Expressions listed in Table I confirm that the contact parameter and the bosonic loss rate follow the same scalings with density and scattering length.

We support this relationship between inelastic losses and Tan's contact by considering a microscopic model where the recombination is described by a three-body Hamiltonian

$$\begin{aligned}\hat{H}_3 = \int & d^3\boldsymbol{r}_b d^3\boldsymbol{r}_\uparrow d^3\boldsymbol{r}_\downarrow g(\boldsymbol{r}_b, \boldsymbol{r}_\uparrow, \boldsymbol{r}_\downarrow) \\ & \times \hat{\Psi}_m^\dagger\left(\frac{\boldsymbol{r}_\uparrow + \boldsymbol{r}_\downarrow}{2}\right)\hat{\Psi}_b^\dagger(\boldsymbol{r}_b)\hat{\Psi}_b(\boldsymbol{r}_b)\hat{\Psi}_\uparrow(\boldsymbol{r}_\uparrow)\hat{\Psi}_\downarrow(\boldsymbol{r}_\downarrow) \\ & + \text{H.c.},\end{aligned} \tag{2}$$

where $\hat{\Psi}_\alpha$ is the field operator for the species α and the coupling g takes significant values only when the three particles are within a distance b [30]. Assuming that b is the smallest distance scale in the problem and that this Hamiltonian can be treated within Born's approximation we find that (see Ref. [31])

$$\dot{n}_b = -\gamma C_2 n_b. \tag{3}$$

The constant γ depends on the coupling g and describes the coupling to deeply bound nonresonant states; hence, γ has essentially no variation with the magnetic field across the fermionic Feshbach resonance.

Equation (3) is the main prediction of this Letter and we explore the consequences of this equation by measuring the lifetime of an ultracold Fermi-Bose mixture of ^{6}Li and ^{7}Li atoms. Our experimental setup is described in Ref. [37].

The ^{6}Li atoms are prepared in a spin mixture $\uparrow,\downarrow$ of $|F = 1/2, m_F = \pm 1/2\rangle$ for which there is a broad Feshbach resonance at 832 G [33]. The ^{7}Li atoms are transferred into the $|F = 1, m_F = 0\rangle$ featuring two Feshbach resonances, a narrow one at 845.5 G and a broad one at 893.7 G [31]. The scattering length between bosons and fermions is $a_{\rm bf} = 40.8 a_0$ and is equal for the $\uparrow,\downarrow$ states. It can be considered constant in the magnetic field range that we explored, 680–832 G. The atoms are confined in a hybrid magnetic-optical trap and are evaporated at the ^{6}Li Feshbach resonance until we reach dual superfluidity or any target temperature. We ramp the magnetic field to an adjustable value in 200 ms and wait for a variable time t. We then measure the atom numbers of the two species by *in situ* imaging or after time of flight.

We first show that the dominant boson loss mechanism on the BEC side of the resonance involves one boson, one fermion $\uparrow$, and one fermion $\downarrow$. This is easily done by comparing the boson losses for spin-balanced and spin-polarized fermionic samples. Figure 2 displays the remaining fraction of bosons and fermions after a waiting time of 1 s for balanced fermions and 1.5 s for spin-polarized fermions with 90% polarization. We observe that the losses for high spin polarization are strongly suppressed indicating that fermions of both spin components are required to eliminate one boson.

Second we show that the losses in the weakly interacting regime $n a_{ff}^3 \ll 1$ (deep BEC side of the resonance, 720 G) are proportional to the fraction of molecules in the sample, $\eta = 2N_m/(N_f + 2N_m)$. This fraction is varied by changing the temperature from 1 μK to 4 μK and ^{6}Li densities from 2×10^{12} cm^{-3} to 1.0×10^{13} cm^{-3}. In these temperature and density ranges, both gases are well described by Maxwell-Boltzmann position and velocity distributions. The molecular fraction is calculated using the law of mass action [31,36] and is assumed to be time independent owing to the high formation rate of halo dimers ($\simeq \hbar a_{ff}^4/m_f$)[38]. We extract the interspecies decay rate by fitting the time evolution of the bosonic population

$$\dot{N}_b = -L_{\rm bf}\langle n_f\rangle N_b - \Gamma_v N_b, \tag{4}$$

where $\langle\cdots\rangle$ represents the trap average, and Γ_v is the one-body residual gas loss rate (0.015 s^{-1}).

The data in Fig. 3(a) show that the boson loss rate is proportional to the molecule fraction of the fermionic cloud. Introducing the boson-fermion dimer molecule loss rate $L_{\rm bm}$ defined by $L_{\rm bm}\langle n_m\rangle = L_{\rm bf}\langle n_f\rangle$, we check the proportionality of $L_{\rm bm}$ with $1/a_{ff}$ predicted in Table I by

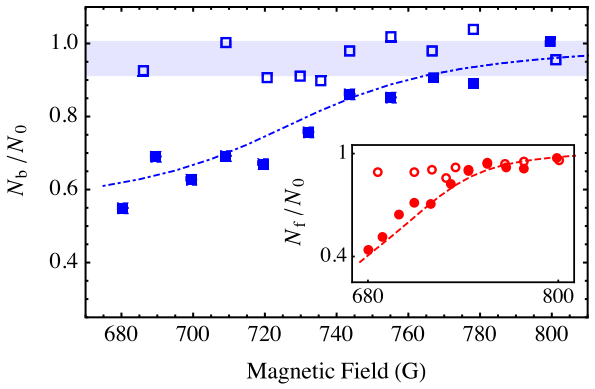

FIG. 2. Remaining fraction of bosons (blue symbols) and fermions (red symbols, inset) after a 1 s and 1.5 s waiting time for spin-balanced (filled symbols), resp. 90% polarized (open symbols) fermions. The blue dash-dotted (red dashed, inset) curve is a coupled loss model describing the competition between boson fermion-dimer decay ($\propto 1/a_{ff}$) and dimer-dimer decay ($\propto 1/a_{ff}^{2.55}$) [27,31]. The blue-shaded area represents the 1σ fluctuations for the remaining fraction of bosons with spin-polarized fermions. The initial atom numbers are 3×10^5 for ^{6}Li and 1.5×10^5 for ^{7}Li at a temperature $T \simeq 1.6$ μK with trap frequencies $\nu_z = 26$ Hz and $\nu_r = 2.0$ kHz.

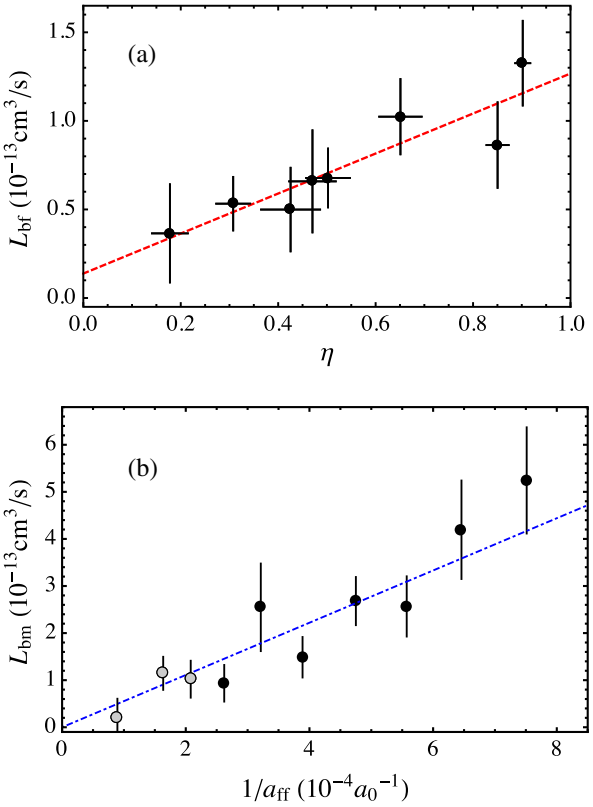

FIG. 3. (a) Boson-fermion loss rate vs molecule fraction. Circles: Experimental data. The vertical error bars represent the statistical errors for $L_{\rm bf}$ from fitting the loss curves. The horizontal error bars represent the statistical errors on the molecule fraction due to ^{6}Li number fluctuations. The red dashed line is a linear fit to the data. (b) Boson-dimer loss rate vs inverse scattering length. The blue dot-dashed line is a linear fit to the data with $n_f a_{ff}^3 \leq 0.025$ (black circles), providing $\gamma = 1.17(11) \times 10^{-27}$ m$^4\cdot$s^{-1}, see Eq. (3).

repeating the loss measurements for different magnetic fields in the interval 690–800 G, see Fig. 3(b). From a linear fit to the data where interaction effects are negligible ($n_f a_{ff}^3 \leq 0.025$), we extract the slope $\gamma = 1.17(11) \times 10^{-27}$ m$^4 \cdot$ s^{-1} entering in Eq. (3).

Since γ doesn't depend on the magnetic field, we can now predict the loss rate anywhere in the BEC-BCS crossover using Eq. (3). The strongly interacting unitary regime ($1/a_{ff} = 0$) is particularly interesting and we measure the boson decay rate at 832 G in the low temperature dual superfluid regime [37]. The mixture is initially composed of about 40×10^3 fully condensed ^{7}Li bosons and 150×10^3 ^{6}Li spin-balanced fermions at a temperature T $\simeq$ 100 nK which corresponds to $T/T_F \simeq 0.1$ where T_F is the Fermi temperature. At this magnetic field value, the atoms are now closer to the boson Feshbach resonance located at 845.5 G and bosonic three-body losses are no longer negligible. The time dependence of the boson number is then given by

$$\dot{N}_b = -L_b \langle n_b^2 \rangle N_b - \Gamma_{\rm bf} N_b - \Gamma_v N_b. \quad (5)$$

To extract $\Gamma_{\rm bf}$ we measure independently L_b with a BEC without fermions in the same trap and inject it in Eq. (5), see Ref. [31]. We typically have $L_b \langle n_b^2 \rangle = 0.1$–$0.4$ s^{-1}, and $L_b = 0.11(1) \times 10^{26}$ cm$^6 \cdot$ s^{-1} consistent with the model of Ref. [35]. Repeating such measurements for different fermion numbers and trap confinement, we now test the expected $n_f^{4/3}$ dependence of the Bose-Fermi loss rate at unitarity (central column in Table I). In this dual superfluid regime, the size of the BEC is much smaller than that of the fermionic superfluid and the BEC will mainly probe the central density region $n_f(r = 0)$. However, it is not truly a pointlike probe, and introducing the ratio ρ of the Thomas-Fermi radii for bosons and fermions, we obtain the finite size correction for Eq. (3) [31]:

$$\Gamma_{\rm bf} = \gamma C_2(0) \left(1 - \frac{6}{7}\rho^2\right), \quad (6)$$

where $C_2(0) = (2\zeta/5\pi)(3\pi^2 n_f(0))^{4/3}$, and the last factor in parenthesis amounts to 0.9. The prediction of Eq. (6) is plotted as a red line in Fig. 4 and is in excellent agreement with our measurements without any adjustable parameter. Alternatively, a power-law fit An^p to the data yields an exponent $p = 1.36(15)$ which confirms the $n_f^{4/3}$ predicted scaling at unitarity. Finally, fixing p to $4/3$ provides the coefficient A and a value of the homogeneous contact $\zeta = 0.82(9)$ in excellent agreement with previous measurements, $\zeta = 0.87(3)$ [17,25]. This demonstrates that impurity losses act as a microscopic probe of quantum correlations in a many-body system.

The bosonic or fermionic nature of the probe is of no importance. Provided the coupling between the impurity and the resonant gas is weak, our method can also be applied to other mixtures. It gives a framework to interpret the experimental data on ^{6}Li/^{40}K [22] and, in particular, to test our prediction on the BCS side of the Feshbach resonance. It can also be applied to the recently observed ^{6}Li/^{174}Yb [39], ^{6}Li/^{41}K [40], and ^{6}Li/^{7}Li [41] dual-superfluid Bose-Fermi mixtures and even to the case where one of the collision partners is a photon as in photoassociation experiments [42,43]. Our observation of a loss rate scaling $\propto n_f^{4/3}$ at unitarity is in stark contrast with the generic case n^p, where the integer p is the number of particles involved in the recombination process. A fractional exponent is also predicted to occur for the resonant Bose gas [5,6] and Fermi gas [27,44].

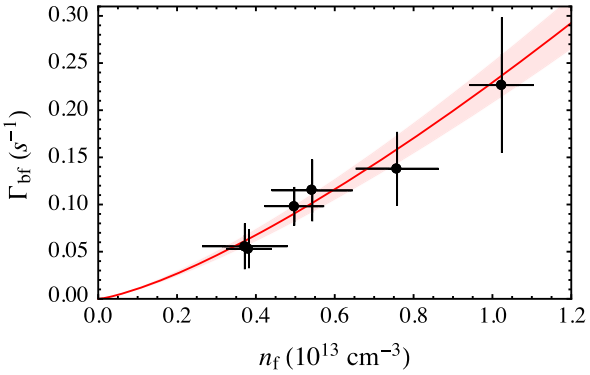

FIG. 4. Boson loss rate versus fermion central density at unitarity, $n_f = n_f(0)$. Circles: Experimental data. The red line is the $n_f^{4/3}$ prediction of Eq. (6) without any adjustable parameter. The red shaded area represents the 1σ uncertainty resulting from the error on γ.

A first extension of this work is to investigate regimes where $a_{\rm bf} \simeq a_{ff} \gg n^{-1/3}$ and the Born approximation breaks down. In this case Efimovian features are expected to occur [45,46]. Second, our method provides a unique microscopic way to measure the contact quasilocally in a harmonic trap. An important perspective is to determine the homogeneous contact of the unitary Fermi gas at finite temperature, whose behavior is largely debated near the normal-superfluid transition [18].

The authors thank G. Shlyapnikov, B. Svistunov, and F. Werner for helpful discussions. They acknowledge support from Région Ile de France (DIM IFRAF/NanoK), ANR (Grant SpiFBox), and European Union (ERC Grant ThermoDynaMix).

*slaurent@lkb.ens.fr
†Present address: FEMTO-ST UMR CNRS 6174—UFC/ENSMM/UTBM, 26 chemin de l'Epitaphe, 25030 Besançon, France.

[1] I. Bloch, J. Dalibard, and W. Zwerger, Many-body physics with ultracold gases, Rev. Mod. Phys. **80**, 885 (2008).

[2] *The BCS-BEC Crossover and the Unitary Fermi Gas*, edited by W. Zwerger, Lecture Notes in Physics Vol. 836 (Springer, Berlin, 2012).
[3] Quantum Matter at Ultralow Temperatures, edited by M. Inguscio, W. Ketterle, S. Stringari, and G. Roati, *Proceedings of the International School of Physics "Enrico Fermi"*, Vol. 191 (IOS Press, Varenna, 2016).
[4] J.-y. Choi, S. Hild, J. Zeiher, P. Schauß, A. Rubio-Abadal, T. Yefsah, V. Khemani, D. A. Huse, I. Bloch, and C. Gross, Exploring the many-body localization transition in two dimensions, Science **352**, 1547 (2016).
[5] P. Makotyn, C. E. Klauss, D. L. Goldberger, E. A. Cornell, and D. S. Jin, Universal dynamics of a degenerate unitary Bose gas, Nat. Phys. **10**, 116 (2014).
[6] F. Chevy and C. Salomon, Strongly correlated Bose gases, J. Phys. B **49**, 192001 (2016).
[7] N. Syassen, D. M. Bauer, M. Lettner, T. Volz, D. Dietze, J. J. Garcia-Ripoll, J Ignacio Cirac, G. Rempe, and S. Dürr, Strong dissipation inhibits losses and induces correlations in cold molecular gases, Science **320**, 1329 (2008).
[8] A. J. Daley, J. M. Taylor, S. Diehl, M. Baranov, and P. Zoller, Atomic Three-Body Loss as a Dynamical Three-Body Interaction, Phys. Rev. Lett. **102**, 040402 (2009).
[9] B. Zhu *et al.* Suppressing the Loss of Ultracold Molecules via the Continuous Quantum Zeno Effect, Phys. Rev. Lett. **112**, 070404 (2014).
[10] T. Kraemer *et al.*, Evidence for Efimov quantum states in an ultracold gas of caesium atoms, Nature (London) **440**, 315 (2006).
[11] S. Tan, Energetics of a strongly correlated Fermi gas, Ann. Phys. (Amsterdam) **323**, 2952 (2008).
[12] S. Tan, Large momentum part of a strongly correlated Fermi gas, Ann. Phys. (Amsterdam) **323**, 2971 (2008).
[13] M. Olshanii and V. Dunjko, Short-Distance Correlation Properties of the Lieb-Liniger System and Momentum Distributions of Trapped One-Dimensional Atomic Gases, Phys. Rev. Lett. **91**, 090401 (2003).
[14] J. T. Stewart, J. P. Gaebler, T. E. Drake, and D. S. Jin, Verification of Universal Relations in a Strongly Interacting Fermi Gas, Phys. Rev. Lett. **104**, 235301 (2010).
[15] E. D. Kuhnle, H. Hu, X.-J. Liu, P. Dyke, M. Mark, P. D. Drummond, P. Hannaford, and C. J. Vale, Universal Behavior of Pair Correlations in a Strongly Interacting Fermi Gas, Phys. Rev. Lett. **105**, 070402 (2010).
[16] R. J. Wild, P Makotyn, J. M. Pino, E. A. Cornell, and D. S. Jin, Measurements of tans contact in an atomic Bose-Einstein condensate, Phys. Rev. Lett. **108**, 145305 (2012).
[17] N. Navon, S. Nascimbène, F. Chevy, and C. Salomon, The equation of state of a low-temperature fermi gas with tunable interactions, Science **328**, 729 (2010).
[18] Y. Sagi, T. E. Drake, R. Paudel, and D. S. Jin, Measurement of the Homogeneous Contact of a Unitary Fermi Gas, Phys. Rev. Lett. **109**, 220402 (2012).
[19] E. D. Kuhnle, S. Hoinka, P. Dyke, H. Hu, P. Hannaford, and C. J. Vale, Temperature Dependence of the Universal Contact Parameter in a Unitary Fermi Gas, Phys. Rev. Lett. **106**, 170402 (2011).
[20] J. P. DIncao and B. D. Esry, Suppression of Molecular Decay in Ultracold Gases without Fermi Statistics, Phys. Rev. Lett. **100**, 163201 (2008).
[21] J. P. D'Incao, C. H. Greene, and B. D Esry, The short-range three-body phase and other issues impacting the observation of efimov physics in ultracold quantum gases, J. Phys. B **42**, 044016 (2009).
[22] F. M. Spiegelhalder, A. Trenkwalder, D. Naik, G. Hendl, F. Schreck, and R. Grimm, Collisional Stability of ^{40}K Immersed in a Strongly Interacting Fermi Gas of ^{6}Li, Phys. Rev. Lett. **103**, 223203 (2009).
[23] A. Y. Khramov, A. H. Hansen, A. O. Jamison, W. H. Dowd, and S. Gupta, Dynamics of feshbach molecules in an ultracold three-component mixture, Phys. Rev. A **86**, 032705 (2012).
[24] J. J. Zirbel, K.-K. Ni, S. Ospelkaus, J. P. DIncao, C. E. Wieman, J. Ye, and D. S. Jin, Collisional Stability of Fermionic Feshbach Molecules, Phys. Rev. Lett. **100**, 143201 (2008).
[25] S. Hoinka, M. Lingham, K. Fenech, H. Hu, C. J. Vale, J. E. Drut, and S. Gandolfi, Precise Determination of the Structure Factor and Contact in a Unitary Fermi Gas, Phys. Rev. Lett. **110**, 055305 (2013).
[26] Y. Kagan, B. V. Svistunov, and G. V. Shlyapnikov, Effect of Bose condensation on inelastic processes in gases, JETP Lett. **42**, 209 (1985).
[27] D. S. Petrov, C. Salomon, and G. V. Shlyapnikov, Weakly Bound Dimers of Fermionic Atoms, Phys. Rev. Lett. **93**, 090404 (2004).
[28] E. Braaten and H.-W. Hammer, Universal relation for the inelastic two-body loss rate, J. Phys. B **46**, 215203 (2013).
[29] G. E. Astrakharchik, J. Boronat, J. Casulleras, and S. Giorgini, Equation of State of a Fermi Gas in the BEC-BCS Crossover: A Quantum Monte Carlo Study, Phys. Rev. Lett. **93**, 200404 (2004).
[30] This Hamiltonian describes the formation of deeply bound fermion-fermion molecules but Eq. (3) is also valid for boson-fermion molecules.
[31] See Supplemental Material at http://link.aps.org/supplemental/10.1103/PhysRevLett.118.103403 for a microscopic three-body loss model, Feshbach resonance data, and methods for loss coefficient extraction, which includes Refs. [32–36].
[32] F. Werner and Y. Castin, General relations for quantum gases in two and three dimensions: Two-component fermions, Phys. Rev. A **86**, 013626 (2012).
[33] G. Zürn, T. Lompe, A. N. Wenz, S. Jochim, P. S. Julienne, and J. M. Hutson, Precise Characterization of ^{6}Li Feshbach Resonances Using Trap-Sideband-Resolved RF Spectroscopy of Weakly Bound Molecules, Phys. Rev. Lett. **110**, 135301 (2013).
[34] N. Gross, Z. Shotan, O. Machtey, S. J. J. M. F Kokkelmans, and L. Khaykovich, Study of Efimov Physics in two nuclear-spin sublevels of 7 Li, C.R. Phys. **12**, 4 (2011).
[35] Z. Shotan, O. Machtey, S. Kokkelmans, and L. Khaykovich, Three-Body Recombination at Vanishing Scattering Lengths in an Ultracold Bose Gas, Phys. Rev. Lett. **113**, 053202 (2014).
[36] C. Chin and R. Grimm, Thermal equilibrium and efficient evaporation of an ultracold atom-molecule mixture, Phys. Rev. A **69**, 033612 (2004).
[37] I. Ferrier-Barbut, M. Delehaye, S. Laurent, A. T. Grier, M. Pierce, B. S. Rem, F. Chevy, and C. Salomon, A mixture of Bose and Fermi superfluids, Science **345**, 1035 (2014).

[38] P. O. Fedichev, M. W. Reynolds, and G. V. Shlyapnikov, Three-body Recombination of Ultracold Atoms to a Weakly Bound *s* Level, Phys. Rev. Lett. **77**, 2921 (1996).

[39] R. Roy, A. Green, R. Bowler, and S. Gupta, Two-element Mixture of Bose and Fermi Superfluids, Phys. Rev. Lett., **118**, 055301 (2017).

[40] X.-C. Yao, H.-Z. Chen, Y.-P. Wu, X.-P. Liu, X.-Q. Wang, X. Jiang, Y. Deng, Y.-A. Chen, and J.-W. Pan, Observation of Two-Species Vortex Lattices in a Mixture of Mass-Imbalance Bose and Fermi Superfluids, Phys. Rev. Lett. **117**, 145301 (2016).

[41] T. Ikemachi, A. Ito, Y. Aratake, Y. Chen, M. Koashi, M. Kuwata-Gonomaki, and M. Horikoshi, All-optical production of a superfluid bose-fermi mixture of ^{6}Li and ^{7}Li, arXiv:1606.09404.

[42] G. B. Partridge, K. E. Strecker, R. I. Kamar, M. W. Jack, and R. G. Hulet, Molecular Probe of Pairing in the BEC-BCS Crossover, Phys. Rev. Lett. **95**, 020404 (2005).

[43] F. Werner, L. Tarruell, and Y. Castin, Number of closed-channel molecules in the bec-bcs crossover, Eur. Phys. J. B **68**, 401 (2009).

[44] X. Du, Y. Zhang, and J. E. Thomas, Inelastic Collisions of a Fermi Gas in the BEC-BCS Crossover, Phys. Rev. Lett. **102**, 250402 (2009).

[45] E. Braaten, H.-W. Hammer, D. Kang, and L. Platter, Three-Body Recombination of ^{6}Li Atoms with Large Negative Scattering Lengths, Phys. Rev. Lett. **103**, 073202 (2009).

[46] T. B. Ottenstein, T. Lompe, M. Kohnen, A. N. Wenz, and S. Jochim, Collisional Stability of a Three-Component Degenerate Fermi Gas, Phys. Rev. Lett. **101**, 203202 (2008).

Few vs many-body physics of an impurity immersed in a superfluid of spin $1/2$ attractive fermions

Matthieu Pierce, Wavier Leyronas, Frédéric Chevy

arXiv:1903.01108v1

Few vs many-body physics of an impurity immersed in a superfluid of spin 1/2 attractive fermions

M. Pierce,[1] X. Leyronas,[2] and F. Chevy[1]

[1] *Laboratoire Kastler Brossel, ENS-Université PSL, CNRS, Sorbonne Université, Collège de France.*
[2] *Laboratoire de physique de l'Ecole normale supérieure, ENS, Université PSL, CNRS, Sorbonne Université, Université Paris-Diderot, Sorbonne Paris Cité, Paris, France.*

In this article we investigate the properties of an impurity immersed in a superfluid of strongly correlated spin 1/2 fermions. For resonant interactions, we first relate the stability diagram of dimer and trimer states to the three-body problem for an impurity interacting with a pair of fermions. Then we calculate the beyond-mean-field corrections to the energy of a weakly interacting impurity. We show that these corrections are divergent and have to be regularized by properly accounting for three-body physics in the problem.

The physics of an impurity immersed in a many-body ensemble is one of the simplest although non-trivial paradigms in many-body physics. One of the first examples of such a system is the polaron problem which was introduced by Landau and Pekar [1] to describe the interaction of an electron with the acoustic excitations of a surrounding crystal. Likewise, in magnetic compounds Kondo's Effect arises from the interaction of magnetic impurities with the background Fermi sea [2, 3]. Similar situations occur in high-energy physics, e.g. in neutron stars to interpret the interaction of a proton with a superfluid of neutrons [4], or in quantum chromodynamics where the so-called Polyakov loop describes the properties of a test color charge immersed in a hot gluonic medium [5]. Finally, impurity problems can be used as prototypes for more complex many body-systems [6], as illustrated by the dynamical mean-field theory [7].

The recent advent of strongly correlated quantum gases permitted by the control of interactions in these systems have opened a new research avenue for the physics of impurities [8–11]. Experiments on strongly polarized Fermi gases [12–14] were interpreted by the introduction of the so-called Fermi polarons, a quasi-particle describing the properties of an impurity immersed in an ensemble of spin-polarized fermions and dressed by a cloud of particle-hole excitations of the surrounding Fermi Sea [15–17]. More recently, the physics of Bose polarons (impurities immersed in a Bose-Einstein condensate) was explored using radio-frequency spectroscopy [18, 19]. Contrary to the Fermi polaron, this system is subject to an Efimov effect [20] and three-body interactions play an important role in the strongly correlated regime [21]. Finally recent experiments on dual superfluids have raised the question of the behaviour of an impurity immersed in a superfluid of spin 1/2 fermions [22–24]. In these experiments, the polaron was weakly coupled to the background superfluid and the interaction could be accurately modeled within mean-field approximation. Further theoretical works explored the strongly coupled regime using mean-field theory to describe the fermionic superfluid [25, 26]. They highlighted the role of Efimov physics in the phase diagram of the system and as a consequence some results were plagued by unphysical ultraviolet divergences. In this letter we address this problem without making any assumption on the properties of the superfluid component. We calculate the first beyond-mean-field corrections to the energy of the polaron and we show that the logarithmic divergence arising from three-body physics can be cured within an effective field theory approach introduced previously in the study of beyond mean-field corrections in Bose gases [27, 28].

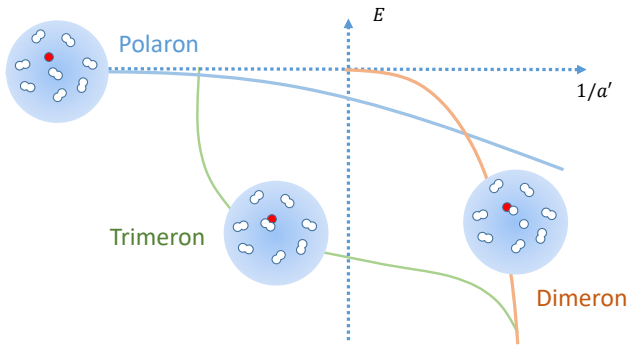

FIG. 1. Sketch of the energy branches of an impurity (red dot) immersed in an ensemble of Cooper-paired fermions when the impurity/fermion scattering length a' is varied. Blue: polaron branch; green: ground-state Efimov trimer branch; orange: dimer branch. According to mean-field calculations [25, 26] the polaron/trimer transition corresponds to a smooth avoided crossing between the two branches.

Qualitatively speaking, the phase diagram of the impurity can be decomposed in three different regions when the strength of the impurity/fermion interaction is varied (see Fig. 1). For a weak attraction, the impurity can be described as a polaronic quasi-particle. When attraction is increased, the impurity binds to an existing Cooper pair and the polaronic branch connects to the resonant Efimov trimer states. Earlier variational calcula-

tions suggest that the transition between the polaron and trimeron states is a smooth crossover [25, 26]. Finally, in the strongly attractive regime, impurity/fermion attraction overcomes Cooper pairing leading to a dimeron state describing an impurity/fermion dimer immersed in a fermionic superfluid medium.

Since the size of the ground-state Efimov trimer is typically much smaller than the interparticle spacing, its binding energy is much larger than the Fermi energy of the fermionic superfluid. As a consequence, except when the Efimov trimer becomes resonant with the atomic continuum, the internal structure of the trimer is only weakly affected by the many-body environment. A first insight on the phase diagram of the system can thus be obtained from the study of the three-body problem to determine the stability domain of the Efimov trimers with respect to the free-atom and atom-dimer continuum. In this pursuit, we use a two-channel model similar to the one presented in e.g. [29] in the case of the bosonic Efimov problem [30]. For the sake of simplicity, we assume here that the masses of the fermions and the impurity are the same, and that the impurity interacts the same way with both spin states of the fermionic ensemble (these assumptions are well satisified in the experiments reported in [22]). The properties of the system are therefore characterized by three different length scales: the fermion-fermion scattering length (a), the fermion-impurity scattering length (a') and the effective range of the interaction potential (R_e) [31]. The corresponding phase diagram is displayed in Fig. 2. When the fermion/fermion interaction strength is varied, the superfluid explores the BEC-BCS crossover [9] that connects the weakly attractive regime ($a \to 0^-$) where the fermions form loosely bound Cooper pairs described by BCS (Bardeen-Cooper-Schrieffer) theory, to the strongly attractive limit ($a \to 0^+$) where they form a Bose-Einstein Condensate (BEC) of deeply bound dimers. As a consequence, the polaronic state smoothly evolves from a Fermi polaron (an impurity immersed in a non-interacting Fermi sea) to a Bose polaron (an impurity immersed in a BEC of dimers). The trimeron stability region is obtained by a numerical resolution of the three-body problem [30]. The polaron-dimeron frontier simply corresponds to a competition between fermion/fermion and fermion/impurity pairings.

Since the trimeron and dimeron regimes are dominated by few-body physics, we now focus on the energy of the polaronic branch that is more strongly affected by the presence of the superfluid. We furthermore assume that the impurity-fermion interaction can be treated perturbatively.

Consider thus an impurity of mass m_i immersed in a bath of spin 1/2 fermions of mass m_f. We write the Hamiltonian of the system as

$$\hat{H} = \hat{H}_\mathrm{imp} + \hat{H}_\mathrm{mb} + \hat{H}_\mathrm{int}, \tag{1}$$

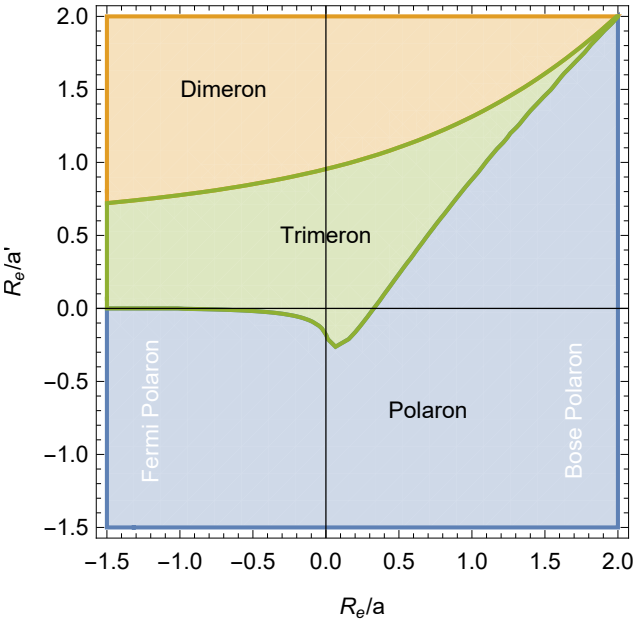

FIG. 2. Stability diagram of the polaron, dimeron and trimeron states with the effective range for $m_\mathrm{f} = m_\mathrm{i}$ using a coupled channel model (see text and [30]). Variational approaches based on a mean-field description of the background superfluid suggest that the polaron/trimeron transition is a crossover [25, 26].

where $\hat{H}_\mathrm{imp}$ (resp. $\hat{H}_\mathrm{mb}$) is the Hamiltonian of the impurity (resp. many-body background) alone, and $\hat{H}_\mathrm{int}$ describes the interaction between the two subsystems. We label the eigenstates of the impurity by its momentum $\boldsymbol{q}$ and its eigenvalues are $\varepsilon_q^{(\mathrm{i})} = \hbar^2 q^2/2m_\mathrm{i}$. The eigenstates and eigenvalues of $\hat{H}_\mathrm{mb}$ are denoted $|\alpha\rangle$ and E_α, where by definition $\alpha = 0$ corresponds to the ground state of the fermionic superfluid.

Assuming for simplicity an identical contact interaction between the impurity and each spin component of the many-body ensemble, we write

$$\hat{H}_\mathrm{int} = g_0' \sum_{\sigma=\uparrow,\downarrow} \int d^3\boldsymbol{r}\, \hat{\psi}_\sigma^\dagger(\boldsymbol{r})\hat{\psi}_\sigma(\boldsymbol{r})\hat{\phi}^\dagger(\boldsymbol{r})\hat{\phi}(\boldsymbol{r}), \tag{2}$$

where $\hat{\psi}_\sigma$ and $\hat{\phi}$ are the field operators for spin σ particles of the many-body ensemble and of the impurity respectively. In this expression, the bare and physical coupling constants g_0' and g' are related through

$$\frac{1}{g_0'} = \frac{1}{g'} - \frac{1}{\Omega}\sum_{k<\Lambda} \frac{1}{\varepsilon_k^{(\mathrm{r})}}, \tag{3}$$

where Ω is the quantization volume, Λ is some ultraviolet cutoff and $\epsilon_k^{(\mathrm{r})} = \hbar^2 k^2/2m_\mathrm{r}$, with m_r the impurity-fermion reduced mass. Assuming that the contact interaction can be treated perturbatively, we have up to

second order

$$g_0' = g' + \frac{g'^2}{\Omega}\sum_{k<\Lambda}\frac{1}{\varepsilon_k^{(\mathrm{r})}} + o(g'^2). \tag{4}$$

Calculating the energy ΔE of the polaron to that same order, we have

$$\Delta E_{\mathrm{pert}} = g'n + \frac{g'^2 n}{\Omega}\sum_{\boldsymbol{q}}\left[\frac{1}{\varepsilon_q^{(\mathrm{r})}} - \chi(\boldsymbol{q}, \varepsilon_q^{(\mathrm{i})})\right]. \tag{5}$$

where n is the particle density in the many-body medium and

$$\chi(\boldsymbol{q}, E) = \frac{1}{N}\sum_{\alpha}\frac{|\langle\alpha|\hat{\rho}_{-\boldsymbol{q}}|0\rangle|^2}{E_\alpha - E_0 + E}, \tag{6}$$

with $\hat{\rho}_{\boldsymbol{q}} = \sum_\sigma \int d^3\boldsymbol{r}\hat{\psi}_\sigma^\dagger(\boldsymbol{r})\hat{\psi}_\sigma(\boldsymbol{r})e^{i\boldsymbol{q}\cdot\boldsymbol{r}}$.

In the sum, the presence of the two terms allows for a UV cancellation of their $1/q^2$ asymptotic behaviours. Indeed, for large q the eigenstates of the many-body Hamiltonian excited by the translation operator $\hat{\rho}_{\boldsymbol{q}}$ correspond to free-particle excitations of momentum $\boldsymbol{q}$ and energy $\varepsilon_q^{(\mathrm{f})} = \hbar^2 q^2/2m_{\mathrm{f}}$. We therefore have

$$\chi(\boldsymbol{q}, E) \simeq \frac{S(q)}{\varepsilon_q^{(\mathrm{f})} + E}, \tag{7}$$

where $S(q) = \sum_\alpha |\langle\alpha|\hat{\rho}_{\boldsymbol{q}}|0\rangle|^2/N$ is the static structure factor of the many-body system. At large momenta, we have $S(q) = 1 + C_2/4Nq + ...$, where C_2 is Tan's contact parameter of the fermionic system and characterizes its short-range two-body correlations [32, 33]. From this scaling we see that the UV-divergent $1/q^2$ contributions in Eq. (5) cancel out. However, the next-to-leading order term in $S(q)$ suggests that this cancellation is not sufficient to regularize the sum that is still log-divergent. This logarithmic behaviour is supported by a directed calculation of χ using BCS mean-field theory [30] and is characteristic of a singularity in the three-body problem for particles with contact interactions that was pointed out first by Wu for bosons [34] and was more recently investigated in the context of cold atoms (see for instance [26, 27, 35, 36]).

To get a better insight on the origin of this singularity, we analyze first the scattering of an impurity with a pair of free fermions. Within Faddeev's formalism [37], the corresponding three-body T-matrix is written as a sum of three contributions, $\hat{T}_{i=1,2,3}$ solutions of the set of coupled equations

$$\begin{pmatrix}\hat{T}_1\\ \hat{T}_2\\ \hat{T}_3\end{pmatrix} = \begin{pmatrix}\hat{t}_1\\ \hat{t}_2\\ \hat{t}_3\end{pmatrix} + \begin{pmatrix}0 & \hat{t}_1 & \hat{t}_1\\ \hat{t}_2 & 0 & \hat{t}_2\\ \hat{t}_3 & \hat{t}_3 & 0\end{pmatrix}\hat{G}_0\begin{pmatrix}\hat{T}_1\\ \hat{T}_2\\ \hat{T}_3\end{pmatrix} \tag{8}$$

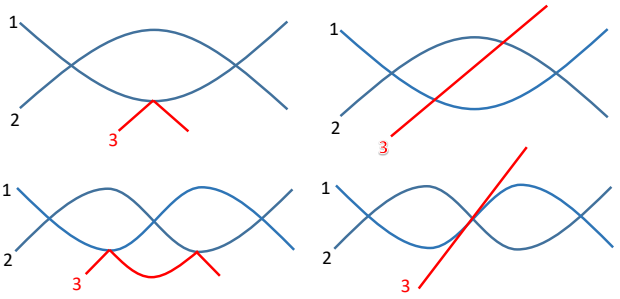

FIG. 3. Singular diagrams at second order of Born's approximation. The red line corresponds to the impurity. In Faddeev's expansion, each interaction vertex corresponds to a two-body t-matrix $\hat{t}_{1,2,3}$. In Born's approximation, the $\hat{t}_{1,2}$'s are expanded to second order in a' which leads to a logarithmic UV divergence of the corresponding terms.

where $\hat{G}_0 = 1/(z - \hat{H}_0)$ is the free resolvant operator and $\hat{t}_i$ is the two-body T-matrix leaving particle i unaffected. The solutions of this equation can be expressed as a series of diagrams where a given two-body t-matrix never acts twice in a row and $\hat{T}_i$ corresponds to the sum of all diagrams finishing by $\hat{t}_i$. Assuming that the impurity is labeled by the index $i = 3$ and that its interaction with the other two atoms ($i = 1, 2$) is weak, we can expand the solutions of Faddeev's equation with $\hat{t}_1$ and $\hat{t}_2$. To be consistent with the polaron-energy calculation outlined in previous section, we proceed up to second order in $\hat{t}_{1,2}$.

When the full 2-body T-matrices $t_{1,2} = g'/\Omega/(1 + ia'k + a'R_e k^2)$ are used, all terms of the expansion are finite. However, when treating them within second order Born's approximation (i.e. taking simply $t_{1,2} = g'(1 - ika')/\Omega$ and stopping the expansion of the T-matrix at second order in a'), some diagrams are logarithmically divergent. The singular diagrams are listed in Fig. 3: they all start and end with t_3 and their contribution can be written as $(t_3)_{\mathrm{out}}\Gamma(t_3)_{\mathrm{in}}$. In Born's approximation the sums over inner momenta are divergent and the integrals are therefore dominated by the large-k behaviour of t_3 and G_0. After a straightforward calculation, we obtain that

$$\Gamma_{\mathrm{Born}} \underset{\Lambda\to\infty}{\sim} \frac{m_f^3}{\hbar^6}g'^2\kappa(\eta = m_b/m_f)\ln(\Lambda) \tag{9}$$

with

$$\begin{aligned}\kappa(\eta) =& \frac{\sqrt{\eta^3(\eta+2)}}{2\pi^3(\eta+1)^2} - \frac{\eta}{2\pi^3}\arctan\left(\frac{1}{\sqrt{\eta(\eta+2)}}\right)\\ &- \frac{4}{\pi^3}\sqrt{\frac{\eta}{\eta+2}}\arctan\left(\sqrt{\frac{\eta}{\eta+2}}\right)^2\end{aligned} \tag{10}$$

Since Γ is finite when the full two-body physics is taken

into account we introduce a three-body characteristic length R_3 such that

$$\Gamma_{\rm Born} - \Gamma_{\rm Faddeev} \underset{\Lambda\to\infty}{=} \frac{m_f^3}{\hbar^6} g'^2 \kappa(\eta) \ln(\Lambda R_3) + o(1), \quad (11)$$

where $\Gamma_{\rm Faddeev}$ corresponds to the value of Γ obtained by using the full two-body T-matrices $t_{1,2}$ to calculate the first three diagrams of Fig. (3). In this perturbative approach, R_3/a' depends on η and R_e/a' and can be computed numerically [30]. Since we work in a regime where the polaron is the ground state and Efimov trimers are absent, we do not have to use non-perturbative approaches compatible with Efimov physics and leading to a log-periodic dependence of R_3 [38].

Following the effective field theory approach discussed in [36], divergences plaguing Born's expansion can be cured by introducing an explicit three-body interaction described by a Hamiltonian

$$\hat{H}_{3b} = g_3(\Lambda) \int d^3\boldsymbol{r} \hat{\psi}_1^\dagger(\boldsymbol{r}) \hat{\psi}_2^\dagger(\boldsymbol{r}) \hat{\psi}_3^\dagger(\boldsymbol{r}) \hat{\psi}_3(\boldsymbol{r}) \hat{\psi}_2(\boldsymbol{r}) \hat{\psi}_1(\boldsymbol{r}) \quad (12)$$

The contribution of this three-body interaction to Γ corresponds to the fourth diagram of Fig. 3 and yields the following expression

$$\Gamma_{\rm 3b} = g_3(\Lambda) \left(\frac{1}{\Omega} \sum_{k<\Lambda} \frac{1}{2\varepsilon_k^{\rm (f)}} \right)^2. \quad (13)$$

Using this three-body interaction to cure Born's approximation, we must have $\Gamma_{\rm Born} + \Gamma_{\rm 3b} = \Gamma_{\rm Faddeev}$, hence the following expression for the three-body coupling constant

$$g_3(\Lambda) \left(\frac{1}{\Omega} \sum_{k<\Lambda} \frac{1}{2\varepsilon_k^{\rm (f)}} \right)^2 = -\frac{m_f^3}{\hbar^6} g'^2 \kappa(\eta) \ln(\Lambda R_3) \quad (14)$$

The introduction of the three-body Hamiltonian implies a new contribution to the second-order energy shift (5). This new term amounts to

$$\Delta E_{3b} = g_3(\Lambda) \langle 0 | \hat{\psi}_1^\dagger(\boldsymbol{r}) \hat{\psi}_2^\dagger(\boldsymbol{r}) \hat{\psi}_2(\boldsymbol{r}) \hat{\psi}_1(\boldsymbol{r}) | 0 \rangle \quad (15)$$

Using Eq. (14) as well as the properties of Tan's contact parameter, we obtain after a straightforward calculation

$$\Delta E_{3b} = -g'^2 \kappa(\eta) \frac{m_{\rm f} C_2}{\hbar^2 \Omega} \ln(\Lambda R_3). \quad (16)$$

Adding this contribution to Eq. (5), we obtain for the polaron energy $\Delta E = \Delta E_{\rm pert} + \Delta E_{3b}$:

$$\Delta E = g' n \Bigg[1 + k_F a' F\left(\frac{1}{k_F a}\right) - 2\pi \frac{m_{\rm f}}{m_{\rm r}} \kappa(\eta) \frac{a' C_2}{N} \ln(k_F R_3) + ... \Bigg], \quad (17)$$

with

$$F\left(\frac{1}{k_F a}\right) \underset{\Lambda\to\infty}{=} \frac{2\pi}{k_F} \left[\frac{\hbar^2}{m_{\rm r}} \int_{q<\Lambda} \frac{d^3\boldsymbol{q}}{(2\pi)^3} \left(\frac{1}{\varepsilon_q^{\rm (r)}} - \chi(q, \varepsilon_q^{\rm (i)}) \right) - \frac{m_{\rm f}}{m_{\rm r}} \kappa(\eta) \frac{C_2}{N} \ln(\Lambda/k_F) \right] \quad (18)$$

Eq. (17) and (18) are the main results of this paper. They show that the second order correction of the polaron energy is the sum of two terms: a regular term characterized by the function F defined by Eq. (17), as well as a second term, characterized by a logarithmic singularity and proportional to the fermionic contact parameter.

The function F is in general hard to compute exactly but we can obtain its exact asymptotic expression in the BEC and BCS limits. When the fermions of the background ensemble are weakly interacting, we must recover the Fermi-polaron problem (see Fig. 2). For the mass-balanced case $\eta = 1$, we obtain $F(-\infty) = 3/2\pi$. In the strongly attractive limit, the fermionic ensemble behaves as a weakly interacting Bose-Einstein condensate of dimers and the polaron energy takes a general mean-field form $g_{\rm ad} n/2$, where $g_{\rm ad}$ is the impurity-dimer s-wave coupling constant and $n/2$ is the dimer density. Since in the BEC limit, $C_2/N = 4\pi/a$, identifying Eq. (17) with the mean-field impurity-dimer interaction implies that

$$F\left(\frac{1}{k_F a}\right) \underset{a\to 0^+}{=} 8\pi^2 \kappa(\eta) \frac{m_{\rm f}}{m_{\rm r}} \frac{\ln(k_F a)}{k_F a} + ... \quad (19)$$

and

$$g_{\rm ad} = 2g' \left[1 - 8\pi^2 \kappa(\eta) \frac{m_{\rm f}}{m_{\rm r}} \frac{a'}{a} \left(\ln(R_3/a) + C_{\rm ad} \right) ... \right], \quad (20)$$

where the constant $C_{\rm ad}$ can be obtained from the direct analysis of the atom-dimer scattering problem [30].

Eq. (17) can be used to benchmark previous works on this problem. Ref. [25, 26] were based on a mean-field description of the superfluid component of the system. The mean-field calculation obeys BCS and BEC asymptotic behaviours similar to those predicted by Eq. (17) except for the value of κ that does not coincide with the present result since the last term in Eq. (10) is missing within a BCS approach [30]. This discrepancy is easily understandable. Indeed, this term corresponds to the

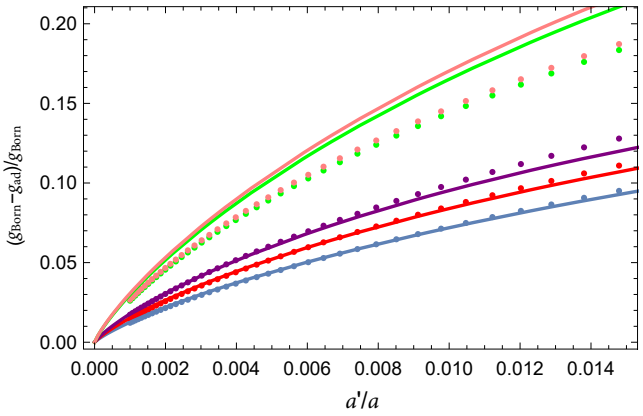

FIG. 4. Atom-dimer s-wave coupling constant relatively to Born's approximation prediction $g_{\rm Born} = 2g'$. Dots: numerical resolution of the three-body problem from [39]. From bottom to top: η= 7/40 (blue), 23/40 (red), 7/6 (purple), 87/6 (orange), 133/6 (green). Solid line: Asymptotic result Eq. (20) where R_3 and $C_{\rm ad}$ are computed numerically and are given in [30]. Here R_3 and $C_{\rm ad}$ are computed taking $R_e = 0$ and the slight discrepancy observable at large η is probably due to the finite range used in [39] to regularize the three-body problem.

third diagram of Fig. (3) where the two fermions interacts between their interaction with the impurity, which contradicts the BCS assumption of non-interacting Bogoliubov excitations. For $\eta = 1$, $\kappa/\kappa_{\rm MF} \simeq 15$, showing that BCS approximation underestimates strongly beyond mean-field contributions. Eq. (20) can also be compared to the numerical calculation of the atom-dimer scattering length reported in [39]. The comparison between numerics and our analytical result for experimentally relevant mass ratios is shown in Fig. (4) which demonstrates a very good agreement between the two approaches. Note also that Eq. (20) clarifies the range of validity of the perturbative expansion. In addition to the diluteness assumption $k_F|a'| \ll 1$, the validity of Born's expansion requires the additional condition $|a'|/a \ll 1$ when $a > 0$.

Finally, the convergence of Eq. (18) entails that χ must obey the large momentum asymptotic behavior

$$\chi(q, \varepsilon_q^{(\rm i)}) \underset{q\to\infty}{=} \frac{1}{\varepsilon_q^{(\rm r)}} \left[1 - \pi^2 \kappa(\eta) \frac{m_{\rm f}}{m_{\rm r}} \frac{C_2}{Nq} + ...\right] \qquad (21)$$

For $m_{\rm i} \to \infty$, $\varepsilon_q^{(\rm i)} = 0$, we have $\kappa(\infty) = -1/4\pi$ and we recover the asymptotic result derived in [40] using operator product expansion. Note that mean-field theory predicts $\kappa_{\rm MF}(\infty) = 0$, and therefore disagrees with this independent result.

Using the mean-field estimate for F at unitarity, we see that the second-order correction to the polaron energy (Eq. (17)) is dominated by the logarithmic contribution. In the case of the polaron oscillation experiments reported in [22], the predicted correction amounts to a 5% shift of the oscillation frequency. Although small, this correction is within the reach of current experimental capabilities and shows that the results presented in this work are necessary to achieve the percent-level agreement between experiment and theory targeted by state of the art precision quantum many-body physics.

The authors thank M. Parish, J. Levinsen, F. Werner, C. Mora, L. Pricoupenko as well as ENS ultracold Fermi group for insightful discussions. They thank Ren Zhang and Hui Zhai for providing the data shown in Fig. 4. This work was supported by ANR (SpifBox) and EU (ERC grant CritiSup2).

[1] L.D. Landau and S.I. Pekar. Effective mass of a polaron. *J. Exp. Theor. Phys*, 18:419–423, 1948.
[2] Jun Kondo. Resistance minimum in dilute magnetic alloys. *Progress of theoretical physics*, 32(1):37–49, 1964.
[3] Philip Warren Anderson. Localized magnetic states in metals. *Physical Review*, 124(1):41, 1961.
[4] W Zuo, ZH Li, GC Lu, JQ Li, W Scheid, U Lombardo, H-J Schulze, and CW Shen. 1s0 proton and neutron superfluidity in β-stable neutron star matter. *Physics Letters B*, 595(1-4):44–49, 2004.
[5] Kenji Fukushima and Vladimir Skokov. Polyakov loop modeling for hot qcd. *Progress in Particle and Nuclear Physics*, 96:154–199, 2017.
[6] Jesper Levinsen, Pietro Massignan, Shimpei Endo, and Meera M Parish. Universality of the unitary Fermi gas: a few-body perspective. *Journal of Physics B: Atomic, Molecular and Optical Physics*, 50(7):072001, 2017.
[7] Antoine Georges, Gabriel Kotliar, Werner Krauth, and Marcelo J. Rozenberg. Dynamical mean-field theory of strongly correlated fermion systems and the limit of infinite dimensions. *Rev. Mod. Phys.*, 68:13–125, Jan 1996.
[8] I. Bloch, J. Dalibard, and W. Zwerger. Many-body physics with ultracold gases. *Rev. Mod. Phys.*, 80(3):885–964, 2008.
[9] W. Zwerger, editor. *The BCS-BEC Crossover and the Unitary Fermi Gas*, volume 836 of *Lecture Notes in Physics*. Springer, Berlin, 2012.
[10] F. Chevy and C. Mora. Ultra-cold Polarized Fermi Gases. *Rep. Prog. Phys.*, 73:112401, 2010.
[11] Pietro Massignan, Matteo Zaccanti, and Georg M Bruun. Polarons, dressed molecules and itinerant ferromagnetism in ultracold Fermi gases. *Reports on Progress in Physics*, 77(3):034401, 2014.
[12] M.W. Zwierlein, A. Schirotzek, C.H. Schunck, and W. Ketterle. Fermionic superfluidity with imbalanced spin populations. *Science*, 311(5760):492–496, 2006.
[13] G.B. Partridge, W. Li, R.I. Kamar, Y. Liao, and R.G. Hulet. Pairing and phase separation in a polarized Fermi gas. *Science*, 311(5760):503–505, 2006.
[14] S. Nascimbène, N. Navon, K. Jiang, L. Tarruell, M. Teichmann, J. McKeever, F. Chevy, and C. Salomon. Collective Oscillations of an Imbalanced Fermi Gas: Axial Compression Modes and Polaron Effective Mass. *Phys. Rev. Lett.*, 103(17):170402, 2009.
[15] F. Chevy. Universal phase diagram of a strongly interacting Fermi gas with unbalanced spin populations. *Phys.*

Rev. A, 74(6):063628, 2006.

[16] C. Lobo, A. Recati, S. Giorgini, and S. Stringari. Normal state of a polarized Fermi gas at unitarity. *Phys. Rev. Lett.*, 97(20):200403, 2006.

[17] N. Prokof'ev and B. Svistunov. Fermi-polaron problem: Diagrammatic monte carlo method for divergent sign-alternating series. *Phys. Rev. B*, 77(2):020408, 2008.

[18] Nils B Jørgensen, Lars Wacker, Kristoffer T Skalmstang, Meera M Parish, Jesper Levinsen, Rasmus S Christensen, Georg M Bruun, and Jan J Arlt. Observation of attractive and repulsive polarons in a Bose-Einstein condensate. *Physical Review Letters*, 117(5):055302, 2016.

[19] Ming-Guang Hu, Michael J Van de Graaff, Dhruv Kedar, John P Corson, Eric A Cornell, and Deborah S Jin. Bose polarons in the strongly interacting regime. *Phys. Rev. Lett.*, 117(5):055301, 2016.

[20] V. Efimov. Energy levels of three resonantly interacting particles. *Nuclear Physics A*, 210(1):157 – 188, 1973.

[21] Jesper Levinsen, Meera M Parish, and Georg M Bruun. Impurity in a Bose-Einstein condensate and the Efimov effect. *Physical Review Letters*, 115(12):125302, 2015.

[22] I Ferrier-Barbut, M. Delehaye, S. Laurent, A.T. Grier, M. Pierce, B.S Rem, F. Chevy, and C. Salomon. A mixture of Bose and Fermi superfluids. *Science*, 345:1035–1038, 2014.

[23] Richard Roy, Alaina Green, Ryan Bowler, and Subhadeep Gupta. Two-element mixture of Bose and Fermi superfluids. *Physical Review Letters*, 118(5):055301, 2017.

[24] Xing-Can Yao, Hao-Ze Chen, Yu-Ping Wu, Xiang-Pei Liu, Xiao-Qiong Wang, Xiao Jiang, Youjin Deng, Yu-Ao Chen, and Jian-Wei Pan. Observation of coupled vortex lattices in a mass-imbalance Bose and Fermi superfluid mixture. *Phys. Rev. Lett.*, 117:145301, Sep 2016.

[25] Yusuke Nishida. Polaronic atom-trimer continuity in three-component Fermi gases. *Physical Review Letters*, 114(11):115302, 2015.

[26] Wei Yi and Xiaoling Cui. Polarons in ultracold Fermi superfluids. *Phys. Rev. A*, 92(1):013620, 2015.

[27] Eric Braaten and Agustin Nieto. Quantum corrections to the energy density of a homogeneous Bose gas. *The European Physical Journal B-Condensed Matter and Complex Systems*, 11(1):143–159, 1999.

[28] Eric Braaten, H.-W. Hammer, and Thomas Mehen. Dilute Bose-Einstein condensate with large scattering length. *Phys. Rev. Lett.*, 88:040401, Jan 2002.

[29] Alexander O Gogolin, Christophe Mora, and Reinhold Egger. Analytical solution of the bosonic three-body problem. *Physical Review Letters*, 100(14):140404, 2008.

[30] See supplementary information.

[31] Note that we define R_e as in [29] that is positive for a two-channel model and whose sign is opposite to the traditional definition of the effective range.

[32] Hui Hu, X-J Liu, and Peter D Drummond. Static structure factor of a strongly correlated Fermi gas at large momenta. *EPL (Europhysics Letters)*, 91(2):20005, 2010.

[33] S. Tan. Large momentum part of a strongly correlated Fermi gas. *Ann. Phys.*, 323(12):2971–2986, 2008.

[34] T.T. Wu. Ground state of a Bose system of hard spheres. *Phys. Rev.*, 115(6):1390–1404, 1959.

[35] Shina Tan. Three-boson problem at low energy and implications for dilute Bose-Einstein condensates. *Physical Review A*, 78(1):013636, 2008.

[36] H-W Hammer. Three-body forces: From cold atoms to nuclei. *Acta Phys. Polon.*, 46:379, 2015.

[37] Ljudvig D Faddeev and Stanislav Petrovich Merkuriev. *Quantum scattering theory for several particle systems*, volume 11. Springer Science & Business Media, 2013.

[38] Paulo F Bedaque, H-W Hammer, and Ubirajara Van Kolck. Renormalization of the three-body system with short-range interactions. *Physical Review Letters*, 82(3):463, 1999.

[39] Ren Zhang, Wei Zhang, Hui Zhai, and Peng Zhang. Calibration of the interaction energy between Bose and Fermi superfluids. *Phys. Rev. A*, 90(6):063614, 2014.

[40] Johannes Hofmann and Wilhelm Zwerger. Deep inelastic scattering on ultracold gases. *Physical Review X*, 7(1):011022, 2017.

Few vs many-body physics of an impurity immersed in a superfluid of spin 1/2 attractive fermions: Supplemental information

M. Pierce,[1] X. Leyronas,[2] and F. Chevy[1]

[1] *Laboratoire Kastler Brossel, ENS-Université PSL, CNRS, Sorbonne Université, Collège de France.*
[2] *Laboratoire de physique de l'Ecole normale supérieure, ENS, Université PSL, CNRS, Sorbonne Université, Université Paris-Diderot, Sorbonne Paris Cité, Paris, France.*

THREE-BODY PHASE-DIAGRAM

Efimov ground state

The Efimov spectrum can be obtained without further regularization of the three-body problem using a two-channel model described by the hamiltonian [1, 2]

$$\hat{H} = \sum_{\mathbf{k},\sigma} \epsilon_k \hat{a}^\dagger_{\mathbf{k},\sigma}\hat{a}_{\mathbf{k},\sigma} + \sum_{\mathbf{K},\sigma}(E_{\sigma,0}+\epsilon_k/2)\hat{b}^\dagger_{\mathbf{K},\sigma}\hat{b}_{\mathbf{K},\sigma} + \frac{\hbar^2}{2m}\sqrt{\frac{2\pi}{R_e}}\sum_{\substack{\mathbf{K},\mathbf{k},k<\Lambda \\ \sigma_1\neq\sigma_2\neq\sigma_3}} (\hat{b}^\dagger_{\mathbf{K},\sigma_1}\hat{a}_{\mathbf{k}+\mathbf{K}/2\sigma_2}\hat{a}_{-\mathbf{k}+\mathbf{K}/2,\sigma_3} + \text{H.c.}). \tag{S1}$$

In this expression, $\sigma \in \{1,2,3\}$ labels the three atomic species, $\hat{a}_{\boldsymbol{k},\sigma}$ is the atomic (open channel) annihilation operator for species σ, $\hat{b}_{\boldsymbol{K},\sigma}$ the molecular (closed channel) annihilation operator describing dimers not involving spin σ atoms, and R_e the effective range of the potential. For the sake of simplicity, we assume that all three atomic species have the same mass m and that the atom-dimer coupling is the same for all three species. The atom-atom scattering lengths are nevertheless controlled independently by the bare molecular binding energies $E_{\sigma,0}$.

The solutions of the two-body problem shows that the scattering length a_σ between two atoms $(\sigma_1,\sigma_2) \neq \sigma$ is given by

$$\frac{1}{a_\sigma} = \frac{2}{\pi}\Lambda - \frac{R_e m E_{\sigma,0}}{\hbar^2}, \tag{S2}$$

where Λ is a UV momentum cut-off.

The three-body bound states are described by the Ansatz

$$|\psi\rangle = \sum_{\boldsymbol{k}_1,\boldsymbol{k}_2} \beta(\boldsymbol{k}_1,\boldsymbol{k}_2)\hat{a}^\dagger_{\boldsymbol{k}_1,1}\hat{a}^\dagger_{\boldsymbol{k}_2,2}\hat{a}^\dagger_{-\boldsymbol{k}_1-\boldsymbol{k}_2,3}|0\rangle + \sum_{\sigma,\boldsymbol{k}} \frac{\alpha_\sigma(\boldsymbol{k})}{k}\hat{a}^\dagger_{-\boldsymbol{k},\sigma}\hat{b}^\dagger_{\boldsymbol{k},\sigma}|0\rangle. \tag{S3}$$

where $|0\rangle$ is the vacuum.

The trimer energy $E_3 = -\hbar^2\kappa^2/m$ is then obtained by solving the set of three equations

$$\left[\sqrt{1+3p^2/4} + \kappa R_e(1+3p^2/4) - \frac{1}{\kappa a_\sigma}\right]\alpha_\sigma(p) = \frac{1}{\pi}\int_0^\infty dq \ln\left(\frac{p^2+q^2+pq+1}{p^2+q^2-pq+1}\right)\left[\sum_{\sigma'\neq\sigma}\alpha_{\sigma'}(q)\right], \tag{S4}$$

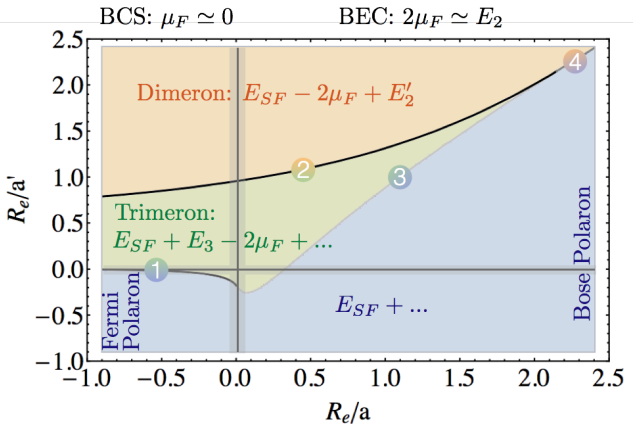

FIG. S1. Phase diagram of an impurity immersed in a fermionic superfluid. The typical energy of each phase (detailed in the text) is written in each domain, the dots in each expression contain the mean-field terms that are negligible compared to the other terms. The typical expression of the chemical potential in the BEC-BCS crossover is given at the top (on the BCS side, it corresponds approximately to the Fermi energy which is negligible compared to the other energy scales presented here, hence the 0). The four numbers correspond to the four frontiers described in the text. The grey bands correspond to the parameter range where many-body effects affect few-body physics for a typical value $k_F R_e = 5\times10^{-2}$.

Frontiers of the stability diagram

We explain here how the different domains of the stability diagram of Fig. S1 are obtained (corresponding to Fig. 2 of the main text).

In experiments, R_e is small compared to the interparticle distance, therefore we have $R_e\, k_F \ll 1$, where the Fermi wavevector k_F is defined by $n \equiv k_F^3/(3\pi^2)$. On the BCS side of the BEC-BCS crossover of the super-

fluid, we have $1/(k_F a) < 0$ and $1/|k_F a| \sim 1$ and therefore $|R_e/a| = R_e\, k_F/|k_F a| \ll 1$. For the same reason, the BEC side corresponds to $1/(k_F a) \sim 1$ and we have $R_e/a = R_e\, k_F/(k_F a) \ll 1$. On the graph of Fig. S1, the crossover region of the superfluid is therefore concentrated in a narrow region around the y-axis. The consequence of this separation of scales is that, except in this narrow region, for $R_e/a > 0$, the superfluid is made of weakly interacting tightly bound dimers, while for $R_e/a < 0$, it is made of extremely loose Cooper pairs corresponding essentially to non-interacting fermions (except for superfluid properties).

Concerning the impurity-fermion interaction regime, we have similarly $(k_F a') = (R_e/a')^{-1}(k_F\, R_e)$, which is a small dimensionless number for R_e/a' not too small. Therefore, except in a narrow region around the x-axis in Fig. S1, we have $k_F|a'| \ll 1$.

In the ($R_e/a' < 0$, $R_e/a < 0$) quadrant (Fermi polaron sector), the energy of the impurity immersed in the superfluid is given by $E_{SF} + g'\, n$, where E_{SF} is the ground state energy of the superfluid without the impurity.

In the Bose-polaron sector ($R_e/a' < 0$, $R_e/a > 0$), the energy of the polaron in the superfluid is given by $E_{SF} + g'_{b-f}\, n$, where g'_{b-f} is the coupling constant between the impurity and a dimer of the superfluid.

In the ($R_e/a' > 0$, $R_e/a < 0$) quadrant the energy of the dimeron in the superfluid is $E_{SF} - 2\mu_f + E'_2 + g'_{b-f} n + gn$. The $-2\mu_f$ contribution originates from Cooper pair breaking. One of the fermions of the pair binds to the impurity to form a dimer of energy E'_2 while the second remains unbound and contributes to the mean-field term gn. For $R_e/a < 0$, $\mu_f \approx \hbar^2 k_F^2/(2m)$ is the chemical potential of an ideal gas. The dimer energy is given by [3] $E'_2 = -\frac{\hbar^2}{m}{\kappa'_2}^2$, with $R_e\, \kappa'_2 = 2\frac{R_e}{a'}\left(1 + \sqrt{1 + 4\frac{R_e}{a'}}\right)^{-1}$.

For ($R_e/a' > 0$), and ($R_e/a > 0$) , the energy of the dimeron in the superfluid is $E_{SF} - E_2 + E'_2 + g'_{b-b} n + gn$ where we have substracted the dimer energy E_2 lost by the binding of a fermion of the bath with the impurity. The expression for E_2 is obtained from the expression of E'_2 by replacing a' by a. g'_{b-b} is the coupling constant characterizing the interaction between the dimeron and the dimers of the superfluid.

Finally, the energy of the trimeron in the superfluid is given by $E_{SF} + E_3 - 2\mu_f + g'_{t-f} n$. E_3 is the trimer energy (a 3-body bound state), g_{t-f} is a trimer-fermion coupling constant, and $-2\mu_f$ is the energy of the two fermions of the trimer coming from the superfluid bath.

Depending on the parameters, we determine which state has the lowest energy. In this limit where k_F tends to zero, all the terms containing n or k_F vanish. All these energies, minus the neglected mean-field terms, are gathered in Fig. S1. We then consider four cases (corresponding to the four numbers displayed in Fig. S1):

1. Fermi polaron ($R_e/a < 0$) vs trimeron. The frontier is obtained by solving $E_3(R_e, a, a') = 0$.

2. Dimeron vs trimeron. The frontier is obtained by solving $E_3(R_e, a, a') = E'_2$.

3. Bose polaron ($R_e/a > 0$) vs trimeron. The frontier is obtained by solving $E_3(R_e, a, a') = E_2$.

4. Bose polaron vs dimeron. The frontier is obtained by solving $E'_2 = E_2$. Since E'_2 and E_2 are given by the same function evaluated for a' and a, this frontier is included in the line $a' = a$, *i.e.* the first bisector in S1.

We end this section by noticing that the Fermi polaron-trimeron frontier approaches the x-axis for $Re/a \to -\infty$. In this region, the calculation is no more controlled (k_F is not negligible anymore). However, since the polaron/trimeron is a crossover [4], the transition line cannot be defined precisely anyway.

Moreover we note that for $a = a'$, our results agree with the calculations reported in [3] for three-component color Fermi gases.

BCS THEORY

This section presents a derivation of the results presented in the paper within the simplified framework of BCS mean-field theory. We first determine χ, then the F function and finally we compare it to the exact expressions presented in this paper.

Since these results will only confirm the general behaviour but will not yield quantitative predictions, we restrain our calculations to the simplest case $m_f = m_i = m$ so for $\eta = 1$, a ratio close to the mass ratio we have with our Lithium experiment (7/6).

Mean-field compressibility

As described in the main text, second order perturbation theory relates the polaron energy shift to the fermionic superfluid dynamical compressibility $\chi(\boldsymbol{q}, E)$ defined by

$$\chi(\boldsymbol{q}, E) = \frac{1}{N}\sum_{\alpha} \frac{|\langle\alpha|\hat{\rho}_{-\boldsymbol{q}}|0\rangle|^2}{E_\alpha - E_0 + E}. \tag{S5}$$

Here, we derive the expression of χ using BCS theory where the fermionic medium is described by the mean-field Hamiltonian

$$\hat{H}_{\rm mb} = \sum_{\boldsymbol{k},\sigma} \xi_k \hat{c}^\dagger_{\boldsymbol{k}\sigma}\hat{c}_{\boldsymbol{k}\sigma} + \Delta^* \sum_{\boldsymbol{k}} \hat{c}_{\boldsymbol{k}\uparrow}\hat{c}_{-\boldsymbol{k}\downarrow} + \text{h.c.} \tag{S6}$$

with $\xi_k = \epsilon_k^{(\mathrm{f})} - \mu$, μ is the chemical potential, and the gap Δ is defined by

$$\Delta = \frac{g_0}{\Omega} \sum_{\boldsymbol{k}} \langle \hat{c}_{-\boldsymbol{k}\downarrow} \hat{c}_{\boldsymbol{k}\uparrow} \rangle. \tag{S7}$$

The Hamiltonian is diagonalized by introducing Bogoliubov operators $\hat{\gamma}_{\boldsymbol{k}\pm}$ defined by:

$$\hat{c}_{\boldsymbol{k}\uparrow} = u_k \hat{\gamma}_{\boldsymbol{k}+} - v_k \hat{\gamma}_{-\boldsymbol{k}-} \tag{S8}$$
$$\hat{c}_{\boldsymbol{k}\downarrow} = u_k \hat{\gamma}_{\boldsymbol{k}-} + v_k \hat{\gamma}_{-\boldsymbol{k}+}, \tag{S9}$$

with

$$u_k = \sqrt{\frac{1}{2}(1 + \frac{\xi_k}{E_k})}, \quad v_k = \sqrt{\frac{1}{2}(1 - \frac{\xi_k}{E_k})} \tag{S10}$$

and $E_k = \sqrt{\xi_k^2 + |\Delta|^2}$.

To derive the BCS expression of the compressibility, we express the matrix elements $\langle \alpha | \hat{\rho}_{-\boldsymbol{q}} | 0 \rangle = \sum_\sigma \langle \alpha | \hat{c}^\dagger_{\boldsymbol{k}-\boldsymbol{q},\sigma} \hat{c}_{\boldsymbol{k},\sigma} | 0 \rangle$ using the Bogoliubov creation and annihilation operators. After a straightforward calculation, we finally obtain

$$\chi^{\mathrm{MF}}(\boldsymbol{q}, E) = \frac{1}{N} \sum_{\boldsymbol{k}} \frac{2u_{k-q}^2 v_k^2 + 2u_k v_k u_{k-q} v_{k-q}}{E_k + E_{k-q} + E}, \tag{S11}$$

where we have used the fact that the excited states $|\alpha\rangle$ correspond to pairs of Bogoliubov excitations, hence $E_\alpha - E_0 = E_k + E_{k-q}$. We use the notation MF to signify that this result is only valid in BCS theory, a mean-field theory.

Perturbative calculation of the energy

In order to calculate the polaron energy shift, we need to consider the perturbative development we obtained in the article, adapted to BCS theory:

$$\Delta E^{\mathrm{MF}}_{\mathrm{pert}} = \left[g'n + \frac{g'^2 n}{\Omega} \sum_{\boldsymbol{q}} \left(\frac{1}{\varepsilon_q^{(\mathrm{r})}} - \chi^{\mathrm{MF}}(\boldsymbol{q}, \varepsilon_q^{(\mathrm{i})}) \right) \right] \tag{S12}$$

After turning sums to integrals and performing the angular integrations we can write this expression as:

$$\Delta E^{\mathrm{MF}}_{\mathrm{pert}} = g'n + \frac{g'^2}{8\pi^4} \frac{m}{\hbar^2} \int k^2 \mathrm{d}k \int q^2 \mathrm{d}q \left(\frac{4v_k^2}{q^2} - \frac{2u_q^2 {v_k}^2 + 2u_k v_k u_q v_q}{kq} \ln \left(\frac{E_k + E_q + \frac{\hbar^2 (k+q)^2}{2m}}{E_k + E_q + \frac{\hbar^2 (k-q)^2}{2m}} \right) \right) \tag{S13}$$

To study the behaviour of these integrals for high k, we perform the variable change $k \to u = (k/k_F)/\sqrt{|\Delta|/E_F}$, $q \to v = (q/k_F)/\sqrt{|\Delta|/E_F}$ and we get

$$\Delta E^{\mathrm{MF}}_{\mathrm{pert}} = g'n \left[1 + k_F a' \frac{3}{2\pi} \left| \frac{\Delta}{E_F} \right|^2 I(\Lambda/k_F) \right] \tag{S14}$$

with I corresponding to the integral left to calculate in Eq. (S13) that depends on the cut-off Λ and also on the ratio $\mu/|\Delta|$.

In the limit $u, v \gg 1$, we can simplify greatly the expression of the integral I.

First, we can see that the terms u_k^2 and v_k^2 can be rewritten, in this limit:

$$u_k^2 \sim 1, \quad v_k^2 \sim \frac{1}{4} \frac{|\Delta|^2}{\xi_k^2} \to \frac{1}{4u^4} \tag{S15}$$

From this last expression, we can also get Tan's contact for two fermions C_2 in BCS theory. Indeed, using the property of momentum distribution [5]:

$$n_\uparrow(k) \underset{k\to\infty}{\sim} n_\downarrow(k) \underset{k\to\infty}{\sim} \frac{C_2}{k^4} \tag{S16}$$

and knowing that in BCS theory we have $n(k) = n_\uparrow(k) + n_\downarrow(k) = 2v_k^2 \Omega$, we see that we have the right dependence for the momentum distribution and we can extract the contact

$$\frac{C_2}{N} = \frac{3\pi^2}{4} \left| \frac{\Delta}{E_F} \right|^2 k_F. \tag{S17}$$

The integral can then be simplified in this limit as

$$I(\Lambda/k_F) = \int \frac{\mathrm{d}u}{u} \int \frac{\mathrm{d}v}{u} \left[1 - \frac{1}{2} \left(\frac{v}{u} + \frac{u}{v} \right) \ln \left(\frac{1 + v/u + (v/u)^2}{1 - v/u + (v/u)^2} \right) \right]. \tag{S18}$$

The second integral (over v/u) converges towards $2\pi^4 \kappa^{\mathrm{MF}}$ and the first integral (over u) gives the logarithmic divergence. We can finally write:

$$I = 2\pi^4 \kappa^{\mathrm{MF}} (\ln(\Lambda/k_F) + ...) \tag{S19}$$

with κ^{MF}:

$$\kappa^{\mathrm{MF}} = \frac{\sqrt{3}}{8\pi^3} - \frac{1}{12\pi^2}. \tag{S20}$$

In the main text we found:

$$\kappa(1) = \frac{\sqrt{3}}{8\pi^3} - \frac{1}{12\pi^2} - \frac{1}{9\pi\sqrt{3}} \tag{S21}$$

The two results are very similar except for the last term of $\kappa(1)$ which does not appear in the mean-field approach because BCS theory does not account for interactions between excitations of the superfluid. This missing term is actually pretty important since it is the leading term in κ, therefore we get a ratio $\kappa(1)/\kappa^{\mathrm{MF}} \simeq 15$.

The F function

We find out analytically that there is again a logarithmic divergence of this second order term, consistently with what we stated before. By combining equations (S14), (S17) and (S19), we get the expression of the energy calculated up to second order in perturbation using BCS theory :

$$\Delta E^{\mathrm{MF}}_{\mathrm{pert}} = g'n\left[1 + k_F a' F^{\mathrm{MF}}\left(\frac{1}{k_F a}\right) + 4\pi\kappa^{\mathrm{MF}} a' \frac{C_2}{N}\ln(\Lambda/k_F)\right] \tag{S22}$$

with F^{MF} a function that can be computed numerically throughout the BEC-BCS crossover by calculating the difference between the exact expression of the integral I defined in Eq. (S13) and the logarithmic term we obtained in Eq. (S19). These numerical calculations show that this function does not depend on the cut-off but only on the parameter $1/(k_F a)$.

Then, by introducing a similar renormalization with a three-body term, we can rewrite the energy as:

$$\Delta E^{\mathrm{MF}} = g'n\left[1 + k_F a' F^{\mathrm{MF}}\left(\frac{1}{k_F a}\right) - 4\pi\kappa^{\mathrm{MF}} \frac{a' C_2}{N}\ln(k_F R_3) + ...\right], \tag{S23}$$

We get a very similar expression to the one we found in this letter, only we replaced F and $\kappa(1)$ by F^{MF} and κ^{MF}.

The function F^{MF} is represented in Fig. S2, and we can observe the two asymptotic behaviours on the BCS and BEC sides:

1. In the BCS limit we recover once again the Fermi-polaron, hence $F^{\mathrm{MF}}(-\infty) = 3/2\pi$ for $\eta = 1$.
2. In the BEC limit, we get a behaviour consistent with the Bose-Polaron:

$$F^{\mathrm{MF}}\left(\frac{1}{k_F a}\right) = 16\pi^2\kappa^{\mathrm{MF}}\frac{\ln(k_F a)}{k_F a} + ... \tag{S24}$$

In conclusion, BCS theory predicts the correct qualitative behaviour for the polaron energy shift but is quantitatively wrong, which is illustrated in Fig. S5 at the end of this supplementary material.

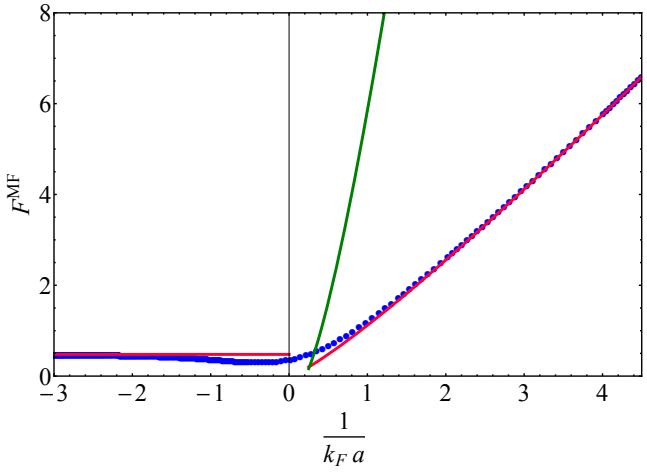

FIG. S2. Blue dots: Representation of the function F^{MF} through the crossover for $\eta = 1$. Red curves: Asymptotic behaviours described in the text on the BCS side: $F^{\mathrm{MF}}(-\infty) = \frac{3}{2\pi}$, and the BEC Side : $F^{\mathrm{MF}}(X) \simeq 16\pi^2\kappa^{\mathrm{MF}} X\ln(1/X) + A_0 X$ with A_0 an adjustable parameter found out to be, after optimization, $A_0 \simeq 1.1$. Green curve: asymptotic behaviour on the BEC side using the true value of κ, C_{ad} and R_3 (the last two are given in the last section of this Supplementary material).

THREE-BODY PARAMETERS

Calculating R_3

We can obtain the three-body parameter R_3 introduced in the equation

$$\Gamma_{\mathrm{Born}} - \Gamma_{\mathrm{Faddeev}} \underset{\Lambda\to\infty}{=} g'^2\kappa(\eta)\ln(\Lambda R_3) + o(1) \tag{S25}$$

by calculating numerically this difference. We break down this term into three parts, each corresponding to one of the first three diagram of Fig. 3 from this letter.

Firstly, in the effective range approximation, the two-body T-matrix is given by

$$\hat{t}_i = \frac{g'/\Omega}{1 + ika' + R_e a' k^2} \tag{S26}$$

where R_e is the effective range of the potential and k is given by:

$$k = \sqrt{2m_r(E + i0^+)/\hbar^2} \tag{S27}$$

with E the energy of the initial state in the center-of-mass frame of the three particles at the moment of the interaction. For the diagrams we want to calculate, we only have to consider the case where the fermions have impulsions of $\boldsymbol{p}$ and $-\boldsymbol{p}$ and the impurity has an impulsion equal to zero (cf Fig. 3 from the article). This leads to:

$$E/\hbar = 0 - (\frac{p^2}{2m_f} + \frac{p^2}{2(m_f+m_b)}) = -\frac{3}{4}\frac{p^2}{m} \qquad \text{(S28)}$$

Finally, the two-body T-matrix can be written as:

$$\hat{t}_i = \frac{g'/\Omega}{1 - \sqrt{\frac{\eta(2+\eta)}{(1+\eta)^2}}a'p - \frac{\eta(2+\eta)}{(1+\eta)^2}(\frac{R_e}{a'})(a'p)^2 + i0^+} = \frac{g'}{\Omega}t(p) \qquad \text{(S29)}$$

Then, we can write below the expressions corresponding to each of these three diagrams.

$$\Gamma^{(1)} = -2\frac{m_f^2}{\hbar^4}\frac{g'}{\Omega}\sum_{\boldsymbol{p}}\frac{1}{p^4}t(p) \qquad \text{(S30)}$$

$$\Gamma^{(2)} = -2\frac{m_f^3}{\hbar^6}\frac{g'^2}{\Omega^2}\sum_{\boldsymbol{p_1},\boldsymbol{p_2}}\frac{1}{p_1^2p_2^2}\frac{t(p_1)t(p_2)}{(p_1^2+p_2^2)(\frac{\eta+1}{2\eta}) - \frac{1}{\eta}\vec{p_1}.\vec{p_2}} \qquad \text{(S31)}$$

$$\Gamma^{(3)} = -4\frac{m_f^3}{\hbar^6}\frac{g'^2}{\Omega^3}\sum_{\boldsymbol{p_1},\boldsymbol{p_2},\boldsymbol{p_3}}\left[\frac{1}{p_1^2p_3^2}\frac{4\pi}{1/a - p_2\sqrt{\frac{\eta+2}{4\eta}}}\right. \qquad \text{(S32)}$$
$$\left.\times\frac{t(p_1)}{p_1^2+p_2^2(\frac{\eta+1}{2\eta}) - \vec{p_1}.\vec{p_2}}\frac{t(p_3)}{p_3^2+p_2^2(\frac{\eta+1}{2\eta}) - \vec{p_3}.\vec{p_2}}\right]$$

In order to calculate the Faddeev term for Γ, one has to use the expression of $t(p)$ given in S29. On the other hand, to obtain the Born term, one has to expand this expression of $t(p)$ up to first order in a' for $\Gamma^{(1)}$ and up to zero order for the other two components (so just replacing it by 1), so that all three components of Γ are expanded up to order two in a'.

For $\Gamma^{(3)}$, we calculate the sum in the limit $1/a \ll 1/a'$ (highly interacting fermions) in which the difference between the Faddeev term and the Born term does not depend on a. To calculate these different sums we proceed similarly as we did in the previous section for BCS theory.

In this framework, one can show that R_3/a' only depends on the ratio R_e/a' and the mass ratio. We show in Fig. S3 the numerical calculations of the difference $\Gamma_{\rm Born} - \Gamma_{\rm Faddeev}$ for the mass ratio $\eta = 7/6$ and $R_e/|a'| = 1$. We see that we indeed get the logarithmic behaviour with $\kappa(7/6)$ as the proportionality constant.

We show in Fig. S4 the parameter $R_3/|a'|$ for different values of the ratio $R_e/|a'|$ in the case $\eta = 7/6$. For $R_e/|a'| \ll 1$, we get the asymptotic behaviour $R_3 \simeq 1.50|a'|$. For $R_e/|a'| \gg 1$, we see that R_3 increases exponentially:

$$R_3 \underset{\frac{R_e}{|a'|}\gg 1}{\propto} \sqrt{R_e|a'|}\exp\left(\frac{\sqrt{3}}{16\pi^2|\kappa(7/6)|}\sqrt{\frac{R_e}{|a'|}}\right). \qquad \text{(S33)}$$

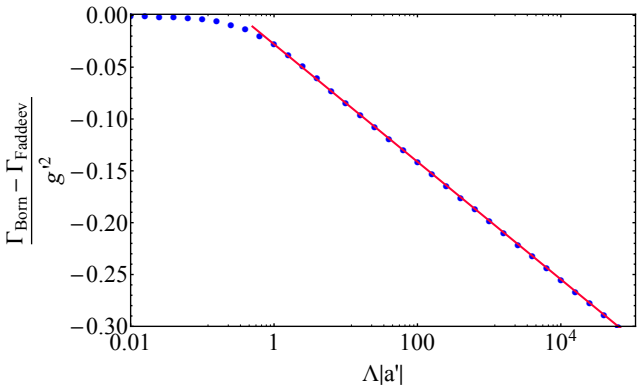

FIG. S3. Blue dots: numerical calculations of the left-hand side of eq. (S25), divided by g'^2, for $\eta = 7/6$ and $R_e = |a'|$. Red curve: fitting curve of the blue dots in the limit $\Lambda|a'| \gg 1$. We fit the data for $\Lambda|a'| \gg 1$ with the function $\kappa(7/6)\ln(X \times A_0)$ with A_0 a fitting parameter. The parameter A_0 gives us the value of $R_3/|a'|$: here we get $A_0 \simeq 3.10$.

At this point we should remind that we consider expansions for $\Lambda|a'| \ll 1$ but with $R_e/|a'|$ as an independent parameter with a given value. Consequently, we consider this exponential term as a constant included in R_3 in our perturbative calculations.

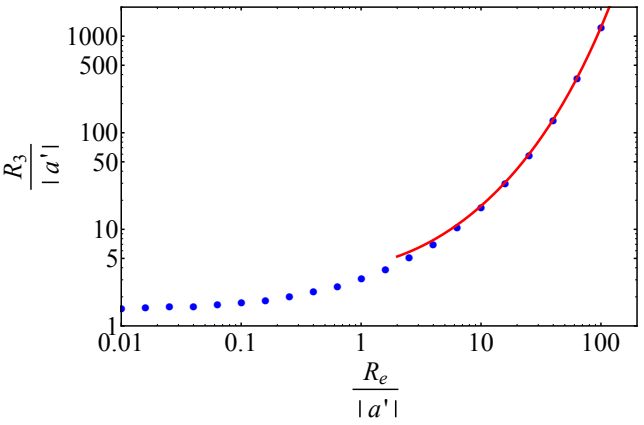

FIG. S4. Blue dots: numerical calculations of $R_3/|a'|$ for different $R_e/|a'|$ ratios and $\eta = 7/6$. Red curve: fit for $R_e/|a'| \gg 1$ using a function $A\sqrt{X}\exp\left(\frac{\sqrt{3}}{16\pi^2|\kappa(7/6)|}\sqrt{X}\right)$, with A an adjustable parameter. $A \simeq 0.8$ after optimization.

To see the dependence on the mass ratio η, Table I lists numerical values of the parameter R_3 that were computed for experimentally relevant mass ratios and $R_e = 0$.

η	7/40	23/40	7/6	87/6	133/6
R_3/a'	1.03	1.41	1.50	1.46	1.46

TABLE I. Dimensionless parameter characterizing the Born expansion of the three-body scattering amplitude (Eq. (S25)) for $R_e = 0$.

Atom-dimer scattering

The atom-dimer T-matrix can be computed using the same approach. Indeed, since the fermions are asymptotically bound, we can treat the impurity-fermion interaction as a perturbation. This leads to the same diagrams as in the three-body scattering problem and the atom-dimer scattering length consequently suffers from the same logarithmic divergence when the range of the potential vanishes. For large Λ the associated T-matrix scales as

$$T_{\rm ad}^{(1)} = \frac{2g'}{\Omega}\left[1 + 8\pi^2 \frac{m_f}{m_r}\kappa(\eta)\frac{a'}{a}\left(\ln(\Lambda a) + C_{\rm ad} + ...\right)\right] \tag{S34}$$

where the constant $C_{\rm ad}$ is computed numerically and is given in Table II for experimentally relevant values of the impurity-fermion mass ratios.

η	7/40	23/40	7/6	87/6	133/6
$C_{\rm ad}$	1.52	1.59	1.56	1.37	1.36

TABLE II. Dimensionless parameter characterizing the Born expansion of the atom-dimer scattering amplitude (Eq. (S34)) for $R_e = 0$.

The logarithmic divergence is once again cured by introducing the three-body interaction. Using the renormalized expression of $g_3(\Lambda)$ the three-body interaction contribution to the atom-dimer T-matrix amounts to

$$T_{\rm ad}^{(2)} = -\frac{16\pi^2 g'}{\Omega}\frac{m_f}{m_r}\kappa(\eta)\frac{a'}{a}\ln(\Lambda R_3). \tag{S35}$$

We indeed recover the asymptotic result Eq. [20] from the main text since we have

$$T_{\rm ad} = T_{\rm ad}^{(1)} + T_{\rm ad}^{(2)} = T_{\rm ad,Born}\left[1 - 8\pi^2 \frac{m_f}{m_r}\kappa(\eta)\frac{a'}{a}\left(\ln(R_3/a) + C_{\rm ad} + ...\right)\right] \tag{S36}$$

where $T_{\rm ad,Born} = 2g'/\Omega$ corresponds to an atom-dimer scattering length $a_{\rm ad,Born}/a' = 4(1+\eta)/(2+\eta)$.

Finally, to highlight the shortcomings of BCS theory and the consistency of our three-body calculations, we fit the atom-dimer scattering length calculated in [6], see Fig. S5. There is no hesitation possible in seeing that the coefficient before the log obtained through BCS theory (including $\kappa^{\rm MF}$) is too small to show the logarithmic behaviour whereas the real κ enables a much better fit.

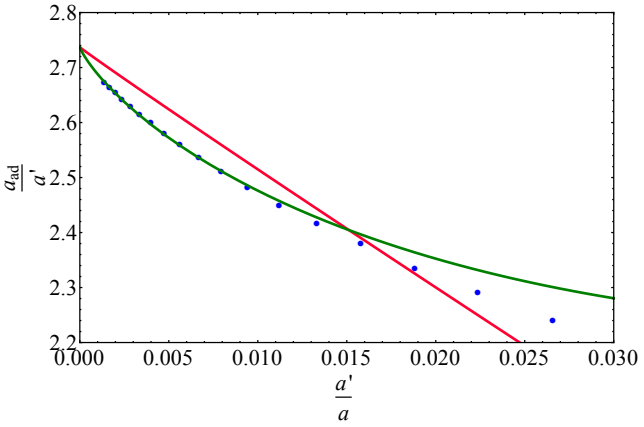

FIG. S5. Blue dots: Points from [6] showing the ratio of the atom-dimer scattering length $a_{\rm ad}$ over a', for $\eta = 7/6$. Red solid curve: fit to the blue dots using the function $a_{\rm ad,\,Born}/a'(1 + AX(\ln X + B))$ where A is a fixed parameter corresponding to the analytical result obtained through BCS theory ($A \propto \kappa^{\rm MF}$) and B is an adjustable parameter. Green solid curve: theoretical curve obtained through three-body calculations, its equation is the same as the one used for the red curve but now with $A \propto \kappa$ and B obtained through $C_{\rm ad}$ and R_3. We see that the curve corresponding to BCS theory (red) does not match at all the results reported in [6], contrary to the other one (green).

[1] Alexander O Gogolin, Christophe Mora, and Reinhold Egger. Analytical solution of the bosonic three-body problem. *Physical Review Letters*, 100(14):140404, 2008.

[2] Mattia Jona-Lasinio and Ludovic Pricoupenko. Three resonant ultracold bosons: Off-resonance effects. *Physical Review Letters*, 104(2):023201, 2010.

[3] Yusuke Nishida. New type of crossover physics in three-component Fermi gases. *Physical Review Letters*, 109(24):240401, 2012.

[4] Yusuke Nishida. Polaronic atom-trimer continuity in three-component Fermi gases. *Physical Review Letters*, 114(11):115302, 2015.

[5] S. Tan. Large momentum part of a strongly correlated Fermi gas. *Ann. Phys.*, 323(12):2971–2986, 2008.

[6] Ren Zhang, Wei Zhang, Hui Zhai, and Peng Zhang. Calibration of the interaction energy between Bose and Fermi superfluids. *Phys. Rev. A*, 90(6):063614, 2014.

Bibliography

[1] W. Pauli. Über den zusammenhang des abschlusses der elektronengruppen im atom mit der komplexstruktur der spektren. *Zeitschrift für Physik*, 31:765–783, 1925.

[2] Heike Kamerligh Onnes. Investigations into the properties of substances at low temperatures, which have led, amongst other things, to the preparation of liquid helium. *Nobel Lecture*, 4, 1913.

[3] P. Kapitza. Viscosity of liquid Helium below the λ-point. *Nature*, 141(3):74, 1938.

[4] J. F. Allen and A. D. Misener. Flow of liquid Helium ii. *Nature*, 141(3):75, 1938.

[5] D. Osheroff, R. Richardson, and D. Lee. Evidence for a new phase of solid ^{3}he. *PRL (Physical Review Letters)*, 28(14):885–888, 1972.

[6] D. C. Tsui, H. L. Stormer, and A. C. Gossard. Two-dimensional magnetotransport in the extreme quantum limit. *Phys. Rev. Lett.*, 48:1559–1562, 1982.

[7] R. B. Laughlin. Anomalous quantum hall effect: An incompressible quantum fluid with fractionally charged excitations. *Phys. Rev. Lett.*, 50:1395–1398, 1983.

[8] D. Osheroff, R. Richardson, and D. Lee. On the Bose-Einstein condensation. *Phys. Rev.*, 54:947–954, 1938.

[9] J. Bardeen, L. N. Cooper, and J. R. Schrieffer. Theory of superconductivity. *Phys. Rev.*, 108(5):1175–1204, 1957.

[10] J. Georg Bednorz and K. Alex Müller. Perovskite-type oxides—the new approach to high-T_c superconductivity. *Rev. Mod. Phys.*, 60:585–600, 1988.

[11] Alfred Kastler. Quelques suggestions concernant la production optique et la détection optique d?une inégalité de population des niveaux de quantification spatiale des atomes. Application à l?expérience de Stern et Gerlach et à la résonance magnétique. *J. phys. radium*, 11:255–265, 1950.

[12] William D. Phillips, John V. Prodan, and Harold J. Metcalf. Laser cooling and electromagnetic trapping of neutral atoms. *J. Opt. Soc. Am. B*, 2(11):1751–1767, 1985.

[13] M. H. Anderson, J. R. Ensher, M. R. Matthews, C. E. Wieman, and E. A. Cornell. Observation of bose-einstein condensation in a dilute atomic vapor. *Science*, 269(5221):198–201, 1995.

[14] K. B. Davis, M. O. Mewes, M. R. Andrews, N. J. van Druten, D. S. Durfee, D. M. Kurn, and W. Ketterle. Bose-einstein condensation in a gas of sodium atoms. *Phys. Rev. Lett.*, 75:3969–3973, 1995.

[15] B. DeMarco and D.S. Jin. Onset of Fermi degeneracy in a trapped atomic gas. *Science*, 285(5434):1703, 1999.

[16] I. Bloch, J. Dalibard, and W. Zwerger. Many-body physics with ultracold gases. *Rev. Mod. Phys.*, 80(3):885–964, 2008.

[17] F. Jendrzejewski, A. Bernard, K. Müller, P. Cheinet, V. Josse, M. Piraud, L. Pezzé, L. Sanchez-Palencia, A. Aspect, and P. Bouyer. Three-dimensional localization of ultracold atoms in an optical disordered potential. *Nature Physics*, 8:398–403, 2012.

[18] Waseem S. Bakr, Jonathon I. Gillen, Amy Peng, Simon Fölling, and Markus Greiner. A quantum gas microscope for detecting single atoms in a hubbard-regime optical lattice. *Nature*, 462:74–77, 2009.

[19] Jacob Sherson, Christof Weitenberg, Manuel Endres, Marc Cheneau, Immanuel Bloch, and Stefan Kuhr. Single-atom resolved fluorescence imaging of an atomic mott insulator. *Nature*, 467:68–72, 09 2010.

[20] Elmar Haller, James Hudson, Andrew Kelly, Dylan Cotta, Bruno Peaudecerf, Graham Bruce, and Stefan Kuhr. Single-atom imaging of fermions in a quantum-gas microscope. *Nature Physics*, 11, 2015.

[21] Ahmed Omran, Martin Boll, Timon A. Hilker, Katharina Kleinlein, Guillaume Salomon, Immanuel Bloch, and Christian Gross. Microscopic observation of pauli blocking in degenerate fermionic lattice gases. *Phys. Rev. Lett.*, 115:263001, 2015.

[22] G. J. A. Edge, R. Anderson, D. Jervis, D. C. McKay, R. Day, S. Trotzky, and J. H. Thywissen. Imaging and addressing of individual fermionic atoms in an optical lattice. *Phys. Rev. A*, 92:063406, 2015.

[23] Lawrence W. Cheuk, Matthew A. Nichols, Katherine R. Lawrence, Melih Okan, Hao Zhang, and Martin W. Zwierlein. Observation of 2d fermionic Mott insulators of ^{40}K with single-site resolution. *Phys. Rev. Lett.*, 116:235301, 2016.

[24] Andrea Bergschneider, Vincent M. Klinkhamer, Jan Hendrik Becher, Ralf Klemt, Gerhard Zürn, Philipp M. Preiss, and Selim Jochim. Spin-resolved single-atom imaging of ^{6}Li in free space. *Phys. Rev. A*, 97:063613, Jun 2018.

[25] Cheng Chin, Rudolf Grimm, Paul Julienne, and Eite Tiesinga. Feshbach resonances in ultracold gases. *Reviews of Modern Physics*, 82(2):1225, 2010.

[26] T Koch, T Lahaye, J Metz, B Fröhlich, Axel Griesmaier, and Tilman Pfau. Stabilization of a purely dipolar quantum gas against collapse. *NATURE PHYSICS*, 4:218–222, 02 2008.

[27] S. Baier, D. Petter, J. H. Becher, A. Patscheider, G. Natale, L. Chomaz, M. J. Mark, and F. Ferlaino. Realization of a strongly interacting fermi gas of dipolar atoms. *Phys. Rev. Lett.*, 121:093602, 2018.

[28] Yijun Tang, Wil Kao, Kuan-Yu Li, and Benjamin L. Lev. Tuning the dipole-dipole interaction in a quantum gas with a rotating magnetic field. *Phys. Rev. Lett.*, 120:230401, 2018.

[29] Jee Woo Park, Sebastian A. Will, and Martin W. Zwierlein. Ultracold dipolar gas of fermionic $^{23}\mathrm{Na}^{40}\mathrm{K}$ molecules in their absolute ground state. *Phys. Rev. Lett.*, 114:205302, 2015.

[30] Sylvain de Léséleuc, Daniel Barredo, Vincent Lienhard, Antoine Browaeys, and Thierry Lahaye. Optical control of the resonant dipole-dipole interaction between rydberg atoms. *Phys. Rev. Lett.*, 119:053202, Aug 2017.

[31] M Aidelsburger. Artificial gauge fields and topology with ultracold atoms in optical lattices. *Journal of Physics B: Atomic, Molecular and Optical Physics*, 51(19):193001, sep 2018.

[32] Richard P. Feynman. Simulating physics with computers. *International Journal of Theoretical Physics*, 21(6):467–488, 1982.

[33] A. Gezerlis and J. Carlson. Strongly paired fermions: Cold atoms and neutron matter. *Phys. Rev. C*, 77(3):32801, 2008.

[34] K. Maeda, G. Baym, and T. Hatsuda. Simulating dense QCD matter with ultracold atomic boson-fermion mixtures. *Phys. Rev. Lett.*, 103(8):85301, 2009.

[35] J. Hubbard and B. H. Flowers. Electron correlations in narrow energy bands. *Proceedings of the royal society of london a: mathematical, physical and engineering sciences*, 276:238–257, 1963.

[36] N. F. Mott and R. Peierls. Discussion of the paper by de boer and verwey. *Proceedings of the Physical Society*, 49(4S):72–73, aug 1937.

[37] M. Greiner, O. Mandel, T. Esslinger, T.W. Hänsch, and I. Bloch. Quantum phase transition from a superfluid to a Mott insulator in a gas of ultracold atoms. *Nature*, 415(6867):39–44, 2002.

[38] R. Jördens, N. Strohmaier, K. Günter, H. Moritz, and T. Esslinger. A Mott insulator of fermionic atoms in an optical lattice. *Nature*, 455(7210):204–207, 2008.

[39] U. Schneider, L. Hackermuller, S. Will, T. Best, I. Bloch, T. A. Costi, R. W. Helmes, D. Rasch, and A. Rosch. Metallic and insulating phases of repuslsively interacting fermions in a 3D optical lattice. *Science*, 322(5907):1520, 2008.

[40] Michael Robin Matthews, Brian P Anderson, PC Haljan, DS Hall, CE Wieman, and EA Cornell. Vortices in a Bose-Einstein condensate. *Physical Review Letters*, 83(13):2498, 1999.

[41] KW Madison, F Chevy, W Wohlleben, and J Dalibard. Vortex formation in a stirred Bose-Einstein condensate. *Physical Review Letters*, 84(5):806, 2000.

[42] JR Abo-Shaeer, C Raman, JM Vogels, and Wolfgang Ketterle. Observation of vortex lattices in Bose-Einstein condensates. *Science*, 292(5516):476–479, 2001.

[43] Richard J Fletcher, Alexander L Gaunt, Nir Navon, Robert P Smith, and Zoran Hadzibabic. Stability of a unitary Bose gas. *Physical Review Letters*, 111(12):125303, 2013.

[44] BS Rem, AT Grier, I Ferrier-Barbut, U Eismann, T Langen, N Navon, L Khaykovich, F Werner, DS Petrov, F Chevy, et al. Lifetime of the Bose gas with resonant interactions. *Physical Review Letters*, 110(16):163202, 2013.

[45] Philip Makotyn, Catherine E Klauss, David L Goldberger, EA Cornell, and Deborah S Jin. Universal dynamics of a degenerate unitary Bose gas. *Nature Physics*, 10(2):116–119, 2014.

[46] A. J. Leggett. Cooper pairing in spin-polarized Fermi systems. *J. Phys. Colloques*, 41(C7):19–26, 1980.

[47] P. Nozières and S. Schmitt-Rink. Bose condensation in an attractive fermion gas: From weak to strong coupling superconductivity. *J. Low Temp. Phys.*, 59(3):195–211, 1985.

[48] W. Zwerger, editor. *The BCS-BEC Crossover and the Unitary Fermi Gas*, volume 836 of *Lecture Notes in Physics*. Springer, Berlin, 2012.

[49] M. Bartenstein, A. Altmeyer, S. Riedl, S. Jochim, C. Chin, J. Hecker-Denschlag, and R. Grimm. Collective excitations of a degenerate gas at the BEC-BCS crossover. *Phys. Rev. Lett.*, 92:203201, 2004.

[50] T. Bourdel, L. Khaykovich, J. Cubizolles, J. Zhang, F. Chevy, M. Teichmann, L. Tarruell, S.J.J.M.F. Kokkelmans, and C. Salomon. Experimental Study of the BEC-BCS Crossover Region in Lithium 6. *Phys. Rev. Lett.*, 93(5):050401, 2004.

[51] C. A. Regal, M. Greiner, and D. S. Jin. Observation of resonance condensation of fermionic atom pairs. *Phys. Rev. Lett.*, 92:040403, 2004.

[52] M.W. Zwierlein, C.A. Stan, C.H. Schunck, S.M.F. Raupach, S. Gupta, Z. Hadzibabic, and W. Ketterle. Observation of Bose-Einstein Condensation of Molecules. *Phys. Rev. Lett.*, 91(25):250401, 2003.

[53] J. Kinast, A. Turlapov, J.E. Thomas, Q. Chen, J. Stajic, and K. Levin. Heat capacity of a strongly interacting Fermi gas. *Science*, 307(5713):1296, 2005.

[54] G. B. Partridge, K. E. Strecker, R. I. Kamar, M. W. Jack, and R. G. Hulet. Molecular probe of pairing in the bec-bcs crossover. *Phys. Rev. Lett.*, 95(2):020404, Jul 2005.

[55] S. Riedl, E.R.S. Guajardo, C. Kohstall, J.H. Denschlag, and R. Grimm. Superfluid Quenching of the Moment of Inertia in a Strongly Interacting Fermi Gas. *arXiv:0907.3814*, 2009.

[56] M.W. Zwierlein, J.R. Abo-Shaeer, A. Schirotzek, C.H. Schunck, and W. Ketterle. Vortices and superfluidity in a strongly interacting Fermi gas. *Nature*, 435(7045):1047–1051, 2005.

[57] Leonid A Sidorenkov, Meng Khoon Tey, Rudolf Grimm, Yan-Hua Hou, Lev Pitaevskii, and Sandro Stringari. Second sound and the superfluid fraction in a Fermi gas with resonant interactions. *Nature*, 498(7452):78, 2013.

[58] Alexander L Gaunt, Tobias F Schmidutz, Igor Gotlibovych, Robert P Smith, and Zoran Hadzibabic. Bose-Einstein condensation of atoms in a uniform potential. *Phys. Rev. Lett.*, 110(20):200406, 2013.

[59] Biswaroop Mukherjee, Zhenjie Yan, Parth B Patel, Zoran Hadzibabic, Tarik Yefsah, Julian Struck, and Martin W Zwierlein. Homogeneous atomic Fermi gases. *Physical Review Letters*, 118(12):123401, 2017.

[60] P. Fulde and R.A. Ferrell. Superconductivity in a strong spin-exchange field. *Phys. Rev*, 135:A550, 1964.

[61] A.I. Larkin and Y.N. Ovchinnikov. Nonuniform state of superconductors. *Zh. Eksp. Teor. Fiz*, 47:1136, 1964.

[62] L.D. Landau. Über die bewegung der elektronen in kristallgitter. *Phys. Z. Sowjetunion*, 3:644–645, 1933.

[63] L.D. Landau and S.I. Pekar. Effective mass of a polaron. *J. Exp. Theor. Phys*, 18:419–423, 1948.

[64] H. Fröhlich. Electrons in lattice fields. *Advances in Physics*, 3(11):325–361, 1954.

[65] J. T. Devreese. Polarons. *Encyclopedia of Applied Physics*, 14:383–409, 1996.

[66] W.J. de Haas, J. de Boer, and G.J. van dën Berg. The electrical resistance of gold, copper and lead at low temperatures. *Physica*, 1(7):1115 – 1124, 1934.

[67] G. J. van den Berg. Anomalies in dilute metallic solutions of transition metals. In J. G. Daunt, D. O. Edwards, F. J. Milford, and M. Yaqub, editors, *Low Temperature Physics LT9*, pages 955–984, Boston, MA, 1965. Springer US.

[68] Jun Kondo. Resistance minimum in dilute magnetic alloys. *Progress of theoretical physics*, 32(1):37–49, 1964.

[69] Kenneth G. Wilson. The renormalization group: Critical phenomena and the kondo problem. *Rev. Mod. Phys.*, 47:773–840, 1975.

[70] Philip Warren Anderson. Localized magnetic states in metals. *Physical Review*, 124(1):41, 1961.

[71] P. W. Anderson. Infrared catastrophe in fermi gases with local scattering potentials. *Phys. Rev. Lett.*, 18:1049–1051, Jun 1967.

[72] Marko Cetina, Michael Jag, Rianne S. Lous, Jook T. M. Walraven, Rudolf Grimm, Rasmus S. Christensen, and Georg M. Bruun. Decoherence of impurities in a fermi sea of ultracold atoms. *Phys. Rev. Lett.*, 115:135302, Sep 2015.

[73] Marko Cetina, Michael Jag, Rianne S. Lous, Isabella Fritsche, Jook T. M. Walraven, Rudolf Grimm, Jesper Levinsen, Meera M. Parish, Richard Schmidt, Michael Knap, and Eugene Demler. Ultrafast many-body interferometry of impurities coupled to a fermi sea. *Science*, 354(6308):96–99, 2016.

[74] L. J. LeBlanc and J. H. Thywissen. Species-specific optical lattices. *Phys. Rev. A*, 75:053612, May 2007.

[75] Marek Kutschera and Włodzimierz Wójcik. Proton impurity in the neutron matter: A nuclear polaron problem. *Phys. Rev. C*, 47:1077–1085, Mar 1993.

[76] W Zuo, ZH Li, GC Lu, JQ Li, W Scheid, U Lombardo, H-J Schulze, and CW Shen. 1s0 proton and neutron superfluidity in β-stable neutron star matter. *Physics Letters B*, 595(1-4):44–49, 2004.

[77] Kenji Fukushima and Vladimir Skokov. Polyakov loop modeling for hot qcd. *Progress in Particle and Nuclear Physics*, 96:154–199, 2017.

[78] Jesper Levinsen, Pietro Massignan, Shimpei Endo, and Meera M Parish. Universality of the unitary Fermi gas: a few-body perspective. *Journal of Physics B: Atomic, Molecular and Optical Physics*, 50(7):072001, 2017.

[79] Antoine Georges, Gabriel Kotliar, Werner Krauth, and Marcelo J. Rozenberg. Dynamical mean-field theory of strongly correlated fermion systems and the limit of infinite dimensions. *Rev. Mod. Phys.*, 68:13–125, Jan 1996.

[80] N. Grewe. *Solid State Communications*, 50:19, 1984.

[81] *Theory of heavy fermions and valence fluctuations*. Springer, Berlin, 1985.

[82] A. N. Wenz, G. Zürn, S. Murmann, I. Brouzos, T. Lompe, and S. Jochim. From few to many: Observing the formation of a fermi sea one atom at a time. *Science*, 342(6157):457–460, 2013.

[83] Sébastien Laurent, Matthieu Pierce, Marion Delehaye, Tarik Yefsah, Frédéric Chevy, and Christophe Salomon. Connecting few-body inelastic decay to quantum correlations in a many-body system: A weakly coupled impurity in a resonant Fermi gas. *Phys. Rev. Lett.*, 118:103403, Mar 2017.

[84] I Ferrier-Barbut, M. Delehaye, S. Laurent, A.T. Grier, M. Pierce, B.S Rem, F. Chevy, and C. Salomon. A mixture of Bose and Fermi superfluids. *Science*, 345:1035–1038, 2014.

[85] G.F. Gribakin and V. V. Flambaum. Calculation of the scattering length in atomic collisions using the semiclassical approximation. *Physical Review A (PRA)*, 48:546–553, 1993.

[86] J. Walraven. Thermodynamic and collisional properties of trapped atomic gases (les houches), 2008. `http://www.phlam.univ-lille1.fr/leshouches/cours08/walraven.pdf`.

[87] H. Bethe and Peierls R. Quantum theory of the diplon. *Proceedings of the Royal Society A*, 148:146–156, 1935.

[88] C. Cohen-Tannoudji. Course at Collège de France (IV Pseudopotentials), 1998-1999. `http://www.phys.ens.fr/~cct/college-de-france/1998-99/1998-99.pdf`.

[89] L. Pricoupenko. Pseudopotential in resonant regimes. *Physical Review A (PRA)*, 73(1):012701, 2006.

[90] B. Marcelis, E. G. M. van Kempen, B. J. Verhaar, and S. J. J. M. F. Kokkelmans. Feshbach resonances with large background scattering length: Interplay with open-channel resonances. *Phys. Rev. A*, 70:012701, 2004.

[91] J. N. Milstein, S. J. J. M. F. Kokkelmans, and M. J. Holland. Resonance theory of the crossover from bardeen-cooper-schrieffer superfluidity to bose-einstein condensation in a dilute fermi gas. *Phys. Rev. A*, 66:043604, Oct 2002.

[92] Vitaly Efimov. Energy levels arising from resonant two-body forces in a three-body system. *Physics Letters B*, 33(8):563–564, 1970.

[93] Eric Braaten and H-W Hammer. Universality in few-body systems with large scattering length. *Physics Reports*, 428(5):259–390, 2006.

[94] Alexander O Gogolin, Christophe Mora, and Reinhold Egger. Analytical solution of the bosonic three-body problem. *Physical Review Letters*, 100(14):140404, 2008.

[95] Felix Werner. *Trapped cold atoms with resonant interactions: unitary gas and three-body problem.* PhD thesis, Université Pierre et Marie Curie - Paris VI, 2008.

[96] GS Danilov. On the three-body problem with short-range forces. *Sov. Phys. JETP*, 13(349):3, 1961.

[97] L. H. Thomas. The interaction between a neutron and a proton and the structure of h^3. *Physical Review*, 47:903–909, 1935.

[98] T. Kraemer, M. Mark, P. Waldburger, JG Danzl, C. Chin, B. Engeser, AD Lange, K. Pilch, A. Jaakkola, H.C. Nägerl, et al. Evidence for Efimov quantum states in an ultracold gas of caesium atoms. *Nature*, 440(7082):315–318, 2006.

[99] F Ferlaino, A Zenesini, M Berninger, B Huang, H-C Nägerl, and R Grimm. Efimov resonances in ultracold quantum gases. *Few-Body Systems*, 51(2-4):113–133, 2011.

[100] Noam Gross, Zav Shotan, Servaas Kokkelmans, and Lev Khaykovich. Observation of universality in ultracold li 7 three-body recombination. *Physical Review Letters*, 103(16):163202, 2009.

[101] Scott E Pollack, Daniel Dries, and Randall G Hulet. Universality in three-and four-body bound states of ultracold atoms. *Science*, 326(5960):1683–1685, 2009.

[102] Matteo Zaccanti, Benjamin Deissler, Chiara D?Errico, Marco Fattori, Mattia Jona-Lasinio, Stefan Müller, Giacomo Roati, Massimo Inguscio, and Giovanni Modugno. Observation of an Efimov spectrum in an atomic system. *Nature Physics*, 5(8):586–591, 2009.

[103] Thomas Lompe, Timo B. Ottenstein, Friedhelm Serwane, Andre N. Wenz, Gerhard Zürn, and Selim Jochim. Radio-frequency association of efimov trimers. *Science*, 330(6006):940–944, 2010.

[104] Shuta Nakajima, Munekazu Horikoshi, Takashi Mukaiyama, Pascal Naidon, and Masahito Ueda. Measurement of an efimov trimer binding energy in a three-component mixture of ^{6}Li. *Phys. Rev. Lett.*, 106:143201, Apr 2011.

[105] V. Efimov. Low-energy properties of three resonantly-interacting particles. *Sov. J. Nucl. Phys.*, 29:546, 1979.

[106] T.L. Ho. Universal thermodynamics of degenerate quantum gases in the unitarity limit. *Phys. Rev. Lett.*, 92(9):90402, 2004.

[107] M. Inguscio, W. Ketterle, and C. Salomon, editors. *Proceedings of the International School of Physics ?Enrico Fermi? on Ultracold Fermi gases, Course CLXIV, Varenna*. Società Italiana di Fisica, 2006.

[108] J. D. Rameau, T. J. Reber, H.-B. Yang, S. Akhanjee, G. D. Gu, P. D. Johnson, and S. Campbell. Nearly perfect fluidity in a high-temperature superconductor. *Phys. Rev. B*, 90:134509, 2014.

[109] Markus Müller, Jörg Schmalian, and Lars Fritz. Graphene: A nearly perfect fluid. *Phys. Rev. Lett.*, 103:025301, 2009.

[110] L.D. Landau, E.M. Lifshitz, D.A. Lavis, A. Lerda, R.L. Liboff, L.B. Loeb, W.H. Louisell, S. Lundqvist, B.M. McCoy, D.K.C. MacDonald, et al. *Statistical Physics*. Pergamon Press, Oxford, UK, 1980.

[111] L. D. Landau and E. M. Lifshitz. *Quantum Mechanics*. Pergamon Press, 1965.

[112] L. Pitaevskii and S. Stringari. *Bose-Einstein Condensation*. Clarendon Press, 2003.

[113] T.D. Lee, K. Huang, and C.N. Yang. Eigenvalues and eigenfunctions of a Bose system of hard spheres and its low-temperature properties. *Phys. Rev.*, 106(6):1135–1145, 1957.

[114] S. B. Papp, J. M. Pino, R. J. Wild, S. Ronen, C. E. Wieman, D. S. Jin, and E. A. Cornell. Bragg spectroscopy of a strongly interacting $^{85}\mathrm{Rb}$ Bose-Einstein condensate. *Phys. Rev. Lett.*, 101:135301, Sep 2008.

[115] N. Navon, S. Piatecki, K. Günter, B. Rem, T.-C. Nguyen, F. Chevy, W. Krauth, and C. Salomon. Dynamics and thermodynamics of the low-temperature strongly interacting Bose gas. *Phys. Rev. Lett.*, 107:135301, Sep 2011.

[116] T.T. Wu. Ground state of a Bose system of hard spheres. *Phys. Rev.*, 115(6):1390–1404, 1959.

[117] Wei Yi and Xiaoling Cui. Polarons in ultracold Fermi superfluids. *Phys. Rev. A*, 92(1):013620, 2015.

[118] Eric Braaten and Agustin Nieto. Quantum corrections to the energy density of a homogeneous Bose gas. *The European Physical Journal B-Condensed Matter and Complex Systems*, 11(1):143–159, 1999.

[119] Shina Tan. Three-boson problem at low energy and implications for dilute Bose-Einstein condensates. *Physical Review A*, 78(1):013636, 2008.

[120] H-W Hammer. Three-body forces: From cold atoms to nuclei. *Acta Phys. Polon.*, 46:379, 2015.

[121] D. S. Petrov. Three-boson problem near a narrow Feshbach resonance. *PRL (Physical Review Letters)*, 93(14):143201, 2004.

[122] T. Weber, J. Herbig, M. Mark, H.-C. Nägerl, and R. Grimm. Three-body recombination at large scattering lengths in an ultracold atomic gas. *Phys. Rev. Lett.*, 91:123201, Sep 2003.

[123] Nir Navon. *Thermodynamics of ultracold Bose and Fermi gases*. PhD thesis, Université Pierre et Marie Curie - Paris VI, 2011.

[124] Munekazu Horikoshi, Masato Koashi, Hiroyuki Tajima, Yoji Ohashi, and Makoto Kuwata-Gonokami. Ground-state thermodynamic quantities of homogeneous spin-$1/2$ fermions from the bcs region to the unitarity limit. *Phys. Rev. X*, 7:041004, 2017.

[125] L. N. Cooper. Bound electron pairs in a degenerate Fermi gas. *Phys. Rev.*, 104(4):1189–1190, 1956.

[126] J. Bardeen, L.N. Cooper, and J.R. Schrieffer. Theory of superconductivity. *Phys. Rev.*, 108(5):1175–1204, 1957.

[127] V. Galitskii. The energy spectrum of a non-ideal fermi gas. *Sov. Phys. JETP*, 7:104, 1958.

[128] T. D. Lee and C. N. Yang. Many-body problem in quantum mechanics and quantum statistical mechanics. *Phys. Rev.*, 105(3):1119–1120, 1957.

[129] R.B. Diener, R. Sensarma, and M. Randeria. Quantum fluctuations in the superfluid state of the BCS-BEC crossover. *Phys. Rev. A*, 77(2):23626, 2008.

[130] D.S. Petrov, C. Salomon, and G.V. Shlyapnikov. Weakly bound dimers of fermionic atoms. *Phys. Rev. Lett.*, 93(9):090404, 2004.

[131] X. Leyronas and R. Combescot. Superfluid equation of state of dilute composite bosons. *Phys. Rev. Lett.*, 99(17):170402, 2007.

[132] M. Greiner, C.A. Regal, and D.S. Jin. Emergence of a molecular Bose-Einstein condensate from a Fermi gas. *Nature*, 426(6966):537–540, 2003.

[133] S. Jochim, M. Bartenstein, A. Altmeyer, G. Hendl, S. Riedl, C. Chin, J. Hecker Denschlag, and R. Grimm. Bose-Einstein condensation of molecules. *Science*, 302(5653):2101, 2003.

[134] T. Bourdel, J. Cubizolles, L. Khaykovich, K. M. F. Magalhães, S. J. J. M. F. Kokkelmans, G. V. Shlyapnikov, and C. Salomon. Measurement of the interaction energy near a feshbach resonance in a ^{6}Li Fermi gas. *Phys. Rev. Lett.*, 91(2):020402, Jul 2003.

[135] C. A. Regal, M. Greiner, and D. S. Jin. Lifetime of Molecule-Atom Mixtures near a Feshbach Resonance in$\hat{}\{40\}$ K. *Phys. Rev. Lett.*, 92(8):83201, 2004.

[136] M. J. H. Ku, A. T. Sommer, L. W. Cheuk, and M. W. Zwierlein. Revealing the superfluid lambda transition in the universal thermodynamics of a unitary Fermi gas. *Science*, 335(6068):563–567, 2012.

[137] Nir Navon, Sylvain Nascimbène, Frédéric Chevy, and Christophe Salomon. The equation of state of a low-temperature Fermi gas with tunable interactions. *Science*, 328(5979):729–732, 2010.

[138] H. Hu, X.J. Liu, and P.D. Drummond. Equation of state of a superfluid Fermi gas in the BCS-BEC crossover. *Europhys. Lett.*, 74:574–580, 2006.

[139] A. Bulgac, J.E. Drut, and P. Magierski. Quantum Monte Carlo simulations of the BCS-BEC crossover at finite temperature. *Phys. Rev. A*, 78(2):23625, 2008.

[140] R. Haussmann, W. Rantner, S. Cerrito, and W. Zwerger. Thermodynamics of the BCS-BEC crossover. *Phys. Rev. A*, 75(2):023610, 2007.

[141] S.Y. Chang, V.R. Pandharipande, J. Carlson, and K.E. Schmidt. Quantum Monte Carlo studies of superfluid Fermi gases. *Phys. Rev. A*, 70(4):43602, 2004.

[142] G.E. Astrakharchik, J. Boronat, J. Casulleras, and S. Giorgini. Equation of state of a Fermi gas in the BEC-BCS crossover: A quantum Monte Carlo study. *Phys. Rev. Lett.*, 93(20):200404, 2004.

[143] S. Pilati and S. Giorgini. Phase separation in a polarized Fermi gas at zero temperature. *Phys. Rev. Lett.*, 100(3):030401, 2008.

[144] Shina Tan. Energetics of a strongly correlated Fermi gas. *Annals of Physics*, 323(12):2952 – 2970, 2008.

[145] S. Tan. Large momentum part of a strongly correlated Fermi gas. *Ann. Phys.*, 323(12):2971–2986, 2008.

[146] Félix Werner and Yvan Castin. General relations for quantum gases in two and three dimensions: Two-component fermions. *Physical Review A*, 86(1):013626, 2012.

[147] E. Braaten. *The BCS-BEC crossover and the unitary Fermi gas*. Springer,Berlin, 2012.

[148] R. Feynman. Forces in molecules. *Physical Review*, 563(1):340, 1939.

[149] M. Olshanii and V. Dunjko. Short-distance correlation properties of the Lieb-Lininger system and momentum distributions of trapped one-dimensional atomic gases. *PRL(Physical Review Letters)*, 91(9):090401, 2003.

[150] Sascha Hoinka, Marcus Lingham, Kristian Fenech, Hui Hu, Chris J. Vale, Joaquín E. Drut, and Stefano Gandolfi. Precise determination of the structure factor and contact in a unitary Fermi gas. *Phys. Rev. Lett.*, 110:055305, Jan 2013.

[151] R. Haussmann, M. Punk, and W. Zwerger. Spectral functions and rf response of ultracold fermionic atoms. *PRA(Physical Review A)*, 80:063612, 2009.

[152] P. Pieri, A. Perali, and G. C. Strinati. Enhanced paraconductivity-like fluctuations in the radiofrequency spectra of ultracold Fermi atoms. *Nature Physics*, 5:736–740, 2009.

[153] E. Braaten, D. Kang, and L. Platter. Short-time operator product expansion for rf spectroscopy of a strongly interacting Fermi gas. *Physical Review Letters (PRL)*, 104(22):223004, 2010.

[154] J.T. Stewart, J.P. Gaebler, and D.S. Jin. Using photoemission spectroscopy to probe a strongly interacting Fermi gas. *Nature*, 454(7205):744–747, 2008.

[155] R. J. Fletcher, R. Lopes, J. Man, N. Navon, R. P. Smith, M. W. Zwierlein, and Z. Hadzibabic. Two and three-body contacts in the unitary Bose gas. *arXiv preprint arXiv:1608.04377*, 2016.

[156] J. T. Stewart, J. P. Gaebler, T. E. Drake, and D. S. Jin. Verification of universal relations in a strongly interacting Fermi gas. *Phys. Rev. Lett.*, 104(23):235301, Jun 2010.

[157] F. Werner, L. Tarruell, and Y. Castin. Number of closed-channel molecules in the BEC-BCS crossover. *Eur. Phys. J. B*, 68(3):401–415, 2009.

[158] Hui Hu, X-J Liu, and Peter D Drummond. Static structure factor of a strongly correlated Fermi gas at large momenta. *EPL (Europhysics Letters)*, 91(2):20005, 2010.

[159] E. D. Kuhnle, H. Hu, X.-J. Liu, P. Dyke, M. Mark, P. D. Drummond, P. Hannaford, and C. J. Vale. Universal behavior of pair correlations in a strongly interacting Fermi gas. *Phys. Rev. Lett.*, 105(7):070402, Aug 2010.

[160] G. Veeravalli, E Kuhnle, P Dyke, and C.J. Vale. Bragg spectroscopy of a strongly interacting Fermi gas. *Phys. Rev. Lett.*, 101(25):250403, 2008.

[161] A.M. Clogston. Upper limit for the critical field in hard superconductors. *Phys. Rev. Lett.*, 9(6):266–267, 1962.

[162] B.S. Chandrasekhar. A note on the maximum critical field of high-field superconductors. *App. Phys. Lett.*, 1(1):7–8, 1962.

[163] P.F. Bedaque, H. Caldas, and G. Rupak. Phase separation in asymmetrical fermion superfluids. *Phys. Rev. Lett.*, 91(24):247002–247002, 2003.

[164] M. Punk, P.T. Dumitrescu, and W. Zwerger. Polaron to molecule transition in a strongly imbalanced Fermi gas. *Phys. Rev. A*, 80:053605–053615, 2009.

[165] F. Chevy and C. Mora. Ultra-cold Polarized Fermi Gases. *Rep. Prog. Phys.*, 73:112401, 2010.

[166] G.B. Partridge, W. Li, R.I. Kamar, Y. Liao, and R.G. Hulet. Pairing and phase separation in a polarized Fermi gas. *Science*, 311(5760):503–505, 2006.

[167] M.W. Zwierlein, A. Schirotzek, C.H. Schunck, and W. Ketterle. Fermionic superfluidity with imbalanced spin populations. *Science*, 311(5760):492–496, 2006.

[168] Y. Shin, M.W. Zwierlein, C.H. Schunck, A. Schirotzek, and W. Ketterle. Observation of phase separation in a strongly interacting imbalanced Fermi gas. *Phys. Rev. Lett.*, 97(3):030401, 2006.

[169] G. B. Partridge, W. Li, Y. A. Liao, R. G. Hulet, M. Haque, and H. T. C. Stoof. Deformation of a trapped Fermi gas with unequal spin populations. *Phys. Rev. Lett.*, 97(19):190407, 2006.

[170] Meera M. Parish and David A. Huse. Evaporative depolarization and spin transport in a unitary trapped fermi gas. *Phys. Rev. A*, 80:063605, Dec 2009.

[171] Pietro Massignan, Matteo Zaccanti, and Georg M Bruun. Polarons, dressed molecules and itinerant ferromagnetism in ultracold Fermi gases. *Reports on Progress in Physics*, 77(3):034401, 2014.

[172] F. Chevy. Universal phase diagram of a strongly interacting Fermi gas with unbalanced spin populations. *Phys. Rev. A*, 74(6):063628, 2006.

[173] C. Lobo, A. Recati, S. Giorgini, and S. Stringari. Normal state of a polarized Fermi gas at unitarity. *Phys. Rev. Lett.*, 97(20):200403, 2006.

[174] N. Prokof'ev and B. Svistunov. Fermi-polaron problem: Diagrammatic monte carlo method for divergent sign-alternating series. *Phys. Rev. B*, 77(2):020408, 2008.

[175] R. Combescot and S. Giraud. Normal state of highly polarized Fermi gases: full many-body treatment. *Phys. Rev. Lett.*, 101(5):050404, 2008.

[176] Y.I. Shin. Determination of the equation of state of a polarized Fermi gas at unitarity. *Phys. Rev. A*, 77(4):041603, 2008.

[177] S. Nascimbène, N. Navon, K. Jiang, L. Tarruell, M. Teichmann, J. McKeever, F. Chevy, and C. Salomon. Collective Oscillations of an Imbalanced Fermi Gas: Axial Compression Modes and Polaron Effective Mass. *Phys. Rev. Lett.*, 103(17):170402, 2009.

[178] R. Combescot, A. Recati, C. Lobo, and F. Chevy. Normal state of highly polarized Fermi gases: simple many-body approaches. *Phys. Rev. Lett.*, 98(18):180402, 2007.

[179] A. Schirotzek, C-H Wu, A Sommer, and M.W Zwierlein. Observation of Fermi Polarons in a Tunable Fermi Liquid of Ultracold Atoms. *Phys. Rev. Lett.*, 102(23):230402, 2009.

[180] C. Mora and F. Chevy. Normal phase of an imbalanced Fermi gas. *Phys. Rev. Lett.*, 104(23):230402, Jun 2010.

[181] S. Nascimbène, N. Navon, K. Jiang, F. Chevy, and C. Salomon. Exploring the Thermodynamics of a Universal Fermi Gas. *Nature*, 463:1057–1060, 2010.

[182] Z. Yu, S. Zöllner, and C. J. Pethick. Comment on "normal phase of an imbalanced Fermi gas". *Phys. Rev. Lett.*, 105(18):188901, Oct 2010.

[183] G.V. Skorniakov and K.A. Ter-Martirosian. Three body problem for short range forces. I. Scattering of low energy neutrons by deuterons. *Sov. Phys. JETP*, 4, 1957.

[184] C. Mora and F. Chevy. Ground state of a tightly bound composite dimer immersed in a Fermi Sea. *Phys. Rev. A*, 80(3):033607–033617, 2009.

[185] R. Combescot, S. Giraud, and X. Leyronas. Analytical theory of the dressed bound state in highly polarized Fermi gases. *EPL (Europhysics Letters)*, 88:60007, 2009.

[186] L. Viverit and S. Giorgini. Ground-state properties of a dilute Bose-Fermi mixture. *Phys. Rev. A*, 66(6):063604, 2002.

[187] F. Alzetto and X. Leyronas. Equation of state of a polarized Fermi gas in the Bose-Einstein-condensate limit. *Phys. Rev. A*, 81(4):043604, Apr 2010.

[188] P. Massignan and G. M. Brunn. Repulsive polarons and itinerant ferromagnetism in strongly polarized Fermi gases. *Eur. Phys. J. D*, 65:83, 2011.

[189] R.F Bishop. On the ground state of an impurity in a dilute fermi gas. *Annals of Physics*, 78(2):391 – 420, 1973.

[190] C. Kohstall, M. Zaccanti, M. Jag, A. Trenkwalder, P. Massignan, G. M. Bruun, F. Schreck, and R. Grimm. Metastability and coherence of repulsive polarons in a strongly interacting fermi mixture. *Nature*, 485:615, 2012.

[191] F. Scazza, G. Valtolina, P. Massignan, A. Recati, A. Amico, A. Burchianti, C. Fort, M. Inguscio, M. Zaccanti, and G. Roati. Repulsive fermi polarons in a resonant mixture of ultracold ^{6}Li atoms. *Phys. Rev. Lett.*, 118:083602, 2017.

[192] R. Schmidt and T. Enss. Excitation spectra and rf response near the polaron-to-molecule transitionfrom the functional renormalization group. *PRA (Physical Review A)*, 83(6):063620, 2011.

[193] Xiaoling Cui and Hui Zhai. Stability of a fully magnetized ferromagnetic state in repulsively interacting ultracold fermi gases. *Phys. Rev. A*, 81:041602, Apr 2010.

[194] D. S. Petrov. Three-body problem in fermi gases with short-range interparticle interaction. *Phys. Rev. A*, 67:010703, Jan 2003.

[195] Rasmus Søgaard Christensen, Jesper Levinsen, and Georg M. Bruun. Quasiparticle properties of a mobile impurity in a bose-einstein condensate. *Phys. Rev. Lett.*, 115:160401, 2015.

[196] Weiran Li and S. Das Sarma. Variational study of polarons in bose-einstein condensates. *Phys. Rev. A*, 90:013618, 2014.

[197] Steffen Patrick Rath and Richard Schmidt. Field-theoretical study of the bose polaron. *Phys. Rev. A*, 88:053632, Nov 2013.

[198] Jesper Levinsen, Meera M Parish, and Georg M Bruun. Impurity in a Bose-Einstein condensate and the Efimov effect. *Physical Review Letters*, 115(12):125302, 2015.

[199] Shuhei M. Yoshida, Shimpei Endo, Jesper Levinsen, and Meera M. Parish. Universality of an impurity in a bose-einstein condensate. *Phys. Rev. X*, 8:011024, Feb 2018.

[200] Ming-Guang Hu, Michael J Van de Graaff, Dhruv Kedar, John P Corson, Eric A Cornell, and Deborah S Jin. Bose polarons in the strongly interacting regime. *Phys. Rev. Lett.*, 117(5):055301, 2016.

[201] Nils B Jørgensen, Lars Wacker, Kristoffer T Skalmstang, Meera M Parish, Jesper Levinsen, Rasmus S Christensen, Georg M Bruun, and Jan J Arlt. Observation of attractive and repulsive polarons in a Bose-Einstein condensate. *Physical Review Letters*, 117(5):055302, 2016.

[202] L. A. Peña Ardila, N. B. Jørgensen, T. Pohl, S. Giorgini, G. M. Bruun, and J. J. Arlt. Analyzing a bose polaron across resonant interactions. *Phys. Rev. A*, 99:063607, 2019.

[203] Gabriele Ferrari. *Simultaneous trapping of the bosonic and fermionic isotopes of lithium, theoretical study of the collisional relaxation in a degenerate Fermi gas*. PhD thesis, Université Pierre et Marie Curie - Paris VI, 2000.

[204] Florian Schreck. *Mixtures of ultracold gases: Fermi sea and Bose-Einstein condensate of lithium isotopes.* PhD thesis, Université Pierre et Marie Curie - Paris VI, 2000.

[205] Leticia Tarruell. *Superfluidité dans un gaz de fermions ultrafroids*. PhD thesis, Université Pierre et Marie Curie - Paris VI, 2008.

[206] Sylvain Nascimbène. *Thermodynamique des gaz de fermions ultrafroids*. PhD thesis, Ecole Normale supérieure, 2010.

[207] G. Zürn, T. Lompe, A. N. Wenz, S. Jochim, P. S. Julienne, and J. M. Hutson. Precise Characterization of ^{6}Li Feshbach Resonances Using Trap-Sideband-Resolved RF Spectroscopy of Weakly Bound Molecules. *Phys. Rev. Lett.*, 110(13):135301, 2013.

[208] E. G. M. v. Kempen, B. Marcelis, and S. J. J. M. F. Kokkelmans. Formation of fermionic molecules via interisotope feshbach resonances. *Phys. Rev. A*, 70:050701, 2004.

[209] J. Zhang, E. G. M. v. Kempen, T. Bourdel, L. Khaykovich, J. Cubizolles, F. Chevy, M. Teichmann, L. Tarruell, S. J. J. M. F. Kokkelmans, and C. Salomon. *In ATOMIC PHYSICS 19: XIX International Conference on Atomic Physics*, pages 228–237, ICAP 2004.

[210] J. Tuoriniemi, J. Martikainen, E. Pentti, A. Sebedash, S. Boldarev, and G. Pickett. Towards Superfluidity of ^{3}He Diluted by ^{4}He. *Journal of Low Temperature Physics*, 129(5-6):531–545, 2002.

[211] J. Rysti, J. Tuoriniemi, and A. Salmela. Effective ^{3}He interactions in dilute ^{3}He-^{4}He mixtures. *Phys. Rev. B*, 85:134529, Apr 2012.

[212] L. Viverit, C. J. Pethick, and H. Smith. Zero-temperature phase-diagram of binary boson-fermion mixtures. *PRA(Physical Review A)*, 61(5):053605, 2000.

[213] I.V. Brodsky, M.Y. Kagan, A.V. Klaptsov, R. Combescot, and X. Leyronas. Exact diagrammatic approach for dimer-dimer scattering and bound states of three and four resonantly interacting particles. *Phys. Rev. A*, 73(3):032724, 2006.

[214] David E. Pritchard. Cooling neutral atoms in a magnetic trap for precision spectroscopy. *Phys. Rev. Lett.*, 51:1336–1339, 1983.

[215] H. J. Metcalf and P. v. d. Straten. *Laser cooling and trapping*. Springer science and business media, 2012.

[216] O. J. Luiten, M. W. Reynolds, and J. T. M. Walraven. Kinetic theory of the evaporative cooling of a trapped gas. *Phys. Rev. A*, 53:381–389, 1996.

[217] R. Grimm, M. Weidemüller, and Y. B. Ovchinnikov. Optical dipole traps for neutral atoms. *Advances in atomic, molecular, and optical physics*, 42:95?170, 2000.

[218] Y. Castin and R. Dum. Bose-Einstein condensates in time-dependent traps. *PRL (Physical Review Letters)*, 77(27):5315–5319, 1996.

[219] W. Ketterle and M. Zwierlein. *Making, probing and understanding ultra-cold Fermi gases in Proceedings of the International School of Physics Enrico Fermi, Course CLXIV, Varenna*. Società Italiana di Fisica, 2008.

[220] D. Jin and C. Regal, editors. *Fermi gas experiments, Proceedings of the International School of Physics Enrico Fermi on Ultracold Fermi gases, Course CLXIV, Varenna*. Società Italiana di Fisica, 2006.

[221] F. M. Spiegelhalder, A. Trenkwalder, D. Naik, G. Hendl, F. Schreck, and R. Grimm. Collisional Stability of ^{40}K Immersed in a Strongly Interacting Fermi Gas of ^{6}Li. *Phys. Rev. Lett.*, 103(22):223203, Nov 2009.

[222] M. Pini, P. Pieri, and G. C. Strinati. Fermi gas throughout the BCS-BEC crossover: A comparative study of t-matrix approaches with various degrees of self-consistency. *arXiv:1903.01960*, 2019.

[223] Nir Navon. PhD Thesis: Thermodynamics of ultracold Bose and Fermi gases. *CCSD Repository tel-01081100*, 2011.

[224] Y. Shin, C.H. Schunck, A. Schirotzek, and W. Ketterle. Phase diagram of a two-component Fermi gas with resonant interactions. *Nature*, 451(4):689–693, 2008.

[225] J.J. Zirbel, K.-K. Ni, S. Ospelkaus, J.P. D?Incao, C.E. Wieman, J. Ye, and D.S. Jin. Collisional stability of fermionic Feshbach molecules. *Phys. Rev. Lett.*, 100(14):143201, 2008.

[226] J. P. D'Incao and B. D. Esry. Suppression of molecular decay in ultracold gases without fermi statistics. *Phys. Rev. Lett.*, 100:163201, 2008.

[227] C. E. Klauss, X. Xie, C. Lopez-Abadia, J. P. D'Incao, Z. Hadzibabic, D. S. Jin, and E. A. Cornell. Observation of Efimov molecules created from a resonantly interacting Bose gas. *PRL(Physical Review Letters)*, 119(14):143401, 2017.

[228] Cheng Chin and Rudolf Grimm. Thermal equilibrium and efficient evaporation of an ultracold atom-molecule mixture. *Phys. Rev. A*, 69:033612, Mar 2004.

[229] P. O. Fedichev, M. W. Reynolds, and G. V. Shlyapnikov. Three-body recombination of ultracold atoms to a weakly bound s level. *Phys. Rev. Lett.*, 77:2921–2924, Sep 1996.

[230] Zav Shotan, Olga Machtey, Servaas Kokkelmans, and Lev Khaykovich. Three-body recombination at vanishing scattering lengths in an ultracold Bose gas. *Phys. Rev. Lett.*, 113:053202, Jul 2014.

[231] Hui Hu, Xia-Ji Liu, and Peter D Drummond. Universal contact of strongly interacting fermions at finite temperatures. *New Journal of Physics*, 13(3):035007, 2011.

[232] F. Palestini, A. Perali, P. Pieri, and G. C. Strinati. Temperature and coupling dependence of the universal contact intensity for an ultracold fermi gas. *Physical Review A (PRA)*, 82:021605, 2010.

[233] Massimo Campostrini, Martin Hasenbusch, Andrea Pelissetto, and Ettore Vicari. Theoretical estimates of the critical exponents of the superfluid transition in $^4\mathrm{He}$ by lattice methods. *Phys. Rev. B*, 74:144506, 2006.

[234] Zhenhua Yu, Georg M. Bruun, and Gordon Baym. Short-range correlations and entropy in ultracold-atom fermi gases. *Phys. Rev. A*, 80:023615, Aug 2009.

[235] Biswaroop Mukherjee, Parth B. Patel, Zhenjie Yan, Richard J. Fletcher, Julian Struck, and Martin W. Zwierlein. Spectral response and contact of the unitary fermi gas. *Phys. Rev. Lett.*, 122:203402, May 2019.

[236] C. Carcy, S. Hoinka, M. G. Lingham, P. Dyke, C. C. N. Kuhn, H. Hu, and C. J. Vale. Contact and sum rules in a near-uniform fermi gas at unitarity. *Phys. Rev. Lett.*, 122:203401, May 2019.

[237] Yoav Sagi, Tara E. Drake, Rabin Paudel, and Deborah S. Jin. Measurement of the homogeneous contact of a unitary Fermi gas. *Phys. Rev. Lett.*, 109:220402, Nov 2012.

[238] R. Rossi, T. Ohgoe, E. Kozik, N. Prokof?ev, B. Svistunov, K. Van Houcke, and F. Werner. Contact and momentum distribution of the unitary fermi gas. *Physical Review Letters (PRL)*, 121(13):130406, 2018.

[239] O. Goulko and M. Wingate. Numerical study of the unitary fermi gas across the superfluid transition. *Physical Review A (PRA)*, 93(5):053604, 2016.

[240] Tilman Enss, Rudolf Haussmann, and W Zwerger. Viscosity and scale invariance in the unitary fermi gas. *Annals of Physics*, 326:770–796, 2011.

[241] Tilman Enss. Quantum critical transport in the unitary fermi gas. *Physical Review A (PRA)*, 86:013616, 2012.

[242] Hui Hu, Xia-Ji Liu, and Peter D Drummond. Universal contact of strongly interacting fermions at finite temperatures. *New Journal of Physics*, 13(3):035007, 2011.

[243] G.E. Volovik, V.P. Mineev, and I.M. Khalatnikov. Theory of solutions of a superfluid Fermi liquid in a superfluid Bose liquid. *Sov. Phys. JETP*, 69(2):675–687, 1975.

[244] A.F. Andreev and E. P. Bashkin. Theory of superconductivity. *Soviet Journal of Experimental and Theoretical Physics*, 42:164, 1976.

[245] C. J. Myatt, E. A. Burt, R. W. Ghrist, E. A. Cornell, and C. E. Wieman. Production of two overlapping Boe-Einstein condensates by sympathetic cooling. *PRL (Physical Review Letters)*, 78:586–589, 1997.

[246] F. Schreck, L. Khaykovich, K.L. Corwin, G. Ferrari, T. Bourdel, J. Cubizolles, and C. Salomon. Quasipure Bose-Einstein Condensate Immersed in a Fermi Sea. *Phys. Rev. Lett.*, 87(8):080403, August 2001.

[247] Z. Hadzibabic, C. A. Stan, K. Dieckmann, S. Gupta, M. W. Zwierlein, A. Görlitz, and W. Ketterle. Two-species mixture of quantum degenerate Bose and Fermi gases. *PRL (Physical Review Letters)*, 88:160401, 2002.

[248] G. Roati, F. Riboli, Modugno G., and M. Inguscio. Fermi-Bose quantum degenerate ^{40}K-^{87}Rb mixture with attractive interaction. *PRL (Physical Review Letters)*, 89:150403, 2002.

[249] C. Silber, S. Günther, C. Marzok, B. Deh, P. W. Courteille, and C. Zimmermann. Quantum-degenerate mixture of fermionic lithium and bosonic rubidium gases. *PRL (Physical Review Letters)*, 95:170408, 2005.

[250] H. Hara, Y. Takasu, Y. Yamaoka, J. M. Doyle, and Y. Takahashi. Quantum degenerate mixtures of alkali and alkaline-earth-like atoms. *PRL (Physical Review Letters)*, 106:205304, 2011.

[251] A. H. Hansen, A. Khramov, W. H. Dowd, A. O. Jamison, V. V. Ivanov, and S. Gupta. Quantum degenerate mixture of ytterbium and lithium atoms. *PRA (Physical Review A)*, 84:011606, 2011.

[252] M. Lu, N. Q. Burdick, and B. L. Lev. Quantum degenerate dipolar Fermi gas. *PRL (Physical Review Letters)*, 108:215301, 2012.

[253] M. Repp, R. Pires, J. Ulmanis, R. Heck, E. D. Kuhnle, M. Weidemüller, and E. Tiemann. Observation of interspecies ^{6}Li-^{133}Cs Feshbach resonances. *PRA (Physical Review A)*, 87:010701, 2013.

[254] V. D. Vaidya, J. Tiamsuphat, S. L. Rolston, and J. V. Porto. Degenerate Bose-Fermi mixtures of rubidium and ytterbium. *PRA (Physical Review A)*, 92:043604, 2015.

[255] Y. Wu, X. Yao, H. Chen, X. Liu, X. Wang, Y. Chen, and J. Pan. A quantum degenerate Bose-Fermi mixture of ^{41}K and ^{6}Li. *Journal of Physics B*, 50:094001, 2017.

[256] Richard Roy, Alaina Green, Ryan Bowler, and Subhadeep Gupta. Two-element mixture of Bose and Fermi superfluids. *Physical Review Letters*, 118(5):055301, 2017.

[257] Xing-Can Yao, Hao-Ze Chen, Yu-Ping Wu, Xiang-Pei Liu, Xiao-Qiong Wang, Xiao Jiang, Youjin Deng, Yu-Ao Chen, and Jian-Wei Pan. Observation of coupled vortex lattices in a mass-imbalance Bose and Fermi superfluid mixture. *Phys. Rev. Lett.*, 117:145301, Sep 2016.

[258] T. Ikemachi, A. Ito, .Y Aratake, Y. Chen, M. Koashi, M. Kuwata-Gonomaki, and M. Horikoshi. All-optical production of a superfluid Bose-Fermi mixture of ^{6}Li and ^{7}Li. *arXiv preprint arXiv:1606.09404*, 2016.

[259] D. S. Hall, M. R. Matthews, J. R. Ensher, C. E. Wieman, and E. A. Cornell. Dynamics of Component Separation in a Binary Mixture of Bose-Einstein Condensates. *Phys. Rev. Lett.*, 81:1539–1542, Aug 1998.

[260] P. Maddaloni, M. Modugno, C. Fort, F. Minardi, and M. Inguscio. Collective oscillations of two colliding Bose-Einstein condensates. *Phys. Rev. Lett.*, 85(12):2413, 2000.

[261] F. Ferlaino, R.J. Brecha, P. Hannaford, F. Riboli, G. Roati, G. Modugno, and M. Inguscio. Dipolar oscillations in a quantum degenerate Fermi–Bose atomic mixture. *Journal of Optics B: Quantum and Semiclassical Optics*, 5(2):S3, 2003.

[262] A. Sommer, M. Ku, G. Roati, and M. W. Zwierlein. Universal spin transport in a strongly interacting Fermi gas. *Nature*, 472:201–204, 2011.

[263] T. Kinoshita, T. Wenger, and D. S Weiss. A quantum Newton's cradle. *Nature*, 440(7086):900–903, April 2006.

[264] Marion Delehaye, Sébastien Laurent, Igor Ferrier-Barbut, Shuwei Jin, Frédéric Chevy, and Christophe Salomon. Critical velocity and dissipation of an ultracold Bose-Fermi counterflow. *Phys. Rev. Lett.*, 115(26):265303, 2015.

[265] Marion Delehaye. *Mixtures of superfluids*. PhD thesis, Ecole Normale Supérieure - ENS PARIS, 2016.

[266] Igor Ferrier-Barbut. *Mixtures of Bose and Fermi superfluids*. PhD thesis, Ecole Normale Supérieure - ENS PARIS, 2014.

[267] Igor Ferrier-Barbut, Holger Kadau, Matthias Schmitt, Matthias Wenzel, and Tilman Pfau. Observation of quantum droplets in a strongly dipolar Bose gas. *Physical Review Letters*, 116(21):215301, 2016.

[268] Hadrien Kurkjian, Yvan Castin, and Alice Sinatra. Landau-khalatnikov phonon damping in strongly interacting fermi gases. *EPL (Europhysics Letters)*, 116(4):40002, nov 2016.

[269] E. Hodby, O. M. Maragò, G. Hechenblaikner, and C. J. Foot. Experimental observation of beliaev coupling in a bose-einstein condensate. *Phys. Rev. Lett.*, 86:2196–2199, Mar 2001.

[270] N. Katz, J. Steinhauer, R. Ozeri, and N. Davidson. Beliaev damping of quasiparticles in a bose-einstein condensate. *Phys. Rev. Lett.*, 89:220401, Nov 2002.

[271] Yu. Kagan and L. A. Maksimov. Damping of trapped bose-einstein condensate oscillations at zero temperature. *Phys. Rev. A*, 64:053610, Oct 2001.

[272] L. Landau. Theory of the superfluidity of helium ii. *Phys. Rev.*, 60:356–358, Aug 1941.

[273] Anna Minguzzi, Gabriele Ferrari, and Yvan Castin. Dynamic structure factor of a superfluid Fermi gas. *The European Physical Journal D-Atomic, Molecular, Optical and Plasma Physics*, 17(1):49–55, 2001.

[274] S. N. Klimin, J. Tempere, and Jeroen P. A. Devreese. Pair excitations and parameters of state of imbalanced fermi gases at finite temperatures. *Journal of Low Temperature Physics*, 165(5):261, Sep 2011.

[275] H. Kurkjian, Y. Castin, and A. Sinatra. Concavity of the collective excitation branch of a fermi gas in the bec-bcs crossover. *Phys. Rev. A*, 93:013623, Jan 2016.

[276] R. Combescot, M. Kagan, and S. Stringari. Collective mode of homogeneous superfluid Fermi gases in the BEC-BCS crossover. *Phys. Rev. A*, 74(4):042717, October 2006.

[277] Yvan Castin, Igor Ferrier-Barbut, and Christophe Salomon. The landau critical velocity for a particle in a Fermi superfluid. *Comptes Rendus Physique*, 16(2):241–253, 2015.

[278] Abad, Marta, Recati, Alessio, Stringari, Sandro, and Chevy, Frédéric. Counter-flow instability of a quantum mixture of two superfluids. *Eur. Phys. J. D*, 69(5):126, 2015.

[279] PO Fedichev and GV Shlyapnikov. Critical velocity in cylindrical Bose-Einstein condensates. *Phys. Rev. A*, 63(4):045601, 2001.

[280] Pierre-Philippe Crépin, Xavier Leyronas, and Frédéric Chevy. Hydrodynamic spectrum of a superfluid in an elongated trap. *EPL (Europhysics Letters)*, 114(6):60005, 2016.

[281] Vijay Pal Singh, Wolf Weimer, Kai Morgener, Jonas Siegl, Klaus Hueck, Niclas Luick, Henning Moritz, and Ludwig Mathey. Probing superfluidity of Bose-Einstein condensates via laser stirring. *arXiv preprint arXiv:1509.02168*, 2015.

[282] Wolf Weimer, Kai Morgener, Vijay Pal Singh, Jonas Siegl, Klaus Hueck, Niclas Luick, Ludwig Mathey, and Henning Moritz. Critical velocity in the BEC-BCS crossover. *Phys. Rev. Lett.*, 114:095301, Mar 2015.

[283] C Raman, M Köhl, R Onofrio, DS Durfee, CE Kuklewicz, Z Hadzibabic, and W Ketterle. Evidence for a critical velocity in a Bose-Einstein condensed gas. *Physical Review Letters*, 83(13):2502, 1999.

[284] R Onofrio, C Raman, JM Vogels, JR Abo-Shaeer, AP Chikkatur, and W Ketterle. Observation of superfluid flow in a Bose-Einstein condensed gas. *Physical Review Letters*, 85(11):2228, 2000.

[285] K. C. Wright, R. B. Blakestad, C. J. Lobb, W. D. Phillips, and G. K. Campbell. Threshold for creating excitations in a stirred superfluid ring. *Physical Review A (PRA)*, 88(6):063633, 2013.

[286] D. E. Miller, J. K. Chin, C. A. Stan, Y. Liu, W. Setiawan, C. Sanner, and W. Ketterle. Critical velocity for superfluid flow across the bec-bcs crossover. *Phys. Rev. Lett.*, 99(7):070402, Aug 2007.

[287] Yusuke Nishida. Polaronic atom-trimer continuity in three-component Fermi gases. *Physical Review Letters*, 114(11):115302, 2015.

[288] Pines. *Elementary excitations in solids*. W.A. Benjamin, 1963.

[289] Temperley, Rowlinson, and Rushbrooke. *Physics of simple liquids*. Wiley Interscience Division, 1968.

[290] V. B. Bobrov. The relation between the static structure factor and the density-density response function in the long wave limit. *J. Phys.: Condens. Matter*, 2:3115–3118, 1990.

[291] Ljudvig D Faddeev and Stanislav Petrovich Merkuriev. *Quantum scattering theory for several particle systems*, volume 11. Springer Science & Business Media, 2013.

[292] Paulo F Bedaque, H-W Hammer, and Ubirajara Van Kolck. Renormalization of the three-body system with short-range interactions. *Physical Review Letters*, 82(3):463, 1999.

[293] Ren Zhang, Wei Zhang, Hui Zhai, and Peng Zhang. Calibration of the interaction energy between Bose and Fermi superfluids. *Phys. Rev. A*, 90(6):063614, 2014.

[294] Johannes Hofmann and Wilhelm Zwerger. Deep inelastic scattering on ultracold gases. *Physical Review X*, 7(1):011022, 2017.

[295] A. Camacho-Guardian, L. A. Peña Ardila, T. Pohl, and G. M. Bruun. Bipolarons in a bose-einstein condensate. *Phys. Rev. Lett.*, 121:013401, Jul 2018.

[296] Miki Ota, Stefano Giorgini, and Sandro Stringari. Magnetic phase transition in a mixture of two interacting bose gases at finite temperature. *arXiv:1812.07411v2*, 2019.

[297] V. N. Popov. *Functional Integrals and Collective Excitations*. Cambridge University Press, Cambridge, 1987.

[298] P. O. Fedichev and G. V. Shlyapnikov. Finite-temperature perturbation theory for a spatially inhomogeneous bose-condensed gas. *Phys. Rev. A*, 58:3146–3158, Oct 1998.

[299] S. Giorgini. Collisionless dynamics of dilute bose gases: Role of quantum and thermal fluctuations. *Phys. Rev. A*, 61:063615, May 2000.

[300] R. S. Lous, I. Fritsche, M. Jag, F. Lehmann, E. Kirilov, B. Huang, and R. Grimm. Probing the interface of a phase-separated state in a repulsive Bose-Fermi mixture. *PRL(Physical Review Letters)*, 120(24):243403, 2018.

[301] A. Bulgac and M. McNeil Forbes. Zero temperature thermodynamics of asymmetric Fermi gases at unitarity. *Phys. Rev. A*, 75:031605, 2007.

[302] K. Van Houcke, F. Werner, E. Kozik, N. Prokof'ev, B. Svistunov, MJH Ku, AT Sommer, LW Cheuk, A. Schirotzek, and MW Zwierlein. Feynman diagrams versus Fermi-gas feynman emulator. *Nature Physics*, 2012.

[303] Michael McNeil Forbes, Stefano Gandolfi, and Alexandros Gezerlis. Resonantly interacting fermions in a box. *Physical Review Letters (PRL)*, 106:235303, 2011.

[304] A. Bulgac, J.E. Drut, and P. Magierski. Spin 1/2 fermions in the unitary regime: A superfluid of a new type. *Phys. Rev. Lett.*, 96(9):90404, 2006.

[305] O. Goulko and M. Wingate. Thermodynamics of balanced and slightly spin-imbalanced Fermi gases at unitarity. *Phys. Rev. A*, 82(5):053621, 2010.

[306] E. Burovski, N. Prokof'ev, B. Svistunov, and M. Troyer. Critical temperature and thermodynamics of attractive fermions at unitarity. *Phys. Rev. Lett.*, 96(16):160402, 2006.

[307] M. Horikoshi, S. Nakajima, M. Ueda, and T. Mukaiyama. Measurement of universal thermodynamic functions for a unitary Fermi gas. *Science*, 327(5964):442, 2010.

[308] R. Rossi, T. Ohgoe, K. Van Houcke, and F. Werner. Resummation of diagrammatic series with zero convergence radius for strongly correlated fermions. *Phys. Rev. Lett.*, 121:130405, Sep 2018.

[309] Thomas Bourdel. *Gaz de Fermi en interaction forte: du condensat de molécules aux paires de Cooper.* PhD thesis, Université Pierre et Marie Curie - Paris VI, 2004.

[310] Yusuke Nishida. New type of crossover physics in three-component Fermi gases. *Physical Review Letters*, 109(24):240401, 2012.

[311] Mattia Jona-Lasinio and Ludovic Pricoupenko. Three resonant ultracold bosons: Off-resonance effects. *Physical Review Letters*, 104(2):023201, 2010.

[312] Xiaoling Cui. Atom-dimer scattering and stability of Bose and Fermi mixtures. *Phys. Rev. A*, 90:041603, Oct 2014.

RÉSUMÉ

La physique des systèmes quantiques à N corps fortement corrélés est un problème très riche au cœur de nombreuses recherches actuelles. En particulier, ces systèmes peuvent posséder des propriétés spectaculaires à l'échelle macroscopique, comme la superfluidité. Les gaz d'atomes froids constituent d'excellents systèmes pour l'étude du problème à N corps du fait de leur grande versatilité et de leur haute contrôlabilité. Cette thèse porte sur l'étude des propriétés d'une impureté plongée dans un gaz de fermions superfluide à deux composantes à travers le crossover BEC-BCS.

Nous étudions expérimentalement le temps de vie d'impuretés bosoniques dans un superfluide fermionique ainsi que les interactions entre impuretés et fermions. La mesure du temps de vie des impuretés dans le superfluide nous renseigne sur la stabilité du système et nous permet d'obtenir le contact de Tan pour deux fermions, lié à la physique des corrélations à courte portée au sein du superfluide dans le crossover. L'étude des interactions entre une impureté et le superfluide est réalisée en analysant les oscillations d'un gaz d'impuretés à l'intérieur du superfluide.

Finalement, nous menons une étude théorique du diagramme de phase de l'impureté faiblement couplée au superfluide, avec une étude approfondie de l'énergie du polaron au-delà de l'approximation de champ moyen en régularisant ce problème à 2N+1 corps grâce à l'utilisation d'une interaction à trois corps. Du point de vue qualitatif, l'obtention de l'énergie de ce système à travers le crossover BEC-BCS nous permet de faire le pont entre les descriptions du polaron de Bose et du polaron de Fermi. Du point de vue quantitatif, ce calcul fournit une correction au terme de champ moyen, nécessaire pour atteindre un accord au pour-cent près entre la théorie et l'expérience, un des objectifs de la physique des systèmes quantiques.

MOTS CLÉS

atomes froids, système quantique à N corps, impureté, polaron, crossover BEC-BCS, mélange Bose-Fermi

ABSTRACT

The physics of strongly correlated quantum many-body systems is a very rich problem under heavy investigation. These systems can present many spectacular properties at the macroscopic scale such as superfluidity. Cold atom gases are excellent systems to investigate quantum many-body physics thanks to their great versatility and their high degree of controllability. This thesis deals with the study of the properties of an impurity immersed in a two-component Fermi superfluid, through the BEC-BCS crossover.

We measure experimentally the lifetime of boson impurities immersed in a Fermi superfluid, as well as the fermion-impurity interactions. The lifetime measurements not only informs us on the stability of the system but also on the short-range correlations of the Fermi gas by giving us access to the two-body fermionic contact parameter. The study of the impurity-fermion interactions is realized with the analysis of the oscillations of a gas of impurities inside a Fermi superfluid.

Finally, we pursue a theoretical study of the phase diagram of an impurity interacting weakly with a Fermi superfluid, as well as a calculation of the polaron energy beyond the mean-field approximation, obtained after a regularization of this 2N+1 body problem using a three-body interaction. Qualitatively speaking, obtaining this energy in the BEC-BCS crossover allows us to bridge between the descriptions of the Bose polaron and the Fermi polaron. Quantitatively-wise, this calculation provides a correction beyond the mean-field term, needed to achieve a percent-level agreement between theory and experiment sought in quantum many-body physics.

KEYWORDS

cold atoms, quantum many-body systems, impurity, polaron, BEC-BCS crossover, Bose-Fermi mixture